

Final Report

Small Autonomous VTOL
Electric Drone
DSE16 Spring 2020



Final Report



saved

Small Autonomous VTOL Electric Drone

by

I. Benyahia - 4662679
C. Bononi Bello - 4667530
P. Campolucci - 4645979
M. Desiderio - 4644158
R. van Ewijk - 4643658
C. Kanaar - 4534034
M. Martinez Ruts - 4656008
A. Nederkoorn - 4559118
E. Pinheiro De Melo Perestrelo - 4648706
E. Rodriguez Plaza - 4649060
M. Trávník - 4652738

on

Friday 27th November, 2020

to obtain the degree of Bachelor of Science

at the Delft University of Technology,

Project duration: April 20, 2020 – July 3, 2020
DSE committee: Dr. Ir. M. I. Gerritsma Tutor
Dr. A. Sciacchitano Tutor
Dr. Ing S. G. P. Castro Coach
Ir. S. Luesutthiviboon Coach

Preface

This project was carried out by 11 students from the Faculty of Aerospace Engineering at Delft University of Technology as part of the Design Synthesis Exercise (DSE AE3200) to obtain a degree of Bachelor of Science in Aerospace Engineering. The project was carried out by working daily from 20-4-2020 until 3-7-2020. This document is the final report in a series of 4 reports.

A special note should be taken that this project was carried out during the COVID-19 crisis. As a result, all communication and collaboration was limited to online means. We are grateful that despite this crisis, the outcome of the project, together with all communication between colleagues, tutors and coaches, came to a satisfying result and we therefore thank Delft University of Technology for making it possible for us to carry out this project online.

We would like to thank everyone involved in contributing to the project. First of all, we are especially grateful for the continuous support and guidance provided during this DSE by our tutors and coaches, Dr. Andrea Sciacchitano, Dr. Ir. Marc Gerritsma, Dr. Ing. Saullo Castro and Ir. Salil Luesutthiviboon.

Additionally, we would like to thank the external experts and teaching assistants involved in the detailed system design. Namely, our thanks go to Sam van Elsloo, Dr. Calvin Rans, Dr. Ir. Tomas Sinnige, Dr. Ir. Roelof Vos, Ir. Jos Sinke and Ir. Mario Coppola.

We look back on a challenging project, in which each of us applied knowledge obtained in the Bachelor of Aerospace Engineering in order to achieve the best design possible.

Executive Overview

SAVED - acronym for Small Autonomous Vertical take-off and landing (VTOL) Electric Drone - is a long range, electric, vertical take-off and landing drone used for the delivery of small medical supplies.

On the 21st of April 2019, Easter Sunday, eight suicide bombers killed 269 people and injured more than 500 others on the island of Sri Lanka. The high number of casualties that resulted from this terrorist attack caused an overflow of patients requiring treatment in the cities where the blasts took place. Despite the country having enough blood to meet the emergency demand, there was still a shortage of blood in the hospitals. This shortage arose from the country lacking an effective delivery system to transport blood to the areas most in need. The Easter Sunday attacks in Sri Lanka placed a major spotlight on the need for better emergency delivery of medical supplies such as blood and life saving medicine. Unfortunately, this need is not uncommon in developing countries and these attacks are only one example of many that shows how, in emergency situations, the performance of a country's healthcare logistics system can mean life or death for many people. Current methods of transportation, especially to remote areas, are extremely inefficient and become restricted during the rain season when roads become inaccessible.

SAVED's end goal is to address the so-called 'last mile problem' by better connecting people in remote rural regions with the larger network of national health distribution. SAVED will be a drone service that ensures on-demand, just-in-time delivery of medical supplies from a centralised inventory to any location. This will allow for faster treatment of patients, reduced stock-outs and a drastic reduction of medicine wastage, in order to ultimately improve the healthcare system and reduce the number of preventable deaths in developing countries.

Nowadays, about 13% of the world's population has no access to all-season roads. Additionally, about 45% of the world's population lives in rural areas. Consequently, villages rely on small and isolated medical centres for basic treatments. It is difficult to consistently supply these remote medical centres and this leads healthcare systems to experience high levels of medicine waste, high numbers of stock-outs, long delivery times for lifesaving treatments, as well as expensive emergency delivery trips. These flaws, which have been present in healthcare systems for decades, are now being augmented and brought to focus of public attention following the COVID-19 global pandemic.

Rural areas are often hardly accessible by road, leaving aerial transport as the only alternative for delivery of medical goods. Using autonomous drones for the delivery of medical supplies is not a novel idea, as multiple companies and organisations are already providing such services. Currently, the biggest competitor is Zipline. Zipline's main drawback, however, is the inability to perform a VTOL manoeuvre, limiting Zipline's mission capabilities and requiring additional infrastructure for drone launch and recovery. Other players in the autonomous drone delivery business consist of Vayu and Wingcopter, both capable of performing a VTOL manoeuvre but lacking a long-range capability like Zipline. An analysis of the current competitive landscape identifies the gap in the market as the need for a medical delivery drone with both VTOL capability to diversify its mission applications and a long range to carry life saving medicines to the most remote locations. This is the gap in the market that SAVED aims to fill.

The profile of a typical mission performed by SAVED starts with the reception of a medical supplies request. Immediately after it, the operators collect the requested medical items and load them, together with the batteries, into the drone. SAVED then switches on and performs a series of automatic pre-flight check and, if the outcome is positive, then the take-off procedure is initiated. Once the drone leaves the ground, it climbs in VTOL mode for about 20 meters and successively to a horizontal attitude and climbs to a cruise altitude of 500 meters, until it is sufficiently close to the target location; at this point the descent and landing phase is initiated. SAVED is able to autonomously recognise the landing spot and thus deliver the payload. The ground medical crew is also able to load SAVED with a return payload, blood samples for instance. Once the drone is cleared for take off, the process is repeated for the return trip to the base.

System Design

SAVED's system design aims to organise all technical departments into one coherent design process. This organisation is essential in order for all the technical departments to effectively communicate and adhere to the same design process. The process for this report starts with the results from the midterm phase, and ends with a well defined design process and system level configuration all technical departments can adhere to.

Summary of Design Trade-off

During the midterm design selection process four distinct drone designs were traded off against each other on the basis of four trade criteria: energy consumption, unit cost, sustainability and reliability. However, there was no clear winner of this selection process. For this reason, an additional concept was developed, exploiting the advantages of the best candidates in the original trade-off. This design then conclusively outperformed the previously proposed ones. In short, the design is a flying wing tail-sitter configuration. It takes off vertically from the ground where it sits on the tips of its wings and the tips of vertical fins. It then transitions to climb and consequently cruises as a typical flying wing would. It is equipped with four non-tiltable engines, used in both vertical and horizontal flight. There is a large elevon (a flap at the trailing edge) on each wing which, together with the engines, helps to provide three-axis control to the drone.

System Overview and Final Design Process

To be able to design the drone on a subsystem level, there first needs to be a clear layout of the overall system and the way in which subsystems themselves influence this layout. The decision was made to concentrate all major subsystems (battery, payload hold, avionics etc.) at the centre of the drone. This is done to avoid control and stability issues and to use the available space as efficiently as possible. A high-level overview of the design process is then as follows. Starting with some initial knowledge about the system (mass budget, wing loading, etc.), a wing planform is designed to conform to stability, trim and stall requirements. Using the newly defined geometry of the wing, subsystems are designed and the performance of the system is evaluated. This may result in an increase/decrease in the assumed mass. Due to this, the process turns into an iterative one, going back to the design of the wing planform design when all updated parameters become known. The design process started with an overall mass budget of 17.8kg and converged to a value of 17.4kg.

Wing Planform and Body Design

The planform parameters that needed to be determined were: surface area, aspect ratio (slenderness), sweep, taper ratio and twist. The surface area follows directly from the total mass and wing-loading. The aspect ratio is then dependent on the surface area and the wingspan (which is fixed to 3 m). Sweep and taper were tuned to achieve a balance between longitudinal stability and trimmability. The resulting planform was an untwisted wing with a quarter chord sweep of 16° and a taper ratio of 0.4.

Finally, as mentioned earlier, most major components are concentrated at the centre of the wing. This means that the required thickness is much larger in the centre than further along the wingspan. This creates the need for a central bulge body. This bulge is designed to envelop the central components without creating a large disturbance to the airflow over the wing (it is to be blended with the wing).

Subsystem Design

This part of the report presents a subsystem design and analysis of each technical department in accordance with the design process defined by the systems engineers. A well defined technical design is essential in ensuring the system complies with all its requirements. Each of the upcoming designs and analyses have been verified and validated in order to assert correct implementation.

Power and Propulsion Design and Analysis

An advanced design of the power and propulsion system is essential in order to meet the challenging range requirement of 150km, whilst flying fully electric and having VTOL manoeuvres in the mission profile. The objective was therefore to select high quality off-the-shelf components that are compatible with each other. First of all, a suitable battery was selected. After a thorough analysis of potential batteries, the KOKAM battery pack was selected as the main battery, mainly due to its incredible specific energy of 246Wh/kg. Thereafter, a detailed trade-off has been performed to select the most desirable propeller-engine configuration. First, a list of potential configurations was made. Thereafter, it was assessed if these configurations met the noise requirements set for take-off and cruise. If this were the case the configuration would participate in the trade-off. In the end, the most suitable engine turned out to be the model KDE4215XF-465 with a compatible triple blade propeller with a 15.5 inch diameter. Based on the chosen engine-propeller configuration the lightest compatible electronic speed controller was selected. All these electrical components, together with the required sensors to ensure the autonomous capability create SAVED's electrical map.

Materials Selection, Structural Design and Analysis

The objective of the Structures, Materials and Manufacturing (SMM) Department has been to find the right balance between performance, reliability, ease of manufacturing and maintainability, while keeping the mass at a minimum. This balance was achieved by extensive use of aluminium and thermoplastic composites to build a box-like wing structure. The skin is held in place by metal clips, which reduce assembly and disassembly time, while still ensuring structural integrity. A structural analysis software was developed and validated in order to perform optimal sizing of the structure. Overall, the structural mass is computed to be of 8kg, which is 300g lighter than the set target, while ensuring multiple fail-safe features. Lastly, it is worthy to note that all the subsystem requirements set during the previous design phase have been successfully met.

Aerodynamic Design and Analysis

SAVED's aerodynamic performance is essential in order to meet the stringent range requirement of 150km whilst flying fully electric. The aerodynamic design of the aircraft is thereby closely related to its energy consumption. The target was therefore to design the aerodynamic performance to be as efficient as possible while keeping into account the requirements of other subsystems and departments. The CAL4014L airfoil was selected to be the most desirable airfoil for SAVED's mission profile. The full aircraft according to the earlier defined design specifications was then analysed using DATCOM and XFLR5 in order to obtain the aerodynamic performance parameters (such as L/D , C_{D_0} , α_{stall} , etc.) necessary for the flight performance, power, and propulsion department to compute if the current design iteration met the required range. Finally, a propeller-wing interaction analysis was performed in order to analyse the effects of the propellers on the aerodynamic loads, stall performance, and velocity profile of the main wing for the defined propeller rotational directions. The propeller-wing interaction analysis showed that the propellers, in their current configuration, proved to be beneficial for the aircraft's stall performance and VTOL controllability, and the structure was sized according to the induced aerodynamic loads.

Stability Performance and Analysis

After the design of the subsystems and its preliminary integration, the stability properties of the system were analysed. This was done to ensure that SAVED was stable to an acceptable extent with the aid of control inputs. Therefore, the analysis is twofold. While static stability is ensured by means of a correct system integration and planform design, the dynamic characteristics are still unknown and thus, to analyse them, a numerical model is constructed. The results of this model assert the static and dynamic longitudinal stability. Moreover, the stability derivatives gathered prove that the landing fin, sized for landing, is sufficient for directional stability. Nonetheless, the dynamic analysis of the lateral behaviour of SAVED showed an unstable eigenmotion, the spiral, which is seen to diverge the lateral states after long periods of time, for which it needs to be correctable with active elevon control. Given the slow period of the spiral, however, this correction is considered feasible. Therefore, while SAVED is entirely stable longitudinally, it is only stable laterally with active control.

Control System and Simulation

A fully autonomous drone has to include an autonomous control framework that determines the control inputs given the state of the drone and the reference state. Throughout the mission it is very important that the position of the drone can be controlled; especially during vertical flight, when it has to avoid obstacles of known position and it has to land on the exact position given by the perception framework. In order to control the position of the drone, different control architectures have been designed to control the position of the drone. In order to do so, the control of the drone was first analysed in the three different axis and then the equations of motion that describe the dynamics of the drone were determined. Thereafter, in order to mimic a real plant (dynamics of the system), a simulation has been developed in Unity where the equations of motion have been modelled. The simulation on Unity has allowed to visualise and analyse the response of the drone to certain control inputs. With that, the controllers have been designed such that the drone state quickly converges to the reference state.

Path Planning

A fully autonomous drone has to determine autonomously a path that connects the drone with the target location. To do so, a path planning framework has been developed. Determining the optimal path does not only consist on determining the shortest path, but a path that improves the mission characteristics. Such path has to avoid known obstacles, navigate in advantageous weather conditions, avoid no-fly areas and avoid highly populated areas so that the noise is generated far from urban areas. A path planning framework has been developed that

accounts with the aforementioned characteristics. This has been done by modelling a cost map that determines how expensive (or inconvenient) it is for the drone to be located in certain areas. Based on this model, the A* algorithm has been used to find the shortest path. Finally a replanning framework has been built to continuously replan the path, since the characteristics of the mission are continuously changing.

Perception Pipeline Design and Analysis

A fully autonomous flying vehicle needs to have a clear and complete sensing of the nearby environment, and take decisions based on it. This is required, in the case of a typical SAVED mission, in order to avoid the presence of unexpected obstacles and detect the position in space of the landing point. To tackle the first issue, a low weight LiDAR sensor, the Velabit™ is placed at the nose of the drone: its 100m lookahead distance and 60° field of view allow for rapid and complete detection of objects that risk to collide with the drone. In order to detect the landing point, a stereo cameras are equipped with YOLO, a deep learning neural network for fast object detection and EdgeStereo, a state of the art depth estimation algorithm. The setup is capable of detecting circular landing points of 3m in diameter at a height of 25m, allowing for safe vertical landing.

State Estimation Design and Analysis

As SAVED is expected to perform the mission given only the initial path coordinates from point A to point B, an accurate and reliable navigation infrastructure is essential. Drone's state can theoretically be estimated with a Global Positioning System (GPS) and a triad of gyroscopes, but such setup is not enough to cope with sensor malfunctioning. As flying vehicles need to be highly reliable, this is therefore not acceptable. To find the right set of sensors in order to increase the robustness of the system, a risk assessment is conducted on its state estimation pipeline, considering the several scenarios where the drone might loose its autonomy. The output of the assessment resulted in a navigation system provided with a GPS, an Inertial Measurement Unit (IMU), a pitot tube, a barometer, a Visual Inertial Odometry (VIO) algorithm and a safe flight-back-to-base emergency program based on a Simultaneous Localisation and Mapping (SLAM) algorithm. Redundant inputs from different sensors are expected to be unified trough an Extended Kalman Filter (EKF), to minimise the accumulation of errors. Non-visual inputs are processed in the PixHawk4 flight controller, while visual ones are retrieved by means of the same cameras used for landing point detection and processed in an external computer, in this case the Raspberry Pi 3B+.

System Characteristics

With the system design and all subsystem design and analysis in place, the system characteristics present a final overview of the designed system from a top level. This presentation is included for the reader to attain an overview of the designed system's performance characteristics, its layout, and its measure of compliance with the initial set requirements.

Flight Characteristics

The flight characteristics shows SAVED's flight performance as a system as a whole. This final system analysis is essential for asserting the compliance of the system with the top level requirements. A flight envelope diagram shows a maximum load factor of 3.8, a minimum load factor of 1.52, and a dive speed of 31.2m/s. A payload-range diagram shows that SAVED's meets the 150km range requirement for the most stringent mission profile: A two-way journey with payload of 3kg on the outward trip and 0kg payload on the return trip an at end-of-life conditions. A performance sensitivity analysis is performed in order to assess the robustness of the system with respect to the system requirements. It is concluded that the structural mass can be increased by 3.7% and the zero lift drag coefficient by 4% whilst still complying with the range requirement.

System Requirements Compliance

A number of requirements have been defined over the course of the design process. However, the most important ones (key requirements) were defined by the customer at the very beginning of the project. The team has been able to verify that the design already complies with six out of nine of these key customer requirements. Most importantly, it was verified that SAVED is able to complete a delivery mission to a target which is located 75km from the base with 3kg, being able to return back without payload. In addition, two requirements which are not possible to verify yet were designed for and will be tested once a prototype is developed. Lastly, a key requirement stating that the design shall satisfy EASA (European Union Aviation Safety Agency) regulations to be considered 'certified' has been partly possible to verify at this point and it will be examined further in the

development process that follows.

Technical Risk Management

SAVED being a fully autonomous delivery drone is in general defined as a high risk system. In order to ensure that SAVED has a high reliability and will not harm itself or any third parties during the mission, SAVED has been designed to mitigate the potential risks to the largest extent possible. 5 risk levels have been distinguished, based on the probability of occurrence and the impact on the performance. After the implementation of the mitigation techniques SAVED has an average risk score of 1.7 out of 5. This is deemed an acceptable risk level for SAVED.

Final Layout

A representation of SAVED's final layout concludes this system characteristics section. SAVED has a wingspan of 3000mm, a length of 836mm and a height of 673mm. The maximum take-off mass is of 17.4kg, 3kg of which consists of payload and 3.6kg of batteries. The cruise speed is of 81km/h and the single trip range, at the beginning of operational life, is of 221km.

Future Project Design and Development

With the top level system overview in place, the attention can be turned to all future operational related activities. These future project design and development activities are essential for a successful launch of SAVED on the market and are therefore extensively discussed in this part of the report.

Production Plan

SAVED's innovative structural design focused on low-weight, easy accessibility and recyclability. A preliminary production plan was devised to identify the manufacturing and assembly processes. Due to the relatively low production numbers, it was decided to outsource the manufacturing of most parts to subcontractors. Only the skin, laser cut parts and 3D printed attachment frames will be self-produced. The assembly process will take place in the same facility, which is envisioned to be in the north-west of Europe, for its good infrastructure and highly skilled workforce. The final assembly is divided in three sub-assemblies for production and mounting purposes: The two outward wing sections and the centre fuselage bulge. A preliminary estimation was made for the manufacturing costs, taking into account the labour, material and tooling costs. The total manufacturing costs amounted to €12.000 per unit. This estimate was expected to decrease significantly, if production numbers increase.

Operational Concept

The operational concept is to provide an alternative solution to the time consuming logistics of road transport. In many countries, critical goods are only centralised at far reaching locations, for which they cannot respond in time to situations of emergency. The operational concept thus aims to change this pull system to a push-pull one by setting a network of bases where the goods are delivered systematically and SAVED has freedom of delivery within its range. Each of these bases consists of a module for storage of goods and recharging of batteries, VTOL platforms, a hangar to store the systems, PV arrays to sustain the energy needs of the base, with the latter managed by technicians. Studying the specific case of Sri Lanka, a prime candidate as country of operations, it is seen that four bases are sufficient to cover all of the General District Hospitals. To ensure availability in all of the possible situations, as well as to depreciate the initial investments, the choice is made to have a drone for each 248,000 inhabitants, for which a total of 22 drones per base are needed. Lastly, a stringent traffic management plan is needed. This focuses on the administrative compliance, adhering to the laws and implementing all constraints into the path planning algorithm. This, together with the collision avoidance algorithm, is to ensure the safest autonomous flight, which is to be overseen by a technician at all times.

Logistical Concept

A feasible logistical concept is fundamental to support the operations of SAVED. These logistics consist of testing, manufacturing, assembly and transport. First, the testing planned depends on the department and its components. For instance, the engine and batteries are to be checked to comply with the manufacturer specifications, while the aerodynamics department has two wind tunnel tests planned. To validate the analysis

on stability and controllability, however, a prototype is built and a test flight performed. When it comes to manufacturing and assembly, most parts are outsourced to subcontractors. The rest are self produced in the assembly facility to save on transport costs. The manufacturing and assembly is to be done in Europe, where the high quality materials and skilled workers can be attained. The assembled system is then transported to the country of operation by boat using rigid containers.

RAMS

In the RAMS analysis the reliability, availability, maintainability and safety of the drone are assessed. It is of utmost importance that these criteria are taken into account while designing, as it will significantly reduce the costs of the drone in the future. The RAMS analysis mostly sums up the work done in the Technical Risk Management and the Operations chapters. First of all, due to the extensive risk mitigation performed while designing, SAVED is deemed to be as reliable and safe as possible. Second of all, regarding the maintainability, several design considerations have been included to reduce the maintenance time significantly. For example, in SAVED's design there are only non-permanent joints considered in the part assembly. All these design considerations also have a positive result on the availability of the drone.

Sustainable Development Strategy

The strategy for a sustainable development of the project, implemented throughout the conceptual design, sees all of the requirements verified in this final phase. Firstly, already in the previous phase it was decided to use a fully electric propulsion system with rechargeable batteries, using a fully sustainable PV array as recharging point. Since no greenhouse gases are emitted during the operational life, a comparison of greenhouse gas emissions is made between the conventional alternative and SAVED accounting for its battery production. This results in verifying the requirements on greenhouse gas emissions. For the sound levels, it is gathered that the noise generated in sound pressure level is 106.2 dB at a distance of 1.5 metre during VTOL and 9.02 dB at a distance of 500 metre during cruise, complying with the requirements. This noise pollution is also avoided by setting in the path planning algorithm a constraint not to fly over areas with a population density of over 20,000 inhabitants per kilometre squared outside a range of 10 km from the target location. When it comes to the SMM department, recyclability requirements are verified by having a total structural weight percentage of 42.3% from recycled materials and a 91% of recyclable ones. Recommendations are made during manufacturing to follow a lean manufacturing methodology. Lastly, the use of separable joints is used for ease of assembly and decommission. In the aerodynamics department, economic sustainability is accounted for when an existing airfoil is selected, reducing the resources for testing. Lastly, sustainable development is also accounted for in the business and operational perspective. This is done by the means of assessing the economic feasibility of the transport and distribution and RAMS aspects of the design.

Business Plan and Financials

In order to launch SAVED, it must meet technical requirements, however it is of paramount importance that a valid and trustworthy business plan is set up. A potential business model is set up which features several important aspects. These incorporate the identification of a potential customer, specific value proposition, partnership & stakeholders, channels of interaction and distribution and revenue streams. For the cost, the analysis was divided into multiple sections. These exist of the development costs, the unit production costs of SAVED, other non-recurring costs such as the mass production of the drones and the bases. Also, recurring costs such as the salaries of the employees need to be taken into account. The production of one drone resulted to be around €16,000. The final cost of all the aforementioned types of costs sum up to €3,500,000. This excludes the recurring costs, since these need to be paid each month and always needs to be done. Moving on, one has the revenues, provided by the Sri Lankan government, is approximated to be €600,000 for all bases. Finally, to obtain the money back from the €3,500,000 investment made, it was estimated that SAVED can break-even after approximately 6 months and can even make a profit of 100 % of the investment costs after one year. To make this project possible, it is important to find institutions, which can possibly fund the initial costs. These can be either private investors or public investors.

Contents

1	Introduction	1	8.5 Final Structural Mass Breakdown	50
I	Project Setup and System Design	3	9	Aerodynamic Design and Analysis 51
2	Market Analysis	4	9.1 Main Wing Airfoil Selection.	51
	2.1 The Last Mile Problem	4	9.2 Aerodynamic Characteristics	54
	2.2 Market Need For On-Demand Delivery of Health Products	4	9.3 Propeller-Wing Interaction Analysis	57
	2.3 Case Study: Sri Lanka	5	10	Stability Performance Analysis 64
	2.4 Secondary Market Opportunity	5	10.1 Preliminary Considerations	64
3	General Mission	6	10.2 Static Stability Analysis.	64
	3.1 Mission Profile	6	10.3 Dynamic Stability Analysis	65
	3.2 Functional Analysis.	6	10.4 Results	71
4	Midterm Selection Process Summary	10	10.5 Verification and Validation Procedures	74
	4.1 Description of Initial Design Concepts	10	10.6 Conclusions and Recommendations	76
	4.2 Concept Selection Process	10	11	Control System and Simulation 77
	4.3 Selected Concept Detailed Design	11	11.1 Reference Frames	77
5	System Overview and Final Design Process	12	11.2 Control Inputs.	78
	5.1 System Components and Positioning	12	11.3 Forces.	78
	5.2 Design Process.	13	11.4 Control Analysis	80
	5.3 Verification and Validation Procedures	14	11.5 Equations of Motion	81
6	General Planform and Fuselage Bulge Design	16	11.6 Control System Architecture	82
	6.1 Wing Planform Design	16	11.7 Controller Design.	82
	6.2 Elevon Sizing	23	12	Path Planning 85
	6.3 Preliminary Bulge Sizing	24	12.1 Cost Map	85
II	Subsystem Design and Analysis	25	12.2 Optimal Path Determination	85
7	Power and Propulsion Design and Analysis	26	12.3 Real-Time Replanning and Optimisation	86
	7.1 Electrical Layout	26	13	Perception Pipeline Design and Analysis 87
	7.2 Energy Consumption and Battery Selection	26	13.1 Design for Obstacle Detection	87
	7.3 Engine and Propeller Selection	34	13.2 Design for Landing Point Detection	88
8	Materials Selection and Structural Design	39	14	State Estimation Design and Analysis 95
	8.1 Functional Analysis.	39	14.1 Baseline Sensor Selection	95
	8.2 Requirement Analysis	39	14.2 Risk Hazard Identification and Mitigation	95
	8.3 Wing Box Design	40	14.3 Low Risk Design	96
	8.4 Other Structural Elements	48	15	Software and Hardware Integration 98
			15.1 Processor Selection	98
			15.2 Hardware and Software Diagram	98

III System Characteristics	100	23 Logistical Concept	126
16 Flight Performance Analysis	101	23.1 Testing Procedures	126
16.1 Performance Diagrams	101	23.2 Manufacturing and Assembly	126
16.2 Performance Sensitivity Analysis	103	23.3 Transport	126
17 System Requirements Compliance	104	24 RAMS Analysis	127
18 Technical Risk Management	107	24.1 Reliability	127
18.1 Risk Identification & Mitigation	107	24.2 Maintainability	127
18.2 Risk Prioritising & Mapping	109	24.3 Availability	128
18.3 Risk Response Planning	110	24.4 Safety	128
19 Final Design Overview	111	25 Sustainable Development Strategy	129
IV Project Design and Development	113	25.1 Power and Propulsion	129
20 Project Design and Development Overview	114	25.2 Structures, Materials and Manufacturing	130
21 Production Plan	116	25.3 Aerodynamics	131
21.1 Logistics of Manufacturing and Cost Estimation Method	116	25.4 Autonomous Flight	131
21.2 Parts Manufacturing	116	25.5 Business, Finance and Operations	131
21.3 Assembly Process and Mounting Divisions	119	25.6 Social Sustainability	132
21.4 Quality Control and Testing	120	26 Business Plan and Financials	133
21.5 Total Manufacturing Cost	121	26.1 Business Model	133
22 Operational Concept	122	26.2 Cost Analysis	133
22.1 General Concept for Operations	122	26.3 Revenue Estimation, ROI and Funding	135
22.2 Case Study	123	27 Concluding Remarks	136
		References	137

Introduction

Developed countries and areas benefit from the luxury of well developed transportation and infrastructure networks on all scale levels. Transport supply meets transport demand and infrastructure is present to accommodate this transport demand. As a result, travellers and cargo are able to be transported almost instantaneous to their target destinations. Additionally, critical supplies can reliably be shipped instantaneous within the required time frame based on demand. "However, this instantaneous access to critical goods and supplies is not a reality for all parts of the world. For example, a significant portion of the world's population (approximately 1 billion people [30]) lives in areas with underdeveloped transport and infrastructure networks. This makes supplying these regions with goods through conventional methods such as delivery trucks extremely difficult, if not impossible, as road networks are seasonally or permanently inaccessible. An especially troubling case is the supply of resources with high urgency, such as medicines, as these are often requested without much prior notice and need to be delivered within a short time after the request. Conventional solutions to this problem are only applicable in the long term, as the development of fully functioning road, rail, barge, or sea transport and infrastructure networks for these regions may take multiple decades [30]." [10]

The described problem is, at its core, the need for time efficient logistics during the delivery of critical supplies. This need originates in countries and areas where these critical goods are centralised in one location and cannot be transported to other regions within a reasonable span of time due to the aforementioned infrastructural shortcomings. This gives rise to the need for a fast implementable solution that bypasses conventional means of transportation.

A promising solution in places of insufficiently developed conventional transport and infrastructure networks is to transport critical supplies via aerial means of transportation. This report therefore focuses on providing a solution to the aforementioned problem by designing a Small Autonomous Vertical take-off and landing (VTOL) Electric Drone for long range small item delivery (SAVED) and all operations needed for a fully functioning drone delivery service. SAVED's end goal is to address the so-called "last mile problem" by better connecting people in remote rural regions with the larger network of national health distribution. A drone service that ensures on-demand just-in-time delivery of medical supplies from a centralised inventory to any location within range allows for faster treatment of patients, reduced stock-outs and a drastic reduction of medicine wastage, in order to ultimately improve the healthcare system and reduce the number of preventable deaths in developing countries. SAVED's key requirements are that it shall deliver critical supplies within a radius of 75 km with a maximum payload of 3 kg by means of an electrical propulsion system that is re-charged through renewable charging station while taking-off and landing vertically and having a sustainable decommissioning program. [9] showed that the most desirable configuration of such a drone is a flying wing with 4 engines and propellers and a vertical fin.

The aim of this report is to present SAVED's final design phase. This constitutes the presentation of SAVED's technical design and operational design. The technical design explores all subsystem design processes in detail in order show that the system complies with all requirements set in [8] and to justify the feasibility and validity of the solution. The operational design all systems outside the drone itself in order to ensure a fully functioning drone delivery service.

The aim is achieved according the following structure. The report consists of four parts ([Part I](#) to [Part IV](#)). [Part I](#) is defined as the project setup and system design and consists of [Chapter 2](#) to [Chapter 6](#). In this part, the project's fundamentals are laid out. In [Chapter 2](#), SAVED's need within in the current drone market is discussed. [Chapter 3](#) then describes SAVED's general mission profile and provides a functional analysis. In [Chapter 4](#), the midterm selection process is summarised and the starting point of the detailed design phase is identified. [Chapter 5](#) then gives an overview of the detailed design process. Finally, in [Chapter 6](#), the process of sizing SAVED's wing planform and main components is described. [Part II](#) is defined as the subsystem design and analysis and consists of [Chapter 7](#) to [Chapter 15](#). In this part each technical department presents its subsystem design. In [Chapter 7](#), SAVED's power and propulsion components are sized and selected. Next, in [Chapter 8](#) the structures and materials are designed and selected. Following this, in [Chapter 9](#), the aerodynamic performance is analysed. [Chapter 10](#) then performs an extensive stability analysis of the drone. [Chapter 11](#) elaborates on this analysis by providing an analysis of SAVED's controllability. [Chapter 12](#) then

explains the workings of the drone's path planning. Continuing, in [Chapter 13](#), SAVED's perception pipeline design is presented. Following this, SAVED's state estimation design and analysis is presented in [Chapter 14](#). Finally, all software and hardware integration is analysed and shown in [Chapter 15](#). [Part III](#) is defined as system characteristics, and consists of [Chapter 16](#), [Chapter 17](#), [Chapter 18](#), and [Chapter 19](#). In this part, the results from all subsystem designs and performance analyses of [Part II](#) are gathered in order to present an overview of the system's performance and layout as a whole. [Chapter 16](#) starts by evaluating SAVED's flight performance. Next, [Chapter 17](#) lists all system and subsystem requirements and checks whether the system complies with these requirements. Next, [Chapter 18](#) assesses the system's technical risk. Finally, the system's performance characteristics and layout are presented in [Chapter 19](#). Concluding, [Part IV](#) is defined as the future project design and development overview and consists of [Chapter 20](#) to [Chapter 27](#). In this part, all post-design synthesis exercise (DSE) design and development activities are presented in order to ensure a successful launch of SAVED on the market. [Chapter 20](#) starts by presenting an overview of all these activities. Next, [Chapter 21](#) presents the production plan of the drone. Following this, SAVED's operational concept is elaborated upon in [Chapter 22](#). SAVED's logistical concept is then described in [Chapter 23](#). Continuing, in [Chapter 24](#), SAVED's future activities relating to the improvement of reliability, availability, maintainability, and safety are elaborated upon. SAVED's sustainable development strategy is then discussed in [Chapter 25](#). In [Chapter 26](#), SAVED's final business plan and financial coverage is presented. Finally, some concluding remarks on the entire project are mentioned in [Chapter 27](#), thereby closing the report.



Project Setup and System Design

2

Market Analysis

There is no doubt that SAVED is in many ways a symbol of the constantly evolving field of technology. Using a small autonomous VTOL electric drone to deliver medical products to inaccessible areas is a good example of how technology can facilitate and even save the lives of countless people. In theory, the adoption of technologies like this one seems like a logical, natural and irrefutable path that will follow in years to come. In reality, however, this idea will never be more than a vision on paper without one crucial element - the single necessary and sufficient condition for a business to exist: a paying customer[6]. This means that a customer-driven approach to the design of this drone is imperative if real world problems are intended to be solved. [Section 2.1](#) introduces the current global humanitarian problem while [Section 2.2](#) explores the market need that stems from it. [Section 2.3](#) presents an example case study that will be used to define the operational and logistical concepts as well as the project's financial feasibility. Finally, [Section 2.4](#) considers the possibility of a secondary market opportunity that SAVED may want to explore in the future.

2.1. The Last Mile Problem

At the time of writing this report (June 2020), the ongoing COVID-19 pandemic has put a strong spotlight on healthcare systems all over the globe. Governments around the world are doing their best to organise people, institutions and resources to deliver health services to meet the current health needs of their populations. What may have previously been small flaws in these healthcare systems are now augmented and brought into the focus of public attention. One of the most problematic issues with healthcare systems, especially urgent in least developed countries, is the "last mile problem". The last mile problem is a phrase commonly used to refer to the difficulties involved in reaching rural, often isolated communities without paved roads and with little access to communication¹. In too many countries, delivering medical products to last mile communities is extremely costly, and even more so when roads become impassable during the rainy season.

2.2. Market Need For On-Demand Delivery of Health Products

To understand how SAVED could add value to developing countries it is important to understand the main problem. The customer, and key stakeholder, in this scenario is the government of a given developing country and their main concern is that their people have access to vital health products, even if they are located in remote, rural areas. There is thus an urgent need for a more effective healthcare logistical system - one that can deliver essential medical supplies to remote areas effectively and on-demand. A drone delivery system from a central storage facility with high stock levels of inventory to any remote area within a certain radius is a possible solution for this current problem. This solution offers a wide variety of benefits in both routine situations and emergency situations. In routine situations, the centralised inventory with just-in-time delivery drastically reduces the number of stock-outs in health facilities as well as the amount of medicine that goes to waste after expiring on the shelves. An example of a medical product where stock-outs and expires are common is blood, which must be kept refrigerated and expires after 42 days[61]. Moreover, a centralised medical storage facility allows for the most effective response to a national emergency situation. Whilst, most of the time, deliveries would be made for routine restocking, in case of an emergency, a drone delivery system can easily concentrate its activities and focus on providing a single remote area with as many medical products as needed in a short amount of time and without being restricted by bad weather. Reducing stock-outs, expiries, delivery times, and potentially the number of lives lost during emergencies are the main features a drone delivery service could offer to a healthcare system. There are a variety of drone-operating companies that focus on the delivery of health products, such as Zipline, Vayu and Wingcopter. Therefore, it is important that SAVED offers a product that will differentiate itself from these competitors and offer a unique service. A full analysis was done on the competitive landscape, examining potential competitors with different characteristics and capabilities, which can be seen in [8]. The main finding of this analysis was that there are two crucial characteristics that SAVED must have to effectively compete in the market: SAVED should be a long-range drone and should have VTOL

¹<https://bit.ly/3fOyBw6> [Cited 15-06-2020]

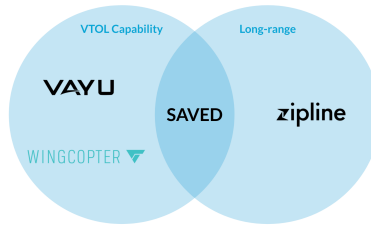


Figure 2.1: Visual depiction of the gap in the market

capability. In terms of range, SAVED should be able to fly at least 150km on one single trip, for the purpose of delivering to remote areas since it minimises the need for building, setting up and operating numerous bases, which represents a large portion of the costs involved. The VTOL capability would allow SAVED to perform missions that are simply not possible for non-VTOL drones, such as retrieving samples from a remote area with poor infrastructure back to the base. Meeting these two requirements will make SAVED a distinctive drone with unique benefits that will supersede any other existing competitor. [Figure 2.1](#) visually depicts this gap in the market and illustrates how SAVED will position itself to be the best drone delivery solution for the last mile problem of the healthcare sector.

2.3. Case Study: Sri Lanka

Although a lot of countries would benefit from a drone delivery service for the healthcare sector, identifying the initial target customer is extremely important. It was decided that for competitive purposes SAVED would not target a country where a similar company or project is already operating in. This issue is especially relevant with regards to the African continent. Although Africa has a lot of countries that fall victim to this last mile problem, there are already a variety of major players combating this struggle. For example, Project Last Mile has been addressing this issue since 2010 and has a strong presence in eight countries (Ghana, Liberia, Mozambique, Nigeria, Sierra Leone, South Africa, Swaziland, and Tanzania)². Additionally, the previously mentioned drone companies Zipline, Vayu and Wingcopter also have operations in countries like Rwanda, Madagascar and Malawi[33]. Although there are more countries in the continent, the ones most feasible for commercial drone operations in the healthcare sector in Africa already have a major player addressing their last mile problem[33]. After exploring a variety of options, Sri Lanka was selected as the best candidate. Although the World Bank praises Sri Lanka for its high-performing health system[31], it also ranks its medical logistics capabilities in the bottom half of all nations it examined³. Sri Lanka does not have any drone-operating company providing a similar service and experts such as Dr. Gotabhaya Ranasinghe, a cardiologist at the National Hospital of Sri Lanka, state that "transport by road is a waste of time and money" and that "drones are the ideal solution" for this problem of healthcare inaccessibility in rural areas of the country. The yearly monsoons bring heavy rainfalls to Sri Lanka for most part of the year, often making roads impassable and leaving many regions inaccessible by road.

2.4. Secondary Market Opportunity

As discussed, the primary market opportunity that SAVED will target is the healthcare logistics sector. However, one other key finding from the market analysis suggests a second possible market opportunity, which may likely evolve into a promising revenue stream in the near future. This refers to the prospect of selling SAVED drones directly to companies rather than using it to provide a drone delivery service. A long-range drone with a VTOL capability like SAVED could be used for a wide variety of tasks. Companies in numerous industries would be able to use the drone to carry out their own specific missions. The possible uses might include security & surveillance, aerial mapping, precision agriculture, conservation and research activities. The reason for including this secondary market is based on the increasingly rapid growth of the commercial drone market. As was found in [8], the commercial drone market will grow eight-fold by 2028 to amount to 66% of the global civil drone market, which will represent a 9.5 billion dollar industry [16]. It would be unwise not to capture this opportunity as the revenues obtained from it could substantially help fund a future expansion strategy into a different country or further technological developments in order to design future versions of the SAVED drone for longer range, faster deliveries or better capabilities. The direct sale of SAVED drones to companies should thus be considered as a secondary market opportunity that would ensure another solid revenue stream.

²<https://bit.ly/2zTqvDp> [Cited 15-06-2020]

³<https://bit.ly/3hWMmer> [Cited 15-06-2020]

3

General Mission

As mentioned in [Chapter 2](#), part of SAVED's complete operation constitutes flying the drone from the drone base to the hospital or medical centre and back. This part of SAVED's operations, which is carried out by the drone itself, is called the mission (the complete operation is described in [Chapter 22](#)). In this chapter, SAVED's general mission configuration is discussed. This is done before delving into detailed subsystem design and analysis in order for the technical departments to obtain an idea of the typical mission that has to be designed for. The general mission is explored by first evaluating the mission profile, followed by a more in depth view of the mission and functions revolving around the mission in the form of a functional analysis. The mission profile is discussed in [Section 3.1](#) and the functional analysis is discussed in [Section 3.2](#).

3.1. Mission Profile

SAVED's mission profile is shown in [Figure 3.1](#). From [Figure 3.1](#), it can be seen that SAVED takes-off vertically to an altitude of 20m [9] from the drone base with the payload required by the medical centre on board. After taking-off, it transitions from a vertical to a horizontal flight configuration and climbs to a cruise altitude of 500m [9]. It then cruises to the target location with a speed of 22.5m/s ([Section 9.2](#)) until it comes sufficiently close to start the descend to transition altitude. Once at the transition altitude, it transitions from a horizontal to a vertical flight configuration and descends to the landing point until ground is touched. The requested payload is then retrieved, and the process is then repeated for the return trip to the drone base. Once at the drone base, SAVED is charged, maintained, and made ready to use for the next mission.

3.2. Functional Analysis

The functional analysis provides a more detailed description of SAVED's mission and the procedures to be carried out in order to set-up and retire the mission. The functional analysis is split into a functional flow diagram (FFD), describing the sequential flow of the functions ([Subsection 3.2.1](#)), and a functional breakdown structure, describing the list of subtasks pertaining to each high level task ([Subsection 3.2.2](#)).

3.2.1. Functional Flow Diagram

The FFD describes the functions required to be performed in order to set-up, operate, and retire the mission in a sequential manner. The FFD is shown in [Figure 3.2](#). The numbering in [Figure 3.2](#) originates from the numbering in [Figure 3.3](#). Block 1 of the FFD (Design transportation system) relates to the design of the transportation system and is encapsulated by [Part II](#) of this report. Block 2 (Manufacture transportation system), relates to the manufacturing of the transportation system and is discussed in [Chapter 21](#). Block 3 (Distribute transportation system) relates to the distribution of the transportation system to the bases it should operate from. This is further discussed in [Chapter 23](#). Block 4 (Operate transportation system) then describes in depth how the mission discussed in [Section 3.1](#) is performed. Finally, Block 5 (Retire transportation system) discusses the retiring of end-of-life (EOL) transportation systems and is further described in [Subsection 25.2.4](#).

3.2.2. Functional Breakdown Structure

The FFD accurately describes the sequential process of the functions needed to be performed. However, functions may appear multiple times in the FFD, thereby saturating the overview of which functions exactly need to be designed for. The FBS serves to compensate for this. In the FBS, the low level functions pertaining to each high level function are broken down. The FBS is shown in [Figure 3.3](#).

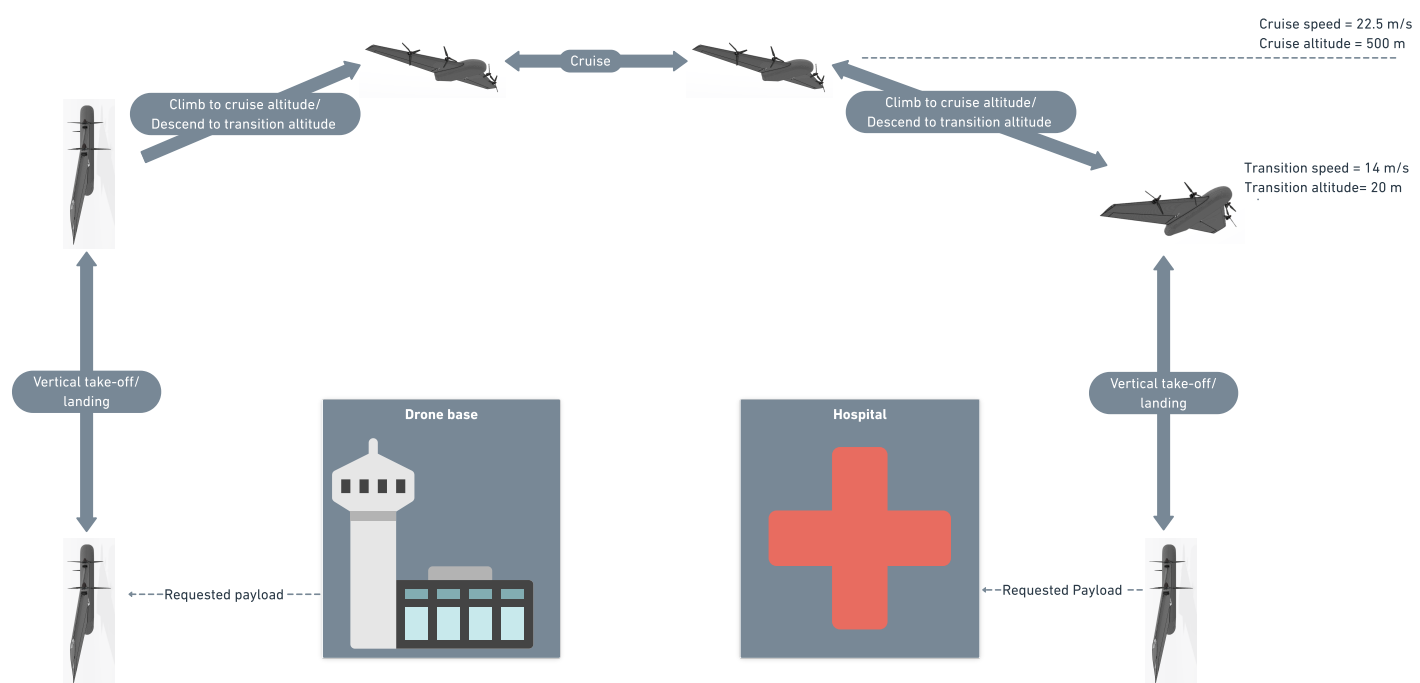


Figure 3.1: SAVED's mission profile

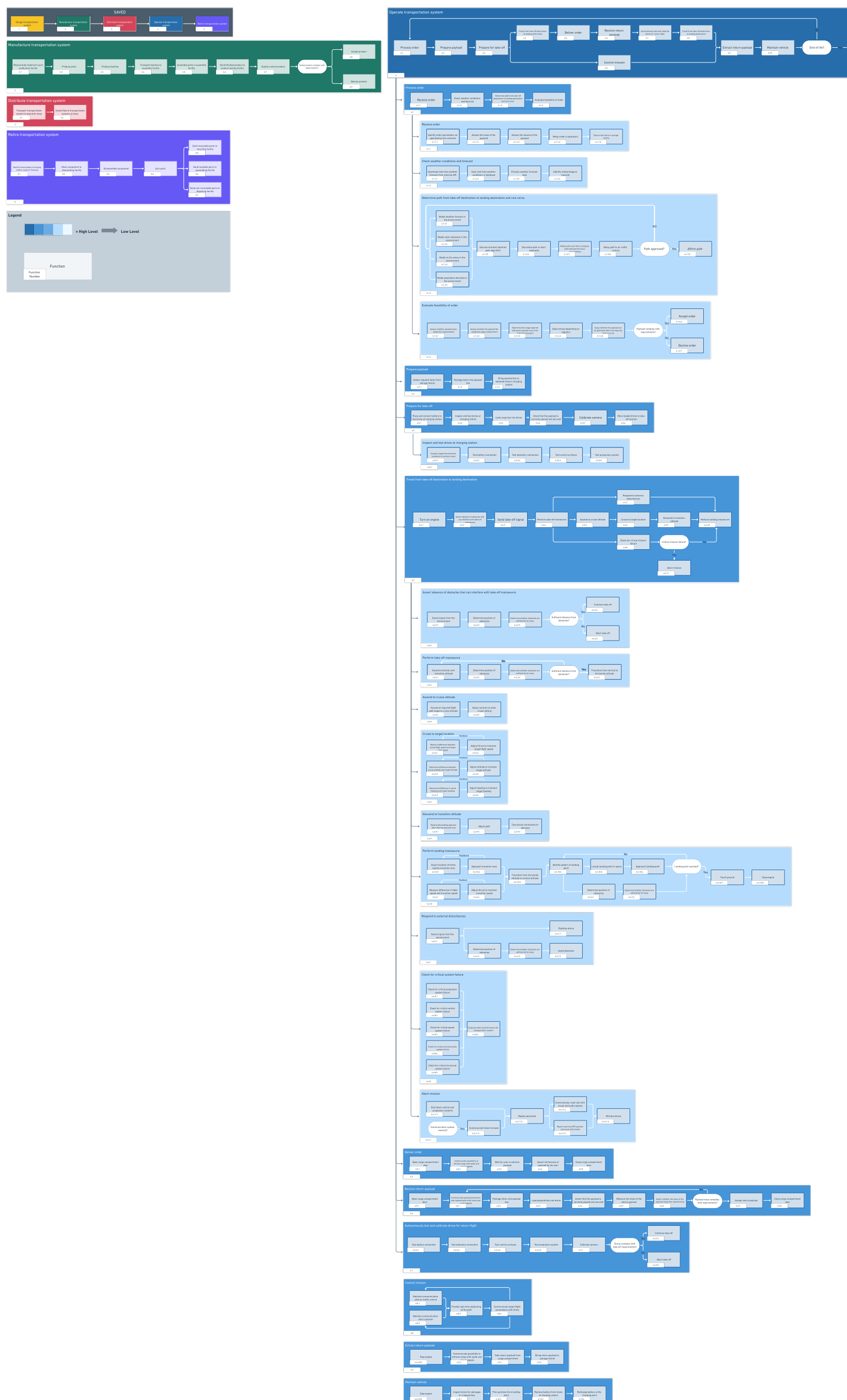


Figure 3.2: SAVED's functional flow diagram.

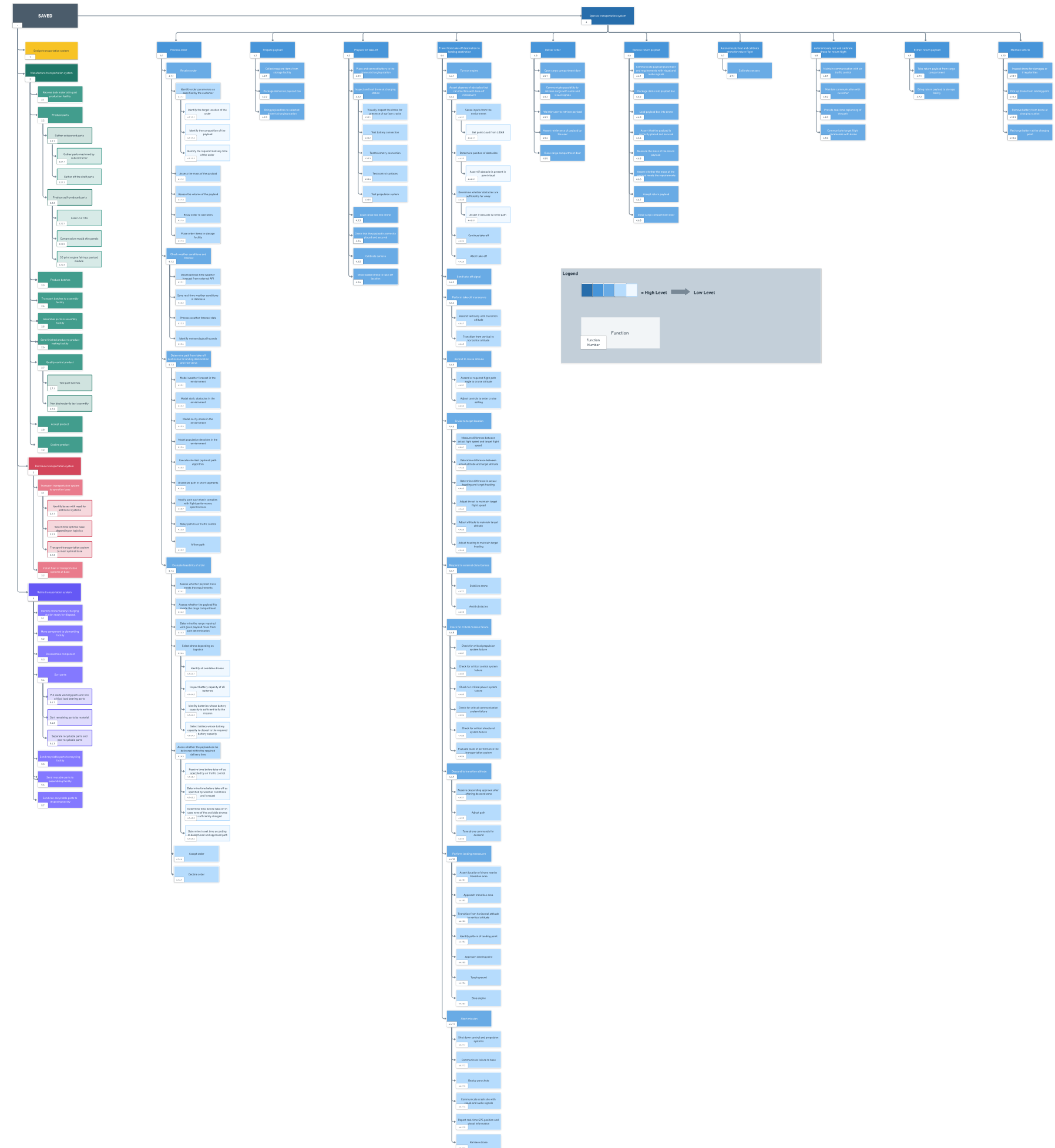


Figure 3.3: SAVED's functional breakdown structure.

4

Midterm Selection Process Summary

This chapter aims to serve an overview of the activities and findings of the design procedure during the midterm selection process. This stage of the design, which preceded the writing of this detailed report consisted most importantly of the selection process of the drone concept and acts as a starting point for the detailed design. In [Section 4.1](#) the concepts are shortly described. Thereafter, in [Section 4.2](#) the selection process and results are briefly summarised. At the end of this chapter, in [Section 4.3](#), the selected concept, which is the object of this detailed report is discussed in more detail. The key aspects identified in this concept from the starting point of the detailed design.

4.1. Description of Initial Design Concepts

At the start of the midterm design selection process, four inherently different concepts were conceived as a possible solution for the design problem stated in the mission objective [9]. These concepts are briefly summarised below:

- Concept A - **Flying wing configuration Pitch 2-rotor VTOL**: This concept, indicated in [Figure 4.1](#) uses a flying wing configuration with two propellers attached to the leading edge. It takes-off and lands vertically on its wing tips and landing fins and pitches at transition altitude to climbing and horizontal flight consequently.
- Concept B - **Bi-plane Flying wing configuration**: This concept, indicated in [Figure 4.2](#) uses two distinct wing planforms stacked in a biplane configuration with 2 rotors attached to each leading edge
- Concept C - **Conventional aircraft configuration**: This concept, indicated in [Figure 4.3](#), uses a tail configuration and 4 rotors, of which the 2 leading edge rotors are tilttable. Its VTOL operations are similar to that of a quadcopter, after which the front propellers tilt during transition.
- Concept D - **Flying wing configuration conventional 4-rotor VTOL**: This concept, indicated in [Figure 4.4](#), uses a flying wing planform, but has a quadcopter rotor configuration during VTOL operations. The front two propellers tilt after transition into cruise flight.

4.2. Concept Selection Process

During the midterm selection process the four concepts were evaluated and compared in terms of energy consumption, unit cost, sustainability and reliability. The energy consumption was an overall measure of how efficiently the drone flew its payload to the target range, the unit cost was a measure of how expensive it was to produce one unit, the sustainability was assessed in terms of recyclability and the reliability was scored by means of a technical risk assessment. The Bi-plane configuration, concept B, was discarded early on in this process for low performance expectations in energy consumption and the need for more time and resources to analyse. Concept A, C and D were analysed in more detail and in the end concept A scored the highest, closely followed by concept D. Due to the close scoring and uncertainty of the estimation, no clear winner could

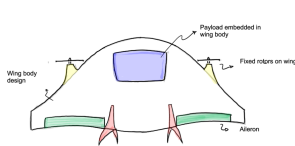


Figure 4.1: Illustrative sketch of Concept A

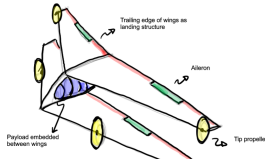


Figure 4.2: Illustrative sketch of Concept B

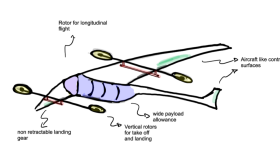


Figure 4.3: Illustrative sketch of Concept C

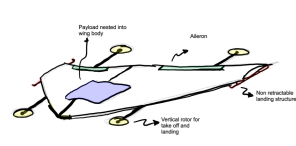


Figure 4.4: Illustrative sketch of Concept D

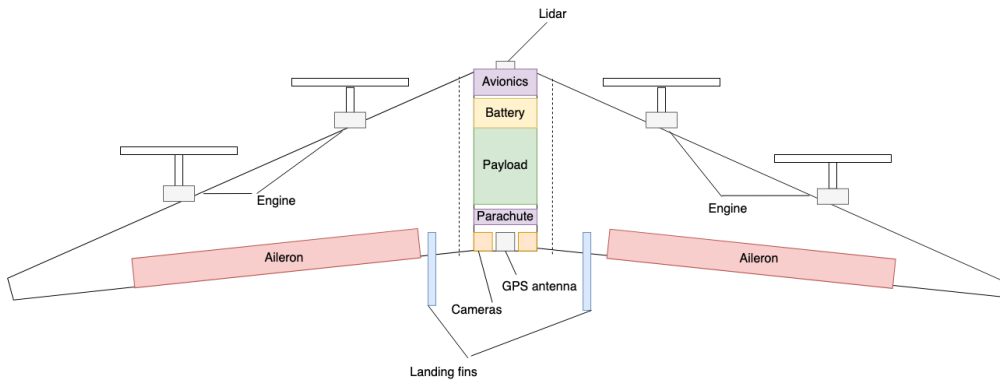


Figure 4.5: Illustrative sketch indicating the main design aspects of the selected concept after the midterm selection process. Note, this is the starting concept of the detailed design phase, not the final layout of the drone

be selected. Therefore, a compromise between A and D was made which would exploit the benefits of each configuration with minimum change in the design. From this, Concept X was conceived, which applies the VTOL operations as concept A, but has 2 additional engines at the leading edge to mitigate the relatively poor technical risk scoring. The impact of the modifications were analysed and concept X came out as the clear winner of the selection process.

4.3. Selected Concept Detailed Design

Concept X, which proved to be the best design solution for the described selection method will be the starting point of the detailed design which is described in this report. A more detailed sketch of the concept is presented in [Figure 4.5](#). The most important properties of this specific design configuration are shortly described below:

- **Tailless configuration:** The flying wing will have no tail nor separate fuselage. The consequences of this aerodynamically efficient planform in terms of trimming, stability and system placement are discussed in [Chapter 6](#)
- **VTOL method:** The drone will take off and land with its leading edge orientated vertically. Transition from take off to climb is done by means of pitching with the elevons located in the slipstream of the propellers. Transition from gliding to landing is by means of intentionally entering stall by pitching up, it will then land vertically on its landing fins and wing tips. This process will be analysed in more detail in [Chapter 11](#)
- **Engine configuration:** The drone will have 4 non-tiltable propellers located at the leading edge of the wing. Yaw control is achieved by means of differential thrust. The sizing and selection process of the engines and propeller is discussed in [Chapter 7](#). The exact mechanism of yaw control using differential thrust is explained in [Chapter 11](#)
- **Elevon placement:** The elevons are placed in the slipstream of the propellers to maintain pitch control during low speed manoeuvres. This results in an important sizing condition for the elevon based on the propeller slipstream. The effects of the propeller on the wing is described in more detail in [Chapter 9](#)
- **Landing Fins:** The drone will land on its wing tips and one or more landing fins which also serve as a vertical stabiliser. The sizing process and drag contribution of this fin are analysed in [Chapter 8](#), and [Chapter 9](#).

These 5 design aspects obtained from the midterm selection process are taken as starting point for the detailed design of SAVED described in the following chapters of this report.

5

System Overview and Final Design Process

In order to attain an overview of the design process and the flow of information between different technical design departments, this chapter aims to explain the technical design process of the detailed design phase. The starting point of this process is based on the results from the end of the midterm selection process [9], as described in [Chapter 4](#). The system overview, together with subsystem and component positioning is discussed in [Section 5.1](#). Thereafter, in [Section 5.2](#) a general outline of the design process followed throughout the detailed design phase is given as well as an explanation on the iteration process. In the end of the chapter, the general verification and validation procedures are explained in [Section 5.3](#).

5.1. System Components and Positioning

One of the first steps in the design process consisted of identifying and assessing the positioning of the major components of the drone. Several design considerations could be identified before starting the design of the wing planform itself. The positioning of components can be seen in [Figure 5.1](#), where x is the chordwise direction and y is the spanwise direction. The process of positioning them is as follows: First the reasoning for positioning the system on the centreline is explained in [Subsection 5.1.1](#). Next the payload positioning is discussed in [Subsection 5.1.2](#). Following this, the positioning of the battery is discussed in [Subsection 5.1.3](#). The positioning of additional components is then elaborated upon in [Subsection 5.1.4](#) and finally the engine positioning is presented in [Subsection 5.1.5](#).

5.1.1. Positioning Major Systems at Centreline

All major components must be positioned along the longitudinal axis of symmetry of the drone. In other words, most non-structural components should be placed at the centre of the drone (except for engines and propellers). This has the following reasons:

- From a lateral and directional stability perspective, it is desired to have symmetry of masses along the span of the drone. Moreover, it helps in the analysis by greatly simplifying the equations of motion.
- From a control point of view it is beneficial to have the mass centred along the longitudinal axis. Additionally, the aircraft has to be approximately symmetric along this axis. therefore, only identical components could be placed in the wing symmetrically.
- Even in the case of such identical elements, for instance battery cells identified in [Section 7.2](#), the placement in the wings would simply not fit, or would need extensive bulging considering the maximum thicknesses of the low-airspeed airfoil thicknesses that are considered in [Section 9.1](#).
- The placement of these systems at the maximum thickness location would interfere with the main structural components such as the spars.

The final location of the centres of gravity of the main components on the centreline as described in the upcoming subsections are given in [Table 5.1](#). This is the final positioning result of the iterative design process described in [Section 5.2](#)

5.1.2. Payload Positioning

As is discussed in more detail in [Subsection 6.1.2](#), both the trimming of the flying wing and longitudinal stability requirement are directly determined by the distance between the neutral point (n.p.) and centre of gravity (c.g.) of the drone. Large fluctuation in the c.g. position during operation would negatively effect both aspects. To avoid this the payload has to be placed as closely as possible to the c.g. of the drone. The dimensions of the payload module stems from **SAVED-CUST-PLD-01** during the midterm selection process [9] and are indicated in [Table 5.2](#).

Table 5.1: Component & c.g. location with respect to leading edge of the wing planform [m]

Component	C.g. location [m]
Avionics	0.35
Battery	0.10
Payload	0.32
Parachute	0.50

Table 5.2: Payload dimensions as obtained from **SAVED-CUST-PLD-01** [9].

Length [m]	Width [m]	Height [m]
0.295	0.278	0.118

5.1.3. Battery Placement

Again, the drone's c.g. should be positioned in front of the n.p. to be able to satisfy the longitudinal stability requirements. From [Subsection 5.1.2](#) and [Subsection 5.1.1](#) it is concluded that the battery system should be placed either in front or after the payload. Since the required payload volume is relatively large, as described in [Table 5.2](#), placing the battery system after the payload is not a feasible option regarding stability considerations. In addition, in the front less bulging is required due to the thicker profile relative to the back of the wing. The battery is therefore placed in front of the payload.

5.1.4. Additional Central Components and Positioning

In addition to the battery and payload, the centre section also needs to store the avionics and a parachute (see [Chapter 18](#) for reasoning behind the need for a parachute).

Any sensor used by the drone to perceive the environment or estimate its state, and any component used for processing this perceived information and command other components of the drone is considered avionics. The components chosen are all discussed in [Chapter 15](#). However, what is most important at the moment is that the laser detection and ranging (LiDAR) should be positioned in the nose of the drone, and the stereo cameras in the back of the drone for perception purposes. The positioning of the rest of the components is flexible and can be adjusted to fit the central section as needed. Lastly, the parachute size is quite significant, but its positioning is also quite flexible as long as it does not interfere with other subsystems. Hence, the parachute position is chosen to be positioned just behind the payload.

5.1.5. Engine Positioning

As mentioned in [Chapter 4](#), there are four engines, two on each wing, located at the leading edge. The inner engine spanwise positioning is decided according to [72] to be at 35% of the half-span, whereas the position of the outer engine is decided to be 70% of the half-span. This positioning allows for propellers of up to 52.5 cm diameter without the propellers overlapping. This is taken into account in the requirements in [Section 7.3](#). The position of the c.g. of each engine with respect to the root-chord leading edge then strictly depends on the leading edge sweep, which is made use of while designing the wing planform in [Chapter 6](#).

5.2. Design Process

With all the components and their relative position to the drone identified ([Table 5.1](#)), it is now necessary to identify the influence and interface that each of these components have with the overall design process of the drone in order to get an accurate understanding of how different subsystem parameters affect the system as a whole. A visualisation of this design process, indicating the relations between subsystem, system and final design is shown in [Figure 5.2](#). Thick arrows indicate a relation with the complete box, thin arrows indicate a relationship with a sub element.

It is now important to identify the starting point of the process. This starting point will be the results of the midterm selection process in terms of estimated values for each system component. The initial budget breakdown of the mass is presented in [Table 5.3](#). It is important to note that these values are not the final values, but the starting point of the detailed design phase. A new iteration starts after the subsystem design loop, yielding new values for the mass breakdown and aerodynamic performance.

An important aspect of this iterative design process is to keep track of the iterations. To assure this, the system

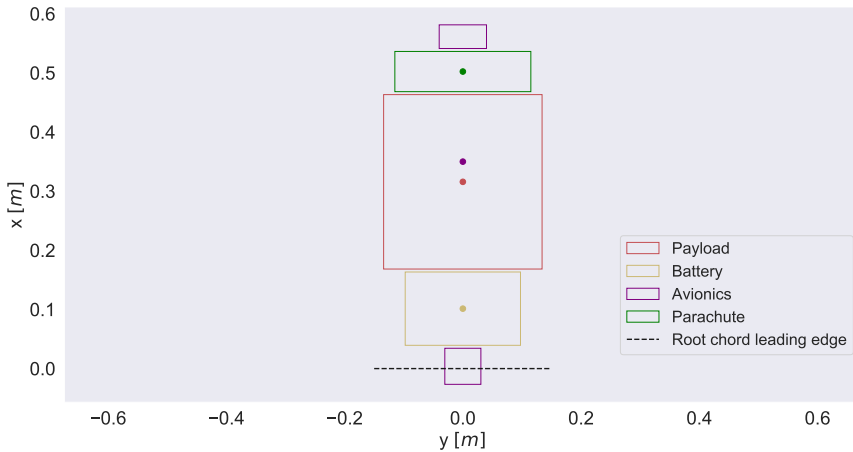


Figure 5.1: Positioning of central components along the centreline. The centre of gravity of each component is indicated by a dot of the same colour. $x=0$ corresponds to the root chord leading edge of the wing planform (not the bulge).

Table 5.3: Initial mass breakdown based on results from the midterm selection process [9]. In the right columns the values for the final iteration are presented which for comparison. These values will be justified during the rest of the report

System	Allocated mass [kg]		Fraction [%]	
	First iteration		Final iteration	
Structural	8.70	48.9	8.03	46.1
Payload	3.00	16.9	3.00	17.2
Battery	2.95	16.6	3.60	20.7
Engines	2.47	13.9	1.51	8.7
Avionics	0.36	2.0	0.36	2.1
Parachute	0.3	1.7	0.50	2.9
Elevon actuators	N.A	N.A	0.40	2.3
Total take-off mass	17.78		17.40	

engineering department has made a clear overview for each iteration, what the values are and what the interface with previous or coming iterations are. It was actively communicated with each technical department, so that all estimations and analyses were conducted using consistent values for each phase of the detailed design process.

5.3. Verification and Validation Procedures

In order to verify the models used for the design of SAVED, both unit tests and system tests have been carried-out. Unit testing is comprised of individual units of code that ensure that a section of the code behaves as intended. In order to test interconnected code serving different modules system testing is has also carried out. System testing consists of the testing of a complete integrated system to evaluate the compliance of its specified requirements. Since both unit testing and system testing are specific for each model, those procedures are explained separately for each model that has been verified.

Similarly, validation is case dependent, as it has been carried-out using different methods depending on the characteristics of the model to be validated. It is for that reason that validation is also explained independently for each model.

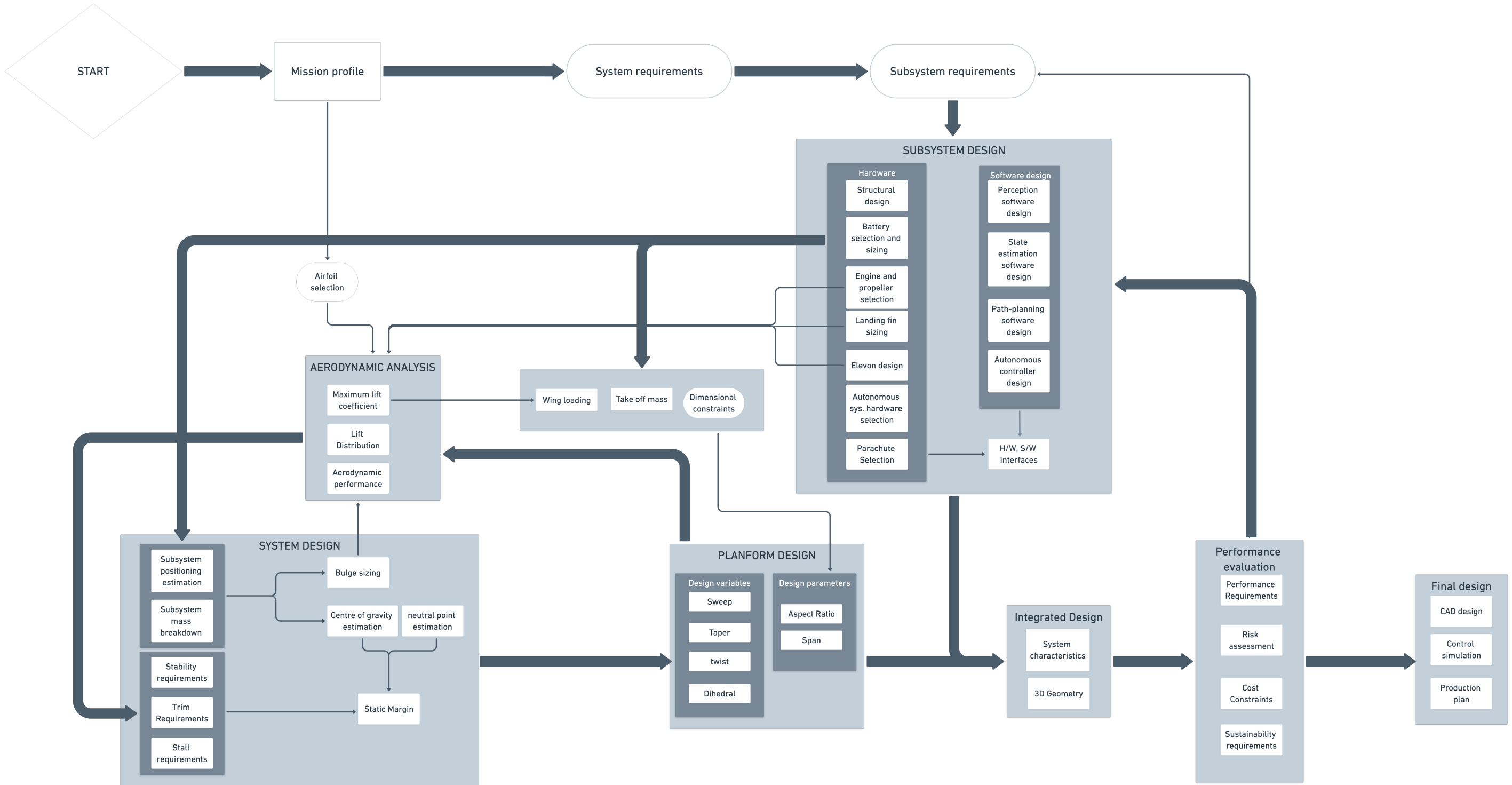


Figure 5.2: Visualisation of the main design process during the detailed design phase. Several iterative loops can be identified in this diagram.

6

General Planform and Fuselage Bulge Design

In this chapter, an extensive overview is presented how SAVED's general wing planform and bulge was designed. Since the wing planform forms the base of the drone it is an extremely important design process that significantly affects all other departments. First, in [Section 6.1](#), the design of the wing planform is explained. Second, the general design of the elevons is discussed in [Section 6.2](#). Finally, the design process of the fuselage bulge is presented in [Section 6.3](#).

6.1. Wing Planform Design

In this section the process of the wing planform design is explained in detail. Firstly, In [Subsection 6.1.1](#), the key parameters are identified and explained. Thereafter, several of the driving requirements concerning stability trim and stall will be discussed in [Subsection 6.1.2](#), [Subsection 6.1.3](#) and [Subsection 6.1.4](#), respectively. In [Subsection 6.1.5](#) and [Subsection 6.1.6](#) considerations regarding the wing planform from other departments are discussed. At the end, in [Subsection 6.1.7](#), the resulting design process for the wing planform is explained and in [Subsection 6.1.8](#) the results are listed. Additionally, in [Subsection 6.1.10](#), verification and validation efforts on the wing planform design tools and results are discussed.

6.1.1. Wing Planform Parameters

In order to define the wing planform the following parameters have to be determined:

- **Required surface area:** The required surface area comes directly from the wing loading derived from the stall condition and total mass. This is an **input** of the wing planform design, not a design variable. Note that geometry of the wing planform influences the stall characteristics and therefore this input value is related to the output maximum lift coefficient $C_{L_{max}}$
- **Aspect ratio:** The aspect ratio of the wing represents the slenderness of the wing and is extremely important in reducing the induced drag. A higher aspect ratio will increase the aerodynamic performance of the drone. The limitations arise from structural considerations and operational constraints in term of maximum span length. From the customer requirements an operational constraint of a span of 3m is obtained. Due to the relatively low loads to the size of the drone relative to conventional aircraft and due to the importance of aerodynamic performance due to the stringent range requirement, the span is assumed to be the maximum value of 3m, as to maximise the aspect ratio. Therefore, the span will be a fixed **input** which determines the aspect ratio based on required surface area.
- **Sweep and taper ratio:** To finalise the 2D planform a combination of sweep, evaluated at quarter chord, and taper ratio are to be defined. These are **design variables** and will not change the surface area or aspect ratio, but affect the location and size of the root, tip chord and therefore MAC. Consequently they influence the location of the wing's centre of gravity (c.g.), neutral point (n.p.) and structural complexity. The purpose of this chapter is to find an optimal combination of these two variables.
- **Wing twist and dihedral:** Given a certain airfoil selection and the parameters described earlier, the 3D planform is defined by the specification of the twist (washout) and dihedral angle. Since the dihedral angle is assumed to be either zero or very small, it does not influence the other parameters of this design process and is therefore shortly discussed independently in [Subsection 6.1.9](#). The twist, however, plays an important role for the trimming, stall behaviour and aerodynamic properties of the wing, and has to be assessed concurrently with the sweep and taper design. Therefore, the twist is considered to be a **design variable**.

From the above it is concluded that the design of the wing planform consists of finding an optimal combination of sweep, taper and twist, given the input values for wing loading and mass. To find an optimum combination for the design variables, it is necessary to first analyse the effect on the performance from such combinations, and to determine the design objective for the wing planform, based on the key requirements.

6.1.2. Stability Requirements

Some of SAVED's most important requirements relevant to wing planform sizing stem from stability. During cruise the drone should be longitudinally, laterally, and directionally stable. Hence the following requirements are stated:

- **SAVED-CONS-FLIGHT-02:** The aircraft shall be longitudinally stable.
- **SAVED-CONS-FLIGHT-06:** The aircraft shall be laterally stable.
- **SAVED-CONS-FLIGHT-07:** The aircraft shall be directionally stable.

For the purpose of this section, only **SAVED-CONS-FLIGHT-02**, is examined deeper. This is because it drives the design of the wing planform to a much larger extent than assuring lateral and directional stability. In fact, it is later shown in [Chapter 10](#) that the design can satisfy lateral and directional stability requirements without being explicitly designed for them.

If an aircraft has static longitudinal stability it means that any disturbance in pitch is automatically generating an opposite moment, which tends to restore the aircraft to its initial orientation. This can only be the case, if the point of application of lift at which the moment generated by the wing stays approximately constant, defined as the aerodynamic centre (a.c.), is located behind the c.g.. This is indicated in [Figure 6.3](#). More formally, this is criteria is defined as that the c.g. must lie in front of the neutral point. The neutral point is the point through which the difference in lift due to a disturbance in angle of attack acts. Since there is no tail, this location coincides with the aerodynamic centre of the wing. Hence these definitions are the same. To obtain the moment equilibrium equation in terms of coefficients, each term has to be divided by not only by the dynamic pressure q , but also by the Mean Aerodynamic Chord (MAC) \bar{c} . As a consequence, the distance between c.g. and a.c. is divided by the length of the MAC and thus expressed as a percentage of the MAC. This percentage is defined as the Static Margin (SM). Therefore, the first requirement can be defined as follows:

- **The static margin of the drone must have a positive value.** The sweep and taper must be selected such that the planform is able to facilitate such a static margin.

Sweep and taper ratio are important in this aspect because they influence both the c.g. and a.c. location of the wing. Increasing sweep will move both points aft. Yet, the a.c. will move aft more relative to the total c.g. of the drone allowing for a larger SM. Increasing taper reduces the lateral location of the MAC and depending on sweep effects both points

6.1.3. Trim Requirements

Another important requirement for the wing planform concerns the trim condition of the aircraft. The stability requirement itself is not enough to assure longitudinal moment equilibrium. Although the positive SM results in an opposite moment relative to the disturbance, the aircraft itself must also have an equilibrium or trim condition during cruise. As indicated in [Figure 6.2](#), the moment generated by the wing must be equal to the moment generated by the lift force around the c.g. In conventional aircraft, this moment would be trimmed by the lift force of the horizontal tail. For tailless aircraft, this trim condition has to be achieved solely by the moment generated by the wing. Therefore as indicated in [Figure 6.2](#) and following the stability constraint, the c.g. must lie in front of the a.c.. The wing must be able to generate a positive moment (pitch up direction). Wings using conventional airfoils create a negative moment around their aerodynamic centre. In order to obtain the positive moment required for equilibrium, a reflexed airfoil must be used for unswept wings ([Section 9.1](#)), or (highly) swept wings can apply some form of twist or washout in such a way that the difference between lift generated at the root and tip, in combination with the longitudinal arm created by the sweep, generate the same effect. Either way, in case the moment generated by the wing is not enough to counter the the moment generated by the lift force at the a.c., the elevons must be deflected to overcome this discrepancy. This deflection will effectively increase the trim drag during cruise and therefore negatively affect the aerodynamic performance of the aircraft. Arguing from this perspective, the trim drag during cruise should be minimised to avoid any negative effects on the ability of the drone to reach its target range. One can also summarise the above in the two following requirements:

- **SAVED-CONS-FLIGHT-04:** The aircraft shall be trimmable.
- **SAVED-CONS-FLIGHT-04:** The aircraft shall fly at maximum L/D during cruise flight.

Which can be rephrased in one statement as follows:

- **Trim drag during cruise must be minimised.** Therefore the planform should be designed in a way that that during cruise conditions the equilibrium of moments is satisfied without using elevon deflection.

6.1.4. Tip Stall Requirement

The third requirement for the wing planform concerns the stall behaviour. In short, it can be stated as the following requirement:

- **SAVED-CONS-FLIGHT-05** The aircraft shall have stable stall behaviour without an increased pitching moment.

As described in [Section 3.1](#), the drone is designed to purposely enter stall during each landing manoeuvre. Therefore it is very important that the drone will have controllable stall behaviour. The three design variables that are assessed in this analysis, taper sweep and twist, greatly influence the stall behaviour of the aircraft. This analysis will particularly focus on tip-stall effect. Generally, tip stall is undesired for the following reasons: Separation at the tip would lead to the loss of outboard placed trailing edge controls, maximise the down-wash on the tail and generate an increased pitch up moment.

The tailless configuration and large elevons spanning the entire propeller slipstream as described in [Section 6.2](#) ensure controllability when the wing tip stalls first. Therefore, the one remaining concern of wing tip stall consists of the pitching up moment. The higher the sweep angle, the larger the forward shift in centre of pressure (c.o.p.), and thus pitching up moment, when stall occurs first at the tips. Sweep does not only aggravate the negative effects of wing tip stall, but also causes it to happen in the first place. The sweep angle at the leading edge, which is determined by both quarter chord sweep and taper ratio, creates an outboard spanwise component of the boundary layer, which prevents the inboard wing sections from stalling [37]. This effect causes the flow separation to start at the outboard sections and thus promotes tip stall. Additionally, taper ratio increases this effect by reducing the local maximum airfoil lift coefficient. Since the nose up pitching moment is the main thing to be avoided during stall, the event of tip stall itself is not necessarily to be avoided. The combination of tip stall with high sweep angles however, which causes the increased pitching up moment during stall, must. Therefore, for this design, either highly swept and tapered wings must apply other measures to avoid wing tip stall, or low sweep and low aspect ratio wings have to be designed. Other measures can include leading edge devices and vortex generators. Swept wings can apply geometric or aerodynamic twist to reduce the effective angle of attack at the outboard sections which causes the wing to stall at the root first.

- **Unstable stall behaviour must be avoided:** The wing planform shall be designed in such a way that during stall a high pitching up moment is avoided.

6.1.5. Structural Considerations

From a structural perspective, sweep increases complexity of the wing structure. All principal elements, such as spars, must be placed at an angle and increase in length which increases both mass and assembly difficulties. Additionally, geometric twist increases the wing complexity and is therefore also considered detrimental for the structural department. Introducing taper actually relieves the bending moments at the root but adds some complexity similar as to sweep to the design. Additionally, taper increases the root chord and leads to less excessive bulging at the centre. Therefore to conclude, from a structural perspective, sweep must be minimised and twist must be avoided, taper has both structural advantages and drawbacks and is therefore allowed to a certain extent.

6.1.6. Aerodynamic Considerations

From an aerodynamic perspective, moderate sweep-back slightly flattens the lift curve slope[37]. Since the drone operates at relatively low Mach numbers nowhere near the transonic regime ($M<0.1$), as indicated in [Section 3.1](#), no sweep has to be applied to increase the critical mach number of the drone. Therefore, from an aerodynamic perspective, sweep has to be minimised. Twist, if perfectly applied can optimise the lift distribution to slightly reduce the induced drag. Yet this geometric or aerodynamic twist has to be built in perfectly, any deviations from this might have the adverse effect on the envisioned increase in performance. Therefore, twist is not deemed necessary from aerodynamics.

6.1.7. Design Process

To conclude from the previous sections; wing twist must be avoided, if possible, and sweep must be minimised. Yet the combination of sweep, taper and twist must be able to facilitate the positive static margin specified by the

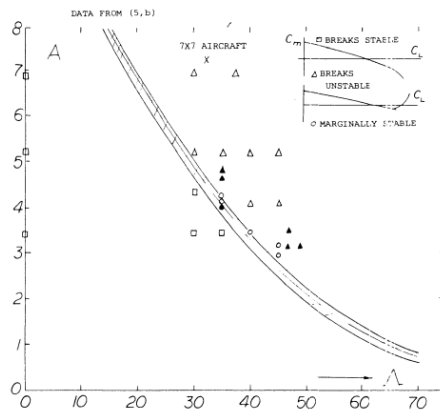


Figure 6.1: Critical sweep angles for which the wing tends to have unstable stall behaviour as a function of aspect ratio [37]

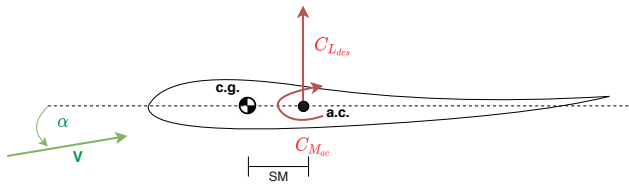


Figure 6.2: Free body diagram indicating that the moment generated by the wing must have a positive value to attain equilibrium of moments with a positive static margin

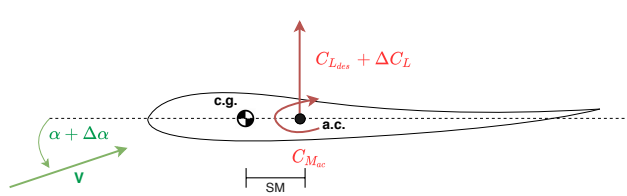


Figure 6.3: Free body diagram indicating the necessity of a positive static margin in order to attain longitudinal static stability.

trim condition and longitudinal stability criteria to minimise the trim drag. The first step consists of investigating the possibility of no twist while still satisfying the trim condition and stall requirement. In order to satisfy the first, it is concluded that the airfoil of the wing must be reflexed as is discussed in Subsection 6.1.2. In Section 9.1 a reflexed airfoil is selected which allows to attain equilibrium without the need of twist. To investigate the stall requirement, the theoretical critical sweep angle is identified from literature to ensure stable stall behaviour. From [37], critical leading edge sweep angles above which the wings stall with an unstable pitch up moment are identified, as a function of a certain aspect ratio wing without preventive measures. This relation is indicated in Figure 6.1. This figure can be used to find an upper limit for the quarter chord sweep angle given a certain aspect ratio input, determined by the wing loading and total mass as described in Subsection 6.1.1.

Now that an upper limit to sweep has been defined based on the stall requirement, a required static margin which satisfies the stability and trim drag requirements can be found. Based on this static margin, a minimum combination of sweep and taper that can facilitate this static margin can be identified. Then the minimum sweep will required will be the design point, if this value lies below the upper limit previously discussed. Assuming perfect equilibrium without geometric twist or elevon deflection, the static margin can be obtained by dividing $C_{M_{ac}}$ by the design lift coefficient $C_{L_{des}}$. As can be obtained from Figure 6.2.

In which the static margin is expressed as a fraction of the length of the MAC. $C_{L_{des}}$ and $C_{M_{ac}}$ indicate the design lift coefficient and moment around the aerodynamic centre of the complete wing and are therefore also influenced by the sweep and taper variables. To investigate the effect on the static margin of both variables on these coefficients, several combinations of sweep and taper were analysed.

Analysing the Relation of Sweep & Taper with $C_{M_{a.c.}}$

To determine the moment coefficient around the aerodynamic centre, XFLR5 [21] was used, given a fixed aspect ratio and the CAL4014I airfoil selected in Section 9.1.

The taper ratio, λ , was varied from 0.25 to 0.65 with a step of 0.1 and the quarter-chord sweep, $\Lambda_{0.25c}$, was varied between 10 and 25° in steps of 3°. For each $\lambda - \Lambda_{0.25c}$ combination, the point along the chord where no variation of the moment coefficient with angle of attack could be observed was recorded (this is the aerodynamic centre). In this way, the corresponding constant moment coefficient was recorded for each combination. The results of this analysis are plotted in Figure 6.4. It can be seen that with an increasing taper ratio, the moment coefficient slightly but consistently decreases. Similarly, at higher values of sweep; close to 25°, a very slight decrease in the moment coefficient can be seen. Based on this it was concluded that $C_{M_{a.c.}}$ did not significantly change in magnitude as function of sweep for the sweep values smaller than 25°. Taper only had a maximum effect of less than 10% between the extremities. This pattern is confirmed by the findings of [64], which provides

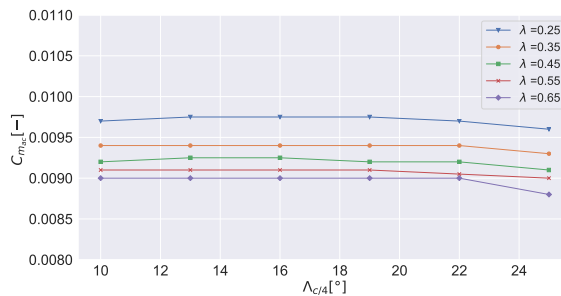


Figure 6.4: Moment coefficient around the aerodynamic centre for different combinations of taper λ and quarter chord sweep $\Lambda_{c/4}$ determined using XFLR5.

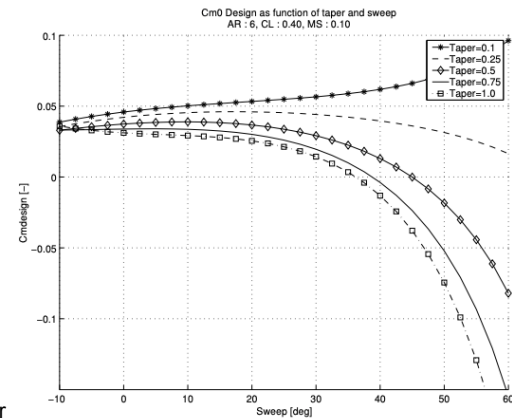


Figure 6.5: Analytically derived moment coefficient around the aerodynamic centre as a function of sweep and taper for a flying wing as found in [64]

an extensive analytical model for trimming and performance coupling for flying wings. The validity between the comparison of these two models is discussed in [Subsection 6.1.10](#). Based on both results of the XFLR5 output and [64], it is assumed $C_{M_{a.c.}}$ stays approximately constant for the range of sweep and taper considered.

Analysing the Relation of Sweep & Taper With $C_{L_{des}}$

In a similar manner, the impact of $C_{L_{des}}$ was evaluated. Rather than using XFLR5, the semi-empirical DATCOM method was used to be able to better assess the effects of the flattening wing lift curve due to the leading edge sweep induced by the combinations of wing sweep and taper. $C_{L_{des}}$ was selected as the lift coefficient at which maximum lift over drag occurs. For each combination of taper and sweep, the lift curve of the wing was constructed using the DATCOM method[73]. Additionally the drag coefficient C_D was determined based on the zero drag coefficient and induced drag. This method is described in more depth in [Section 9.2](#). Important to note is that for this process C_{D_0} was assumed to be independent of sweep and taper for the given range of sweep. Also, the suction coefficient R used to analytically assess the magnitude of the Oswald efficiency e was assumed constant. Again, this process is described in more depth in [Chapter 9](#). It was found that $C_{L_{des}}$ was affected only very little by the sweep and taper ratio. For the evaluated range of sweep and taper the resulting change in $C_{L_{des}}$ was less than 2%. Therefore, $C_{L_{des}}$ was assumed to be constant for the combination of sweep and taper. This yields the conclusion that the required static margin is independent of the wing planform for moderate sweep angles. Therefore, a minimum required sweep angle and corresponding taper ratio can be determined to facilitate a required static margin. In the following two sections, it is explained how this minimum value of sweep and corresponding taper ratio is found, given a required static margin.

Relating Sweep and Taper Ratio to the Aerodynamic Centre

The static margin has two components; the location of the neutral point, which corresponds to the aerodynamic centre for the tailless design, and the location of the centre of gravity. First, the methods to assess the location of the aerodynamic centre are explained. This location consist of a geometric function and a correction factor to account for the destabilising affects of the wing mounted engines and fuselage bulge. For low speed, subsonic airfoils, the aerodynamic centre of the wing can be assumed to be located at 25% of the MAC [53]. Using this approximation, a simple geometric function was derived to determine the distance between the leading edge and the aerodynamic centre of the wing as function of quarter chord sweep and taper ratio, given a certain wing loading input and aspect ratio fixed for a certain iteration.

The resulting value was corrected by subtracting 5% to account for the destabilising effects of the engine and the fuselage bulge [53]. This factor is an approximation obtained from [18] which evaluated the wing-fuselage effect on the location of the aerodynamic for several fuselage configurations. A conservative value of 5% was selected based on the results for short forward and rear fuselage configuration. This value is only an approximation and could be re-evaluated in more detail in more advanced designed stages with wind-tunnel tests of a scale model as is described in [Chapter 20](#).

Relating Sweep and Taper Ratio to the Centre of Gravity

The relation between the sweep and taper combination and the centre of gravity of the drone was more complicated to derive. The c.g. location of the complete drone is a function of the location and masses of all

system components and the structural wing geometry and mass. The latter is a direct function of the sweep and taper combination. Since during conceptual design, the exact structural composition of the wing structure is unknown, empirical methods have to be used to assess this component beforehand. From [58] an empirical relation for the wing structural mass was obtained:

- The longitudinal position of the wings structural weight is approximated to be 70% of the distance between the main and aft spar of the chord length at 35% of the semi-span [58]

Again, this is an empirical approximation which limits the accuracy of the analysis. A more detailed value can be iterated in this process once the structural composition of the drone is established in more detail. A component that had to be related to this wing c.g. are the engines. The sizing of the 4 engines is described in more detail in [Chapter 7](#). The results from the latter are implemented in this analysis. The c.g. of the engines is assumed as the intersection of the lateral placement specification and the leading edge. Therefore, this component is also a function of the sweep and taper ratio and was included in the tool.

The remaining components of the c.g. estimation consist of the placement and masses of the other subsystems. All these systems are placed in accordance to the explanation in [Section 5.1](#). The battery mass and dimensions are input from [Chapter 7](#), the payload dimensions and mass stem from the requirements in [Chapter 17](#) and the avionics and structural components are derived from [Chapter 13](#) and [Chapter 8](#), respectively. Note that most of these inputs are iterative and change in value during the design stages.

To account for the uncertainty in the process of the c.g. estimation of the drone, a correction factor of 10% is assumed during this analysis, based on the contingency of the structural mass. In this case, the resulting c.g. location from this tool is increased by 10% to assess the worst case scenario in terms of longitudinal stability in which the actual c.g. would be located 10% more aft than estimated. Any discrepancy resulting from this estimation can be resolved later when the c.g. is estimated more accurately by moving, for instance, the location of the battery system to fit the required Static margin for trim. This uncertainty may seem large, yet this is not the final c.g. estimation used for the analysis of the drone's performance. This conservative value for the c.g. is used with the corresponding estimation of the neutral point to pinpoint a (conservative) minimum sweep angle necessary for the required static margin. If as expected the actual c.g. is located more aft, then the minimum sweep angle based on the latter condition is not violated but would actually decrease. Therefore, the planform variables can be selected and frozen at a certain point during the design by using the contingency for the c.g. location of the drone.

6.1.8. Results of Wing Planform Design

Given the assumptions justified earlier, the required static margin to trim the flying wing without the use of elevon deflection or geometric twist is independent of sweep and taper for the described range of quarter chord sweep values, lower than 25 degrees. Therefore, given a certain $C_{L_{des}}$ and $C_{M_{a.c.}}$, calculated based on iterative inputs for the aspect ratio and zero lift drag coefficient, a fixed static margin independent of sweep and taper ratio variables could be established. Then a minimum sweep angle and corresponding taper ratio were selected that could facilitate this required static margin, based on iterated values of the subsystem masses and locations. This iterative process is illustrated in [Figure 5.2](#), the result is depicted in [Figure 6.6](#) and the optimal values for sweep and taper are listed in [Table 6.2](#), together with their corresponding input values for the final iteration to freeze the wing planform design parameters.

Accounting for Uncertain C_{D_0} estimation methods

Firstly, as indicated in [Figure 6.4](#), the independent value of $C_{M_{a.c.}}$ was around 0.01. Then, using the findings in [Chapter 9](#), a value for the C_{D_0} of 0.099 was used for the final iteration to determine the $C_{L_{des}}$.

Noting that the semi-empirical estimated C_{D_0} is a rather uncertain value for the flying wing configuration, a range of C_{D_0} was implemented to account for an increase in required static margin due to the decreased $C_{L_{des}}$. This was to assure that the wing planform does not have to be changed drastically later in more detailed design phases. As is discussed in [Chapter 9](#), the limitations of the C_{D_0} estimation method used could very well result in a considerable decrease in actual C_{D_0} , when validation is performed during wind tunnel testing. Therefore, a lower value, as is indicated in [Table 6.1](#), is used to find the maximum required static margin. Note this lower value is not the expected value, rather a lower limit given the uncertainty. The effect of the uncertainty of the zero-lift drag coefficient on the aircraft's performance is analysed in [Section 16.2](#).

This yielded a required static margin range between 2.2 & 2.5 % which indicates that the reflexed airfoil alone can provide sufficient longitudinal stability in terms of static margin, without using twist and sweep. An additional contingency is applied of 0.5% to account for the fact that the payload mass could be off centred and more aft

C_{D_0}	AR	$C_{M_{ac}}$	SM
0.0085 -0.0099	6.8	0.01	2.2-2.5% (+0.5%)

Table 6.1: Aerodynamic input values and the resulting required static margin for trim condition.

$\Lambda_{c/4}$ [deg]	λ [-]	β_{geo} [deg]	Γ [deg]
16	0.4	0	0

Table 6.2: Resultant planform design variables based on the trim condition and stall requirement for the static margin of 3% and an aspect ratio of 6.8.

than initially expected. Note that this contingency is only used for the determination of the minimum sweep limit and can be corrected later by shifting the locations of the subsystems to precisely fit the trim conditions.

Using the conservative value of 3% for the required static margin, a graph indicating the minimum required sweep and taper combination, based on methods described throughout this chapter, was constructed and is shown in [Figure 6.6](#). In this graph, the upper limit of quarter chord sweep for an aspect ratio of approximately 7, arising from the stall requirement as indicated in [Figure 6.1](#), is indicated by the lower line. The lower limit is indicated with the dotted line, this is the minimum sweep angle and taper combination required to facilitate the 3% static margin. Based on this graph the design point is selected on the point below the upper limit with the minimum required sweep angle. This gives the final planform design variables indicated in [Table 6.2](#).

6.1.9. Determination of Dihedral Angle

The dihedral angle, Γ , mostly concerns the lateral stability of the design and was assessed independently from the other design variables of the wing planform. Due to the engine placement on the leading edge, inclusion of a significant dihedral angle would result in the engines not being on the same lateral line. This would greatly complicate the control of the aircraft. Therefore no built in dihedral was included in the design unless it proved necessary for the lateral stability of the drone, thanks to the induced dihedral effect of the swept-back wing [65]. From [Chapter 10](#), it was concluded that given the small instability due to the spiral, easily correctable with active control, the inclusion of dihedral is redundant and therefore discarded.

6.1.10. Verification and Validation of the Wing Planform Design Process

The tool used to evaluate the wing planform analysis, incorporating all relevant equations was structured to be extendable and eventually grew to a considerably large and complex program. Due to the size and complexity of this tool it became very important to include an overall system test to see whether the code was implemented according to the models. Of course, simple visual unit tests of independent code units were also performed but are not described here in detail. The second important thing is to validate the tool based on the output results.

- **System verification test:** To verify the final output values of the program, the program included a scaled

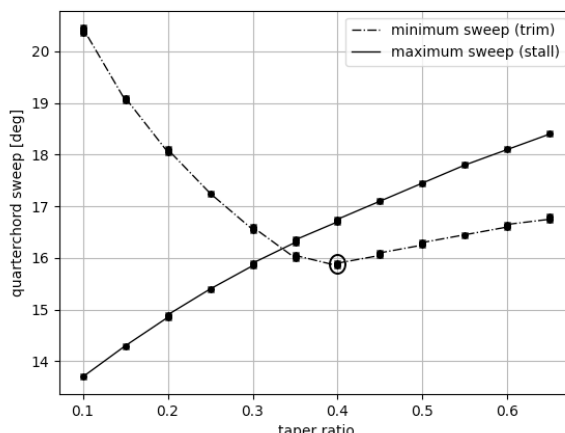


Figure 6.6: Upper and lower limits of design combinations of sweep and taper following minimum trim condition and stable stall behaviour for a static margin of 3.0% and an aspect ratio of 6.8. The design point has been selected as the minimum sweep point.

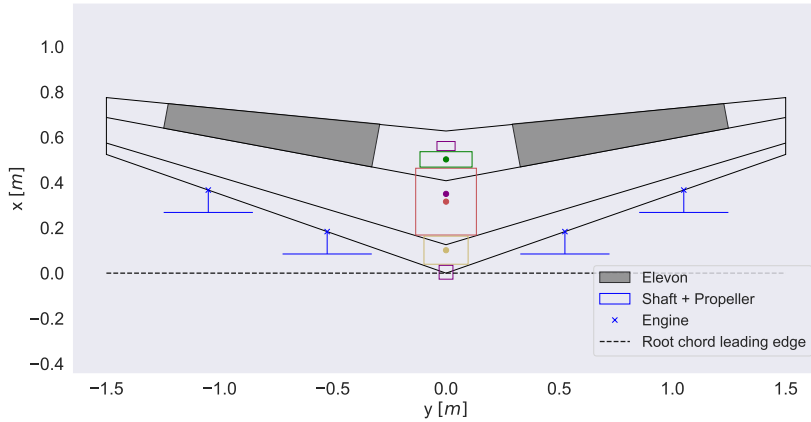


Figure 6.7: The determined wing planform overlaying the central components.

sketch pinpointing both input and output values and drawing the resultant wing planform on this sketch for a range of sweep and taper inputs. This also included the indication of the locations of the subsystems and their corresponding c.g.'s. Using this, initial errors in reference frame and unit could be resolved early on. Additionally, this was useful to spot whether a certain output bulge size was correct in the sense that every subsystem had to geometrically fit inside it.

- **$C_{M_{ac}}$ output comparison:** The obtained values of $C_{M_{ac}}$ as indicated in [Figure 6.4](#) are validated by means of the findings of [64]. Although it is not an experimental method used in this paper, it uses a different analytic approach and finds the same result that for the sweep range between 10 and 25 degrees, the moment necessary to trim the aircraft does not vary with sweep. This paper uses an aspect ratio of 6 and a CL of 0.4 which are very comparable (6.8 & 0.42). The magnitude of the moments can be accounted for by correcting for the static margin with a factor of 4. This justifies the assumption that $C_{M_{ac}}$ can be considered independent of sweep and taper for the given range of values.
- **Output static margin discussion:** The required static margin for trim without twist, is calculated to be in the range of 2.2-2.5. To assert whether this value is realistic it was compared with values for flying wing configurations from literature. According to [36], typical values for flying wings range from 2-5 percent. This indicates that our findings for the required static margin for trim without twist are within the feasible range in terms of stability according to data on general tailless aircraft. Also, the fact that our design is unmanned and computer controlled puts less restrictions on the static margin from a stability perspective. The longitudinal static stability requirement itself was conceived to avoid high risk and drag in the case of constant active control. The fact that a positive required static margin is obtained and that its value corresponds within the range of general tailless aircraft designs indicates a realistic output of the model, which validates the use of this method.

6.2. Elevon Sizing

In this section, the process of sizing SAVED's elevons is described. The elevons function as ailerons and due to a lack of empennage, also as elevators (hence the name), thereby allowing for roll and pitch control. [Subsection 6.2.1](#) discusses the sizing of the elevon's span and [Subsection 6.2.2](#) discusses the sizing of the elevon's chord.

6.2.1. Elevon Span

Contrary to conventional aileron sizing processes in which the ailerons' span are sized based on a roll rate requirement, the elevons' span were sized based on the spanwise spacing of the propellers. The reason for this is that an initial assumption was made that when the elevons span the distance between the most outboard part of the outboard propeller and the most inboard part of the inboard propeller, SAVED would achieve both roll and pitch control. The assumption was based on the propeller-wing interaction analysis ([Section 9.3](#)) which shows that the propellers induce extra velocity to the flow and thereby increase the local lift behind in the slipstream. If the elevons pass through these propeller slipstreams, they would benefit from the increase in induced velocity and thereby local lift, increasing controllability. The elevon's leading edge therefore spans from $-\frac{D_{prop}}{2} + 0.35\frac{b}{2}$ to $\frac{D_{prop}}{2} + 0.7\frac{b}{2}$. The spanwise location of the elevons is visualised in [Figure 6.9](#).

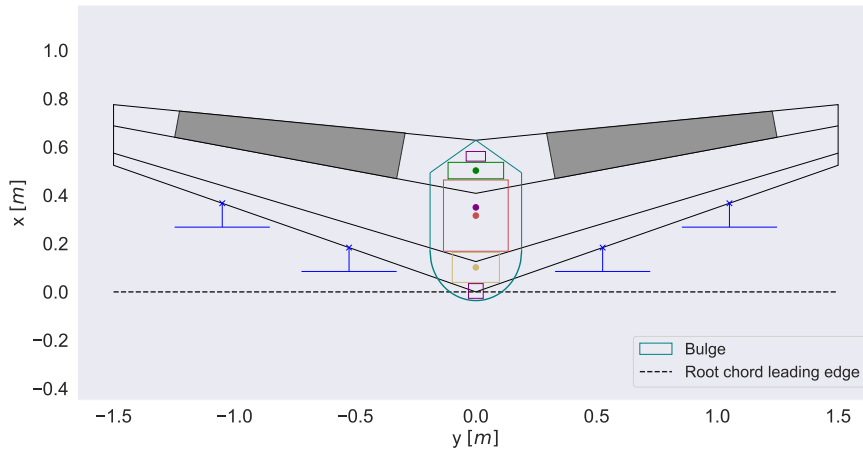


Figure 6.9: Complete wing planform and bulge fitting around central components.

6.2.2. Elevon Chord

The elevon's chord is sized based on the chordwise location of the main wing's aft spar. This means the leading edge of the elevon is located at the aft spar which is at 69% of the chord ([Chapter 8](#)), and the trailing edge of the elevon is located at the trailing edge of the main wing. The reason for this dimension is to obtain a maximum elevon surface area without compromising the structural integrity of the main spar (discontinuities would have to be introduced in the aft spar if the leading edge would reach in front it). The elevons thereby rotate around the aft spars, meaning the chord is parallel to the main wing's airfoil. The chordwise location of the elevons is visualised in [Figure 6.9](#).

6.3. Preliminary Bulge Sizing

As can be seen from [Figure 6.7](#), the central components of the wing stick out of the nose. This is due to the fact that it is desired to keep the centre of gravity of the payload near the centre of gravity and the battery and LiDAR in front of it ([Section 5.1](#)). This and the fact that the central section will be significantly thicker than the rest of the wing is the reason for including a central, fuselage-like, bulging to encapsulate the central components. This kind of design can be seen in various flying wing drone designs [1 2](#). The purpose of this section is to describe how a preliminary size of the bulge body is obtained, based on the positioning of the subsystems described in [Section 5.1](#). This information is desired especially to be able to estimate the added drag of this design choice. This is done in [Section 9.2](#) and requires the maximum height of the bulge body d , the maximum length of the bulge body l_b and the wetted area of the body $S_{b,wet}$.

To give a reasonable estimation of these parameters, a simple geometric shape is fitted around the central section as can be seen in [Figure 6.9](#). The shape consists of a straight central section encapsulating the payload, where some space needs to be left next to the payload such that a rounded shape (an ellipse is used) can be fitted around the payload, if one was to look from the front (see [Figure 6.8](#)). Furthermore, the bulge has a triangular tail section, converging to the tail of the root chord. Finally, the nose of the bulge is a half-ellipse, fitted around the LiDAR in the front (again a margin is used such that the front view can be an ellipse). By fitting this geometrical shape one can determine the following values: $d = 0.167\text{m}$, $l_b = 0.664\text{m}$, $S_{b,wet} = 0.42\text{m}^2$. As mentioned earlier, these values will be used for an initial estimation of parasite drag, the final design of the bulge will not be exactly as sized here, but will be blended better with the wing as indicated in [Chapter 19](#)

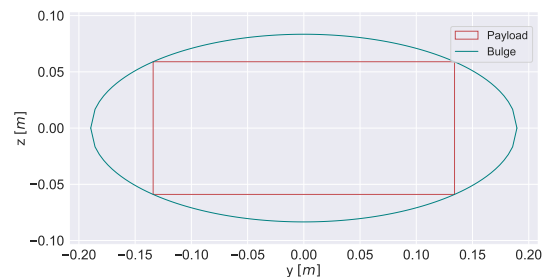
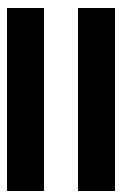


Figure 6.8: Frontview of the preliminary bulge.

¹<http://bitly.ws/8NG5> [Cited on 19-06-2020]

²<http://bitly.ws/8NG7> [Cited on 19-06-2020]



Subsystem Design and Analysis

Power and Propulsion Design and Analysis

In this chapter SAVED's power and propulsion subsystem is designed and analysed. The goal of this chapter is to find suitable off-the-shelf power and propulsion components SAVED will use during its mission, such as the main battery and the engine-propeller configuration. The chapter begins by presenting the electrical layout of SAVED in [Section 7.1](#). This section shows all the required components and how they are interconnected. Consequently, the energy consumption analysis and the battery selection can be found in [Section 7.2](#). Finally, the engine and propellers are selected in [Section 7.3](#).

7.1. Electrical Layout

In this section the layout of the electrical subsystem of SAVED will be displayed in the form of an electrical map. This map can be used as guidance throughout this chapter and provides a detailed picture of how all the electrical components are interconnected. In order to comply with the European Aviation Safety Agency (EASA) requirements and be allowed to fly beyond visual line of sight, a custom electronic design was necessary [11]. As seen in [Figure 7.1](#), the electrical map consists of two independently powered circuits. The first circuit is where all the control and navigation systems are interconnected. This is SAVED's main electrical circuit and is powered by the main battery. The second one is the flight termination device, which deploys the parachute in case the main power circuit malfunctions. This circuit is powered by a small 1 cell back up battery which is added mostly for risk management reasons. Note that a thorough explanation of all sensors and hardware utilised by SAVED can be found the [Chapter 13](#) and [Chapter 14](#).

7.2. Energy Consumption and Battery Selection

In this section, the energy consumption of SAVED for a typical mission is evaluated. The energy consumption dictates the sizing of the battery, which is a parameter of paramount importance. Firstly, a functional analysis is given in [Subsection 7.2.1](#) to outline the functional performance. From this functional analysis, a list of requirements to be met by the battery is obtained in [Subsection 7.2.2](#). Consequently, the analysis of the power and energy required is presented in [Subsection 7.2.3](#) and [Subsection 7.2.4](#) respectively. Next, the actual battery is selected in [Subsection 7.2.5](#). Finally, the energy consumption tool is verified and validated in [Subsection 7.2.6](#).

7.2.1. Functional Analysis

In this subsection the functional analysis of the battery is discussed. The functions are as stated below:

- **SAVED-P&P-FUNC-BAT-01:** Provide sufficient energy to the electric subsystems during its lifetime;
- **SAVED-P&P-FUNC-BAT-02:** Provide sufficient voltage to the electric subsystems;
- **SAVED-P&P-FUNC-BAT-03:** Provide sufficient current to the electric subsystems;
- **SAVED-P&P-FUNC-BAT-04:** Provide sufficient power to the electric subsystems;
- **SAVED-P&P-FUNC-BAT-05:** Fit within the bulge;

7.2.2. Requirement Analysis

This subsection provides the list of requirements the battery must meet. These requirements are based on the functional analysis in [Subsection 7.2.1](#).

- **SAVED-CUST-RANGE-02-P&P-BAT-01:** The battery shall have a specific energy of at least 200W h/kg;
- **SAVED-CUST-RANGE-02-P&P-BAT-02:** The battery mass shall weigh no more than 3.6kg;

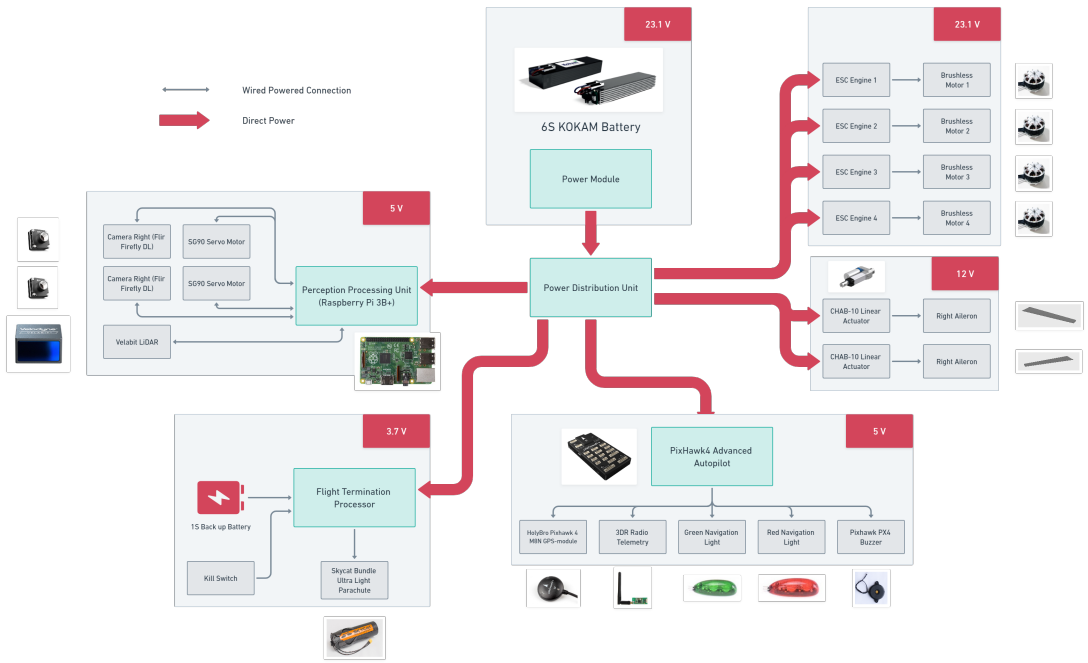


Figure 7.1: SAVED's electrical map

Table 7.1: SAVED's aerodynamic input parameters

$C_{L_{max}}$ [-]	$C_{D_{climb}}$ [-]	$C_{L_{cruise}}$ [-]	L/D [-]	C_{D_0} [-]
1.137	0.0746	0.444	22.48	0.0099

- **SAVED-CONS-SD-EM-02-P&P-BAT-01:** The battery shall be able to give power to the subsystems for at least 3000 cycles;
- **SAVED-CUST-PLD-01-P&P-BAT-01:** The battery shall have a maximum dimension of $0.59 \times 0.25 \times 0.13$ m \times m \times m;
- **SAVED-CONS-SD-EM-02-P&P-BAT-02:** The battery shall never discharge more than 90%;
- **SAVED-CUST-RANGE-02-P&P-BAT-03:** The battery shall provide SAVED with sufficient energy to attain a range of 150km at end-of-life (EOL).

7.2.3. Analysis of Power Required

Now that the layout of the electrical map is defined, the power required can be evaluated. In order to do so, the mission is separated into the flight phases as described in [Section 3.1](#). The momentary power required within each flight phase is calculated using a set of aerodynamic, physical and geometric parameters. Note that the power required at a certain moment in time during the mission can also be a function of the dynamic pressure. Therefore, the power required is not necessarily constant, and average values are thus presented. The aerodynamic, physical and mission profile parameters given in [Table 7.1](#), [Table 7.2](#), and [Table 7.3](#), respectively, are constant throughout the mission. The values in [Table 7.1](#) all originate from [Chapter 9](#), battery cell mass is given in [Subsection 7.2.5](#) and propeller disk area is given in [Section 7.3](#). Wing surface area S and total mass m_{tot} originate from [Chapter 6](#) and [Chapter 5](#), respectively. Furthermore, V_{des} and V_{to} are taken from [24], K_{to} and $K_{landing}$ come from engine requirements as given in [Subsection 7.3.2](#), and γ follows from a rate of climb (ROC) of 5m/s as also given in [Subsection 7.3.2](#).

Based on these parameters, a model for the power required must be established. These are the output pow-

Table 7.2: SAVED's physical input parameters

m_{tot} [kg]	$m_{bat,cells}$ [kg]	S [m^2]	A_{prop} [m^2]
17.475	3.15	1.318	0.4869

Table 7.3: SAVED's mission profile input parameters and requirements

V_{cruise} [m/s]	V_{des} [m/s]	V_{TO} [m/s]	K_{TO} [-]	$K_{landing}$ [-]	γ [$^{\circ}$]
22.3	4	6	1.2	1	17

ers, so no efficiencies will be accounted for yet. Note that performance parameters will be elaborated on in [Section 7.3](#). The analysis for each flight phase is as follows:

Vertical Take-off

During the vertical take-off, the power required can be obtained through the actuator disk theory, as described by [43]. By using this momentum theory and treating the propeller as a disk, (7.1) can be obtained [68] [24].

$$P_{TO} = \frac{T_{TO}V_{TO}}{2} \left(\sqrt{1 + \frac{2T_{TO}}{\rho_{\infty}V_{TO}^2 A_{prop}}} \right) \quad (7.1) \quad T_{TO} = K_T W \quad (7.2)$$

Where P_{TO} is the momentary power during take-off [W], A_{prop} the total propeller area [m^2], and T_{TO} and V_{TO} the take-off thrust [N] and velocity [m/s], respectively. They are based on requirements that are listed in [Section 7.3](#). The thrust is given by (7.2). The requirements state that the vertical acceleration shall be $0.2g$, and therefore K_t [-] has been set equal to this acceleration ($K_t = 1.2$), to ensure the requirement is met. Furthermore, the ρ_{∞} is the local air density [kg/m^3].

Climb

The power required is obtained through multiplication of the thrust and velocity. The thrust and velocity are given by (7.3) and (7.4), respectively [24].

$$T_{climb} = W \sin(\gamma) + C_{D_{climb}} q_{\infty} S_{wing} \quad (7.3) \quad V_{climb} = 1.2 \sqrt{\frac{2W}{S_{wing} \rho_{SL} C_{L_{max}}}} \quad (7.4)$$

Where the first term in the equation for the thrust is the contribution of the weight, dependent on the flight path angle γ [$^{\circ}$], and the second term is the drag [N]. The drag itself is a function of the drag coefficient C_D [-], dynamic pressure q_{∞} and the wing surface area S_{wing} [m^2].

Cruise

The power required for cruise can be obtained by simply setting the thrust equal to the drag, and consequently multiplying the thrust by the cruise velocity. Therefore, the power required for cruise is given by (7.5):

$$P_{cruise} = V_{cruise} q_{\infty} S_{wing} C_D \quad (7.5)$$

Where V_{cruise} is the cruise speed. The drag coefficient is obtained using the cruise speed and the lift over drag, and by realising that the lift is equal to the weight in cruise [N].

Glide

For the gliding phase, it is assumed that the engines can be fully turned off. Therefore, the engines have no power required in this phase.

Landing

The power during landing can be modelled by again considering the propeller disk theory. This leads to (7.6) [24].

$$P_{landing} = K_{landing} W (V_i - V_{des}) \quad (7.6)$$

In this equation $K_{landing}$ and V_{des} are respectively equal to 1 and 4m/s as given in [Table 7.3](#). The induced velocity V_i is given by (7.7) [24]. Where x can be found employing (7.8) [24]. Where T_{hover} is equal to the weight of the drone and ρ_{SL} is the sea level density.

$$V_i = (k - 1.125x - 1.372x^2 - 1.718x^3 - 0.655x^4) \sqrt{\frac{T_{hover}}{2\rho_{SL} A_{prop}}} \quad (7.7) \quad x = -\frac{V_{des}}{\sqrt{\frac{T_{hover}}{2\rho_{SL} A_{prop}}}} \quad (7.8)$$

Table 7.4: Power required for power demanding hardware

$P_{Raspberry}$ [W]	$P_{Velabit}$ [W]	$P_{Pixhawk}$ [W]	$P_{Firefly}$ [W]	$P_{totalhardware}$ [W]
12.75	8	2.5	2	25.25

Table 7.5: SAVED's constant input parameters and requirements

η_{motor} [-]	η_{ESC}	k [-]	σ [-]
0.886	0.95	1.15	0.054

Hardware

Throughout the entire mission, the hardware will be switched on. They will continuously require power of the battery. Therefore, it is necessary to take the power required for these elements. They are given by [Table 7.4](#).

7.2.4. Analysis of Energy Required

In order to assess the energy required for a typical SAVED mission, it is important to first state the assumptions made in this analysis. All assumptions are listed below:

- For the analysis of the time spent in climb and cruise, it is assumed that the final velocities V_{climb} and V_{cruise} are achieved instantly. This means accelerations will not be taken into account in this analysis;
- The total efficiency of the process in take-off and landing is assumed to be a multiplication of the motor efficiency, electronic speed controller (ESC) efficiency and the hovering efficiency. The losses due to wiring for example, are neglected. The motor efficiency comes from the selected engine-propeller configuration which is determined in [Subsection 7.3.3](#). The ESC efficiency comes from the selected ESC, which is selected as it is compatible with the selected engine;
- The total efficiency of the process in climb and cruise is assumed to be a multiplication of the motor efficiency, ESC efficiency and the propeller efficiency;
- It is assumed that there is no wind during the mission.

Furthermore, the energy will be evaluated for each flight phase, again compliant with the mission profile as described in [Section 3.1](#). In order to do so, a model has been established. For this model, the constant input parameters are given in [Table 7.5](#).

Firstly, the energy consumption for each phase can be described, by the use of the equations for the power required as described in [Subsection 7.2.3](#).

Vertical Take-off

Since the vertical manoeuvre is a very demanding flight phase, the acceleration had to be taken into account since it makes a significant difference. The simulation starts with a velocity and height of 0m, and ends when the transition height of 20m has been reached. By this time, the take-off speed will already have been reached. By looking at the electrical map as given in [Section 7.1](#) and also by keeping the assumptions in mind, it is clear that a total of three efficiency factors are required in order to calculate the input power. While the motor and ESC efficiencies are constants, the hovering efficiency requires a closer look. Hovering efficiency can be assessed by taking into account the figure of merit (FM) [43], and is given by (7.9) [13].

$$FM = \frac{\frac{C_T^{3/2}}{\sqrt{2}}}{\frac{kC_T^{3/2}}{\sqrt{2}} + \frac{\sigma C_D 0}{8}} \quad (7.9)$$

$$C_T = \frac{T}{\rho A_{prop} V_{tip}^2} \quad (7.10)$$

Where k is a constant and has been set to 1.15 for non-ideal losses [13] and σ , the (co)axial constant, has been set equal to 0.054 because of the coaxial (i.e. counter-rotating) configuration of the rotors [13]. Furthermore, C_T , the thrust coefficient[-], is given by (7.10), where V_{tip} is the velocity of the tip of the blades. Multiplying all efficiencies consequently yields the total efficiency, given by (7.11).

$$\eta_{total} = \eta_{motor} \eta_{ESC} FM \quad (7.11)$$

Table 7.6: Model outputs during take-off including payload

T_{TO} [N]	P_{output} [W]	$\eta_{total_{TO}}$ [-]	P_{input} [W]	t [s]	$E_{total_{TO}}$ [kJ]
205.72	2757.73	0.510	5407.32	4.81	26.00

Table 7.7: Model outputs during take-off excluding payload

T_{TO} [N]	P_{output} [W]	$\eta_{total_{TO}}$ [-]	P_{input} [W]	t [s]	$E_{total_{TO}}$ [kJ]
170.40	2045.45	0.508	4026.48	4.81	19.37

By using this efficiency, the required power output of the take-off can be translated to the input power that must be supplied by the battery to the engines. Because the input and output power depend on the density, and therefore also on the height of the drone, they slightly differ during take-off. The average results for take-off are presented in [Table 7.6](#) and [Table 7.7](#) including and excluding the payload, respectively.

Climb

As mentioned in [Section 3.1](#), during the climb the drone climbs from 20m to cruise altitude, at 500m. It is assumed that the climb speed is instantly reached when the climb starts. For the climbing phase, the efficiency differs from the efficiency during take-off. Instead of the hovering efficiency, the propeller efficiency must now be taken into account. The propeller efficiency is given by (7.12) [71], where V_∞ is the free stream velocity and V_a is the propeller induced axial velocity given by (7.13) [71].

$$\eta_{prop} = \frac{1}{1 + \frac{V_a}{V_\infty}} \quad (7.12) \quad V_a = \frac{1}{2} \left(-V_\infty + \sqrt{V_\infty^2 + \frac{2T}{\rho_\infty A_{prop}}} \right) \quad (7.13)$$

Using the propeller efficiency, and combining it with the other efficiencies, (7.14) can be obtained.

$$\eta_{total} = \eta_{motor} \eta_{ESC} \eta_{prop} \quad (7.14)$$

Again, the height and density will not be constant. The average values for the input and output power are displayed in [Table 7.8](#) and [Table 7.9](#) including and excluding payload respectively, as well as the total time spent in the climbing phase, the total efficiency and the total energy consumption.

Cruise

For cruise, the cruise distance has to be considered. Since there are two other phases that also cover a certain horizontal distance, this distance covered must be subtracted from the cruise distance. This can be seen from the mission profile representation in [Figure 3.1](#). From simple geometry, the horizontal climb distance can be computed to be 1642 m. Furthermore, the horizontal gliding distance can be obtained through (7.15) [62].

$$s_{glide} = \left(\frac{L}{D} \right)_{max} H_{diff} \quad (7.15)$$

Where H_{diff} is the difference in height, and $(L/D)_{max}$ is the highest lift over drag ratio [-]. By using a height difference of 480m as explained in [Section 3.1](#), a gliding distance of 10788m can be computed. From [Figure 3.1](#), it becomes obvious that the cruise distance follows from subtracting the gliding and climb distance from the total range. Therefore, the cruise distance is equal to 62570m.

For the simulation of the cruise phase, it is also assumed that the cruise speed is instantly reached and therefore the accelerations are neglected. Also, the efficiencies are considered in the same way as for climb. The total efficiency is thus the product of the motor efficiency, ESC efficiency and propulsive efficiency, as given by (7.14). Because the cruise altitude is constant, the density does not change, and therefore the input and output power are constant. The model outputs are given by [Table 7.10](#) and [Table 7.11](#).

Table 7.8: Model outputs during climb including payload

T_{climb} [N]	P_{output} [W]	$\eta_{total_{climb}}$ [-]	P_{input} [W]	t [s]	$E_{total_{climb}}$ [kJ]
66.75	1092.42	0.548	1993.48	100.13	199.61

Table 7.9: Model outputs during climb excluding payload

T_{climb} [N]	P_{output} [W]	$\eta_{total,climb}$ [-]	P_{input} [W]	t [s]	$E_{total,climb}$ [kJ]
54.80	825.46	0.547	1509.07	110.02	166.02

Table 7.10: Model outputs during cruise including payload

T_{cruise} [N]	P_{output} [W]	$\eta_{total,cruise}$ [-]	P_{input} [W]	t [s]	$E_{total,cruise}$ [kJ]
7.73	191.25	0.808	236.70	2795.2	661.62

Vertical Landing

The last flight phase that must be considered is the landing. This is done analogously to the take-off analysis. Because vertical landing is also very demanding, accelerations will not be neglected. Also, the efficiency is again the product of motor efficiency, ESC efficiency and the FM. By using (7.9) and (7.10), the latter can be calculated. The density and velocity are again not constant in this flight phase. Therefore, the averages are presented in [Table 7.12](#) and [Table 7.13](#).

Hardware

In order to calculate the total energy consumption, the sensors and other power demanding hardware must also be considered. In order to calculate their required energy, the total time of the mission must be calculated, since these are active throughout the entire mission. This total mission time, including the power required for all hardware, is given in [Table 7.14](#).

Total Energy

Now that the energy required for all phases and all subsystems has been evaluated, the results can be compiled. The results of this are given in [Table 7.15](#). With these results, compliance with requirement **SAVED-CUST-RANGE-02-P&P-BAT-03** is shown. Note that the total energy consumed, $E_{consumed}$, is the sum of all previously mentioned components, and consequently dividing by the efficiency of the battery, which is given in [Subsection 7.2.5](#). Furthermore, the total energy required by the battery, $E_{required,bat}$, is obtained by dividing the consumed energy by the maximum DoD, as also given in [Subsection 7.2.5](#). Then, the required battery mass can be found by consequently dividing this required battery energy by the EOL correction factor of 0.7 depicted by k_{EOL} , and then dividing by the specific energy of the battery as both given in [Subsection 7.2.5](#). This can all be summarised by (7.16).

$$m_{bat,required} = \frac{E_{required,bat}}{k_{EOL}} = \frac{E_{consumed}}{k_{EOL}} \cdot \frac{1}{DoD} \quad (7.16)$$

Graphically, the consumption over time can be visualised by [Figure 7.2](#).

Also, by using the same battery characteristics, the state of charge can be given as function of time as well. This is graphically depicted in [Figure 7.3a](#) and [Figure 7.3b](#) for beginning of life (BOL) and EOL respectively.

7.2.5. Battery Selection and Specifications

In this subsection, a detailed analysis of SAVED's battery is given. In order to comply with the requirements set in [Subsection 7.2.2](#) and the energy required for the entire mission determined in [Subsection 7.2.4](#) a battery with a high specific energy is required. In [9], the battery type was decided to be a Lithium Polymer (LiPo), because of its high specific energy and its increased safety over a Lithium Ion battery. With this in mind, suitable off-the-shelf batteries were selected and compared.

A detailed trade off for the batteries was not considered necessary, because the selected battery scored significantly better than the other batteries. The battery that is selected for SAVED consists of cells which have

Table 7.11: Model outputs during cruise excluding payload

T_{cruise} [N]	P_{output} [W]	$\eta_{total,cruise}$ [-]	P_{input} [W]	t [s]	$E_{total,cruise}$ [kJ]
6.31	149.21	0.808	184.66	3071.2	567.11

Table 7.12: Model outputs during landing including payload

$T_{landing}$ [N]	P_{output} [W]	$\eta_{total_{landing}}$ [-]	P_{input} [W]	t [s]	$E_{total_{landing}}$ [kJ]
171.43	1980.25	0.508	3898.13	5.90	23.00

Table 7.13: Model outputs during landing excluding payload

$T_{landing}$ [N]	P_{output} [W]	$\eta_{total_{landing}}$ [-]	P_{input} [W]	t [s]	$E_{total_{landing}}$ [kJ]
142.00	1491.38	0.509	2930.01	5.90	17.29

Table 7.14: Model outputs for power demanding hardware

$t_{mission_{tot}}$ [s]	$E_{Raspberry}$ [kJ]	$E_{Velabit}$ [kJ]	$E_{Pixhawk}$ [kJ]	$E_{Firefly}$ [kJ]	$E_{total_{hardware}}$ [kJ]
7367.17	93.93	58.94	18.42	14.73	186.02

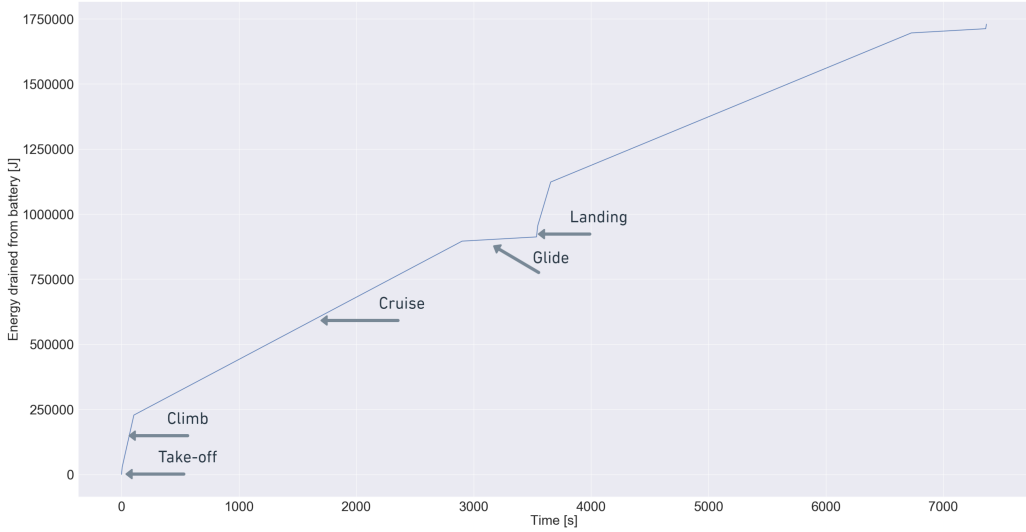


Figure 7.2: Energy consumed throughout the mission. A two way journey is indicated, flight phases on right-hand side are equivalent to left-hand side flight phases

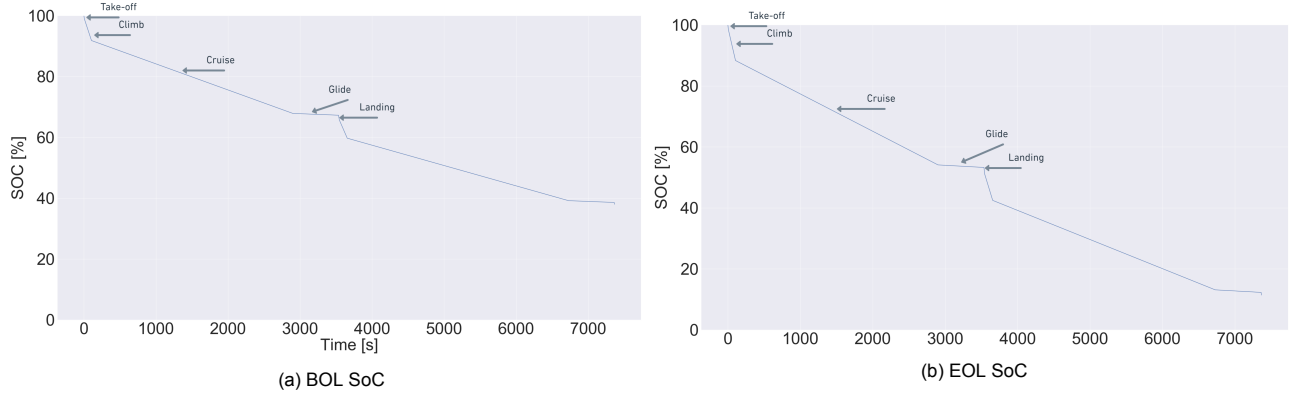


Figure 7.3: State of charge over time throughout a typical mission. A two way journey is indicated, flight phases on right-hand side are equivalent to left-hand side flight phases

Table 7.15: Model outputs for complete mission

$t_{mission}$ [s]	$E_{consumed}$ [MJ]	$E_{required_{bat}}$ [MJ]	$m_{bat_{actual}}$ [kg]	$m_{bat_{required}}$ [kg]
7367	1.73	1.92	3.6	3.55

Table 7.16: SAVED's battery pack specifications

Cell capacity [Ah]	Nominal Voltage [V]	e [Wh/kg]	Dimensions[m]	m_{cells} [kg]	m_{casing} [kg]
11.6	23.1	246	0.59x0.25x0.13	3.15	0.45

Table 7.17: Energy consumption verification

	Energy Consumption Model	Verification Model	% difference
P_{TO}	2757.73 [W]	2716.70	-1.48 %
$P_{landing}$	1980.25	1894.69 [W]	-4.32 %

a specific energy of 246Wh/kg, thereby complying with requirement **SAVED-CUST-RANGE-02-P&P-BAT-01**. This battery is produced by a company called KOKAM. KOKAM are experts at developing UAV batteries, which have an exceptional energy density and safety¹. In order to comply with the required voltage of the electrical subsystems, six battery cells are placed in series to form a battery pack. Additionally, to meet the energy required and the required current, three of these battery packs are needed, which are placed in parallel to each other. These three battery packs will form the main battery of SAVED. The specifications of the entire battery can be found in [Table 7.16](#). From this table it becomes clear that requirement **SAVED-CUST-PLD-01-P&P-BAT-01** and **SAVED-CUST-RANGE-02-P&P-BAT-02** are met. Furthermore, it is specified in the Kokam's technical data sheet [42] that by cycling at 90% DoD, a cycle life of >3000 cycles can be attained. By this time, 70% of the original capacity remains. Therefore, requirements **SAVED-CONS-SD-EM-02-P&P-BAT-01** and **SAVED-CONS-SD-EM-02-P&P-BAT-02** are met. Lastly, since lithium batteries have a battery efficiency η_{bat} of nearly 100%², a battery efficiency of 99% is chosen for the model, which is already accounted for in the model.

From [Section 7.1](#) it becomes clear that besides the main battery a smaller battery is needed in order to deploy the parachute when the main electrical circuit malfunctions. For this system, one small off-the-shelf LiPo cell battery of 13.2g was considered sufficient to supply the required power, as it must only perform one handling. This battery is produced to power the EMAX Tinyhawk drone.³

7.2.6. Verification and Validation of Energy Consumption

In this subsection the verification and validation procedures of the energy consumption tool are discussed. First, the verification of the tool will be reviewed by comparing the outcomes of the equations used in [Subsection 7.2.3](#) to the well known hover equation. Subsequently, the validity of the tool will be discussed by taking the Wingtra One drone as input for the entire model and consequently comparing the battery mass the model gives as an output to the actual Wingtra One battery.

Verification Energy Consumption Tool

The analytical model described in [Subsection 7.2.3](#) and [Subsection 7.2.4](#) mostly uses scientifically proven equations, well known physical theories and manufacturer data to determine the total energy required for the mission. These equations are verified by performing simple unit tests with the Cessna 310 plane as input. However, the equations used to determine the power required for take off and landing are not widely used, therefore the outcomes of these equations have been compared to outcomes of the hover equation, which can be found in (7.17) [13]. To match the equations used in [Subsection 7.2.3](#) for take-off and landing the same acceleration is included in the hover equation. This resulted in the differences shown in [Table 7.17](#), including the mass of the payload. The differences between the two models are so small that based on this outcome the energy consumption model is deemed to be verified.

$$P = \frac{T^{\frac{3}{2}}}{\sqrt{2\rho A}} \quad (7.17)$$

¹<https://bit.ly/3hIbjK6> [Cited on: 29-05-2020]

²<https://bit.ly/3110UmS> [Cited on: 18-06-2020]

³<https://bit.ly/2zHDPKQ> [Cited on: 15-06-2020]

Table 7.18: Energy consumption validation

	Predicted by tool	Actual Wingtra One	% difference
Battery Mass [kg]	0.623	0.604	3.15 %

Table 7.19: Energy consumption validation inputs

A_{prop} [m ²]	S [m ²]	$C_{Lcruise}$ [-]	V_{des} [m/s]	m_{bat_cells} [kg]	m_{bat_casing} [kg]	m_{tot} [kg]	r [m]	e [W h/kg]
0.142	0.438	0.473	3	0.529	0.076	4.50	49560	187.32

Validation Energy Consumption Tool

The validation of the energy consumption tool is crucial to determine if the correct model has been built. To analyse this the Wingtra One drone, which is also a flying wing and also cruises at 500m altitude⁴, is used as an input and ultimately the battery masses of the tool and the actual Wingtra One drone are compared. For this analysis the assumption was made that the aerodynamic parameters of SAVED and Wingtra One are identical. This approach was deemed acceptable as both drone are flying wings with vertical fins as stabilisers and have a similar mission profile. The results of this analysis are presented in [Table 7.18](#). The difference in battery mass is so small that this tool is deemed validated.

The list of input parameters for this validation is given in [Table 7.19](#), where A_{prop} and the chord (which is a component of surface area S) have been estimated on geometry of the drone. $C_{Lcruise}$ has been based on the cruise speed. Lastly, V_{des} , m_{bat_cells} , m_{bat_casing} , m_{tot} , r , e and the wingspan (which also affects the surface area S) are all based on the Wingtra one's technical specification sheet [75]. All other parameters, C_{Lmax} , C_{Dclimb} , γ , L/D and C_{D_0} are assumed to be equal to SAVED's parameters. Lastly, the power required for hardware is also assumed to be equal. Since SAVED is a much bigger drone, it is also expected to demand more power for hardware. This is a possible cause of the difference between the predicted battery mass and the actual Wingtra One battery mass.

7.3. Engine and Propeller Selection

In this section the engine-propeller configuration of SAVED will be determined. To start, in order to obtain an idea of the performance requirements a functional analysis is given in [Subsection 7.3.1](#). This functional analysis is converted into a list of requirements in [Subsection 7.3.2](#). Followed by this the actual trade-off is performed in [Subsection 7.3.3](#) and finally an analysis on the noise assessment tool can be found in [Subsection 7.3.4](#).

7.3.1. Functional Analysis

In this subsection, the functional analysis regarding the performance of the engine-propeller configuration is given.

- **SAVED-P&P-FUNC-ENG-01:** Provide sufficient power during VTOL;
- **SAVED-P&P-FUNC-ENG-02:** Provide sufficient power during cruise;
- **SAVED-P&P-FUNC-ENG-03:** Provide sufficient power during climb;
- **SAVED-P&P-FUNC-ENG-04:** Provide sufficient power during acceleration and control manoeuvres;
- **SAVED-P&P-FUNC-ENG-04:** Fit within the design;
- **SAVED-P&P-FUNC-ENG-05:** Be environmentally friendly;
- **SAVED-P&P-FUNC-ENG-06:** Shall not disturb the usual sound level during cruise;
- **SAVED-P&P-FUNC-ENG-07:** Shall be compatible with the battery.

7.3.2. Requirement Analysis

This subsection provides the list of requirements that must be met by the engine-propeller configuration. This list is created following the functional analysis in [Subsection 7.3.1](#).

⁴<https://bit.ly/3dgEYqs> [Cited on: 19-06-2020]

Table 7.20: Engine-propeller configurations

	Engine	Propeller
Configuration 1	KDE4215XF-465	15.5x5.3 Triple Blade
Configuration 2	KDE4215XF-465	15.5x5.3 Dual Blade
Configuration 3	KDE5215XF-435	15.5x5.3 Dual Blade
Configuration 4	KDE5215XF-330	18.5 x 6.3 Dual-Blade

Table 7.21: Maximum sound pressure level (SPL) at a radius of 1.5m for take-off and 500m for cruise

	$RPM_{take-off}$	RPM_{cruise}	$SPL_{take-off}$ [dB]	SPL_{cruise} [dB]	Compliance
Configuration 1	8166	1719	106.20	9.02	Yes
Configuration 2	9245	1953	110.52	24.63	No
Configuration 3	9286	1905	111.05	24.90	No
Configuration 4	7080	1375	106.65	23.00	Yes

- **SAVED-CUST-VTOL-01-P&P-ENG-01:** The engine-propeller configuration shall provide sufficient power to at least accelerate with 0.2g during VTOL;
- **SAVED-CONS-FLIGHT-01-P&P-ENG-01:** The engine-propeller configuration shall provide sufficient power to at least attain a ROC of 5m/s during climb;
- **SAVED-CONS-DIM-01-P&P-ENG-01:** The propellers shall have a maximum diameter of 0.525m (compliant with the geometric limits mentioned in [Subsection 5.1.5](#));
- **SAVED-CONS-SD NOI-01:** The sound pressure level shall be below 110dB at a distance of 1.5m during take-off;
- **SAVED-CONS-SD NOI-02:** The sound pressure level shall be below 35dB at a distance of 500m during cruise conditions;
- **SAVED-CUST-RANGE-02-P&P-BAT-ENG-01:** The engines shall have a nominal voltage of 23.1V.

7.3.3. Engine and Propeller Trade-Off

In this subsection the process of trading-off the different engine-propeller configurations is discussed. To start, a selection of configurations for further analysis is presented. Subsequently, the methodology of analysing the configurations' performance parameters is discussed. Following this, the trade-off methodology is explored. Finally, the results of the trade-off are presented.

Selection of Possible Engine-Propeller Configurations

For this trade-off, off-the-shelf components were considered that met the power requirements set in [Subsection 7.3.2](#). Based on these requirements, four engine-propeller configurations are determined. Note that by doing this, compliance with requirements **SAVED-CUST-VTOL-01-P&P-ENG-01**, **SAVED-CONS-FLIGHT-01-P&P-ENG-01**, **SAVED-CONS-DIM-01-P&P-ENG-01** and **SAVED-CUST-RANGE-02-P&P-BAT-ENG-01** is already shown. These four configurations all come from the UAV engine manufacturer KDE Direct, which is one of the leading companies worldwide in the manufacturing of UAV engines.⁵ KDE Direct has already tested the configurations and provides a detailed data sheet with the configurations which is used in this trade-off. The four configurations that are considered can be found in [Table 7.20](#).

Performance Analysis Methodology

The first performance parameter that is analysed for each configuration is the noise level, for which the approach is explained in [Subsection 7.3.4](#). This parameter is set as a binary parameter, which means that if the configuration does not meet the noise requirements set in [Subsection 7.3.2](#), it will automatically be discarded as a feasible design option. [Table 7.21](#) provides the noise levels of the four configurations during take-off. How these noise levels are obtained will be further analysed in [Subsection 7.3.4](#).

From [Table 7.21](#) it becomes clear that configuration 2 and configuration 3 do not meet the noise requirement of 110dB, which is clearly the limiting requirement. The main cause for configurations 2 and 3 not meeting the

⁵<https://bit.ly/3d8mete> [Cited on: 12-06-2020]

Table 7.22: Specifications configuration 1 and configuration 4

	Efficiency [g/W]	Cost [\$]	Mass[kg]	Geometric Considerations [m]
Configuration 1	11	148	0.250	0.39
Configuration 4	13.53	195	0.36	0.47

Table 7.23: Engine-Propeller Trade-Off Weights

	Efficiency	Cost	Mass	Geometric Considerations
Weights	0.4	0.1	0.2	0.3

requirement is their exceptionally high RPM, which can be observed in [Table 7.21](#) as well as their two-blade configuration. For this reason these configurations are excluded from the trade-off. Furthermore, it can be seen that configuration 1 has a far superior performance during cruise, due to its triple blade configuration. The two remaining configurations will be further analysed on the following parameters:

- | | |
|---|---|
| <ul style="list-style-type: none"> • Efficiency [g/W] • Cost [\$] | <ul style="list-style-type: none"> • Mass [kg] • Geometric Considerations [m] |
|---|---|

The first three parameters are relatively straightforward and are obtained from manufacturer data. However, for the last one, geometric considerations might need some more explanation. Geometric considerations considers how well the configuration integrates in the design as a whole. Based on the wingspan of 3m and the fact that SAVED has four propellers, a constraint of 0.525m for the propeller diameter was set. This is the largest off-the-shelf propeller that would fit into the design. However, a slightly smaller propeller is more desirable for design considerations. In [Table 7.22](#) the parameters per configuration can be observed.

Trade-Off Methodology

In order to quantitatively trade-off the engine-propeller configurations based on their performance parameters, the Weighted Sum Method (WSM) is used. The WSM assigns a score P_i to alternative A_i for N criteria for $1 \leq i \leq M$ where M is the number of alternatives based on [\(7.18\)](#) [70]. Furthermore, for the WSM, [\(7.19\)](#) holds.

$$P_i = \sum_{j=1}^N a_{i,j} W_j \quad (7.18)$$

$$\sum_{j=1}^N W_j = 1 \quad (7.19)$$

$$\delta'_{k,i,j} = \frac{P_j - P_i}{a_{jk} - a_{ik}} \frac{100}{W_k} \quad (7.20)$$

Where $a_{i,j}$ and W_j in [\(7.18\)](#) correspond to the measurement of performance corresponding to alternative i and criterion j . As the units of different criteria need to comply with each other in the WSM [70], the measurements of performance a in [\(7.18\)](#), have been normalised between 0 and 1, where the worst performing alternative has been assigned a score of 0 and the best performing alternative has been assigned a score of 1. Everything in between has been scored according to a linear scoring function for all criteria mentioned in the previous subsection. A sensitivity analysis, resulting in a sensitivity matrix, is performed on the result of the trade-off in order to assess the most critical criterion. That is, the sensitivity analysis shows the minimal percentage a weight corresponding to a certain criterion has to change in order to swap the ranking between the most desirable outcome of the WSM, and the alternative to which the most critical criterion belongs. The relative quantity $\delta'_{k,i,j}$ by which W_k belonging to criterion k needs to be changed in order to reverse the ranking of A_i and A_j is given by [\(7.20\)](#) [70] [9].

Trade-Off Results

The performance parameters of configuration 1 and configuration 4 are obtained from KDE Direct as previously mentioned. The weights for the WSM corresponding to the trade-off criteria mentioned in performance analysis methodology can be found in [Table 7.23](#). From [Table 7.23](#) it can be noted that efficiency has been given the highest weight as this is one of the most critical design parameters of the power and propulsion department. Next, cost has been assigned a relatively low score as a price difference of US\$47 is not a significant difference when looking at the total cost. Furthermore, it can be seen that mass has been assigned a weight of 0.2 as it has a large impact on the power required for the drone to take-off. Lastly, geometric considerations have been given the second highest weight as it has a big impact on the integration of the propulsive subsystem in the design.

When plugging in the trade-off parameters and the aforementioned weights into [Equation 7.18](#), the most desirable engine-propeller configuration is configuration 1. The most critical criterion is the efficiency, which must be increased by 50% for the outcome of the trade-off to change. This percentage is considered large enough to accept the outcome of the trade-off.

7.3.4. Noise Assessment

In order to construct a proper trade-off, the engine-propeller combinations must also be evaluated in terms of noise emission. As mentioned in [9], an analytical tool is built to assess the noise levels of SAVED. This assessment is crucial to the engine-propeller trade-off, since in case a configuration does not meet the requirements, it cannot enter the final trade-off. The requirements are defined to be 1) **SAVED-CONS-SD NOI-01** (The sound pressure level shall be below 110dB at 1.5m during VTOL conditions) and 2) **SAVED-CONS-SD NOI-02** (The sound pressure level shall be below 35dB at a distance of 500m during cruise conditions). Note that compliance with both requirements is already shown in [Table 7.21](#) for the chosen configuration.

Assumptions of Noise Model

The reason that the noise is evaluated for all points on a circle is that the sound level depends on angular position. It is assumed that if no point on the circle exceeds the maximum sound pressure level (SPL), the requirement is met. Some other assumptions are necessary in order to successfully evaluate the noise emission of the drone. It is firstly assumed that the noise only consists of two sources of rotating propeller noise [22], as further explained in the model description. Thus, it is assumed that other sources of noise are negligible. Furthermore, the propellers are assumed to be point noise sources. With this assumption, spherical spreading can be considered, which results in the sound pressure level varying inversely with distance squared from the source [46]. Also, this 'Geometric' Attenuation is assumed to be the only attenuation, thereby neglecting atmospheric attenuation. Lastly, it is assumed that for all points considered, the noise of the four propellers constructively interfere. All these assumptions lead to an overestimation of the noise, and can therefore be considered justified. Also, throughout the analysis it was found that for the current applications, the 1st harmonic always returned the highest SPL. Therefore, all SPL's given are for the first harmonic.

Model Description

As mentioned in the assumptions, only two noise sources are considered. They are ordered rotational noise, and broadband vortex noise. The former originates from the static pressure field generated by the blades, causing harmonic loads [22]. The latter is generated by the shedding of vortices from the trailing edge of the blades [22]. From [46], the theory of rotational noise can be modelled by [\(7.21\)](#) for engineering use.

$$p_m = \left| \frac{169.3 o B R M_{tip}}{s A_{prop}} \left[\frac{0.76 P_h}{M_{tip}^2} - T \cos \theta \right] J_{oB}(x) \right| \quad (7.21) \quad x = 0.8 M_{tip} o B \sin \theta \quad (7.22)$$

Where x is given by [\(7.22\)](#), o is the order of harmonic, P_h is the power in horsepower, T is the thrust in lb, A_{prop} the propeller disk area in ft², M_{tip} the tip Mach number, B the number of blades, R the radius in ft, s the distance from the source in ft, θ the angle from the forward propeller axis to observer in rad and J_{oB} the Bessel function of order oB . Note that this equation returns the sound pressure level p_m in dynes/cm².

Secondly, the broadband vortex noise can be modelled by [\(7.23\)](#) [46].

$$SPL_{300ft} = 10 \log \frac{k A_{blade} (V_{0.7})^6}{10^{-16}} \quad (7.23)$$

Where k is the constant of proportionality, taken equal to $3.8 \cdot 10^{-27}$ [38], A_{blade} is the propeller blade area, and $V_{0.7}$ the velocity of the blade at 0.7 radius. Note that this function returns the SPL in dB at 300 ft distance.

To convert [\(7.21\)](#) to a SPL in dB, [\(7.24\)](#) can be used [46].

$$SPL = 20 \log \frac{p_m}{p_{ref}} \quad (7.24)$$

Where p_m is obtained from [\(7.21\)](#) and p_{ref} is equal to 0.0002 dynes/cm². Furthermore, in order to obtain the noise profile around SAVED, these SPL values need to be converted to various distances. As mentioned in the assumptions, only geometric attenuation is assumed, and therefore the easily be converted from one location to another by using the ratio of distances. The loss or gain can then be expressed by [\(7.25\)](#) [17], with a_g the difference in dB, s_1 as the distance from the source to original location, and s_2 as distance from the source to the new location.

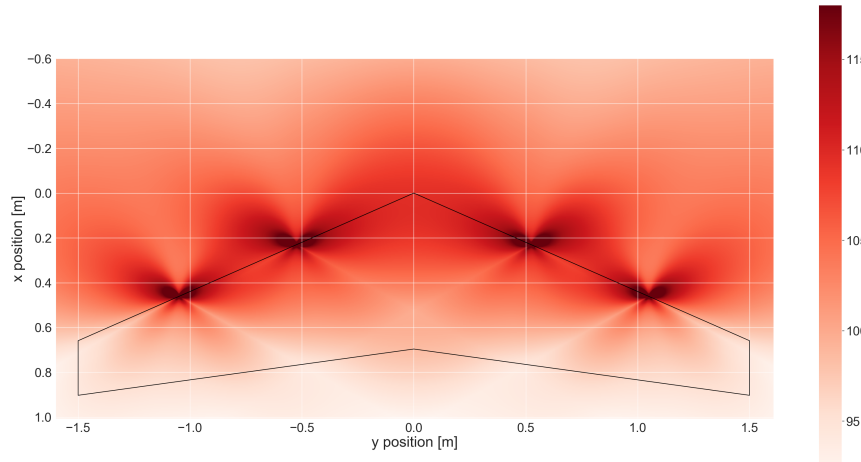
Figure 7.4: Heatmap of SAVED's sound pressure level in dB during take-off, 1st harmonic

Table 7.24: Verification of sound model

	σ [-]	s [ft]	R [ft]	P_h [HP]	T [lb]	B [-]	M_t [-]	Θ [rad]	Model [dB]	Verification [dB]
1 st sample	1	300	4	1000	12030	3	0.9	0.262	111	109
2 nd sample	1	300	4	2000	2376	8	0.4	0.262	59	64
3 rd sample	3	300	6	6000	33417	8	1.0	0.262	110	111
4 th sample	2	300	8	4000	29110	6	0.7	0.262	84	86
5 th sample	4	300	10	8000	59408	3	0.8	0.262	100	102
6 th sample	2	300	10	6000	23206	6	0.5	0.262	53	55

$$a_g = 20 \log \frac{S_2}{S_1} \quad (7.25)$$

Model Outputs

Having defined the calculation method of the model, the outputs can now be given. Firstly, the requirement on take-off and landing is assessed. By utilising technical data of the manufacturer, a relation between RPM and engine thrust can be established. They are given by (7.26) and (7.27), with the thrust T in N.

$$RPM = 1237T^{0.479} \quad (7.26)$$

$$T = \frac{RPM}{1237}^{2.087} \quad (7.27)$$

Since take-off requires more thrust and power, this is the limiting case. From the requirements, the maximum sound pressure level is 110dB during take-off on a radius around the centre of gravity. The outputs can be found in Table 7.21. Note that again the first harmonic is given since it returned the limiting SPL for all configurations. Next to this, the outputs for the assessment of the requirement during cruise is also displayed in Table 7.21. Lastly, the noise profile around SAVED can be illustrated using a heat map. This is done by evaluating the sound pressure level at all points surrounding the drone. the result of this can be found in Figure 7.4.

Verification and Validation of Noise Emission Tool

In order to verify the sound model, the outcomes of the sound model is compared with outcomes of [38]. In order to do so, the inputs of the sound model naturally matched the inputs of the verification model. The result of this analysis can be seen in Table 7.24. Since this verification must be done manually (i.e. the inputs have to entered by hand), a sample batch with inputs that are as discrete as possible has been selected to enter the verification process. This is done that the model return correct outputs for the entire range of inputs it was intended for. Note that the angle Θ is fixed at 0.262 rad, since that value corresponds to the location of most noise emission [38]. From Table 7.24, it becomes clear that the sound model accurately matches the results of the verification model for a wide variety of input parameters. Therefore, the model can be considered verified.

Also, according to [46], the model "gives reasonable agreement with experimental results for the first few harmonics of conventional propellers operating at moderate tip speeds and forward velocities". Therefore, the model can also be considered validated.

Materials Selection and Structural Design

State-of-the-art structural design is a fundamental feature of any high-performance aerospace vehicle for a series of reasons. Banally, the failure of a critical, single path structural component will result in a crash of the drone. Less trivially however, excessive compliance and play of load-carrying structures will cause performance losses and faster degradation, resulting into higher operational costs. Additionally, manufacturing costs and sustainability considerations are strictly related to materials selection and design choices. All of this needs to be balanced while taking into account that structural components do not increase the drone's performance, meaning that the structural mass fraction needs to be as small as possible, while allowing the rest of the subsystems to perform their function at optimal levels. The objective of the Structures, Materials and Manufacturing (SMM) department has thus been to find the right balance between performance, reliability, ease of manufacturing and maintainability. The findings are thus extensively and accurately presented in this chapter. The structure will be the following: [Section 8.1](#) will present the wing's functional analysis with respect to SMM; [Section 8.2](#) will present the wing requirements (which have been generated in the previous design phase); [Section 8.3](#) will present a detailed overview of the wing box's design process; [Section 8.4](#) will present the preliminary sizing of other structural elements (which need however to be considered equally important). Lastly, the total structural mass breakdown is presented in [Section 8.5](#). It is finally worth to note that the drone structure is divided into three different sections, namely two wings and a centre section, in order to allow for ease of manufacturing, maintenance and transportability.

8.1. Functional Analysis

Based on a general functional analysis of the wing structure purpose performed at a previous stage of the design [9], the following functions were identified. These are converted into specific requirements in [Section 8.2](#).

- **SAVED-STR-FUNC-01:** Provide sufficient strength to the wings following all operational loads.
- **SAVED-STR-FUNC-02:** Provide sufficient stiffness to the wings following all operational loads.
- **SAVED-STR-FUNC-03:** Maintain the aerodynamic profile of the wing.
- **SAVED-STR-FUNC-04:** Provide an attachment frame for other subsystems.

8.2. Requirement Analysis

In the previous design phase [9], the following requirements were generated:

- **SAVED-CONS-CERT-01-WING-STR-01:** The principal structural elements of the wing shall be able to carry the normal stresses induced by bending under 150% of the ultimate loading condition without failure.
- **SAVED-CONS-CERT-01-WING-STR-02:** The principal structural elements of the wing shall be able to carry the shear stresses induced by the transverse shear and torque under 150% of the ultimate loading conditions without failure.
- **SAVED-CONS-CERT-01-WING-STR-03:** The wing skin shall not buckle when subjected to cruise flight loads.
- **SAVED-CUST-RANGE-02-WING-STR-04:** The wingtip shall not deflect more than 5% of the length of the semi-span relative to its root position during normal cruise flight.
- **SAVED-CONS-CERT-01-WING-STR-05:** The wing shall be stiff enough to allow a torsional deformation rate smaller than or equal to 1deg/m when the elevons are actuated to their maximum deflection angle.
- **SAVED-CUST-RANGE-02-WING-STR-06:** During cruise flight, the wing skin shall not deform by more than 5% of the local airfoil thickness, relative to its design position.

- **SAVED-WING-STR-07:** The maximum normal stress experienced by each structural element, of a given material, during cruise flight, shall be below the stress amplitude required to achieve a lifetime of 20,000 cycles¹ for that given material.

Since the wing functionality has not changed since the midterm phase [9], the aforementioned requirements are kept unchanged. It is worthy to note that the identifiers have changed, in order to improve the traceability of their origin.

8.3. Wing Box Design

This section will provide an overview of the design process followed in order to perform an accurate sizing of the wing box. Firstly, an overview of the structural layout is provided in [Subsection 8.3.1](#). Secondly, the considered load cases are described in [Subsection 8.3.2](#). Thirdly, [Subsection 8.3.3](#) will guide the reader through the procedures followed in order to develop a structural analysis software. [Subsection 8.3.4](#) will provide an overview of the procedures used in order to verify and validate the developed software. Lastly, [Subsection 8.3.5](#) will summarise the final wing box design; requirements are also verified.

8.3.1. Structural Layout and Selected Materials

Regarding the structural layout, two main concepts were briefly considered: a box-like stiffened structure and a foam-filled one. Following recyclability considerations, the latter was immediately discarded and thus the former was selected for further development.

Key structural elements thus consist of a load-carrying skin, stiffening elements, a main spar, an aft spar, and ribs. Following manufacturing and performance considerations, the skin and the stiffeners are made of a quasi-isotropic (QI) Carbon Reinforced polyether ether ketone (PEEK) composite, given the high stiffness and strength to weight ratio [2]. The ribs and spars are instead made of aluminium 6061-T6 alloy [2]; given the relatively low loads, higher grade (and thus more expensive both in terms of raw material and manufacturing) aluminium alloys were seen as unnecessary.

The two spars are mainly necessary for ribs alignment and have low bending stiffness. The ribs are slid onto the spars and fixed in place with aluminium rings located at either side of the rib. As the aft spar is perpendicular to the ribs, 3D printed adaptors are required in order to create a proper connection between the main spar and the ribs.

The wing skin is additionally attached to the ribs by means of aluminium clips, as shown in [Figure 8.4](#). Bolted and riveted connections were kept at a minimum in order to allow for laser cutting of rib elements in order to limit the costs, reduce weight, as well as ensure faster manufacturing and maintainability procedures². The designed joints rely on the stiffness of the clip in order to exert a clamping force on the ribs. Such clamping force ensures out-of-plane strength of the joint, while the resulting frictional forces will provide the sufficient shear strength required to transfer these kind of loads. It is important to note that because of low reliability of friction-based joints due to the high dependence of friction to environmental conditions (e.g. moisture), a ‘solid wall’ on both sides of the clip is required in order to ensure an additional constraint. Nevertheless, testing of multiple clips designs and stiffness will be required in order to ensure a solid and play-less joint in most environmental conditions, as the ‘wall’ is essentially a fail-safe feature.

Lastly, it is worthy to note that materials selection has been performed while keeping the sustainability requirements, stated in [Subsection 25.2.1](#) in mind. This also led to the choice of using thermoplastic composites rather than thermosets.

8.3.2. Load Case Analysis and Generation

In order to model the wing structure as accurately as possible, it was fundamental to identify relevant load cases and correctly model them. In general, the wing will be loaded in three different modalities: shear, bending and torsion. These three modalities are discussed in this subsection.

¹A minimum lifetime of 20,000 cycles would ensure a depreciation of the drone cost to about 1\$/mission, following the cost estimates set in the Baseline Report [8]

²During maintenance, the operator would only need to un-secure a limited amount of bolts and successively exert a pulling force on the skin

Shear of The Wing Box

For this analysis, four main shear force components were identified, namely lift, weight, thrust and drag. All of them were included in the model. Thrust is modelled as point loads at the engine locations, as defined in [Section 6.1](#) of 51.5N each in magnitude as described in [Subsection 11.3.2](#). The lift distribution including propeller effects was modelled by the aerodynamics department, as documented in [Subsection 9.3.3](#). The drag force distribution was successively approximated by dividing the lift distribution by lift-over-drag (L/D) as given in [Section 9.2](#). The weight distribution was generated by computing the mass of each subsystem, dividing it by the area over which it is located (wing or centre section) and, successively, this ‘pressure’ was multiplied by the scaling defined by (8.1) [9], in which c_r [m] is the root chord, x [m] is the local spanwise location and h [m] is the height of the triangle having the root chord as a base and the two sides coinciding with the wing’s leading and trailing edges.

$$A_x(x) = \frac{\partial A(x)}{\partial x} = c_r(1 - x/h) \quad (8.1)$$

The overall shear force distribution was simply computed by superimposing the four different components.

Bending of The Wing Box

Wing box bending is primarily caused by the lift and the mass of the structure itself, by the torque that the propellers need to rotate, by the thrust force and by the drag. The first two cases cause bending about the x-axis³, while the thrust and drag forces induce bending about the z-axis⁴. For this analysis, bending loads induced by the propeller torque have not been considered for a number of reasons. First of all the propeller rotational direction was not decided until later in the design, and thus assuming an incorrect sign for the induced bending would have been detrimental for the design. Additionally, it was assumed that the most likely case would be one in which two propellers of a single wing would be counter-rotating, and thus the net bending moment contribution at the root - the most critical location - would be essentially null. The internal bending moment distribution was simply computed as the antiderivative of the internal shear force distribution.

Torsion of The Wing

Regarding wing torsion, the following components were identified:

- Pitching moment during cruise flight: the pitching moment created by the wing sweep is essentially a torsional force acting on the wing structure.
- Lift and drag forces do not act through the shear centre: the lift and drag were modelled to be acting at the aerodynamic centre of each cross section. Since the aerodynamic centre does not generally coincide with the cross section’s shear centre, this offset will induce a twist of the wing structure.
- Thrust force may not act through the shear centre: generally, a small offset is expected between the line of action of the thrust force and the cross section’s shear centre. This is however still a design variable to be addressed in the future⁵ and therefore was not considered for this analysis, given that the net expected contribution is small.
- Pitching moment induced by elevon deflection. The spanwise pitching moment coefficient distribution was obtained using XFLR5 [21] with elevons fully deflected as described in [Chapter 11](#). An on-off switch is used to model the wing both with and without elevon deflection.

8.3.3. Structural Analysis of The Wing Box

The first step towards the wing’s structural design was to develop a structural analysis tool which would allow for fast design iterations and optimal spars and stiffening elements placement. Such tool was built using structural analysis methods from Megson [49] and Kassapoglou [41]. The program essentially slices the half-wing at N locations and structural computations are successively performed for each of those locations.

Model Assumptions and Simplifications

When building a structural model of the wing using the analytical approaches proposed by Megson and, to a smaller extent, by Kassapoglou, multiple simplifications are made.

³Being the x-axis defined in chordwise direction.

⁴With the z-axis normal to x and pointing up.

⁵The ‘vertical’ engine placement will affect stability and control, and aerodynamics other than structures.

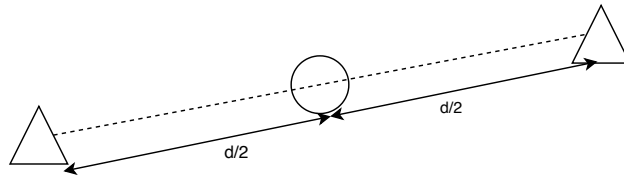


Figure 8.1: New generated point (circle) is equidistant to previously existing nodes (triangles)

First of all, the wing box was assumed to be made of an isotropic, homogeneous single material. While this is not the case in real life, where multiple anisotropic materials are employed, this was neglected as, at this stage of the design, such complexity and accuracy is not required. However, as the use of different materials introduces further uncertainty about the final size of the structure, using the material properties of the stiffer (or stronger) one would lead to an under-designed structure, resulting in an increase in structural mass of the drone at a later stage of the design process and thus loss in performance. As a consequence, the material properties used to model the wing box belong to the most compliant material (in absolute terms) between those employed, namely carbon fibre reinforced composites (CFPR) with a QI layup, as this would at most result into an increase in performance of the drone later in the design, in case the structure results to be lighter than expected.

Secondly, Megson's method lies its foundation in beam theory; this analysis method is a valid approach as long as deflections are small. This is a valid assumption for this model as SAVED-CUST-RANGE-02-WING-STR-04 sets a limit to the maximum wing compliance. Also, beam theory assumes that the cross section of the beam does not deform and remains planar.

Thirdly, the wing skin and stiffening elements are collapsed into small point areas (booms). As a consequence, the shear flow between two booms is constant, which, in practice, leads to an underestimation of the actual shear flow. Therefore, a fine mesh will be required in order to limit such inaccuracies.

Additionally, the model assumes the wing to have a constant sweep and taper ratio, meaning that the cross-section is linearly scaled from root to tip; this is indeed the case for SAVED, as displayed in [Figure 6.7](#).

It is further assumed that lifting forces act through the aerodynamic centre of the wing. This will result in a torsional moment in the likely case in which the shear centre of the cross section does not overlap with the aerodynamic centre of the airfoil.

It is worthy to note that the two spars have been excluded from structural computations for two reasons: their contribution to the second moments of area is negligible ($\approx 2\%$ at the root and 10% at the wing tip) and therefore they will have extremely limited impact on the bending stiffness of the structure. Regarding torsional loads, the ribs are not constrained from rotation about the main spar; any torsional load would therefore be transferred to the two spars by means of differential bending and, as already mentioned, the bending stiffness of the two spars is negligible.

Finally, the chosen reference frame of the structural simulation is a right-handed Cartesian reference frame with origin located at the leading edge of the airfoil, the positive x-axis pointing towards the trailing edge and the z-axis pointing up. The y-axis is consequently in spanwise direction.

Cross Section Properties

The structural analysis software is initialised by loading the cross section. The wing cross section is loaded by using a set of 81 points in x-y coordinates of the selected CAL4014L airfoil ([Section 9.1](#)), retrieved from [74]. The cross section is then interpolated and successively discretised into 2000 different points (equally spaced along the x-axis) in order to improve the accuracy of the calculations. The structure is then idealised using booms as proposed by Megson. This method essentially collapses the skin and stiffening elements into point-areas, which are connected by a zero-thickness skin. The booms provide bending stiffness, while the zero-thickness skin panels between each boom carry the shear flow. In order to compute the boom locations, new points were generated such that each new point would be equidistant to two previously generated points, as shown in [Figure 8.1](#). Defining $d/2$ [m] as the Euclidean distance between boom 1 and the adjacent nodes as shown in [Figure 8.1](#), the area assigned to each boom was simply computed using (8.2)

$$A_{boom1} = d \cdot t \quad (8.2) \quad A_{boom1} = \frac{bt}{6} \left(2 + \frac{\sigma_2}{\sigma_1} \right) \quad (8.3)$$

in which t is the skin thickness [m] and d the distance between the two adjacent nodes. This is a limit case of (8.3) [49] for $\sigma_1 \rightarrow \sigma_2$ and if the skin portion is condensed over a single point instead of two. In (8.3) b is the distance between two booms[m] and σ the normal stresses [MPa].

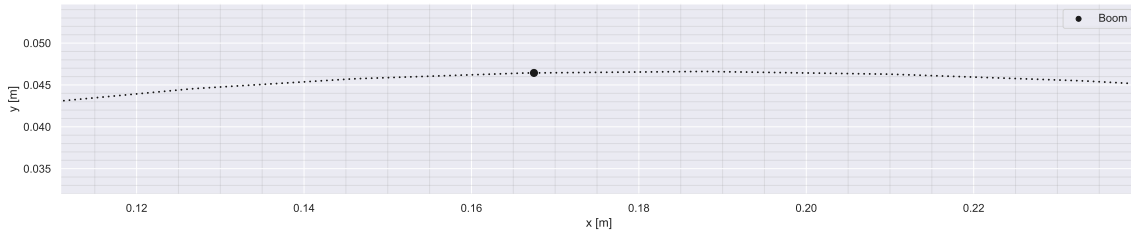


Figure 8.2: The skin of the wing box is modelled by multiple (small) booms. The single larger boom represents a stiffener.

Spars and stiffening elements are also reduced to point areas, with magnitude varying according to the geometry of the structural elements. A representative sketch of this can be visualised in Figure 8.2, in which each small dot is a boom representing the skin and the single, big one represents a stiffening element.

Once all the boom areas are obtained, the centroid location and second moments of area are easily obtained using (8.4) to (8.6) (identical equations were used to compute \bar{z} and I_{zz}), in which A_i is the area of a single boom [m^2], x_i [m] and z_i [m] are respectively the boom x and z-coordinates, \bar{x} and \bar{z} are the centroid x and z-coordinates and n the total number of booms.

$$\bar{x} = \frac{\sum_{i=0}^n (A_i x_i)}{\sum_{i=0}^n A_i} \quad (8.4)$$

$$I_{xx} = \sum_{i=0}^n (A_i (x_i - \bar{x})^2) \quad (8.5)$$

$$I_{zx} = \sum_{i=0}^n (A_i (x_i - \bar{x})(z_i - \bar{z})) \quad (8.6)$$

The last step in the computation of the cross-section properties is the calculation of the shear centre location. As a reminder to the reader, the shear centre is defined as the point through which a shear load will produce no twist [49]. The shear centre location is thus computed using the approach proposed by Megson: if a unit shear load, S_x , is acting outside the shear centre, then it will create a moment about the shear centre which will be equal to the moment generated by the induced shear flows about the shear centre itself. This is schematised in Figure 8.3 and formalised in (8.7), where S_x is a general shear force acting through the origin [N], ξ_0 [m] is the y-coordinate of the shear centre (z-coordinate in the chosen reference frame), q is the shear flow [N/m], r is the shear flow moment arm [m] and ds is an infinitesimal increment along the perimeter of the cross section [m].

$$S_x \xi_0 = \oint q_s r \times ds \quad (8.7)$$

In order to compute the shear centre, S_x is set to 1N, the shear flow is consequently computed according to the procedure that will be presented later in this subsection, and (8.7) is finally solved.

Bending of The Wing

Once cross section properties and loads were computed, the normal stress at all booms locations was computed using (8.8) [49].

$$\sigma_{yy} = \left(\frac{M_z I_{xx} - M_x I_{zx}}{I_{xx} I_{zz} - I_{zx}^2} \right) x + \left(\frac{M_x I_{zz} - M_z I_{zx}}{I_{xx} I_{zz} - I_{zx}^2} \right) z \quad (8.8)$$

in which M [Nm] are the internal bending moments and x and z are the relative location of each boom with respect to the cross section's centroid.

Shear of The Wing

The shear flows induced by pure shear of the wing are computed according to (8.9) [49], in which q_s is the shear flow distribution, q_b is the open-section shear flow and $q_{s,0}$ is the closed section shear flow.

$$q_s = q_b + q_{s,0} \quad (8.9)$$

These ‘open’ and ‘closed section’ definitions arise since it is generally not possible to select a point of a closed section at which the shear flow is null. As a consequence, the procedure to compute the shear flow of a closed-section is the following: first a ‘cut’ is made, thus assuming the shear flow to be null at said point and the section

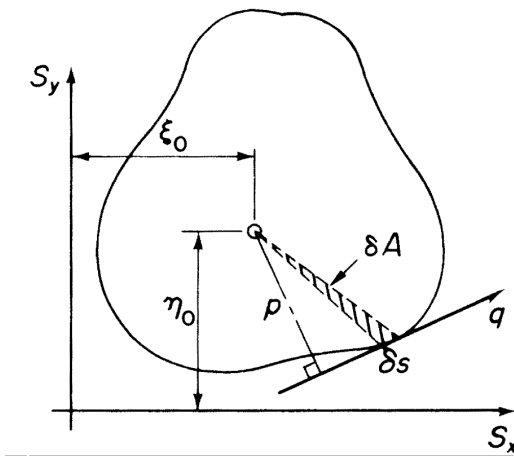


Figure 8.3: The moment created by a force acting outside the shear centre is equal to the moment generated by the induced shear flow about the shear centre [49]

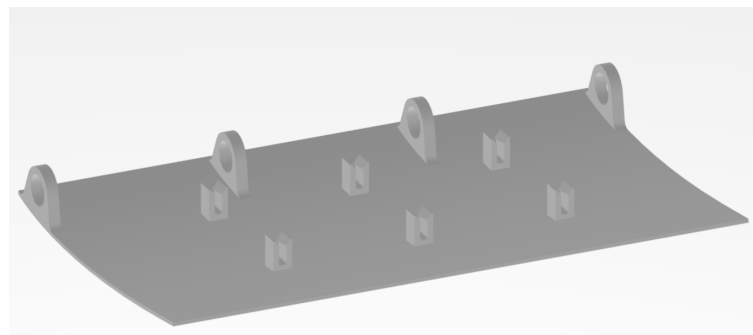


Figure 8.4: Prototype of a skin panel with the clips attached. This prototype, together with a mock-up of ribs and main spar is currently being 3D-printed in order to test the design.

will be treated as open. Successively, the ‘open section’ shear flow is computed according to (8.10) [57] (where S is the shear force).

$$q_b = - \left(\frac{S_x I_{xx} - S_z I_{xz}}{I_{xx} I_{zz} - I_{xz}^2} \right) \left[\sum_{i=0}^n A_i z_i \right] - \left(\frac{S_z I_{zz} - S_x I_{zx}}{I_{xx} I_{zz} - I_{xz}^2} \right) \left[\sum_{i=0}^n A_i x_i \right] \quad (8.10)$$

Finally, the section is ‘closed’ by applying the following relation [57]:

$$q_{s,0} = - \frac{\oint (q_b/Gt) ds}{\oint ds/Gt} \quad (8.11)$$

in which G is the shear modulus [MPa]; all the other variables have already been addressed early in this section and thus this will not be repeated here.

Finally, as already mentioned, the two shear flows are superimposed using (8.9). Note that this is procedure was also used to compute the shear centre coordinates. As a consequence of this, when performing verification of the model, the shear flow solver was verified by simply checking the correctness of the shear centre location (as the solver itself was used to compute the coordinates).

Torsion of The Wing

As already mentioned in Subsection 8.3.2, if the torsion induced by thrust is disregarded, wing torsion has two remaining components: torsion caused by shear forces acting outside the shear centre and torsion caused by the wing’s pitching moment (and thus sweep). Once the internal twisting moment are computed, the resultant shear flow is computed using (8.12), in which \mathcal{T}_y is the torsional moment [Nm] and A_m is the area enclosed by the cross section.

$$q = \frac{\mathcal{T}_y}{2A_m} \quad (8.12) \qquad \tau_{xy} = \frac{q_{tot}}{t_{sk}} \quad (8.13)$$

Shear Stress

Once all the shear flow components have been computed, the total wing’s shear flow is simply computed by superposition of all the components. Subsequently, the shear stresses at each boom location is computed using (8.13), in which q_{tot} is the total shear flow and t_{sk} the skin thickness, which is assumed to be constant.

Von-Mises Stresses

Once normal and shear stresses were computed, in order to check for possible material failure regions, the von Mises stresses were computed in accordance with von Mises’ theory of elastic failure [49] (8.14), where σ represents normal stresses, while τ shear stresses. Note that for this specific case, $\sigma_{xx} = 0$.

$$\sigma_{VM} = \sqrt{\sigma_{xx}^2 + \sigma_{yy}^2 - \sigma_{xx}\sigma_{yy} + 3\tau_{xy}^2} \quad (8.14)$$

Following this analysis, it was concluded that no material yielding or fracture will occur ($(\sigma_{VM})_{max} = 7.8 \text{ MPa}$ for unstiffened skin at the root) and therefore buckling will be the design-driving failure mode.

Skin Buckling

For this preliminary buckling analysis, the each panel encompassed by two stiffening elements and two ribs was modelled as a flat plate. Each half-wing was sliced into 10 different segments at which the critical buckling stress is computed. Buckling of think plates can occur due to both shear and compressive loads. The critical compressive buckling stress, σ_{CR} [MPa], is given by (8.15) [49], in which k is a compressive buckling coefficient depending on boundary conditions (set equal to 4) and panel aspect ratio, E is the elastic modulus of the material [MPa], t is the skin thickness, b the panel width and ν the material's Poisson ratio. The shear buckling is given by an equation similar to (8.15), which however uses a shear buckling coefficient k_{shear} , which was set equal to 5 according to [49].

Trivially, when a panel is loaded both axially and in shear, the two load cases will interact with each other and thus it is critical to understand how the effective buckling of the panel is affected by such loading condition. In order to ensure no premature failure, the effect of the combined compression and shear was taken into account by using the interaction curves method, according to (8.16) [41].

$$\sigma_{CR} = \frac{k\pi^2 E}{12(1-\nu^2)} \left(\frac{t}{b}\right)^2 \quad (8.15) \quad \frac{\sigma_{yy}}{\sigma_{yycrit}} + \left(\frac{\tau_{xy}}{\tau_{xycrit}}\right)^2 \leq 1 \quad (8.16)$$

Essentially, to avoid buckling, the left-hand side of (8.16) must be smaller than 1. In (8.15), for a fixed skin thickness, the only free variable is b and thus the number of stiffeners and their relative placement was the design parameter to be varied. The skin thickness was set as fixed to 0.6mm as, from the preliminary analysis conduced earlier in the design phase, a thickness between 0.5mm and 0.6mm was seen to be as the most optimal solution. The reasoning behind the choice of such skin thickness has already been discussed in Subsection 8.3.5 and thus will not be repeated here again.

Out Of Plane Deformation of The Skin

According to **SAVED-CUST-RANGE-02-WING-STR-06**, the out-of-plane deformation of the skin due to the air pressure shall not be greater than 5% of the local airfoil thickness. This requirement sets another constraint on the ribs placement. The maximum out-of-plane displacement of a flat plate under a constant pressure load with simply supported edges is given by (8.17) (an Empirical relation) [12], in which a is the minor length [m] and b is the major length of the rectangular plate [m], p is the uniform pressure loading [N/m²], t is the plate thickness and E is the Young's modulus.

$$z_{MAX} = \frac{0.142pa^4}{Et^3[2.21(a/b)^3 + 1]} \quad (8.17)$$

The uniform pressure load was approximated by dividing the maximum value of the lift distribution [N/m] by the mean aerodynamic chord [m]. Given a fixed number of stiffeners, the rib spacing was tuned such that **SAVED-CUST-RANGE-02-WING-STR-06** was met.

Displacement Of the Wing Due To Bending

Given a bending moment and second moments of area spanwise distribution, the wing deflecting was simply computed by integrating (8.18) [49].

Displacement of The Wing Due To Torsion

The twist of the wing due to the internal torsional moments was computing by integrating (8.19) at multiple spanwise locations and applying proper initial conditions [49].

$$\frac{d^2w(x)}{dx^2} = \frac{M(x)}{E(x)I(x)} \quad (8.18) \quad \frac{d\phi}{dz} = \frac{T}{4A_m^2} \oint \frac{ds}{Gt} \quad (8.19)$$

8.3.4. Verification and Validation of Structural Analysis Software

Given the high complexity of the developed software, meticulous verification procedures were required. Note that no validation was required as the methods proposed by Megson, Kassapoglou and other cited sources have already been validated and are representative of the physics involved [49][41][12]. Furthermore, it was thoroughly checked that the assumptions in which those methods lie their roots are also valid for the developed

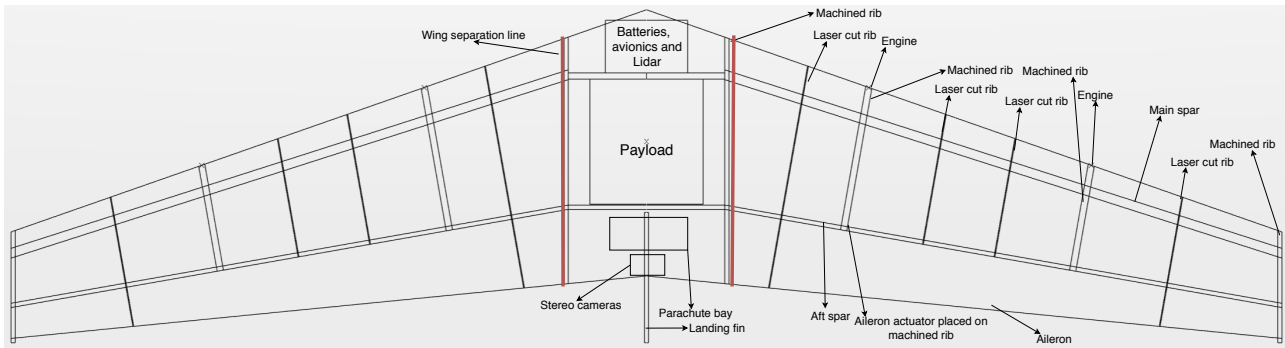


Figure 8.5: Representative sketch of wing planform design.

model. For instance, regarding beam theory, in order to achieve high accuracy, it is fundamental that there is no significant deformation of the cross section, as well as that the beam deflection is small. **SAVED-CUST-RANGE-02-WING-STR-06** sets a further requirement on the cross section deformation. Furthermore, post-buckling behaviours are not analysed and this indeed ensures that the analysis is limited to the case in which the cross-section remains planar and unreformed. Additionally, **SAVED-CUST-RANGE-02-WING-STR-06** sets a limit to the overall wing deflection, which can be reasonably classified as small.

Overall, the developed code consists of multiple functions and each function performs a specific calculation. Verification simply consisted of unit tests, comparing the outputs of said functions with known analytical solutions, given as an input a standard cross section with known cross-section properties. A 5% margin of error was deemed to be acceptable in order to account for discretization errors. Figure 8.10 provides a visual reference about the verification of the centroid, and shear centre computations, as well as the normal stress distribution, which is clearly symmetric about the cross section's symmetry axis.

8.3.5. Final Wing Box Design

Following multiple iterations with different rib spacing, number of stiffening elements and their chordwise location, the proposed final wing-box design will be presented in this subsection. A representative sketch of the wing planform can be found in Figure 8.5.

Stiffened skin

The wing box is composed by a 0.6mm thin CFRP skin. As already mentioned, it was previously decided that skin thickness values of 0.5-0.6mm are optimal for buckling performance [9]. The 0.6mm thickness is achieved by using three different layers of composite material. Two of the layers are composed by a woven PEEK⁶ prepeg, each of them having a thickness of 0.25mm, while the third layer is a uni-directional (UD) PEEK prepeg in spanwise direction, with a thickness of 0.1mm. This configuration allows to have fibres placed in $\pm 45^\circ$, 0° , and 90° directions, thus ensuring a QI layup with additional stiffness in spanwise direction thanks to the UD layer.

The upper surface of the skin is stiffened by 5 round, solid stiffeners (6mm in diameter) made of PEEK CFRP, while only 2 similar stiffening elements are placed on the lower surface.

The stiffened skin layout of the wing-box is summarised in Table 8.1.

Ribs Placement

Following the out-of plane skin displacement due to pressure loads requirement, which resulted being the most critical condition⁷, a maximum rib spacing of 225mm was computed. The computed spacing sets an upper bound to the maximum distance between two ribs; however, due to the presence of other subsystems (such as elevon actuators, engines), in practice, the ribs pitch will be slightly smaller than said value as, for instance, for each engine a rib is required. Since this maximum rib spacing requirement is fulfilled for all ribs, requirement number **SAVED-CUST-RANGE-02-WING-STR-06** is automatically satisfied.

A summary of the ribs placement and their relative mass can be found in Table 8.2. Although laser cutting was selected as the preferred manufacturing method for the ribs, due to the presence of interfaces, some ribs required machining to allow for bolted connections.

⁶Thermoplastic, for recyclability purposes

⁷Other requirements for ribs spacing could have been skin buckling and beam buckling, both of which set a higher rib spacing requirement

Table 8.1: Mass of each stiffening element for half-wing and total stiffeners mass for the full flying wing. Position is indicated as a percentage of chord length.

Item	Position [% c]	Mass [g/item]
Stiff. up 1	12.01	57
Stiff. up 2	25.02	57
Stiff. up 3	38.53	57
Stiff. up 4	54.04	57
Stiff. up 5	73.06	57
Stiff. low 1	21.92	57
Stiff. low 2	41.93	57
Wing skin	N.A.	1245
Total mass [g]		3288

Table 8.2: Mass of each rib for one half-wing. (M) indicates a machined 3D rib, used when bolted connections are required, while (L) indicated a laser cut 2D rib. The position indicates the y-coordinate of the rib's leading edge.

Item	LE y-pos. [mm]	Mass [g/item]
Rib 1 (M)	190	123.1
Rib 2 (L)	381.5	46.0
Rib 3 (M)	525	90.0
Rib 4 (L)	706.7	33.0
Rib 5 (L)	870.7	27.3
Rib 6 (M)	1050	48.7
Rib 7 (L)	1265.2	15.7
Rib 8 (M)	1500	23.1
Total mass [g]		813.8

Table 8.3: Summary of spars location and mass.

Item	Position [% chord]	Mass [g/item]
Main spar	15	359.9
Aft spar	69	101.9
Total mass [g]		923.6

Wing Spars

As already mentioned, wing spars are not the main load-carrying structural elements; instead, their main functionality is to provide attachment for other subsystems, such as engines and the elevon, as well as to align all the ribs during assembly. The main spar is located at 15% of the chord, which is where the airfoil has its maximum thickness. The aft spar is instead located at 69% of the chord, in order to maximise the elevon surface area. The positioning of the payload set a constrain to the most forward location of the aft spar. A summary of the overall spars location and mass is found in [Table 8.3](#).

Failure Analysis of Final Design

Once the final structural layout was defined, the design was validated by running once again the structural analysis software. The von Mises stress distribution along the wing profile, at the root, can be found in [Figure 8.6](#). Given a maximum σ_{VM} of approximately 5.3MPa, no material failure is expected and thus requirements number **SAVED-CONS-CERT-01-WING-STR-01** and **SAVED-CONS-CERT-01-WING-STR-02** are satisfied. Furthermore, given a material fatigue strength between 253MPa and 307MPa [2], requirement number **SAVED-WING-STR-07** is automatically satisfied as well.

The ‘interaction curves coefficient’, defined by [\(8.16\)](#), is shown in [Figure 8.7](#), regions corresponding to tensile stress have been masked as no buckling is expected.

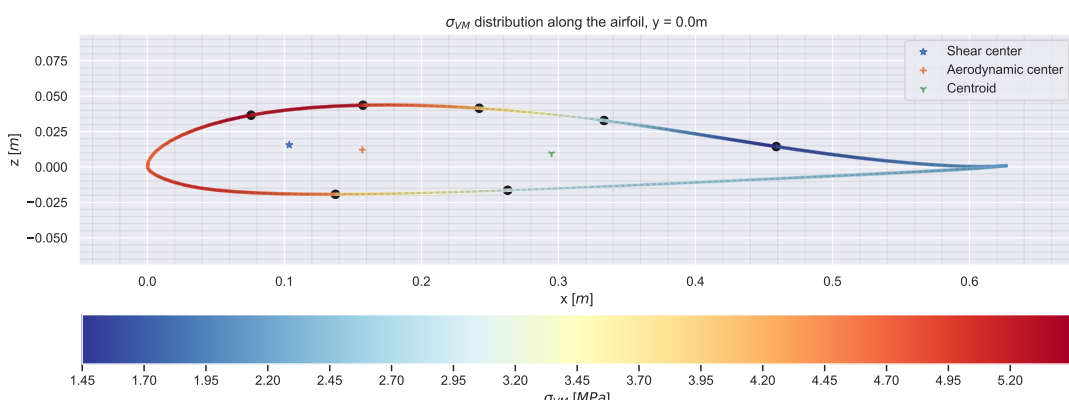


Figure 8.6: Von Mises stress distribution along the airfoil profile at the root of the wing. The black dots represent stiffening elements.

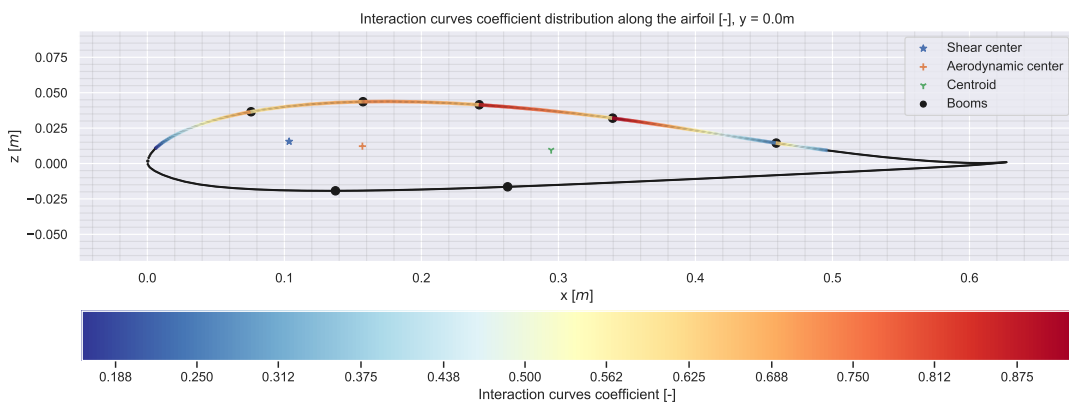


Figure 8.7: Interaction curved coefficient distribution along the root airfoil profile. Areas in which a tensile stress is present have been masked.

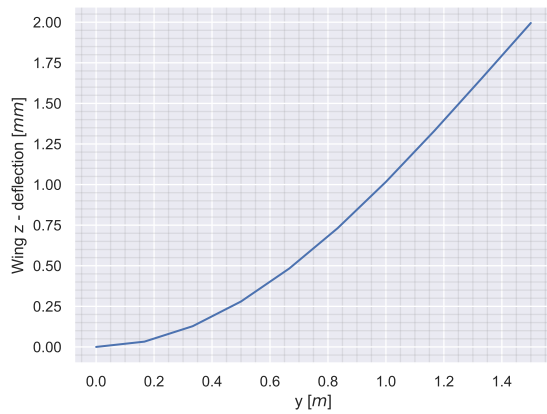


Figure 8.8: Spanwise wing deflection in the z-direction during cruise flight, in mm

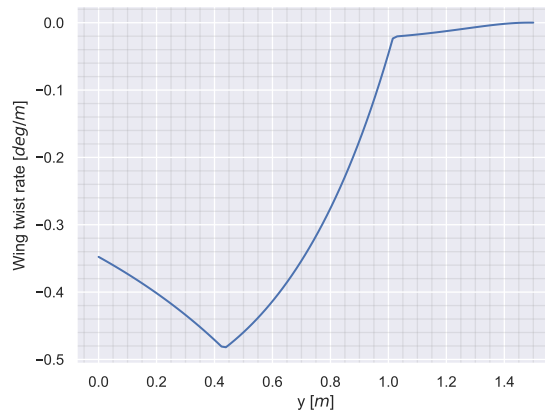


Figure 8.9: Spanwise wing twist rate deg/m with elevon fully deflected

From Figure 8.7, it is clear that at all critical locations (8.16) is satisfied, hence ensuring that requirement number **SAVED-CONS-CERT-01-WING-STR-03** is met.

Compliance Analysis

By means of double integration of (8.18), the maximum wing deflection during cruise flight is of 2mm, as shown in Figure 8.8. As a 2mm deflection is significantly smaller than 5% of the semi-wing span, requirement number **SAVED-CUST-RANGE-02-WING-STR-04** is fully satisfied. Similarly, Figure 8.9 clearly shows a maximum, wing deflection rate, with elevon fully deflected, of approximately 0.48°/m, which is smaller than the required 1°/m and therefore **SAVED-CONS-CERT-01-WING-STR-05** is fully satisfied as well.

8.4. Other Structural Elements

Besides the wing box, other structural elements were identified and preliminary sizing was performed in order to allocate a mass budget. This section will thus present the findings of such sizing. Subsection 8.4.1 will present the conceptual design of the centre section supports. Subsection 8.4.2 will cover the elevon mechanism concept. Successively, Subsection 8.4.4 will present a payload bay mass update from the Midterm design phase. Lastly, Subsection 8.4.5 will conclude this section by showing a preliminary sizing of the central fin.

8.4.1. Centre Section

The wing box's centre section is providing a connection between the two half wings. As further development of such structure is expected to take place in the future, no extensive analysis was performed. Nevertheless, it was quickly evaluated that two closed rectangular sections, 2mm in thickness, located in correspondence of the main and aft spar, would most likely be able to carry the loads and therefore a mass budget was allocated

Table 8.4: Summary of centre supports location and mass

Item	Position [% of chord]	Mass [g/item]
Main centre element	15	272.9
Aft centre element	69	236.0
Total mass (full wingspan) [g]		508.9

for such standard profiles. The root profile has an height of 118mm and a width of 15mm, while the aft profile has an height of 100mm and a width of 15mm. Both profiles are 380mm long. The mass breakdown is shown in [Table 8.4](#).

8.4.2. Elevon Actuator Mechanism

The elevon is attached at both extremities to the aft spar by means of spherical bearings in order to minimise the risk of jamming. The elevon is deflected using a linear actuator attached to the second machined rib (with location specified in [Table 8.2](#)) in order to reduce structural complexity. This type of actuator was chosen over a servo as it allows for placement in a chordwise location, and thus optimal packaging. In XFLR5 it was found that the maximum elevon hinge moment is of 1.8Nm. As an elevon deflection rate still needs to be defined, at this stage of the design it is not yet possible to pinpoint a solution, however the SFK CAHB-10 series⁸ is a promising solution in terms of mass (\approx 150-200g). While a single actuator can cost about 300€⁹, it must be considered that SFK¹⁰ is at the cutting edge of engineering design; this will be a guarantee of quality and reliability of such critical component, which is fundamental for the success of the drone.

It is worthy to note that although the actuators' preliminary selection and budgeting was performed in this chapter, they will not be included in the structural mass breakdown, as only load-carrying components are considered in [Table 8.5](#). Their mass will be budgeted in [Table 5.3](#). For such reason, a contingency of 10% is already applied over the actuators mass. To conclude, the budgeted mass for the elevon mechanism is of 440g and the cost is of 600€. A representative view of the elevon actuator connection is shown in [Figure 8.11](#). Note that this is only indeed representative and, for the sake of simplicity, spherical bearings have been omitted and the design is simplified as much as possible.

8.4.3. Engine Mounts

Similarly to what was done with the centre section and the elevon actuator mechanism, a top level sizing of the engine mounts was performed. The engine mounts are assumed to be made of an internal load-carrying structure and an external aerodynamic shell. The load-carrying structure is composed by three plates, two of which attach to the corresponding rib and the third one is holding the engine in place. All the elements have a thickness of 3mm. The inboard engine mount mass is of 141g while the outboard one weights 123g. The combined aerodynamic fairing mass is of 72g. These figures hold for each half-wing.

8.4.4. Payload Bay

The payload bay remains essentially unchanged since the previous design phase [9]. To summarise, the payload bay dimensions are of 118x278x295mm. It was however decided to reduce the outer shell thickness from 2mm to 1mm since the expected loads are negligibly small. The new computed mass of the payload bay is of 650g.

8.4.5. Landing Fin

The landing fin is a non-retractable structure, which, other than providing support while the drone is on the ground, improves the directional stability of the vehicle ([Chapter 10](#)). SAVED's tip over requirements were laid in the midterm report [9] and have since then been kept unchanged. Since the main function is still to provide landing support, no requirements on the surface area were generated. During the design process it was however considered to be crucial to reduce the size of the fin as much as possible both in order to keep the mass down, as well as because excessive directional stability would have an adverse effect on controllability.

⁸<https://bit.ly/2Bh0MVE> [Cited on 17-06-2020]

⁹<https://bit.ly/37BMICe> [Cited on 17-06-2020]

¹⁰<https://bit.ly/3hEwv3Z> [Cited on 17-06-2020]

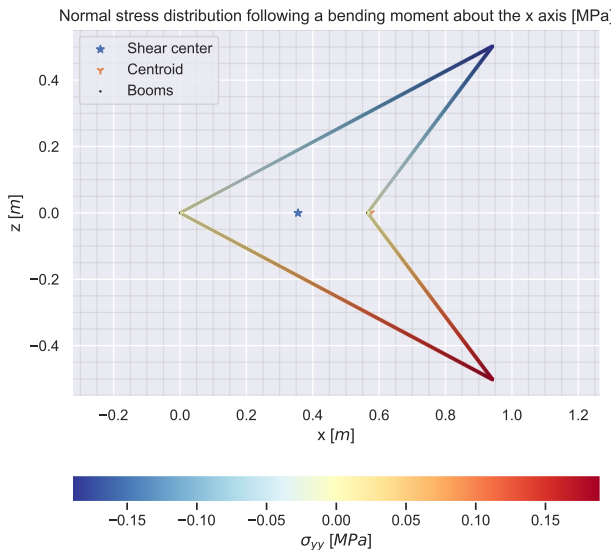


Figure 8.10: Verification of centroid, shear centre and normal stresses computations. The centroid and shear centre locations matched those of an identical cross section in [49]. The normal stress matched hand computations. Note the symmetric stress distribution about the cross section's symmetry axis.

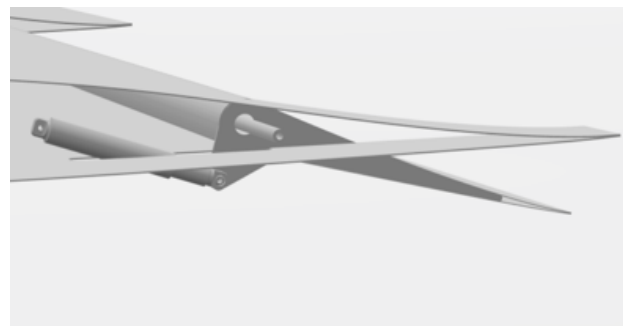


Figure 8.11: Representative 3D model of the elevon actuator mechanism. A linear actuator is employed. For the sake of clarity, stiffening elements and ribs have been omitted. Note that such mechanism design also ensures that actuator forces increase with increased deflection angle, which is a desirable effect.

- **SAVED-LG-STR-04:** The landing structure shall be able to withstand 300% of the MTOM without failure.
- **SAVED-LG-STR-05:** The landing structure shall be wide enough to avoid drone tip over with cross winds lower or equal to 12m/s ¹¹

A further 55° tip-over constraint, measured between the centre of gravity and the lines connecting the landing struts, as defined in [53], was set in order to provide an additional constraint. The landing fin can be visualised in Figure 19.2. It can be noticed that it has a wing-like shape. The root chord is of 150mm. The tip chord is of 30mm and the semi-span is of 336mm. The leading edge sweep is of 38.6°. The landing fin is made of a 3D-printed thermoplastic filament. The budgeted mass is of 450g.

8.5. Final Structural Mass Breakdown

The final structural mass breakdown is finally presented in Table 8.5.

Table 8.5: Final structural mass breakdown.

Item	Number	Mass [g]	Material	Recyclability	Recycled source
Stiffeners	14	798	Thermoplastic	Yes	No
Skin	6	2490	Thermoplastic	Yes	No
Ribs	16	813.8	Aluminium	Yes	Yes
Spars	4	923.6	Aluminium	Yes	Yes
Centre section elements	2	508.9	Aluminium	Yes	Yes
Payload bay	1	650	Thermoplastic	Yes	Semi
Engine mounts	4	527.6	Aluminium	Yes	Yes
Engine fairings	4	144	Thermoplastic	Yes	Semi
Landing fin	1	450	Thermoplastic	Yes	Semi
Subtotal [g]		7305.9		-	
Contingency	10%	730.6	-	Assumed not	Assumed not
Total [g]		8036.5	Total % recyclability	91%	42.3%

¹¹This requirement was generated by setting that SAVED shall be able to operate in 95% of the planet's windiest areas and the data was then retrieved from <https://bit.ly/3dddbHC> [Cited on 19-06-2020].

9

Aerodynamic Design and Analysis

The aerodynamic performance of an aircraft is closely related to its flight performance. Performance parameters like range, endurance, wing mass, and cruise speed all depend on the aerodynamic design, thereby making it an essential step in the design iteration process. In this chapter, SAVED's aerodynamic performance is designed and analysed. For each iteration, the aerodynamics department takes in the current planform parameters, and outputs aerodynamic parameters relevant to other departments. The airfoil selection is explained and performed in [Section 9.1](#). Next, the aerodynamic parameters of the entire aircraft are computed in [Section 9.2](#). Finally, the propeller-wing interaction is analysed in [Section 9.3](#).

9.1. Main Wing Airfoil Selection

In this section, the process of selecting the main wing's airfoil is discussed. A main wing airfoil is selected instead of designed because of sustainability and organisational concerns. A selected airfoil requires less performance validation than a designed airfoil as this has been tested already. To start, in order to obtain an idea of the airfoil's required performance, a functional analysis is performed in [Subsection 9.1.1](#). This functional analysis is translated into a list of airfoil requirements in [Subsection 9.1.2](#). The airfoil trade-off process is explained and performed in [Subsection 9.1.3](#). Finally, the verification and validation methods for the tools used in the trade-off are discussed in [Subsection 9.1.4](#).

9.1.1. Functional Analysis

The derivation of the main wing's functions with respect to its airfoil remained unchanged compared to the midterm phase [9]. The functions are thereby given as follows:

- **SAVED-AIR-FUNC-01**: Trim the pitching moment induced by the lift from the main wing;
- **SAVED-AIR-FUNC-02**: Provide maximum lift over drag ($\frac{L}{D}$) during cruise;
- **SAVED-WING-FUNC-01**: Provide sufficient lift during cruise;
- **SAVED-WING-FUNC-02**: Provide sufficient lift during transition;
- **SAVED-WING-FUNC-03**: Generate sufficient lift under all mission operating conditions.

9.1.2. Requirement Analysis

In this subsection, the requirement analysis is derived from the functional analysis as discussed in [Subsection 9.1.1](#). First, the methods behind computing some general parameters are discussed. Next, the list of requirements is set up.

General Analysis

The first step in the airfoil selection process is to compute the airfoil's design lift coefficient ($C_{l_{des}}$) [-] [54]. The design lift is the lift that is most prominent in an aircraft's mission profile [54]. For SAVED, this corresponds to the cruise phase. $C_{l_{des}}$ is given by (9.1) [54].

$$C_{l_{des}} = \frac{MTOW}{\frac{1}{2}\rho_{\infty}(V_{\infty} \cos \Lambda_{0.25c})^2 S} \quad (9.1)$$

$$Re = \frac{\rho_{\infty} V_{\infty} c_{mgc}}{\mu_{\infty}} \quad (9.2)$$

Where in (9.1): $MTOW$ is the aircraft's maximum take-off weight [N], ρ_{∞} is the free stream air density [kg/m^3], V_{∞} is the free stream air speed [m/s], $\Lambda_{0.25c}$ is the quarter chord sweep angle [$^\circ$], and S is the wing surface area [m^2].

Next, the Reynolds numbers (Re) [-] for analysis are defined. All parameters expect for those related to stall performance are evaluated at Re_{cruise} . The stall performance parameters (e.g. airfoil maximum lift coefficient ($C_{l_{max}}$ [-]) and maximum angle of attack (α_{stall}) [$^\circ$]), are evaluated at Re_{stall} in order to avoid an overestimation of the airfoil's stall performance [54]. Re is given by (9.2). Where c_{mgc} in (9.2) is the mean geometric chord [m], defined as $\frac{S}{b}$, and μ_∞ is the free stream dynamic viscosity [Pa s].

List of Requirements

The following requirements are generated based on the functions mentioned in Subsection 9.1.1. **SAVED-AIR-FUNC-01** can be translated into a requirement by stating that the airfoils pitching moment coefficient at the aerodynamic centre ($C_{m_{a.c.}}$ [-]) shall be positive. **SAVED-WING-FUNC-01** and **SAVED-WING-FUNC-01** can not be translated into a requirement related to $C_{l_{des}}$ as it can not be verified for a selected airfoil that $C_{l_{des}}$ meets a certain value as opposed to shape optimisation. Furthermore, no requirement can be set on **SAVED-AIR-FUNC-02**, as the process of selecting airfoils can not guarantee maximum $\frac{L}{D}$ during cruise as opposed to shape optimisation. Furthermore, no requirement can be set on **SAVED-WING-FUNC-03** as information on designed flow regime of most airfoils is not available, meaning it can not be verified whether a selected airfoil is laminar flowing or not. The requirements are then as follows:

- **SAVED-CONS-FLIGHT-02-AERO-AIR-01:** The airfoil's $C_{m_{a.c.}}$ shall be positive.

9.1.3. Trade-Off

In this subsection the process of trading-off the different airfoils is discussed. To start, a selection of airfoils for further analysis is presented based on qualitative argumentation. Next, the methodology of analysing the airfoils' performance parameters is discussed. Following this, the trade-off methodology is discussed. Finally, the performance analysis methodology and trade-off methodology are applied to the selected airfoils and most desirable airfoil is selected.

Qualitative Selection of Airfoils to be Analysed

To start the trade-off process, a selection of promising airfoils to undergo further analysis is performed qualitatively. The selection is comprised of a collection National Advisory Committee for Aeronautics (NACA) 5 digit airfoils, some airfoils proven to perform well in low speed applications [74] [52], and some airfoils similar to the highest performing airfoil in the collection of [74]. In total this adds up to a selection of 42 airfoils to be analysed.

The reason for considering NACA 5 digit airfoils is as follows: "The benefit in considering NACA airfoils in general is that the required design parameters such as $C_{l_{des}}$ and maximum thickness over chord ratio $(\frac{t}{c})_{max}$ can be translated into the name of the airfoil by adhering to the digit code convention. The reason for considering NACA 5 digit airfoils as opposed to NACA 4 or 6 digit (or even 7 or 8, though these are rarely used and therefore will not be discussed), lies in their characteristics. NACA 5 digit airfoils feature higher values of $C_{l_{max}}$ than NACA 4 digit airfoils but more abrupt stall behaviour [54]. Since stall behaviour is not a driving parameter Subsection 9.1.1, this can be traded for higher values of $C_{l_{max}}$. Furthermore, unlike NACA 4 digit airfoils, which are applicable to many different flight envelopes, NACA 5 digits airfoils can be shaped according to a specific $C_{l_{des}}$, which is beneficial for SAVED as the biggest part of the mission profile is cruising. NACA 6 digit airfoils are more applicable to high speed aircraft due to their smooth pressure gradient at the nose and reach lower values of $C_{l_{max}}$ than NACA 5 digit airfoils [54]. Furthermore, due to relying on reaching extended zones of laminar flow, NACA 6 digit airfoils are very susceptible to the roughness of the airfoil [54]. That is, any speck of filth or other particles (e.g. insects) can gravely determent the drag performance of the airfoil." [9].

Performance Analysis Methodology

The following airfoil parameters relevant to the trade-off are analysed for each airfoil:

- | | |
|---|--|
| <ul style="list-style-type: none"> • $(\frac{C_l}{C_d}) _{C_{l_{des}}}$ [-] • $(\frac{t}{c})_{max}$ [-] | <ul style="list-style-type: none"> • $C_{m_{a.c.}}$ [-] • $C_{l_{max}}$ [-] • α_{stall} [$^\circ$] |
|---|--|

Where $(\frac{C_l}{C_d})|_{C_{l_{des}}}$ is the lift over drag at the design lift coefficient [-]. These parameters serve as the criterion in the trade-off method. In order to obtain these parameters for each of the airfoils mentioned in the previous

Table 9.1: WSM weights for measurements of performance for Concept A and D.

	$\left(\frac{C_l}{C_d}\right) _{C_{l_{des}}}$	$C_{m_{a.c.}}$	$C_{l_{max}}$	α_{stall}	$(t/c)_{max}$
Weight	0.5	0.05	0.05	0.2	0.2

subsubsection, the following performance analysis methodology was applied: "The coordinates of the airfoil were loaded into JavaFoil [34]. All airfoils analysed showed a large drag bucket around the cruise angle of attack (α_{cruise}) [$^\circ$] and therefore the drag performance outside this drag bucket was not quantitatively assessed any further. The performance data per airfoil was then gathered by analysing the lift coefficient (C_l) [-], drag coefficient (C_d) [-], $\frac{L}{D}$, and pitching moment coefficient at quarter chord ($C_{m_{0.25c}}$) [-] vs. α per airfoil for different ranges of α depending on the airfoil in steps of 0.5 deg at Re_{cruise} and Re_{stall} . $\left(\frac{C_l}{C_d}\right)|_{C_{l_{des}}}$ was computed by creating continuous function of α vs. C_l to find $\alpha|_{C_{l_{des}}}$. This $\alpha|_{C_{l_{des}}}$ corresponds to α_{cruise} and was then plugged into a continuous function of $\frac{L}{D}$ vs. α to find $\frac{C_l}{C_d}|_{C_{l_{des}}}$. $C_{m_{a.c.}}$ was found by considering $C_{m_{0.25c}}$ at $C_l = 0$. $\alpha|_{C_l=0}$ was found using the continuous function of α vs. C_l . This $\alpha|_{C_l=0}$ was then plugged into a continuous function of $C_{m_{0.25c}}$ vs. α to arrive at $C_{m_{a.c.}}$. $C_{l_{max}}$ was found by considering the maximum of the continuous C_l vs. α function. This $C_{l_{max}}$ was then plugged into the continuous α vs. C_l function to find α_{stall} ." [9]. It should be noted that $\left(\frac{C_l}{C_d}\right)|_{C_{l_{des}}}$ and $C_{m_{a.c.}}$ are evaluated at Re_{cruise} , and $C_{l_{max}}$ and α_{stall} at Re_{stall} .

Trade-Off Methodology

The weighted sum method (WSM) was applied to trade-off the airfoil based on their normalised performance measurements in a similar fashion as explained in [Table 7.3.3](#). Each performance parameter was normalized between 0 and 1 according to a linear scoring function for this analysis.

Trade-Off Results

The class of NACA 5 digit airfoils to be selected for further analysis in JavaFoil [34] corresponds to NACA3P1XX. The performance parameters of the class of NACA 5 digit airfoils, together with the airfoils mentioned in qualitative selection of airfoils to be analysed, are obtained using the previously described performance analysis methodology. The weights for the WSM corresponding to the aforementioned criteria are shown in [Table 9.1](#). Concerning [Table 9.1](#), $\left(\frac{C_l}{C_d}\right)|_{C_{l_{des}}}$ has been assigned the highest weight as $\frac{L}{D}$ in general is one of SAVED's most critical performance parameters. In order for the aircraft to meet the required range, the main wing's airfoil needs to have a high $\left(\frac{C_l}{C_d}\right)|_{C_{l_{des}}}$. Next $C_{m_{a.c.}}$ has been assigned a relatively low weight as the values for all the analysed airfoils were positive, meaning they complied with **SAVED-AIR-AERO-01**, and the values did not differ by much, meaning that the difference between the highest $C_{m_{a.c.}}$ and the lowest $C_{m_{a.c.}}$ did not have a significant effect on airfoil performance. The same holds for $C_{l_{max}}$, which for the same reasons as mentioned for $C_{m_{a.c.}}$ has been assigned a relatively low weight. α_{stall} has been assigned a relatively high weight, as the values of α_{stall} between the airfoils differed by a lot and this difference had a large effect on SAVED's stall performance, which is deemed an essential performance parameter according to [Subsection 9.1.1](#). Finally, as an increase in $\left(\frac{t}{c}\right)_{max}$ decreases the structural weight of the wing [54], a relatively high weight has been assigned to this parameter.

When plugging in the performance parameters and weights according to [Table 9.1](#) into [\(7.18\)](#), the most desirable outcome is the CAL4014L. The most critical criterion is $\left(\frac{C_l}{C_d}\right)|_{C_{l_{des}}}$. The weight corresponding to this criterion should be decreased by 59.19% in order to change the most desirable outcome to the NACA34116. This percentage is considered robust enough in order to accept the outcome as presented. Finally, with a $C_{m_{a.c.}}$ of 0.018, the CAL4014L complies with **SAVED-CONS-FLIGHT-02-AERO-AIR-01**.

9.1.4. Verification and Validation

In this subsection, the verification and validation procedures of the design tools are discussed. First the validity of JavaFoil [34] for SAVED's design applications is discussed. Next, the verification of the trade-off methodology is discussed.

Validation of JavaFoil

The analysis in JavaFoil is applicable for subsonic speeds and low Reynolds numbers [35], making it applicable to SAVED's design. JavaFoil is based on potential flow analysis, meaning it does not inherently model laminar separation bubbles and turbulent flow separation¹. However, in order to still be able to model airfoil stall effects, empirical correction factors have been implemented based on procedures described by Eppeler [26] [27]. Based on this potential flow analysis including the empirical stall models, JavaFoil shows resemblance to test data for NACA5 digit airfoils² which is deemed accurate enough for the purpose of this analysis. It should be noted that numerical methods like JavaFoil and XFOil tend to overestimate the stall performance of the airfoil. However, this overestimation is within an acceptable range [34] meaning it will not be taken into account in further performance analysis of SAVED.

Verification of Trade-Off Methodology

The implementation of the WSM was verified against the results shown in [70]. The example case shown in [70] was loaded into the implemented WSM. The score matrix according to (7.18) was asserted to be close to the results shown in [70] with a relative tolerance of 0.001. The sensitivity analysis of this example case was also loaded into the implemented WSM. The resulting sensitivity was asserted to be close to the result shown in [70] with a relative tolerance of 0.001.

9.2. Aerodynamic Characteristics

This section discusses and analyses SAVED's aerodynamic performance parameters. In the previous section the airfoil was selected; however, only 2D aspects of the wing were taken into account. This section will elaborate on the 3D effects of the airfoil parameters. These performance parameters are of paramount importance to the other departments (e.g. Power & Propulsion and Flight Performance), since these can be used to perform design iterations in order to converge to a solid design. First, in Subsection 9.2.1, an aerodynamic analysis is performed whereby the methodology of obtaining the aerodynamic parameters is brought into detail. Then, the results obtained from the aerodynamic analysis are presented and elaborated on in Subsection 9.2.2. Finally, the tools used to obtain the aerodynamic parameters are verified and validated in Subsection 9.2.3.

9.2.1. Aerodynamic Analysis Description

In this section the methodology to obtain the aerodynamic characteristics of SAVED is presented. This methodology is based on the Data Compendium (US Air Force) (DATCOM) method [73] as well as XFLR5 [21]. This subsection starts off with the computation of the complete aircraft's lift-curve slope ($C_{L\alpha}$) [$1/\text{°}$] followed by the complete aircraft's zero-lift angle of attack ($\alpha_{L=0}$) [°]. Then, the complete aircraft's maximum lift coefficient (C_{Lmax}) [-] is determined together with the stall angle of attack (α_{stall}). Furthermore, the complete drone's lift coefficients (C_L) [-] below stall can be computed, which are dependent on the four parameters mentioned before. Finally, the drag coefficient (C_D) [-] below stall are elaborated on, which includes the zero-lift drag coefficient (C_{D_0}) [-] and the lift-induced drag (C_{D_L}) [-]. Note that all equations and figures have been collected from DATCOM [73], unless stated otherwise.

Lift-Curve Parameters

The lift curve slope is the derivative of the C_L with respect to the α for the linear regime of the lift curve. In order to model the lift-curve, this parameter is therefore of absolute necessity. It can be computed according to DATCOM and can be observed in (9.3).

$$C_{L\alpha} = \frac{2\pi AR}{2 + \sqrt{\frac{AR^2\beta^2}{\eta_{airfoil}} \left(1 + \frac{\tan^2 \Lambda_{0.5c}}{\beta^2}\right) + 4}} \quad (9.3)$$

$$\alpha_{L=0} = \alpha_{des} - \frac{C_{l_{des}}}{C_{l\alpha}} \quad (9.4)$$

In (9.3), AR is the main wing aspect ratio [-], β is the Prandtl-Glauert compressibility factor, defined as $\sqrt{1 - M^2}$ [-], $\Lambda_{0.5c}$ is the main wing half-chord sweep angle [°], and $\eta_{airfoil}$ is the airfoil efficiency [-], defined as $\frac{C_{l\alpha}}{2\pi}$. $\alpha_{L=0}$ is also a fundamental parameter to generate the lift-curve. In order to compute this (9.4) (DATCOM [4.1.3.1-a]) can be employed. In (9.4), α_{des} [°] is the angle of attack at $C_{l_{des}}$ and $C_{l\alpha}$ is the airfoil's lift curve slope [$1/\text{°}$].

If twist is present in the main wing, (9.5) (DATCOM [4.1.3.1-c]) is more appropriate to utilise:

¹<https://bit.ly/2B21nKK> [Cited on 8-6-2020]

²<https://bit.ly/3cSOgc1> [Cited on 8-6-2020]

$$\alpha_{L=0_{tw}} = \alpha_{L=0} + \frac{\Delta\alpha_0}{\phi} \quad (9.5)$$

$$C_{L_{max}} = \frac{C_{L_{max}}}{C_{l_{max}}} C_{l_{max}} \quad (9.6)$$

In (9.5), $\alpha_{L=0_{tw}}$ is the zero-lift angle of attack including twist [$^\circ$], ϕ is the wing twist angle [$^\circ$], $\Delta\alpha_{L=0}$ is a change in zero-lift angle of attack, and the ratio $\frac{\Delta\alpha_{L=0}}{\phi}$ is the change in $\alpha_{L=0}$ with ϕ [-].

The maximum lift coefficient can be computed utilising (9.6) (DATCOM [4.1.3.4-d]). The ratio $\frac{C_{L_{max}}}{C_{l_{max}}}$ [-] is a function of the leading edge (LE) sweep and was retrieved from DATCOM.

The angle of attack at the maximum lift coefficient is also known as the stall angle of attack. The stall angle of attack has been computed using (9.7) (DATCOM [4.1.3.4-e]). $\Delta\alpha_{C_{L_{max}}}$ is once again a function of the LE sweep and was, again, retrieved from DATCOM. It refers to the angle of attack increment before $C_{L_{max}}$, so the difference between α_{stall} and the angle of attack at which the linear part ends.

$$\alpha_{stall} = \frac{C_{L_{max}}}{C_{L_\alpha}} + \alpha_0 + \Delta\alpha_{C_{L_{max}}} \quad (9.7)$$

The lift coefficients below the stall angle of attack are computed utilising (9.8) (DATCOM [4.1.3.3-a]).

$$C_L = C_N \cos \alpha = \left(C_{N_\alpha} \frac{\sin 2\alpha}{2} + C_{N_{\alpha\alpha}} \sin \alpha |\sin \alpha| \right) \cos \alpha \quad (9.8)$$

C_N is the normal force coefficient [-] and C_{N_α} is the normal-force curve slope [$1/^\circ$], which can be approximated as C_{L_α} . $C_{N_{\alpha\alpha}}$ is a non-linear coefficient, which follows from (9.9) (DATCOM [4.1.3.3-b]).

$$C_{N_{\alpha\alpha}} = (C_{N_{\alpha\alpha}})_{ref} + \Delta C_{N_{\alpha\alpha}} \quad (9.9)$$

$\Delta C_{N_{\alpha\alpha}}$ was retrieved from DATCOM and it is a function of the wing shape parameter, j , defined in (9.11) (DATCOM [4.1.3.3-e]), where C_1 and C_2 are constants depending on the taper ratio [-], λ . $(C_{N_{\alpha\alpha}})_{ref}$ is the reference non-linear coefficient [-], which is based on the normal force coefficient at $C_{L_{max}}$. The latter can straightforwardly be computed employing (9.8). Finally, $(C_{N_{\alpha\alpha}})_{ref}$ is computed by invoking (9.10) (DATCOM [4.1.3.3-d]).

$$(C_{N_{\alpha\alpha}})_{ref} = \frac{C_N|_{C_{L_{max}}} - \frac{1}{2} C_{L_\alpha} \sin(2\alpha_{C_{L_{max}}})}{\sin \alpha_{C_{L_{max}}} |\sin \alpha_{C_{L_{max}}}|} \quad (9.10)$$

$$j = 0.3 (C_1 + 1) \frac{AR}{\beta} \cos \Lambda_{LE} \left((C_1 + 1) (C_2 + 1) - \left[\frac{(C_1 + 1) AR \tan \Lambda_{LE}}{7} \right]^3 \right) \quad (9.11)$$

Now that all the equations are known, the lift coefficient below the stall regime for any angle of attack can be computed.

Drag Coefficient

The two main contributors to SAVED's aerodynamic drag are skin friction and pressure drag, which are both accounted for in the DATCOM method. They are computed based on empirical data. The drag coefficient is related to the lift-induced drag and the zero-lift drag coefficient as shown in (9.12).

$$C_D = C_{D_0} + C_{D_i} \quad (9.12)$$

To elaborate on (9.12), first C_{D_i} is discussed. C_{D_i} is described by (9.13) (DATCOM [4.1.5.2-h]).

$$C_{D_i} = \frac{C_L^2}{\pi AR e} + C_L \phi C_{l_\alpha} v + (\phi C_{l_\alpha})^2 w \quad (9.13)$$

In (9.13), if there is no twist, the left term on the right hand side becomes the only contributor to C_{D_i} , which is the standard equation for the lift-induced drag. v is the induced-drag factor due to linear twist [-] and w is the zero-lift drag factor due to linear twist [-]. Both of these terms are acquired from figures illustrated in DATCOM. Furthermore, e is the Oswald's efficiency factor [-], which can be computed employing (9.14) (DATCOM [4.1.5.2-i]). \mathcal{R} is known as the airfoil's leading-edge-suction parameter [-]. It is the ratio of the actual leading-edge suction over the theoretical leading-edge suction.

$$e = \frac{1.1 C_{L_\alpha}}{AR \left(\mathcal{R} \frac{C_{L_\alpha}}{A} + (1 - \mathcal{R}) \pi \right)} \quad (9.14)$$

Table 9.2: Aerodynamic characteristics of SAVED.

$(\frac{L}{D})_{max}$ [-]	C_{D_0} [-]	e [-]	$C_{Lcruise}$ [-]	α_{cruise} [°]	C_{Lmax} [-]	α_{stall} [°]	$C_{L\alpha}$ [°⁻¹]	V_{cruise} m/s
22.5	0.0099	0.932	0.444	5.3	1.137	16.3	4.65	22.5

Moving on to the left term in (9.12), C_{D_0} has multiple contributors, depending on the aircraft's configuration. The C_{D_0} breakdown is found in (9.15): the drone consists of four main components, namely wing, body, landing fin and propellers, which have been excluded in the computation of C_{D_0} , as their influence is negligible compared to all the other terms.

$$C_{D_0} = C_{D_0wing} + C_{D_0body} + C_{D_0fin} \quad (9.15)$$

Each of the separate contributions to C_{D_0} are evaluated using the DATCOM method except for C_{D_0wing} . The reason for this is that the DATCOM method tends to overestimate C_{D_0wing} . Consequently, a Vortex Lattice Method (VLM) analysis of the main wing in XFLR5 is performed, whereby viscous effects are taken into account without any ground effects. Then, for the body, (9.16) (DATCOM [4.2.3.1-a]) is used.

$$C_{D_0body} = C_f \left(1 + 60 \left(\frac{d}{l_b} \right)^3 + 0.0025 \frac{l_b}{d} \right) \frac{S_{b_{wet}}}{S_{ref}} \quad (9.16)$$

In (9.16), C_f is the turbulent flat-plate skin-friction coefficient [-], d is the maximum body height [m], l_b is the body length [m], $S_{b_{wet}}$ is the wetted body area [m^2] and S_{ref} [m^2] is the reference surface area of the wing. In order to compute C_{D_0fin} , (9.17) (DATCOM [4.1.5.1-a]) is employed.

$$C_{D_0fin} = C_f \left(1 + \mathcal{L} \left(\frac{t}{c} \right)_{avg} + 100 \left(\frac{t}{c} \right)_{avg}^4 \right) R_{L.S.} \frac{S_{fin_{wet}}}{S_{ref}} \quad (9.17)$$

In (9.17), \mathcal{L} is the airfoil thickness parameter [-]. It possesses a value of 2 if $\left(\frac{t}{c} \right)_{max}$ is located before 30 % of the chord and 1.2 otherwise. $\left(\frac{t}{c} \right)_{avg}$ is the spanwise average maximum thickness-over-chord ratio. $R_{L.S.}$ is the lifting-surface correction factor [-], whereas $S_{fin_{wet}}$ is the wetted fin surface area [m^2].

9.2.2. Aerodynamic Analysis Results

In this section the results obtained from employing the methodology explained in the previous subsection is discussed. Important parameters that needed to be provided to the other departments were C_{D_0} , $(\frac{L}{D})_{max}$, $C_{Lcruise}$, α_{cruise} , e , C_{Lmax} , α_{stall} , $C_{L\alpha}$ and V_{cruise} . These parameters and their final values, after performing several iterations with other departments, are listed in Table 9.2.

C_{D_0} , C_{Lmax} , α_{stall} and $C_{L\alpha}$ were obtained utilising the methodology in Subsection 9.2.1. The maximum lift-over-drag was determined from Figure 9.1. Based on this lift-over-drag ratio, α_{cruise} was determined together with $C_{Lcruise}$ from the lift curve. The cruise speed was updated utilising (9.18). Note that a hysteresis can not be generated utilising DATCOM, however after-stall performance ($\alpha > \alpha_{stall}$) can be computed, but was not deemed relevant as this will not effect the design in this phase.

$$V_{cruise} = \sqrt{\frac{W}{S} \frac{2}{\rho} \frac{1}{C_{Lcruise}}} \quad (9.18)$$

9.2.3. Verification and Validation

The implementation of the equations mentioned in Subsection 9.2.1 needs to be verified and the tool's application needs to be validated in order to ensure a reliable analysis. After the verification is discussed, the validation will be elaborated on.

The software tool must be verified such that it can be asserted that the model is rightly build and operates correctly. Unit tests have been performed on each part of the code. This has been done by implementing sample exercises in the DATCOM book [73]. Also, some equations were computed manually for extra precautions. The results turned out to be similar to the code results, thus the code deems to be verified. For C_{D_0wing} , which has

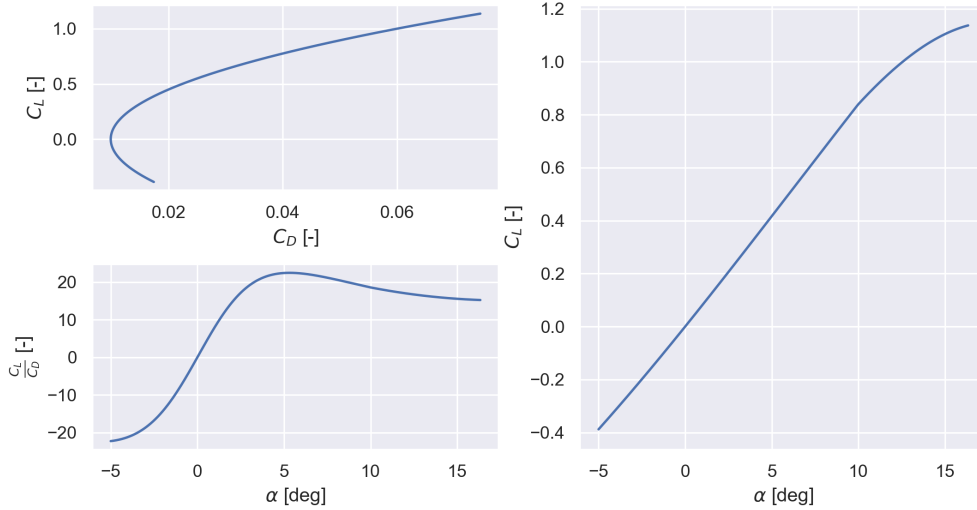


Figure 9.1: (Top-left) Lift-drag polar of SAVED. (Bottom-left) Lift-over-drag ratio plotted against the angle of attack. (Right) Lift-curve of SAVED. $Re = 637,000$

been obtained from XFLR5, verification was not necessary, since XFLR5 is already a verified tool. Validation of XFLR5 will be required. Nevertheless, in Subsection 9.3.4, a lifting model tool is developed and the results show strong similarities to the XFLR5 results. This outcome can thus be used not only to verify the lifting line tool, but also as a sanity check of the correct implementation of the XFLR5 model.

Observing if the right model was built, validation is also an aspect of importance. However, it should be noted that DATCOM has already been validated by the US Air Force and NASA using empirical data. Additionally, the applicability of DATCOM to this specific design is further confirmed by [14], in which the aerodynamic characteristics of a similar flying wing UAV were estimated using DATCOM and XFLR5, and successively validated in a wind tunnel. Consequently, no validation of the tool is required, as a verified tool is automatically validated in this case.

9.3. Propeller-Wing Interaction Analysis

For the airspeeds in SAVED's mission profile, as well as the ratios between the size of SAVED's propellers and its main wing, the effects of propeller slipstream on the main wing's performance can not be neglected. The induced velocities of the propeller slipstream on the main wing influence the main wing's lift distribution and the velocity profile over, and at the trailing edge. These effects both increase and detriment the performance of the main wing [51]. Examples of such effects are the increase of lift for a lower airspeed due to the increased velocity over the wing, and the delay of wing tip stall due to reduction of effective angle of attack by the propellers (thereby retaining effectiveness of outboard control surfaces). In order to take into account these effects, the propeller slipstream velocities are induced on Prandtl's classical lifting line (LL) model in order to create an adapted LL model. This adapted LL model takes into account the induced velocity by the propellers, and thereby models the main wing's lift distribution including propellers, which is relevant for the structural sizing of the wing as well as the induced velocity profile over the wing, which is relevant for the controllability analysis of the aircraft. The propeller induced flow velocities are modelled in Subsection 9.3.1. Next, the propeller induced LL is modelled in Subsection 9.3.2. The results according to this model when applied to SAVED are shown in Subsection 9.3.3. Finally, the methods used in this section are verified and validated in Subsection 9.3.4.

9.3.1. Modelling Propeller Induced Flow Velocities

The propeller induced velocities in the axial and radial direction are required to be implemented in Prandtl's classical LL theory [3] in order to arrive at the adapted LL model. In order to obtain these velocities, the propellers are modelled according to actuator disk theory [71]. The assumptions related to this model are first discussed. Next, the analysis is performed.

Assumptions

As the propellers are modelled according to actuator disk theory, the following assumptions hold:

- The propeller is infinitely thin [51].
- The propeller has an infinite amount of blades [51].
- The flow through the propeller is steady, inviscid, incompressible, and adiabatic [71].
- The pressure and loading is uniform over the disk [71].
- The propeller slipstream is modelled as

a streamtube [71]. Outside this streamtube, conditions are equivalent to free stream. Inside this streamtube, propeller induced conditions hold.

- The flow velocity at a certain section along the span is uniform along the chord. That is, there is no slipstream contraction [71].
- Aerodynamic characteristics of the propeller blades are neglected [51].

Model Description

The axial velocity induced by the propeller (V_a) [m/s] is given by (9.19) [71]:

$$V_a = \frac{1}{2} \left(-V_\infty + \sqrt{V_\infty^2 + \frac{2T}{\rho_\infty A_{prop}}} \right) \quad (9.19)$$

In (9.19), T is the thrust generated by the propeller [N] and A_{prop} is the frontal propeller disk area [m^2]. As mentioned in the assumptions, this axial velocity is constant along the streamtube. The swirl velocity induced by the propeller, V_r [m/s] is defined by (9.20) [20].

$$V_r = \frac{2V_\infty V_a}{\omega r} \quad (9.20)$$

In (9.20), ω is the propeller's rotational velocity [rad/s] and r is the radial distance from the centre of the propeller to the point of interest [m]. As V_r is dependant on r in (9.20), the swirl velocity is not constant along the span of the streamtube. Furthermore, V_r changes direction when moving from the "upgoing" side of the propeller to the "downgoing" side of the propeller. This means V_r is positive for the upgoing side of the propeller, and negative for the downgoing part of the propeller, as z is defined positive upwards for this analysis.

To summarise, this model results in a streamtube with constant velocity along the chord (x) direction of the wing, but varying velocity along the span (y) and height (z) direction of the wing. These velocities can be induced on the LL and are also used in the simulation in order to predict the speed of the flow across the elevons.

9.3.2. Modelling The Propeller Induced Lifting Line

In this section, the propeller induced LL/adapted LL is discussed and modelled. First, the assumptions on which the model is based on are discussed. Next the actual model is described.

Assumptions

For the adapted LL model, the following assumptions hold:

- The propeller is infinitely far away from the wing. That is, effects of the wing on the propeller are not taken into account.
- The LL is modelled as a straight line on the $x - y$ -plane. Therefore, wing sweep, thickness, and dihedral are not taken into account.
- The airfoil's $C_{l\alpha}$ and $\alpha_{l=0}$ are constant along the span of the wing. This assumption was verified by plotting the main wing's airfoil's $C_{l\alpha}$ vs. Re according to (9.2) for a range of Re with c_{tip} to c_{root} .
- Lift effects due to SAVED's body and fin are not taken into account, only the wing and propellers are modelled.
- The propellers do not induce interference effects on each other.

Model Description

The main wing's lift distribution including the propeller induced velocities can be modelled according to an adapted version of Prandtl's classical LL model for general lift distributions [51]. This subsection describes the workings of the adapted LL model.

The main wing is modelled by a bound vortex filament with circulation Γ [m^2/s]. As a bound vortex can not end in the flow according to Helmholtz's theorem [3], the vortex filament continues as two free vortices trailing

downstream into infinity at $\frac{-b}{2}$ and $\frac{b}{2}$, resulting in a horseshoe-shaped vortex (horseshoe vortex). The main wing is then divided into N spanwise stations, and is thereby modelled by N horseshoe vortices with circulation Γ . According to the Kutta-Joukowski theorem, the lift is a function of the circulation distribution is given by (9.21) [3].

$$l(y) = \rho_\infty V_\infty \Gamma(y) \quad (9.21)$$

$$C_l = C_{l\alpha} (\alpha_{eff}(y) - \alpha_{l=0}) \quad (9.22)$$

In (9.21), l is the local lift [N/m]. The aim of the adapted LL model is therefore to obtain the circulation distribution with slipstream velocities induced by the propeller, and thereby the propeller induced lift distribution.

To start, the C_l for each of the N spanwise station is given by (9.22) [3]. In (9.22), α_{eff} is the effective angle of attack [$^\circ$], where α_{eff} [$^\circ$] is defined by (9.23) [51].

$$\alpha_{eff}(y) = \alpha_g + \alpha_t(y) - \alpha_{l=0} + \alpha_i(y) \quad (9.23)$$

In Equation 9.23, α_g is the geometric angle of attack [$^\circ$], α_t is the angle of attack induced by the geometric twist of the wing [$^\circ$], and α_i is the induced angle of attack [$^\circ$]. Where the induced angle of attack, for small angles in case of the adapted LL model is given by (9.24) [25].

$$\alpha_i(y) = \arctan \left(\frac{w_w + V_r}{V_\infty + V_a} \right) \approx \frac{w_w(y) + V_r(y)}{V_\infty + V_a(y)} \quad (9.24)$$

In (9.24), w_w is the downwash velocity induced by the wing [m/s]. $V_a(y)$ and V_r are computed according to the model in Subsection 9.3.1. Note that for the actuator disk model described in Subsection 9.3.1, V_a and V_r in (9.24) are 0 for spanwise sections outside the propeller slipstream tubes. This means that each spanwise station will experience its own induced velocity, depending on the position along the span, resulting in an induced velocity profile of N stations. Equating the Kutta-Joukowski to the dimensionalised airfoil lift, re-writing the expression for α_{eff} accordingly, and introducing the main wing downwash as a function of the circulation distribution results in an adapted version fundamental equation of Prandtl's LL theory. This is given by (9.25) [51].

$$\frac{2\Gamma(y)}{V(y)c(y)C_{l\alpha}} + \alpha_{l=0} = \alpha_g - \alpha_t(y) - \frac{1}{V(y)} \left(\frac{1}{4\pi} \int_{-\frac{b}{2}}^{\frac{b}{2}} \frac{\frac{d\Gamma}{dy}}{y_0 - y} dy + V_r(y) \right) \quad (9.25)$$

Equation 9.25 has to be solved numerically for non-elliptical lift distributions [51]. This can be done by representing the circulation distribution as Fourier sine series. For K Fourier coefficients, this is shown in (9.26) [3].

$$\Gamma(\theta) = \sum_{k=1}^K A_k \sin(k\theta) \quad (9.26)$$

$$y = -\frac{b}{2} \cos(\theta) \quad (9.27)$$

Where θ in this section indicates the spanwise location in terms of radial coordinates (as opposed to twist in Section 9.2). $0 \leq \theta \leq \pi$ in (9.26). The transformation between y and θ is given by (9.27).

The derivative of the circulation distribution in terms of the Fourier sine series is then given by (9.28) [3].

$$\frac{d\Gamma}{dy} = \frac{d\Gamma}{d\theta} \frac{d\theta}{dy} = 2bV_\infty \sum_{k=1}^K kA_k \cos(k\theta) \frac{d\theta}{dy} \quad (9.28)$$

Plugging in (9.26) and (9.28) into (9.25) results in (9.29) [7] [51].

$$\frac{V_\infty}{V(y)} \frac{4b}{c(y)C_{l\alpha}} \sum_{k=1}^K A_k \sin(k\theta) + \alpha_{l=0} = \alpha_g + \alpha_t(y) - \frac{1}{V(y)} \left(\frac{1}{4\pi} \int_\pi^0 \frac{2bV_\infty \sum_{k=1}^K A_k \cos(k\theta)}{-\frac{b}{2} \cos(\theta_0) + \frac{b}{2} \cos(\theta)} d\theta + V_r(y) \right) \quad (9.29)$$

Rearranging (9.29) results in (9.30) [51] [7]:

$$\frac{V_\infty}{V(y)} \frac{4b}{c(y)C_{l\alpha}} \sum_{k=1}^K A_k \sin(k\theta) = \alpha(y) - \frac{V_r(y)}{V(y)} - \frac{V_\infty}{V(y)} \frac{1}{\pi} \int_\pi^0 \frac{\sum_{k=1}^K kA_k \cos(k\theta)}{\cos(\theta) - \cos(\theta_0)} d\theta \quad (9.30)$$

Where $\alpha = \alpha_g - \alpha_t(y) - \alpha_{l=0}$ in (9.30). Finally, (9.30) can be rewritten to (9.31) [7].

$$\sum_{k=1}^K A_k \sin(k\theta) \sin(\theta) + k \frac{c(y)C_{l\alpha}}{4b} = \frac{c(y)C_{l\alpha}}{V(\theta)} \left(\alpha + \frac{V_r(\theta)}{V(\theta)} \right) \quad (9.31)$$

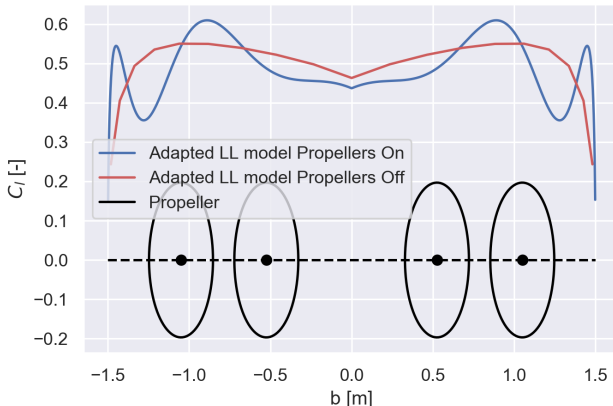


Figure 9.2: C_l vs. y for SAVED with propellers turned on in cruise phase. $Re = 651085$.

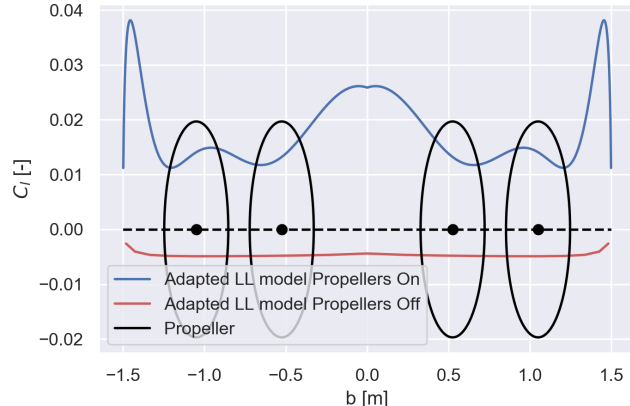


Figure 9.3: C_l vs. y for SAVED with propellers turned on in VTOL phase. $Re = 0$.

The A 's in (9.31) can be solved for by setting up (9.31) for every θ_n along the wingspan for where $1 \leq n \leq N$ and $K \leq N$. This results in a system of equations of N equations and K unknowns, which can be written in matrix form by (9.32) [51] [7].

$$\mathbf{M}\mathbf{A} = \mathbf{b} \quad (9.32)$$

Where the entries in \mathbf{M} are given by (9.33).

$$M(n, k) = \sin(k\theta_n) \left(\sin(\theta_n) + k \frac{c(\theta_n)C_{l_\alpha}}{4b} \right) \quad (9.33)$$

And the entries in \mathbf{b} are defined by (9.34).

$$b(n) = \frac{c(\theta_n)C_{l_\alpha}}{4b} \frac{V_\infty}{V(\theta_n)} \left(\alpha + \frac{V_r(\theta)}{V(\theta)} \right) \sin(\theta_n) \quad (9.34)$$

In case $K < N$, the system is overdetermined. (9.32) can then be solved by a least squares solution method. Solving the system of (9.32) for \mathbf{A} results in K Fourier coefficients which can be plugged in to (9.26) to solve for the circulation distribution. The α_i distribution is can also be expressed in terms of the solved Fourier coefficients by (9.35).

$$\alpha_i = \sum_{k=1}^K k A_k \frac{\sin(k\theta)}{\sin(\theta)} \quad (9.35) \quad C_l = \frac{2\Gamma(y)}{V_\infty c(y)} \quad (9.36)$$

The main wing's lift distribution can then be generated by applying (9.21) to the circulation for each spanwise station along the wing. Intuitively, $V(y)$, that is, the propeller induced velocity at a certain spanwise station would be used instead of V_∞ for this. However, studies have shown that this results in an inaccurate lift distribution, and that using V_∞ in (9.21) results into a more accurate representation of the propeller induced LL³ [51]. In other words, the circulation distribution is computed with the propeller induced velocities, but the Kutta-Jowkowski theorem is applied with the free stream velocity. The C_l distribution (resulting from equation the Kutta-Joukowski theorem to the dimensional airfoil lift) can be computed by (9.36). Where the division by V_∞ instead of $V(y)$ is done for the same reasons as mentioned before.

9.3.3. Propeller Induced Lifting Line Model Results

The results of the model described in Subsection 9.3.2 applied to SAVED's final configuration and performance parameters are shown in this subsection. The adapted LL is analysed in cruise and VTOL, where VTOL is modelled as $V_\infty = 0$ m/s at and $\alpha_g = 0^\circ$ (hovering case). The adapted LL (C_l vs. y for cruise and VTOL for the propeller rotational directions mentioned in Section 11.2 are shown in Figure 9.2 and Figure 9.3 for $N = 1000$ and $K = 10$.

The propeller rotational directions, as mentioned in Section 11.2, reduce the likelihood of wingtip stall occurring, which is apparent from Figure 9.4 and Figure 9.5, which show that α_i decreases near the wing tips for both the cruise and VTOL phase. With respect to the model's reference frame, this means that a decrease in effective

³Dr.Ir. Sinnige, personal communication. [Cited on 3-6-2020]

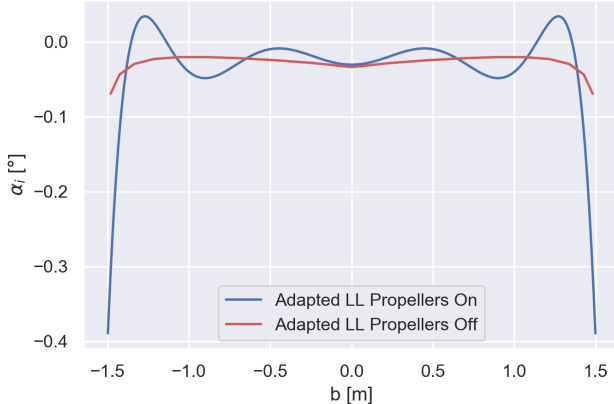


Figure 9.4: α_i vs. y for SAVED with propellers turned on in cruise phase. $Re = 651085$.

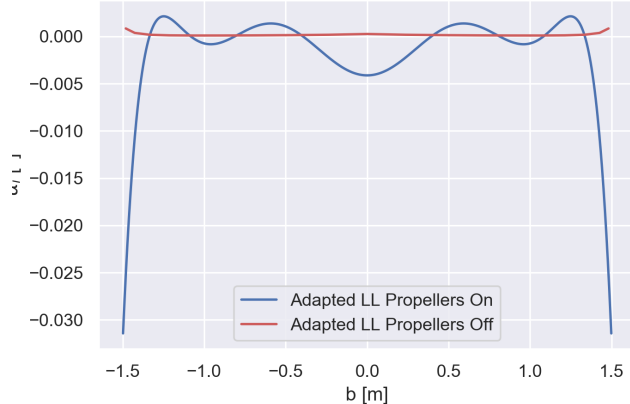


Figure 9.5: α_i vs. y for SAVED with propellers turned on in VTOL phase. $Re = 0$.

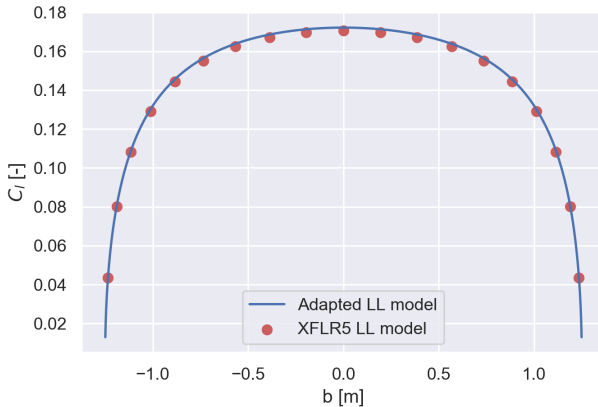


Figure 9.6: C_l vs y according to XFLR5 and the adapted LL model for the LL verification planform. $Re = 955165$.

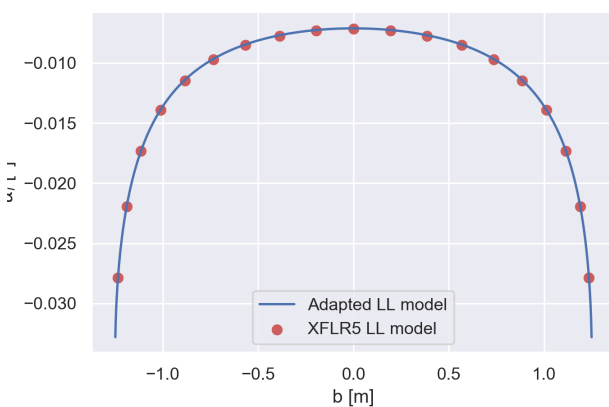


Figure 9.7: α_i vs y according to XFLR5 and the adapted LL model for the LL verification planform. $Re = 955165$.

angle of attack is experienced near the wing tips, thereby delaying wing tip stall. This reduces the risk of loss of lift over the most effective part of the elevons (the most outboard parts), thereby reducing risk as described in [Chapter 18](#).

9.3.4. Verification and Validation

In this subsection, the models described in [Subsection 9.3.1](#) and [Subsection 9.3.2](#) are verified and validated. First, the adapted LL with switched off propellers is verified against results from XFLR5 [21] in order to assert that the model has been implemented correctly. Next, the adapted LL model with switched on propellers is validated against experimental wind tunnel data in order to assert that the model resembles real life.

Verification of The Adapted LL Model Against XFLR5

For the case of propeller switched off, the adapted LL model is verified against the results of XFLR5 [21]. The reason for verifying against XFLR5 with propellers turned off is because software like XFLR5 and AVL do not include propeller-wing interaction effects. Verification is performed on both a custom design LL verification planform, as this is a verification case similar to that mentioned in [51], and SAVED's third iteration planform.

A LL simulation was run in both XFLR5 and the adapted LL model for $V_{cruise} = 28\text{m/s}$ at $\alpha = 2^\circ$ at altitude (h) = 500m for a wing with dihedral angle (Ψ) = 0°, and twist angle (ϕ) = 0°, $b = 2.5^\circ$, taper ratio (λ) = 1, $c_{mgc} = 0.5\text{m}$, and a NACA0012 airfoil (LL verification planform). The number of spanwise stations N for the XFLR5 simulation is 19, whereas $N = 1000$ and $K = 100$ for the adapted LL model. When sampling α_i and C_l at the spanwise locations of the XFLR5 data, it asserted that the values match with XFLR5 for a relative tolerance of 0.01. This is visually confirmed by [Figure 9.6](#) and [Figure 9.7](#).

For the case of SAVED's wing planform with $\Lambda_{0.25c} = 0^\circ$, an XFLR5 analysis with $N = 19$ and an adapted LL

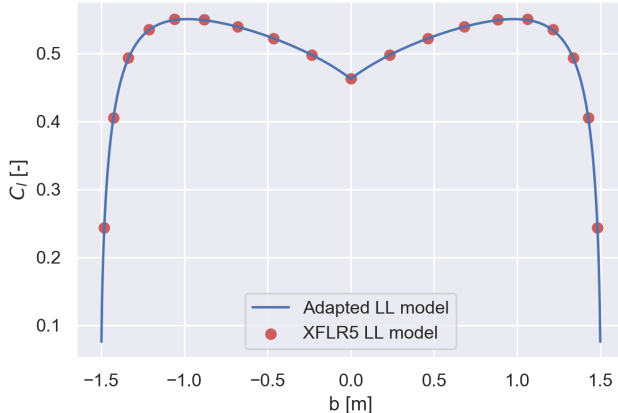


Figure 9.8: C_l vs y according to XFLR5 and the adapted LL model for SAVED's planform. $Re = 651085$.

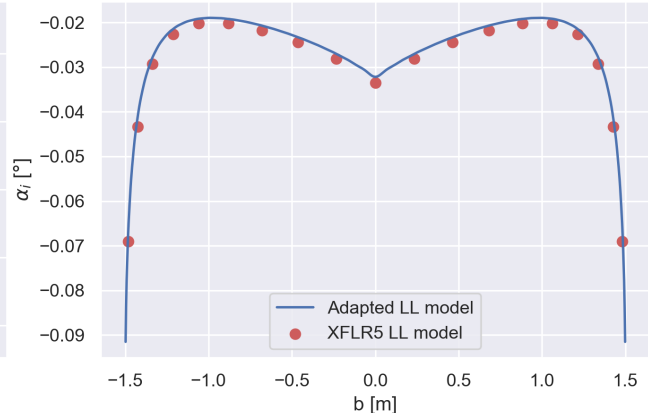


Figure 9.9: α_i vs y according to XFLR5 and the adapted LL model for SAVED's planform. $Re = 651085$.

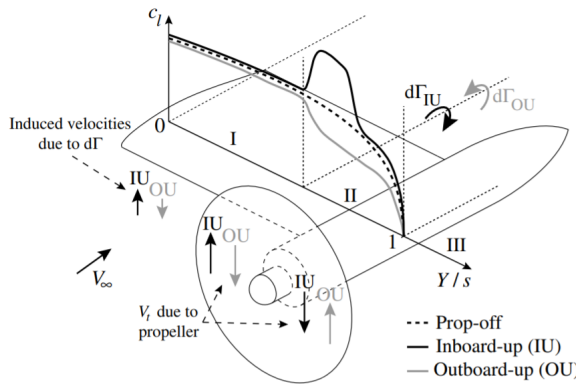


Figure 9.10: Schematic representation of the validation test configuration used in [66].

analysis with $N = 1000$ and $K = 100$ was run. Discrepancies between the adapted LL model and XFLR5's LL grow larger for α_i compared to the LL verification planform, though within an acceptable range for analysis. This increase in discrepancy is assumed to be caused by the fact that SAVED's wing planform analysis was performed at a higher angle of attack than the LL verification planform analysis and due to the inclusion of taper in the wing. The verification of the adapted LL model against XFLR5's LL model can be seen in Figure 9.8 and Figure 9.9.

Based on the error analysis and Figure 9.6, Figure 9.7, Figure 9.8, and Figure 9.8, the method is confirmed to be verified.

Validation of The Adapted LL Model Against Wind Tunnel Data

In order to validate the implementation of the propeller in the adapted LL model, the model is validated against wind tunnel data of C_l vs. y for different propeller advance ratios (J) [-] for a tractor propeller configuration used in [66].

The test configuration featured a straight, untapered wing with $b/2 = 0.292\text{m}$, $c = 0.247\text{m}$, and a NACA64₂A015 airfoil with a flap at $0.75c$. The propeller was located outboard at 0.327m and 44% of the propeller's diameter (D_{prop})[m] in front of the wing's LE, where $D_{prop} = 0.237\text{m}$. Tests were run at $V_\infty = 40\text{m/s}$ at $\alpha_g = 0^\circ$ at sea level conditions for a flap deflection δ_f of $+10^\circ$ and -10° [66]. The flap deflections were used to simulate an inboard up (IU) rotating direction of the propeller as well as an outboard up rotating direction (OU) without having to change the propeller [66]. Figure 9.10 schematically shows the test configuration including the propeller rotational directions [66]. As only one half of the wing was suspended in the wind tunnel, the reference frame was redefined by setting $b' = \frac{b}{2} = 0.292\text{m}$ and the origin of the reference frame at half of the half span, thereby complying with the reference frame used in Subsection 9.3.2.

Tests were performed at $J = 1.0, J = 0.9, J = 0.8$, and $J = 0.7$ for IU and OU rotations [66]. Where J is defined

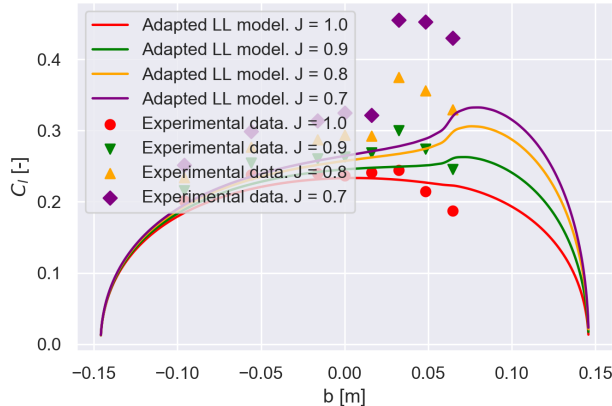


Figure 9.11: C_l [-] vs. y [m] for the adapted LL model and the experimental data from [66] (IU). $Re = 657471$.

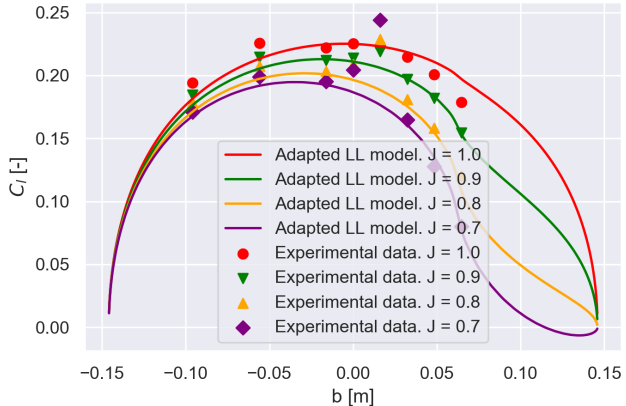


Figure 9.12: C_l [-] vs. y [m] for the adapted LL model and the experimental data from [66] (OU). $Re = 657471$.

by (9.37) [66].

$$J = \frac{V_\infty}{n\mathcal{D}_{prop}} \quad (9.37)$$

In (9.37), n is the propeller rotational frequency [Hz]. As the data in [66] is only provided in terms of J and the thrust coefficient (C_T) [-], some intermediate steps had to be taken to arrive at the required parameters to be able to solve (9.19) and (9.20). (9.37) was solved for n in order to find the rotational velocities corresponding to each of the advance ratios. An interpolation of J vs. C_T was then performed in order to find the thrust coefficients belonging to each of the aforementioned advance ratios. Using the computed thrust coefficients and rotational velocities corresponding to the different advance ratios, the propeller thrust corresponding to each advance ratio could be computed by (9.38).

$$T = \rho_\infty n^2 \mathcal{D}_{prop}^4 C_T \quad (9.38)$$

Using the results from (9.38), V_a and V_r could be computed from (9.19) and (9.20), respectively. These parameters were used as described in Subsection 9.3.2 to create the adapted LL for the configuration of for the IU and OU rotating case.

The results of the adapted LL model for $N = 1000$ and $K = 100$ are shown together with the experimental data for the IU and OU case in Figure 9.11 and Figure 9.12, respectively. Figure 9.11 and Figure 9.12 show sensible results. T increases with lower J , meaning the propeller produces more lift with decreasing J in Figure 9.11 and more downforce for decreasing J in Figure 9.12. This is both apparent from the data and the adapted LL.

Discrepancies between the experimental data and the adapted LL are present, though this is more likely to be the case due to the many simplifying assumptions the adapted LL model makes as mentioned in Subsection 9.3.2 as opposed to an incorrect implementation. Figure 9.11 shows that the lift induced by the propeller is underestimated. Figure 9.12 shows that the downforce is modelled much more accurately and almost perfectly matches the data.

Wing-propeller interaction effects are present for the experimental situation, as the propeller is placed a finite distance away from the wing. This is not taken into account by the adapted LL model as mentioned in Subsection 9.3.2. Slipstream axial velocities are not constant for the experimental situation, and aerodynamic parameters of the propeller such as lift and drag are not taken into account by the actuator disk model. Furthermore, swirl recovery is present for experimental situation, and is not taken into account by the adapted LL model [51]. Each of these effects, including many more lead to discrepancies between the model and the experimental data. However, considering the simple nature of the model compared to the experimental situation, it is still judged to resemble the experimental data accurately enough in order to consider the model validated.

Stability Performance Analysis

After breaking down the main subsystem design, the stability properties of the system are to be analysed. Stability is defined as the ability of the system to correct itself after disturbances act on it, whether they are due to control inputs or a sudden change in their state. This assessment is thus desired to determine the inherent stability properties of the system and how it behaves to certain disturbances from the equilibrium conditions. Therefore, it is necessary to ensure that SAVED is statically stable and laterally stable to the extent at which it can be corrected by means of active control. The chapter is structured as follows: [Section 10.1](#) summarises the preliminary considerations drawn during the midterm phase of the conceptual design. The analysis then delves into the specifics of the detailed phase with [Section 10.2](#) and [Section 10.3](#) with the static and dynamic stability properties of SAVED, respectively. Thereafter, the results attained are shown in [Section 10.4](#). The verification and validation procedures are explained in [Section 10.5](#). Finally, conclusions are drawn in [Section 10.6](#).

10.1. Preliminary Considerations

During the midterm phase [9], the aim was to analyse the stability properties of the concepts in a qualitative manner for their comparison. It was determined that stability was a requirement to be met, together with controllability, rather than a means of comparison. For this reason, stability was included in the decision criteria of reliability. This assessment was to give a greater insight on how well each of the concepts performed on a series of stability derivatives. By doing so, recommendations were made to the departments of structures, materials, and manufacturing (SMM) and Aerodynamics in terms of features that would ensure a better system stability. Some of which, such as the inclusion of positive sweep, were taken into account for the preliminary design of the wing ([Chapter 6](#)), yet they were still open to compromise between departments. In other words, preliminary design considerations followed after considering the most critical stability derivatives during the preliminary phase. For the final conceptual design, however, the final iteration of the design is assessed.

After this final design iteration is obtained, the aim of this analysis is to assess its stability properties. Although this follows after the values are considered frozen, they are still subjected to change in the case the results attained are not acceptable. Despite the preliminary considerations are expected to make the design converge to a stable system, it must be noted that concern is raised specifically on the directional stability of the system, for which active actuation of the control inputs would be needed in the case the vertical surface proved not to be sufficient. Given this uncertainty, the unstable motions need to be identified with the aim of having a better understanding of what situations require of active control to ensure stability.

10.2. Static Stability Analysis

The stability analysis is thus divided between static and dynamic stability, with this section considering the former. Static stability is the condition in which the forces and moments acting on a body generated by a disturbance tend initially to return the body to its equilibrium position [4]. This equilibrium is the trim condition, in which the moments around the centre of gravity are zero. In other words, given a disturbance, the system's initial behaviour is to react against it. For instance, consider a positive increase in angle of attack, effectively pitching up SAVED. Given this disturbance, static stability would be ensured if the force generated by this increase in angle of attack would pitch down SAVED, opposing the disturbance and hence maintaining the system stable longitudinally. It is clear the static stability properties of SAVED come heavily influenced by the overall geometry and configuration of SAVED's system integration, as explained in [Chapter 6](#) (requirement **SAVED-CONS-FLIGHT-02**).

For this to take place several conditions must be met. Firstly, the change in pitching moment coefficient with change in angle of attack ($C_{m\alpha}$) needs to be negative, meaning that with a positive change in angle of attack the increase in moment generated will be negative, and vice versa. This results in a stabilising longitudinal motion in which the system counters the effective pitching moment due to a disturbance in angle of attack. For the case of a flying wing, since there is no other lifting surface than the main wing, the neutral point coincides with the aerodynamic centre of the wing. Therefore, to comply with this condition, it is needed for the aerodynamic

centre of the main wing to be aft of the centre of gravity. This distance between the centre of gravity and the aerodynamic centre is called the static margin [4], and its determination is based on a compromise between stability and controllability. This is determined already in [Subsection 6.1.2](#) for a system requirement for stability, and accounted for in the planform design ([Chapter 6](#)) before designing the subsystems. Moreover, it must be noted that the vertical stabiliser of SAVED, sized for landing loads in [Chapter 8](#), also contributes to the performance of longitudinal stability. Due to this vertical surface having sweep, once SAVED pitches up or down, the lower or upper half tail, respectively, will face the airspeed more than the other, and the one facing the airspeed more will have more drag. When it comes to longitudinal stability, this increased drag aids SAVED in correcting and pitch to the airspeed again. This is only stabilising, as the fin is a symmetric airfoil.

The second condition for static stability is that the pitching moment coefficient at the aerodynamic centre ($C_{m_{a.c.}}$) should be positive such that, once the disturbance acts and the initial motion is to correct it, an equilibrium condition can be found (requirement **SAVED-CONS-FLIGHT-04**). For this, it is recommended to choose a reflexed airfoil. Generally, these are only used in flying wings, as their drawback is that their performance is more affected by a change in Reynolds number. Therefore, it is deemed preferable to other means such as twist for the aerodynamic analysis during the conceptual design phase [28]. This, as explained in [Subsection 6.1.3](#), is also considered early in the design as a system requirement before the airfoil selection commences.

The outcomes of accounting for these considerations during the planform design in [Chapter 6](#) can also be seen in the results in [Section 10.4](#), where the symmetric responses are shown to be bounded and thus fully stable. This confirms the design decisions made and proves the static stability of SAVED.

10.3. Dynamic Stability Analysis

The second part of the analysis consists of assessing SAVED's dynamic behaviour. Dynamic stability is defined as the ability of the system to eventually return to and remain in its equilibrium position after a disturbance away from it [4]. The main difference between static and dynamic stability is that, while the former depicts the initial behaviour after the disturbance is applied, the latter considers the response of the system over a certain period of time, where stability is achieved if the output is eventually bounded.

The aim of this section is to guide the reader through the development of a numerical model capable of describing the dynamic behaviour of SAVED during cruise, analogously to [50]. This section is thus structured as follows: [Subsection 10.3.1](#) starts by listing the assumptions used to derive the equations of motion, as shown in [Subsection 10.3.2](#). Once the equations of motion are derived, they are formulated in state space form in [Subsection 10.3.3](#). Lastly, having identified all necessary variables, these are gathered in [Subsection 10.3.4](#).

10.3.1. Assumptions

The numerical model used is to describe the dynamic behaviour of the system as accurately as possible during cruise conditions. When these are specified, the reality of interest can be focused with the aim to further simplify the analysis. If done adequately to the context being studied, the introduction of errors in the model is considered acceptable. The following list itemises the assumptions made, adapted from [50].

- **Flat Earth:** the short range of the mission justifies neglecting the Earth's curvature.
- **Non-rotating Earth:** the short duration of the mission justifies neglecting the angular rotation of the Earth, thus excluding Coriolis and centripetal accelerations.
- **Constant gravity:** small variations in altitude during the mission justify neglecting variations in gravity.
- **Constant mass:** particularly justified due to the fully electric propulsion system.
- **Rigid body:** despite being a less stiff structure than conventional aircraft, the low airspeeds and short span of the system justify neglecting aeroelastic effects.
- **SAVED has a symmetry plane:** designing the system with a symmetry plane allows for neglecting mass asymmetries along SAVED's span. This greatly simplifies the equations of motion.
- **No rotating masses:** during cruise, it is assumed there are no rotating masses creating a change in centre of gravity. This is not valid for large elevon deflections (the transition phase). Nonetheless, for cruise conditions it is valid to assume a smaller deflection in elevon and no shift in gravity centre, considering the inputs are modelled as impulses and steps of small magnitudes.
- **No wind:** originally, the airspeed is solely influenced by SAVED's flight path angle. Flight is thus symmetric as there is no sideslip at the start of the analysis. Wind gusts, however, can be modelled afterwards.

10.3.2. Derivation of the Equations of Motion

In this subsection, the general equations of motion (EOM) are derived. First, the general formulation is set up, after which the equations are linearised. Finally, the linearised equations are made non-dimensional. The reference frame is chosen out of convenience for this analysis and specific to this chapter only. While the general formulation of the EOM is done on a body frame, the analysis continues on the stability frame, both of which are explained below.

General Formulation

Adhering to the assumptions above, the general formulation of the EOM is reduced (following from [50]) to the force equations along three orthogonal body axes: X_b , Y_b and Z_b and their moment equations rolling moment (L), pitching moment (M) and yawing moment (N), respectively, which include all of the contributions to the moments [N m] (10.1). X , Y and Z are thus force vectors [N] acting along their respective body axes and include the aerodynamic and thrust forces acting in each of their respective axis. Equation (10.2), on the other hand, gives the three main kinematic relations to be used [50]. The frame of reference chosen is a body frame: X_b axis in the symmetry plane, Y_b to the right wing and Z_b orthogonal to both. This frame, however, is not fixed in the actual direction of X_b [50]. This is specified after, for which the angles depend on this decision.

$$\begin{aligned} -W \sin \theta + X &= m(\dot{u} + qw - rv) \\ +W \cos \theta \sin \varphi + Y &= m(\dot{v} + ru - pw) \\ +W \cos \theta \cos \varphi + Z &= m(\dot{w} + pv - qu) \\ L &= I_{xx}\dot{p} + (I_{zz} - I_{yy})qr - I_{xz}(\dot{r} + pq) \\ M &= I_{yy}\dot{q} + (I_{xx} - I_{zz})rp + I_{xz}(p^2 - r^2) \\ N &= I_{zz}\dot{r} + (I_{yy} - I_{xx})pq - I_{xz}(\dot{p} - rq) \end{aligned} \quad (10.1)$$

$$\begin{aligned} \dot{\phi} &= p + q \sin \varphi \tan \theta + r \cos \varphi \tan \theta \\ \dot{\theta} &= q \cos \varphi - r \sin \varphi \\ \dot{\psi} &= q \frac{\sin \varphi}{\cos \theta} + r \frac{\cos \varphi}{\cos \theta} \end{aligned} \quad (10.2)$$

In (10.1), W is the weight [N], m is the mass [kg], u , v , and w are the velocity [m/s] components along the X_b , Y_b , Z_b axes, respectively. \dot{u} , \dot{v} , and \dot{w} are the acceleration components [m/s^2] along the X_b , Y_b , Z_b axes, respectively. p , q , and r are the roll, pitch, and yaw rates, respectively, [rad/s] and \dot{p} , \dot{q} , and \dot{r} are the roll, pitch, and yaw accelerations, respectively [rad/s^2]. Furthermore, I is the second moment of area [kg m^2], ϕ is the bank angle, and θ is the pitch angle [rad].

Linearisation

In order to retrieve the desired information on the system's dynamic behaviour, it is necessary to linearise these equations about a specific condition. This allows for using a set of first order ordinary differential equations (ODE)s, the state space of the system, as seen in Subsection 10.3.3. This formulation of the system's model is used to retrieve the characteristic modes, providing information on the inherent stability properties of the system. This representation is also used to numerically compute the responses of the system to disturbances. Linearisation is accurate within a narrow region around the point that is being linearised about. Its use is therefore justified, as the behaviour of interest for this chapter originates from a small disturbance in a specific instant, and its convergence again to that point within a small range of angles.

After justifying the use of linearisation, the point to specifically linearise about is to be determined. The sole requirement for it is to be a stable instant for the responses not to deviate quickly, compromising the validity of the results [50]. For simplicity, the choice is made to linearise about steady, straight and symmetric flight conditions. This means that there is no sideslip and no variation in either horizontal velocity or flight path angle. Moreover, it is also chosen for the latter to be zero (level flight), as it is cruise that is being analysed in this chapter.

To further simplify the linearisation of the equations of motion, two more simplifications are made. Firstly, the coupling between the symmetric and asymmetric motions is neglected. In other words, small symmetric disturbances do not influence asymmetric forces and moments, and vice versa [50]. This is justified based on the fact that the disturbances are small and results in having two sets of ODEs for each of the analysis. Furthermore, a characteristic of the LTI system to be constructed is neglecting the influence of most parameter variations through time, which results in removing most of the derivatives from the analysis.

After making the choice of the point to linearise about, the frame of reference can be chosen. It is decided for the continuation of the analysis to use the stability frame, corresponding with the body frame of reference fixing the X_S axis to the airspeed's projection into the symmetry plane, a right-handed orthogonal frame with the origin at the centre of gravity. Commonly used for the study of steady, straight and symmetric flight [55], this frame is characterised by the following relations [50]; (10.3) establishes that the X_S axis points to the airspeed, making the angle of attack with that axis to be zero (10.4). In all four instances the subscript zero refers to the state before a disturbance is applied or, in other words, the point at which it is being linearised about.

$$\begin{aligned} u_0 &= V \\ w_0 &= 0 \end{aligned} \quad (10.3)$$

$$\begin{aligned} \alpha_0 &= 0 \\ \theta_0 &= \gamma_0 \end{aligned} \quad (10.4)$$

Once all of the simplifications to the linearisation of the EOM are made, both sides of the equations (10.1) can be linearised with respect to all variables: the states and control inputs. While the states are the same as a conventional aircraft, the inputs are not. The control inputs are the RPM setting for each of the four engines and the deflection of each elevon (δ_e). These are extended in the same and opposite way to provide pitch and roll, respectively, reason for which the control inputs are separated. The four propellers generally contribute to the forces in X direction and moments of M and N . Lastly, trim tab and rudder are not included in SAVED.

The following linearised equations represent how a change in a state or input in the LHS of (10.1) contributes to the motion. For instance, Z_u represents how the force in Z axis changes with a change in horizontal velocity u . This rate of change is then multiplied to the change in u itself to yield the new contribution in Z force due to a change in u . For the sake of readability, all of the notations indicating a small change are dropped. The symmetric and asymmetric cases are shown in (10.5) and (10.6), with the new kinematic relations in (10.7).

$$\begin{aligned} -W \cos \theta_0 \theta + X_u u + X_w w + X_q q + X_{\delta_{e_I}} \delta_{e_I} + X_{\delta_{e_{II}}} \delta_{e_{II}} + X_{RPM_1} RPM_1 \\ + X_{RPM_2} RPM_2 + X_{RPM_3} RPM_3 + X_{RPM_4} RPM_4 = m \dot{u} \\ -W \sin \theta_0 \theta + Z_u u + Z_w w + Z_w \dot{w} + Z_q q + Z_{\delta_{e_I}} \delta_{e_I} + Z_{\delta_{e_{II}}} \delta_{e_{II}} = m(\dot{w} - qV) \\ M_u u + M_w w + M_w \dot{w} + M_q q + M_{\delta_{e_I}} \delta_{e_I} + M_{\delta_{e_{II}}} \delta_{e_{II}} + M_{RPM_1} RPM_1 \\ + M_{RPM_2} RPM_2 + M_{RPM_3} RPM_3 + M_{RPM_4} RPM_4 = I_{yy} \dot{q} \\ \dot{\theta} = q \end{aligned} \quad (10.5)$$

$$\begin{aligned} W \cos \theta_0 \varphi + Y_v v + Y_{\dot{v}} \dot{v} + Y_p p + Y_r r + Y_{\delta_{e_I}} \delta_{e_I} + Y_{\delta_{e_{II}}} \delta_{e_{II}} + = m(\dot{v} + rV) \\ L_v v + L_p p + L_r r + L_{\delta_{e_I}} \delta_{e_I} + L_{\delta_{e_{II}}} \delta_{e_{II}} = I_{xx} \dot{p} - I_{xz} \dot{r} \\ N_v v + N_{\dot{v}} \dot{v} + N_p p + N_r r + N_{\delta_{e_I}} \delta_{e_I} + N_{\delta_{e_{II}}} \delta_{e_{II}} + N_{RPM_1} RPM_1 \\ + N_{RPM_2} RPM_2 + N_{RPM_3} RPM_3 + N_{RPM_4} RPM_4 = I_{zz} \dot{r} - I_{xz} \dot{p} \\ \dot{\psi} = \frac{r}{\cos \theta_0} \\ \dot{\phi} = p + r \tan \theta_0 \end{aligned} \quad (10.6)$$

$$\begin{aligned} \dot{\phi} &= p + \tan \theta_0 r \\ \dot{\theta} &= q \\ \dot{\psi} &= \frac{1}{\cos \theta_0} r \end{aligned} \quad (10.7)$$

Formulation in Non-Dimensional Form

Since forces and moments are given non-dimensionalised, the linearised EOM are to be formulated in the same manner for SAVED, analogously to [50]. Forces are made non dimensional by multiplying with $\frac{1}{\frac{1}{2} \rho V^2 S}$.

Where ρ is the air density, V is the airspeed and S is the reference surface area. Forces already differentiated, on the other hand, with $\frac{1}{\frac{1}{2} \rho V S}$. Moment components differ between the symmetric and asymmetric cases as

they are non-dimensionalised by $\frac{1}{\frac{1}{2} \rho V^2 S c}$ and $\frac{1}{\frac{1}{2} \rho V^2 S b}$, respectively. Where c is the reference chord and b is the reference span. A more extensive explanation on the variables used is shown in Subsection 10.3.4. Using relations (10.8) to (10.11), the EOM can be rewritten to (10.16) and (10.17) for the symmetric and asymmetric cases, respectively. Lastly, the non-dimensional moments of inertia are given in (10.12) to (10.15). In (10.16) and (10.17), α is the angle of attack, β is the sideslip angle, and γ is the flight path angle.

$$\begin{aligned} C_{X_0} &= \frac{W \sin \theta_0}{\frac{1}{2} \rho V^2 S} \\ C_{Z_0} &= -\frac{W \cos \theta_0}{\frac{1}{2} \rho V^2 S} \end{aligned} \quad (10.8)$$

$$\begin{aligned} \hat{u} &= \frac{u}{\bar{V}} \\ \alpha &= \frac{\dot{V}}{V} \end{aligned} \quad (10.9)$$

$$\begin{aligned} D_c &= \frac{\bar{c}}{\bar{V}} \frac{d}{dt} \\ D_b &= \frac{\bar{b}}{V} \frac{d}{dt} \end{aligned} \quad (10.10)$$

$$\begin{aligned} \mu_c &= \frac{m}{\rho S \bar{c}} \\ \mu_b &= \frac{m}{\rho S b} \end{aligned} \quad (10.11)$$

$$K_X^2 = \frac{I_{xx}}{mb^2} \quad (10.12)$$

$$K_Y^2 = \frac{I_{yy}}{m\bar{c}^2} \quad (10.13)$$

$$K_Z^2 = \frac{I_{zz}}{mb^2} \quad (10.14)$$

$$K_{XZ} = \frac{I_{xz}}{mb^2} \quad (10.15)$$

$$\begin{aligned} C_{Z_0} \theta + C_{X_u} \hat{u} + C_{X_\alpha} \alpha + C_{X_q} D_c \theta + C_{X_{\delta e_I}} \delta_{e_I} + C_{X_{\delta e_{II}}} \delta_{e_{II}} + C_{X_{RPM_1}} RPM_1 \\ + C_{X_{RPM_2}} RPM_2 + C_{X_{RPM_3}} RPM_3 + C_{X_{RPM_4}} RPM_4 = 2\mu_c D_c \hat{u} \\ -C_{X_0} \theta + C_{Z_u} \hat{u} + C_{Z_\alpha} \alpha + C_{Z_q} D_c \alpha + C_{Z_{\delta e_I}} \delta_{e_I} + C_{Z_{\delta e_{II}}} \delta_{e_{II}} = 2\mu_c (D_c \alpha - D_c \theta) \\ C_{m_u} \hat{u} + C_{m_\alpha} \alpha + C_{m_\alpha} D_c \alpha + C_{m_q} D_c \theta + C_{m_{\delta e_I}} \delta_{e_I} + C_{m_{\delta e_{II}}} \delta_{e_{II}} + C_{m_{RPM_1}} RPM_1 \\ + C_{m_{RPM_2}} RPM_2 + C_{m_{RPM_3}} RPM_3 + C_{m_{RPM_4}} RPM_4 = 2\mu_c K_Y^2 D_c \frac{q\bar{c}}{V} \\ \frac{\dot{\theta}\bar{c}}{V} = \frac{q\bar{c}}{V} \end{aligned} \quad (10.16)$$

$$\begin{aligned} C_L \varphi + C_{Y_\beta} \beta + C_{Y_\beta} D_b \beta + C_{Y_p} \frac{pb}{2V} + C_{Y_r} \frac{rb}{2V} + C_{Y_{\delta e_I}} \delta_{e_I} + C_{Y_{\delta e_{II}}} \delta_{e_{II}} = 2\mu_b \left(D_b \beta + 2 \frac{rb}{2V} \right) \\ C_{\ell_\beta} \beta + C_{\ell_p} \frac{pb}{2V} + C_{\ell_r} \frac{rb}{2V} + C_{\ell_{\delta e_I}} \delta_{e_I} + C_{\ell_{\delta e_{II}}} \delta_{e_{II}} = 4\mu_b \left(K_X^2 D_b \frac{pb}{2V} - K_{XZ} D_b \frac{rb}{2V} \right) \\ C_{n_\beta} \beta + C_{n_\beta} D_b \beta + C_{n_p} \frac{pb}{2V} + C_{n_r} \frac{rb}{2V} + C_{n_{\delta e_I}} \delta_{e_I} + C_{n_{\delta e_{II}}} \delta_{e_{II}} \\ + C_{n_{RPM_1}} RPM_1 + C_{n_{RPM_2}} RPM_2 + C_{n_{RPM_3}} RPM_3 + C_{n_{RPM_4}} RPM_4 = 4\mu_b \left(K_Z^2 D_b \frac{rb}{2V} - K_{XZ} D_b \frac{pb}{2V} \right) \\ \frac{1}{2} D_b \psi = \frac{1}{\cos \gamma_0} \frac{rb}{2V} \\ \frac{1}{2} D_b \varphi = \frac{pb}{2V} + \frac{rb}{2V} \tan \gamma_0 \end{aligned} \quad (10.17)$$

10.3.3. Formulation in State Space System

Having non-dimensionalised the linearised EOM, the state space equations can be constructed. This is used as the final form of the linearised EOM, as it allows for dealing with a Multiple Input Multiple Output (MIMO) problem in the time domain. The complete state space model is described with (10.18) and (10.19), where \bar{x} is the state vector, containing all state variables, \bar{y} the output vector, containing all variables of interest and \bar{u} the input vector, containing the inputs. Matrices A , B , C and D are the state, input, output and feedthrough matrix.

$$\dot{\bar{x}} = A\bar{x} + B\bar{u} \quad (10.18)$$

$$\bar{y} = C\bar{x} + D\bar{u} \quad (10.19)$$

The EOM in (10.16) and (10.17) can then be posed in this form as follows. Firstly, the variables multiplying each state or control input are grouped separately for each equation. Afterwards, the states are separated from the control inputs in each side of the equations, yielding (10.20) and (10.21).

$$\begin{bmatrix} C_{X_u} - 2\mu_c D_c & C_{X_\alpha} & C_{Z_0} & C_{X_q} \\ C_{Z_u} & C_{Z_\alpha} + (C_{Z_\alpha} - 2\mu_c) D_c & -C_{X_0} & C_{Z_q} + 2\mu_c \\ 0 & 0 & -D_c & 1 \\ C_{m_u} & C_{m_\alpha} + C_{m_{\dot{\alpha}}} D_c & 0 & C_{m_q} - 2\mu_c K_Y^2 D_c \end{bmatrix} \begin{bmatrix} \hat{u} \\ \alpha \\ \theta \\ \frac{q\bar{c}}{V} \end{bmatrix} = \begin{bmatrix} -C_{X_{\delta e_I}} & -C_{X_{\delta e_{II}}} & -C_{X_{RPM_1}} & -C_{X_{RPM_2}} & -C_{X_{RPM_3}} & -C_{X_{RPM_4}} \\ -C_{Z_{\delta e_I}} & -C_{Z_{\delta e_{II}}} & 0 & 0 & 0 & 0 \\ 0 & 0 & 0 & 0 & 0 & 0 \\ -C_{m_{\delta e_I}} & -C_{m_{\delta e_{II}}} & -C_{m_{RPM_1}} & -C_{m_{RPM_2}} & -C_{m_{RPM_3}} & -C_{m_{RPM_4}} \end{bmatrix} \begin{bmatrix} \delta_{e_I} \\ \delta_{e_{II}} \\ RPM_1 \\ RPM_2 \\ RPM_3 \\ RPM_4 \end{bmatrix} \quad (10.20)$$

$$\begin{bmatrix} C_{Y_\beta} + (C_{Y_\beta} - 2\mu_b) D_b & C_L & C_{Y_p} & C_{Y_r} - 4\mu_b \\ 0 & -\frac{1}{2}D_b & 1 & 0 \\ C_{\ell_\beta} & 0 & C_{\ell_p} - 4\mu_b K_X^2 D_b & C_{\ell_r} + 4\mu_b K_{XZ} D_b \\ C_{n_\beta} + C_{n_{\dot{\beta}}} D_b & 0 & C_{n_p} + 4\mu_b K_{XZ} D_b & C_{n_r} - 4\mu_b K_Z^2 D_b \end{bmatrix} \begin{bmatrix} \beta \\ \varphi \\ pb \\ \frac{2V}{2b} \end{bmatrix} = \begin{bmatrix} -C_{Y_{\delta e_I}} & -C_{Y_{\delta e_{II}}} & 0 & 0 & 0 & 0 \\ 0 & 0 & 0 & 0 & 0 & 0 \\ -C_{\ell_{\delta e_I}} & -C_{\ell_{\delta e_{II}}} & 0 & 0 & 0 & 0 \\ -C_{n_{\delta e_I}} & -C_{n_{\delta e_{II}}} & -C_{n_{RPM_1}} & -C_{n_{RPM_2}} & -C_{n_{RPM_3}} & -C_{n_{RPM_4}} \end{bmatrix} \begin{bmatrix} \delta_{e_I} \\ \delta_{e_{II}} \\ RPM_1 \\ RPM_2 \\ RPM_3 \\ RPM_4 \end{bmatrix} \quad (10.21)$$

For brevity, the derivation continues for the symmetric case, with the asymmetric obtained analogously. Renaming the matrices in (10.20) as $S\bar{x} = I\bar{u}$, the next step is to make use of the differential operators in S to attain \dot{x} . Therefore, matrix S can be separated in two as $S = S_I + S_{II}$, with S_I containing the differential operators as in (10.10). These differential operators can be used to multiply with the state vector to obtain \dot{x} by having $S'_I \dot{x} = -S_{II} \bar{x} + I\bar{u}$, with S'_I , $-S_{II}$ and I as (10.22), (10.23) and the RHS of equation (10.20), respectively.

$$S'_I = \begin{bmatrix} -2\mu_c \frac{\bar{c}}{V} & 0 & 0 & 0 \\ 0 & (C_{Z_\alpha} - 2\mu_c) \frac{\bar{c}}{V} & 0 & 0 \\ 0 & 0 & -\frac{\bar{c}}{V} & 0 \\ 0 & C_{m_{\dot{\alpha}}} \frac{\bar{c}}{V} & 0 & -2\mu_c K_Y^2 \frac{\bar{c}}{V} \end{bmatrix} \quad (10.22)$$

$$-S_{II} = \begin{bmatrix} -C_{X_u} & -C_{X_\alpha} & -C_{Z_0} & 0 \\ -C_{Z_u} & -C_{Z_\alpha} & C_{X_0} & -(C_{Z_q} + 2\mu_c) \\ 0 & 0 & 0 & -1 \\ -C_{m_u} & -C_{m_\alpha} & 0 & -C_{m_q} \end{bmatrix} \quad (10.23)$$

Once \dot{x} is found, it is to be isolated by multiplying $-S_{II}$ and I with the inverse of S'_I , as $S'_I \dot{x} = -S_{II} \bar{x} + I\bar{u}$ is equivalent to $\dot{x} = S'^{-1}(-S_{II})\bar{x} + S'^{-1}I\bar{u}$, with $A = S'^{-1}(-S_{II})$ and $B = S'^{-1}I$. By doing so, the state equation (10.18) is attained numerically using Python. The output equation, on the other hand, is constructed depending on what outputs are desired to know. If the outputs chosen are simply the states, the output matrix C is solely an identity matrix, while the feedthrough matrix D is a zero matrix, thus completing the state space model.

10.3.4. Stability and Control Derivatives

Having constructed the complete state space model numerically, it is necessary to gather the stability and control derivatives identified in (10.20) and (10.21).

Stability Derivatives

The stability derivatives are retrieved in its entirety from XFLR5 [21], as the dimensional values as output correspond with the stability reference frame. Thereafter, these are non-dimensionalised as in [50]. The full list of dimensional derivatives as attained from XFLR5, their non-dimensionalisation relation and the final values used in the state space are shown in Table 10.1 for both symmetric and asymmetric cases.

Table 10.1: Stability derivatives for the symmetric (left) and asymmetric case (right)

Dimensional	Relation	Non-dimensional	Dimensional	Relation	Non-dimensional
$X_u = -0.5777$	$\frac{1}{\frac{1}{2}\rho VS}$	$C_{X_u} = -0.0313$	$Y_v = -12.509$	$\frac{1}{\frac{1}{2}\rho VS}$	$C_{Y_\beta} = -0.6786$
$X_w = 2.8376$	$\frac{1}{\frac{1}{2}\rho VS}$	$C_{X_\alpha} = 0.1539$	$Y_p = 0.3964$	$\frac{1}{\frac{1}{2}\rho VSb}$	$C_{Y_p} = 0.0143$
$Z_u = -4.9369$	$\frac{1}{\frac{1}{2}\rho VS}$	$C_{Z_u} = -0.2678$	$Y_r = 5.5729$	$\frac{1}{\frac{1}{2}\rho VSb}$	$C_{Y_r} = 0.2016$
$Z_w = -85.786$	$\frac{1}{\frac{1}{2}\rho VS}$	$C_{Z_\alpha} = -4.6539$	$L_v = -0.6735$	$\frac{1}{\frac{1}{2}\rho VSb}$	$C_{\ell_\beta} = -0.0122$
$X_q = 0$	$\frac{1}{\frac{1}{2}\rho VS\dot{c}}$	$C_{X_q} = 0$	$L_p = -104.82$	$\frac{2}{\frac{1}{2}\rho VSb^2}$	$C_{\ell_p} = -1.2637$
$Z_q = -67.512$	$\frac{1}{\frac{1}{2}\rho VS\dot{c}}$	$C_{Z_q} = -7.2526$	$L_r = 3.3465$	$\frac{2}{\frac{1}{2}\rho VSb^2}$	$C_{\ell_r} = 0.0403$
$M_u = 0.00295$	$\frac{1}{\frac{1}{2}\rho VS\dot{c}}$	$C_{m_u} = 0.00031$	$N_v = 5.0258$	$\frac{1}{\frac{1}{2}\rho VSb}$	$C_{n_\beta} = 0.0909$
$M_w = -23.315$	$\frac{1}{\frac{1}{2}\rho VS\dot{c}}$	$C_{m_\alpha} = -2.5047$	$N_p = -1.2813$	$\frac{2}{\frac{1}{2}\rho VSb^2}$	$C_{n_p} = -0.0155$
$M_q = -12.724$	$\frac{1}{\frac{1}{2}\rho VS\dot{c}^2}$	$C_{m_q} = -2.7068$	$N_r = -1.9316$	$\frac{2}{\frac{1}{2}\rho VSb^2}$	$C_{n_r} = -0.0233$

Note that all of the derivatives with respect to the rate of change in angle of attack ($\dot{\alpha}$) are assumed zero, as from literature it is clear its main contribution is the horizontal stabiliser [50], absent in SAVED. Moreover, X_q is immediately assumed zero as well, as for such low velocities and disturbances, pitch rate does not influence the longitudinal force. Lastly, derivatives with respect to the rate of change in sideslip angle ($\dot{\beta}$) are also neglected, as it is often done for aircraft with an aspect ratio of over 4 [50], which is the case for SAVED.

Lastly, attention must be paid to those derivatives considered as critical during the previous phase [9]. For lateral stability, the following are required. First, a negative C_{ℓ_β} helps for a stable roll with a sideslip disturbance and is achieved through a high wing configuration, dihedral and positive sweep, resulting in a value of -0.0122. Secondly, a negative C_{ℓ_p} is desired for roll damping and attained with the main wing and the vertical surface, resulting in a value of -1.2637. Lastly, a positive C_{n_β} is desired for directional stability and achieved with the vertical surface, resulting in a value of 0.0909. All in all, all previously drawn derivatives prove to comply with the preliminary recommendations in [9] and, most importantly, a positive C_{n_β} shows that directional stability is achieved inherently, without the need for active differential thrust.

Control Derivatives

The control derivatives describe how the states change with respect to the control inputs, namely the RPM of each engine and the elevon deflections. While the former is obtained by differentiating the analytic equation for the thrust, the latter relies on XFLR5 data.

On the one hand, the RPM of each engine continuously changes its respective thrust, aligned with the body and only contributing to the direction of the X axis. Although it is the stability axis that is being analysed, the difference is only the angle of attack during cruise of 5.3 °, for which it can also be assumed to only act on the X axis of the stability frame. Thus, the contributions of these forces are only for longitudinal force and yawing moments. In other words, since no moment is created around the Y axis, all $C_{m_{RPM}}$ derivatives turn zero. To compute the derivatives, the force in X (the summation of all aerodynamic forces and each of the thrusts, each related to their respective RPM setting) is differentiated with respect to each of the RPM inputs. All forces thus cancel except for its specific thrust, for which thrust as a function of RPM is considered. Rearranging, thrust as a function of RPM is attained as in (10.24) for each engine. By differentiating this equation (10.25) and substituting for cruise settings (1720 RPM), the rate of change in thrust with a change in RPM input during cruise is obtained for each propeller, yielding $\frac{1}{413}$. For the yawing moment, on the other hand, the same procedure is followed, accounting for the sign of the moment created by the thrust and the distance to the centre of gravity. This distance with the inner and outer propellers is of 35% and 70% of the half span, respectively (Chapter 6). Results are shown in Table 10.2. Note: the right hand rule is used as yawing sign convention and the engine numbering is spanwise, left to right.

$$T = \left(\frac{RPM}{1237} \right)^{2.088} \quad (10.24)$$

$$\frac{dT}{dRPM} = 7.3 \cdot 10^{-7} RPM^{1.088} \quad (10.25)$$

Table 10.2: Control derivatives of RPM inputs for the symmetric (left) and asymmetric case (right)

Dimensional	Relation	Non-dimensional	Dimensional	Relation	Non-dimensional
$X_{RPM_1} = \frac{1}{413}$	$\frac{1}{\frac{1}{2}\rho VS}$	$C_{X_{RPM_1}} = 1.31 \cdot 10^{-4}$	$N_{RPM_1} = \frac{0.7b}{413}$	$\frac{1}{\frac{1}{2}\rho VSb}$	$C_{n_{RPM_1}} = 9.195 \cdot 10^{-5}$
$X_{RPM_2} = \frac{1}{413}$	$\frac{1}{\frac{1}{2}\rho VS}$	$C_{X_{RPM_2}} = 1.31 \cdot 10^{-4}$	$N_{RPM_2} = \frac{0.35b}{413}$	$\frac{1}{\frac{1}{2}\rho VSb}$	$C_{n_{RPM_2}} = 4.598 \cdot 10^{-5}$
$X_{RPM_3} = \frac{1}{413}$	$\frac{1}{\frac{1}{2}\rho VS}$	$C_{X_{RPM_3}} = 1.31 \cdot 10^{-4}$	$N_{RPM_3} = -\frac{0.35b}{413}$	$\frac{1}{\frac{1}{2}\rho VSb}$	$C_{n_{RPM_3}} = -4.598 \cdot 10^{-5}$
$X_{RPM_4} = \frac{1}{413}$	$\frac{1}{\frac{1}{2}\rho VS}$	$C_{X_{RPM_4}} = 1.31 \cdot 10^{-4}$	$N_{RPM_4} = -\frac{0.7b}{413}$	$\frac{1}{\frac{1}{2}\rho VSb}$	$C_{n_{RPM_4}} = -9.195 \cdot 10^{-5}$

Table 10.3: Control derivatives of the elevon, as extracted from XFLR5

Control derivative	Value	Control derivative	Value
$C_{Z_{\delta_e}}$	-1.0194	$C_{m_{\delta_e}}$	-0.295
$C_{X_{\delta_e}}$	$-0.354 * \delta_e \approx -0.0177$	$C_{l_{\delta_e}}$ (absolute value)	0.217

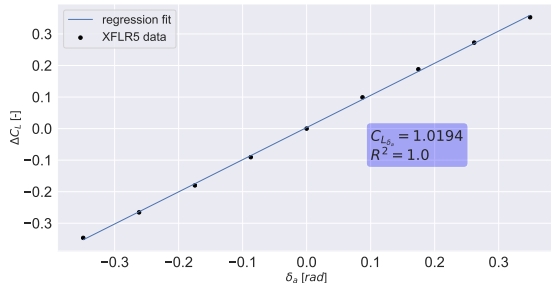
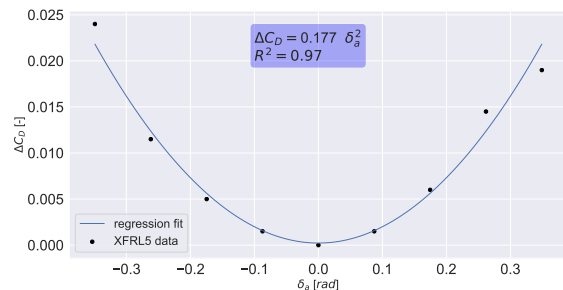
The second set of control inputs are the elevon deflections. Upon further consideration of the given case, the elevon's influence in lateral force and yawing moment is neglected (all $C_{Y_{\delta_e}}$ and $C_{n_{\delta_e}}$ are zero). Therefore, its only contributions are assumed to be the forces in the plane of symmetry and the pitching and rolling moments. The coefficients of these are obtained in the aerodynamic frame using XFLR5. For the wing at $\alpha = 0^\circ$ the elevons are deflected from -20 to 20° in steps of 5° and the coefficients C_L , C_D , C_m and C_l for lift, drag, pitching and rolling moment respectively are recorded for each deflection. Consequently, each of these states is then compared to a state with zero elevon deflection and a change in each coefficient is hence defined. Finally, this data is processed in Python to create regression fits. It can be seen that for ΔC_L , ΔC_m and ΔC_l , shown in [Figure 10.1](#), [Figure 10.3](#), [Figure 10.4](#) respectively, the data very closely follows a linear trend. For ΔC_D one can then see a quadratic trend as shown in [Figure 10.2](#). This behaviour is not at all surprising considering how elevators and ailerons behave [50]. The lift and drag derivatives can then be transformed to the stability frame by simply switching the signs of the forces from L to Z and from D to X . As there is no sideslip angle and α is unchanged, this is a valid approximation, yielding the results in [Table 10.3](#). Note, each derivative accounts for the contribution of a single elevon deflection, being equal to δ_{eI} and δ_{eII} . Also, $C_{X_{\delta_e}}$ is taken at about 0.05 radians. Lastly, the sign of $C_{l_{\delta_e}}$ depends on the elevon being deflected.

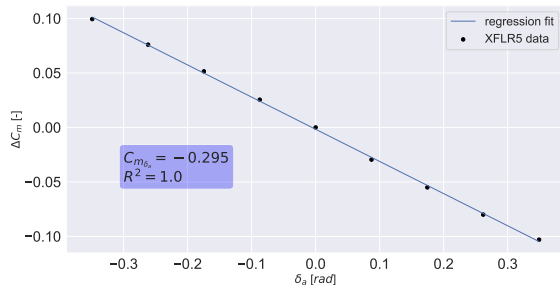
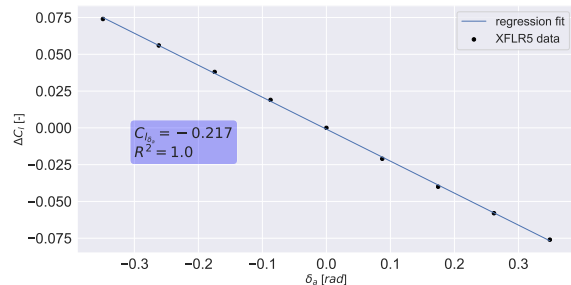
10.4. Results

After constructing the numerical model and gathering the necessary data, the static and dynamic stability properties can be assessed. This consists of examining the properties of each eigenmotion in [Subsection 10.4.1](#) and seeing how the system responds to specific disturbances, as shown in [Subsection 10.4.2](#).

10.4.1. Characteristic Modes

The characteristic modes describe the passive stability of the system, independently of the inputs. This is because their magnitude and type do not affect the passive stability of the system. These modes are the eigenmotions of the aircraft i.e. the motions of the aircraft after a disturbance from equilibrium. For SAVED,

Figure 10.1: ΔC_L vs δ_e for one elevonFigure 10.2: ΔC_D vs δ_e for one elevon

Figure 10.3: ΔC_m vs δ_e for one elevon.Figure 10.4: ΔC_ℓ vs δ_e for one elevon.

these are retrieved numerically from the matrix A of the state space model and verified in [Section 10.5](#).

The eigenmodes are represented by eigenvalues, which have a real and imaginary part. The real part is described by an exponential aperiodic function. For stability this is required to be negative, as the motion then tends to zero. The imaginary part, however, represents a periodic (oscillating) contribution to the motion, and always comes in a conjugate pair. If all real parts are negative, the disturbed motion is to eventually return to equilibrium condition. If one of the real parts is positive, the equilibrium is unstable after a disturbance and is to eventually diverge away. If all real parts are zero, the system is neutrally stable. The larger the absolute value of the real part, the more damped the motion is and the faster it returns to equilibrium. The larger the absolute value of the imaginary part, the more pronounced the oscillation is. All of the eigenmotions present in aircraft analysis, as well as the corresponding eigenvalues as retrieved from the numerical model for SAVED, are shown in [Table 10.4](#) and explained below. Note that this set of eigenvalues accounts for the contributions of $\frac{V}{c}$ and $\frac{V}{b}$ for the symmetric and asymmetric cases, respectively, as they are retrieved numerically from matrix A (which increases the absolute value).

Table 10.4: Eigenmotions and their respective pairs of eigenvalues

Eigenmotion	Real part	Imaginary part
Short period oscillation	-12.13	$\pm 24.68j$
Phugoid oscillation	$-1.49 \cdot 10^{-2}$	$\pm 0.36j$
A-periodic roll	-23.31	$\pm 0j$
Dutch roll	-0.5535	$\pm 4.675j$
A-periodic spiral	$1.369 \cdot 10^{-2}$	$\pm 0j$

On the one hand, two complex eigenmotions are given for the symmetric case: a highly damped and a less damped one. The former corresponds to the short period motion: fast and predominantly visible in the pitch rate, with velocity barely affected. Due to inertia, this motion is gone before the velocity changes significantly. Alternatively, a lightly damped motion, the phugoid, results from a sudden change in horizontal speed and it consists of a slow, lightly damped motion where velocity, pitch angle and pitch rate are mostly affected [50].

On the other hand, the asymmetric eigenmotions consist of a damped, aperiodic motion, a set of complex conjugate eigenvalues and an unstable motion. The real, stable motion is the a-periodic roll, resulting from favourable roll damping. The complex eigenmotion is the Dutch roll, when SAVED yaws and rolls after sideslipping. This is bounded and thus stable. Lastly, the diverging motion is the a-periodic spiral. This motion is usually positively or negatively damped in aircraft analysis, yet usually small [50]. For SAVED this results to be a small, yet unstable motion. This means that, after sideslipping, SAVED slowly yet progressively has higher bank angle and smaller turn radius, eventually diverging. This is usually acceptable for manned aircraft, as the divergence is so slow that the pilot can correct it. For this unmanned system, however, this must be accounted for in the control system by means of a correcting rolling with the elevons, as explained in [Subsection 11.4.1](#).

10.4.2. Responses

Having determined the inherent dynamic behaviour of SAVED, this can be represented by showing the responses of the linear system to disturbances coming from either its initial state or control inputs

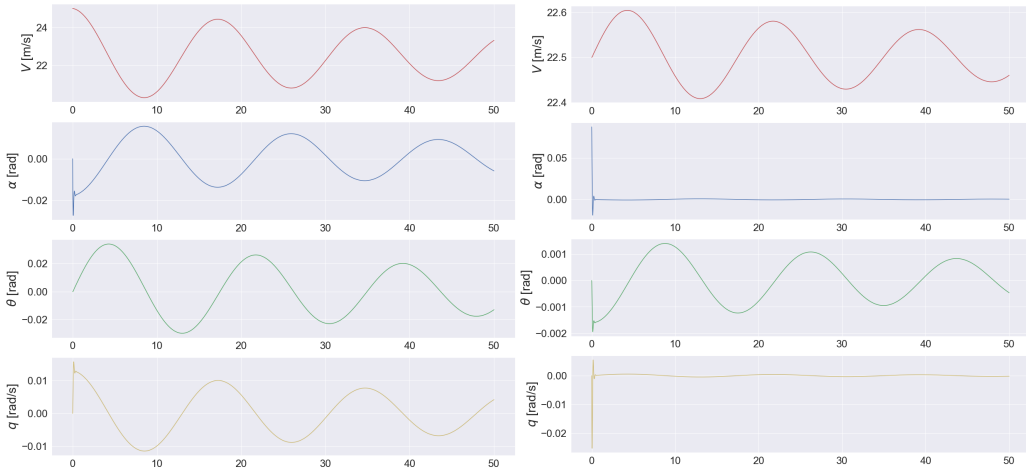


Figure 10.5: Response of symmetric states to a disturbance in airspeed of 2.5m/s

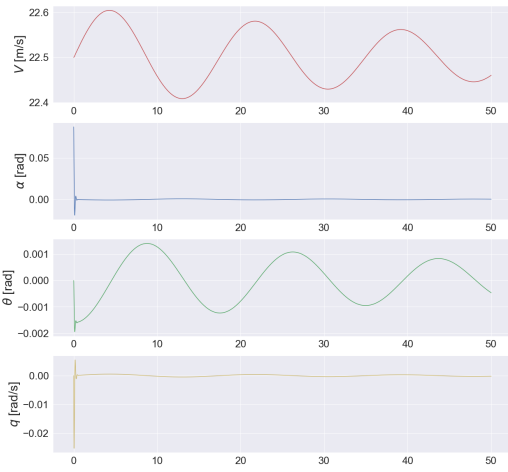


Figure 10.6: Response of symmetric states to a disturbance in α of 5°

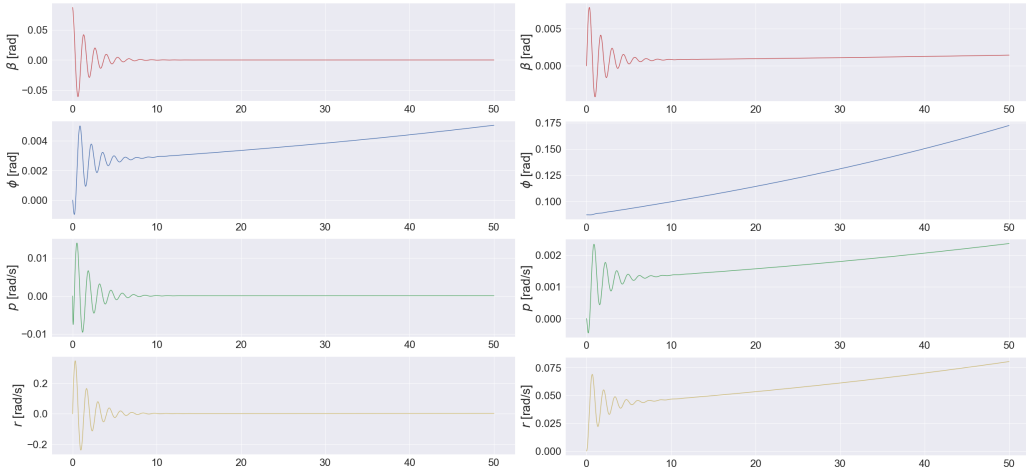


Figure 10.7: Asymmetric response to a disturbance in β of 5°

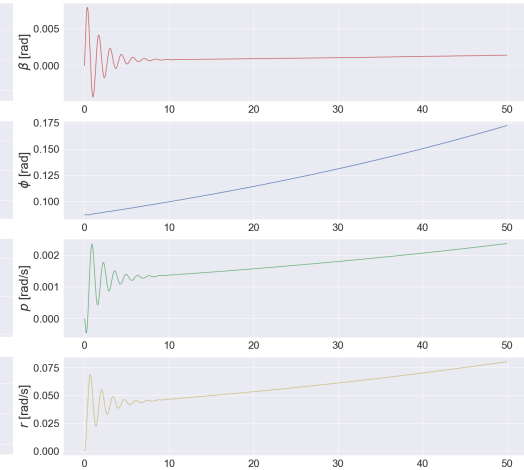


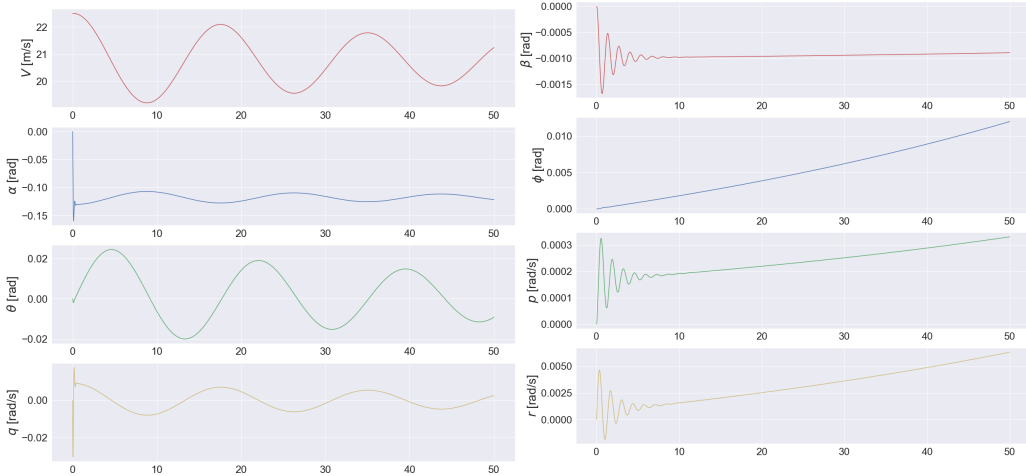
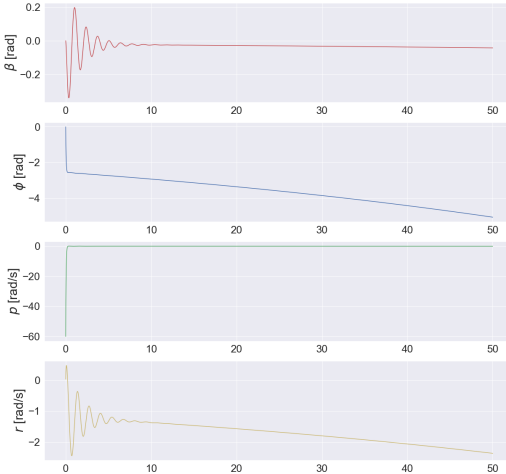
Figure 10.8: Asymmetric response to a disturbance in ϕ of 5°

Disturbances in Initial States

The responses of the states to a disturbance in their initial conditions can for instance be used to model wind gusts and examine the resulting behaviour. For the symmetric case, the responses to the states to a disturbances in V and α are shown as an example in Figure 10.5 and Figure 10.6. The former represents the phugoid motion, a long period oscillation. For the latter, V barely changes due to inertia and the response is highly damped, visible in q in a very short period. All the states are bounded eventually, proving the longitudinal static and dynamic stability of SAVED. For the asymmetric case, the responses to an initial disturbance in β and ϕ are computed. A disturbance of 5° in sideslip and roll angle disturbance are shown in Figure 10.7 and Figure 10.8. In these responses the effect of the unstable spiral can be seen: after the roll is disturbed indirectly as in Figure 10.7, it slowly diverges. This is more prominent in Figure 10.8, where the disturbance is applied directly to the roll angle and it immediately becomes unbounded.

Disturbances in Control Inputs

Analogously, the responses of the states to the control inputs can be computed. For the stability analysis of small disturbances, these inputs are modelled as steps or impulses. Out of all of the possible combinations that could be shown for states, inputs chosen and their type, for brevity is decided to give three examples. Firstly, Figure 10.9 shows how the symmetric states change to a step input in δ_{eI} . This makes sense, as a new (negative) alpha is found to trim SAVED. Alternatively, a step in RPM_1 is seen in the asymmetric states in Figure 10.10. This is also coherent: since the first engine is the leftmost, a step in this input creates a positive yawing moment. The response thus shows negative sideslipping and a positive, progressively increasing, angle and rate of roll and yaw, which represents the unbounded spiral eigenmotion. This behaviour is also congruent with, for instance, the response to an impulse input in the second elevon, as seen in Figure 10.11. By deflecting the right elevon, a negative rolling disturbance is created. This rate returns to zero immediately (as seen by the

Figure 10.9: Symmetric response to a step input in δ_{eI} Figure 10.10: Asymmetric response to a step input in RPM_1 Figure 10.11: Asymmetric response to an impulse in δ_{eII}

negative impulse in p). Nonetheless, combined with the induced sideslip, this creates a negatively increasing roll angle and thus yawing angle r , which essentially represent the spiral motion induced inversely.

10.5. Verification and Validation Procedures

Firstly, in order to verify the correct construction of the numerical model, as derived in [Section 10.3](#), its characteristic modes need to be checked with another model. This consists of the eigenvalue verification and is explained in [Subsection 10.5.1](#). Furthermore, to verify that the stability derivatives, as output from XFLR5, are sensible, another verification procedure is done and explained in [Subsection 10.5.2](#). Other verification and validation techniques, although not applicable at this point of the design, are planned in [Subsection 10.5.3](#).

10.5.1. Eigenvalue Verification

To verify the numerical model used for to analyse SAVED's dynamic stability, the eigenvalues of the state space system are checked. This consists of using an alternative method to extract the eigenvalues analytically. First, this method is explained, to which the eigenvalue comparison follows.

The eigenvalues of the numerical model are extracted numerically from the A matrix. Alternatively, the eigenvalues of the matrix S from [Subsection 10.3.3](#) can be retrieved analytically as established in [50]. As shown in [\(10.20\)](#) and [\(10.21\)](#), the S matrices contain the contributions to the state vector \dot{x} . For the numerical model, the S matrix is split, with the matrices containing the differential operators being then multiplied with the state vector to attain \dot{x} . For the analytical model, however, those differential operators are treated as a variable (λ) to group the values inside matrix S and thus compose the characteristic equation, which is used to obtain the eigenvalues of a matrix analytically. For brevity, the derivation is shown only for the symmetric case.

Table 10.5: Comparison between the eigenvalues as obtained from the numerical and analytical models

Eigenmotion	Numerical Model	Analytical Model
Short period oscillation	$-12.131 \pm 24.686j$	$-12.131 \pm 24.686j$
Phugoid oscillation	$-1.49 \cdot 10^{-2} \pm 0.36j$	$-1.49 \cdot 10^{-2} \pm 0.36j$
A-periodic roll	$-23.306 + 0j$	$-23.306 + 0j$
Dutch roll	$-0.5534 \pm 4.675j$	$-0.5534 \pm 4.675j$
A-periodic spiral	$1.368 \cdot 10^{-2} + 0j$	$1.368 \cdot 10^{-2} + 0j$

To obtain this characteristic equation, the matrix multiplying the state vector (S) is isolated and made homogeneous. Using relations (10.10), D_c is separated between $\frac{\dot{c}}{V}$ and $\frac{d}{dt}$, renaming the latter to λ . By doing so, the homogeneous matrix is thus a collection of numerical data, with some elements multiplying λ , as shown in (10.26). The characteristic equation is thus the determinant, shown in (10.27). The coefficients are computed analytically as shown in (10.28) [50]. The roots λ of the polynomial in (10.27) are then obtained numerically using Python. For the asymmetric case, the same procedure follows analogously by using the S matrix in (10.21) with $D_b = \frac{b}{V} \frac{d}{dt}$, thus using again $\frac{d}{dt}$ as the variable in the polynomial of the characteristic equation.

The eigenvalues of both numerical and analytical models are gathered in Table 10.5. It can be seen that the eigenvalues extracted numerically from the numerical model match perfectly those gathered using the analytical equations in (10.28) for every eigenmotion, verifying the numerical model and the resulting eigenvalues.

$$\begin{bmatrix} C_{X_u} - 2\mu_c \frac{\dot{c}}{V} \lambda & C_{X_\alpha} & C_{Z_0} & 0 \\ C_{Z_u} & C_{Z_\alpha} + (C_{Z_{\dot{\alpha}}} - 2\mu_c) \frac{\dot{c}}{V} \lambda & -C_{X_0} & C_{Z_q} + 2\mu_c \\ 0 & 0 & -\frac{\dot{c}}{V} \lambda & 1 \\ C_{m_u} & C_{m_\alpha} + C_{m_{\dot{\alpha}}} \frac{\dot{c}}{V} \lambda & 0 & C_{m_q} - 2\mu_c K_Y^2 \frac{\dot{c}}{V} \lambda \end{bmatrix} \quad (10.26)$$

$$C_1 \lambda^4 + C_2 \lambda^3 + C_3 \lambda^2 + C_4 \lambda + C_5 = 0 \quad (10.27)$$

$$\begin{aligned} 4\mu_c^2 K_Y^2 (C_{Z_{\dot{\alpha}}} - 2\mu_c) &= C_1 \\ C_{m_{\dot{\alpha}}} 2\mu_c (C_{Z_q} + 2\mu_c) - C_{m_q} 2\mu_c (C_{Z_{\dot{\alpha}}} - 2\mu_c) - 2\mu_c K_Y^2 \{C_{X_u} (C_{Z_{\dot{\alpha}}} - 2\mu_c) - 2\mu_c C_{Z_\alpha}\} &= C_2 \\ C_{m_\alpha} 2\mu_c (C_{Z_q} + 2\mu_c) - C_{m_u} \{2\mu_c C_{X_0} + C_{X_u} (C_{Z_q} + 2\mu_c)\} + \\ C_{m_q} \{C_{X_u} (C_{Z_{\dot{\alpha}}} - 2\mu_c) - 2\mu_c C_{Z_\alpha}\} + 2\mu_c K_Y^2 (C_{X_\alpha} C_{Z_u} - C_{Z_\alpha} C_{X_u}) &= C_3 \\ C_{m_u} \{C_{X_\alpha} (C_{Z_q} + 2\mu_c) - C_{Z_0} (C_{Z_{\dot{\alpha}}} - 2\mu_c)\} - C_{m_\alpha} \{2\mu_c C_{X_0} + C_{X_u} (C_{Z_q} + 2\mu_c)\} + \\ C_{m_\alpha} (C_{X_0} C_{X_u} - C_{Z_0} C_{Z_u}) + C_{m_q} (C_{X_u} C_{Z_\alpha} - C_{Z_u} C_{X_\alpha}) &= C_4 \\ -C_{m_u} (C_{X_0} C_{X_\alpha} + C_{Z_0} C_{Z_\alpha}) + C_{m_\alpha} (C_{X_0} C_{X_u} + C_{Z_0} C_{Z_u}) &= C_5 \end{aligned} \quad (10.28)$$

10.5.2. Stability Derivatives Verification

The stability derivatives as given by XFLR5 are verified and validated in [19] by means of a comparison with AVL and experimental data. Alternatively, they can be verified simply by plotting specific forces or moments with a specific velocity, angle of attack or sideslip, the slopes can be attained and compared with the derivatives as directly given. Yet another, more intuitive way of verifying the derivatives, consists of changing the design in XFLR5 itself and seeing how the derivatives change as predicted. For instance, the derivatives Y_v and N_v are -12.509 and 5.0258, respectively. This is sensible, as it is stating that the force in Y changes negatively with increasing side velocity, yet the yawing moment created is positive. When the vertical tail is removed, however, Y_v and N_v turn $-1.7198 \cdot 10^{-5}$ and 0.028785. This is to be expected, as the side force is negligibly small and the yawing moment is decreased significantly due to the absence of the vertical tail.

10.5.3. Future Verification and Validation Procedures

Having verified the numerical model used, it is ensured that the results attained in Section 10.4 are correctly calculated. This however does not validate the analysis. So as to ascertain the correct correspondence between the model and the reality aimed to describe, a validation model is required. This entails a detailed overview of

the responses of the vehicle to the inputs, which in the given case are unique to SAVED, making it impossible to find a useful validation model. Without a prototype to test and compare flight data, validation procedures of the model are not possible at the current stage. Therefore, as a recommendation for further stability analysis, a flight test for the prototype is to be set up so as to analyse the real responses to the control inputs.

10.6. Conclusions and Recommendations

All in all, SAVED has proven to be a largely stable system when analysed in cruise conditions, both for static and dynamic stability along all axes. First, it is ensured it is entirely statically stable. Following from an extensive analysis during the planform design and a careful system integration, the static margin is proven to allow for sufficient static stability without compromising the controllability, as seen from the bounded responses of the symmetric motions.

When it comes to the dynamic stability analysis, several conclusions are drawn. Firstly, and despite the initial concerns about the vertical surface, sized for landing, it has proven to be enough to ensure passive directional stability. This is ensured by means of the stability derivatives gathered and makes active thrust for directional stability redundant. Moreover, all derivatives considered for good stability properties in [9] are attained as desired. This translates into ensuring not only directional stability, but also a largely stable roll with sideslip and favourable roll damping. Secondly, the eigenvalues of the numerical model show that all eigenmotions except for the aperiodic spiral are stable. This means that SAVED is entirely stable longitudinally but not fully laterally, as it often occurs in conventional aircraft. While this does not pose an issue for manned vehicles, given the long period of time it takes for the motion to become unstable, SAVED is to overcome this with active roll control using the elevons. Since the motion only becomes unbounded for a long period of time, it can definitely be overcome, thus not posing a problem for the mission if active roll control with the elevons is accounted for. Lastly, the behaviour represented by the eigenvalues is shown in the responses as plotted, which asserts the notion that SAVED is largely stable in all axes, despite eventually becoming unbounded due to the spiral eigenmotion, as it occurs after a significant period of time. All in all, despite the small yet expected instability of the aperiodic spiral, eventually diverging the lateral states, it is concluded that SAVED is considered entirely statically and dynamically longitudinally stable, as well as considering it laterally stable with active control of the elevons. Moreover, this asserts its resilience to disturbances such as wind gusts, as required from [30].

As recommendations for further stability analysis for SAVED, the stability during VTOL and transition phases are to be studied. For these, however, two issues arise. Firstly, linearisation is not to provide valid results during these phases, dependant on large angle transitions. Secondly, these phases rely heavily in large magnitudes of control inputs creating large disturbances, diverging away the state from the confidence region of the linearisation. Moreover, the assumption made on no rotating masses is also invalid. For these reasons, further stability analysis is recommended to be integrated with control and studied with a more developed simulation covering all phases. These analysis are to be validated with the aforementioned flight test of the first prototype.

Control System and Simulation

This chapter introduces the approach followed to build the control architecture of SAVED. The ultimate objective of control is to develop a framework for controlling the drone using control inputs optimally such that the state of the drone quickly converges to a reference state. To do so, the forces and moments acting on the drone are first described so that the dynamics of the drone (plant) can be modelled. The process to describe the dynamics of the drone is different in nature from [Chapter 10](#). This is because in stability, the equations of motion have to be linearized so that the dynamics of the drone can be described as a system of first order differential equations and the eigenmotions can be extracted. For control, however, it is more convenient to not linearize the equations of motion, as the dynamics of the drone are non-linear and the non-linear equations of motion therefore represents the dynamics of the drone more accurately. The modelled dynamics therefore replace the dynamics of a real plant, so that the controllers can be designed to determine the optimum control inputs. Such process is described in the following form.

First, [Section 11.1](#) introduces the three reference frames that have been used to describe the forces acting on the drone. Thereafter, [Section 11.2](#) describes the six control inputs of the drone. Next, [Section 11.3](#) describes all the forces acting on the drone in their convenient reference frames. Then, [Section 11.4](#) explains how roll, pitch and yaw control are ensured both during horizontal and vertical flight. Subsequently, [Section 11.5](#) then describes the equations of motions, which describe the dynamics of the drone given the forces and moments acting on the drone. After that, [Section 11.6](#) presents the use of a simulation that models the real dynamics of a the drone so that the controllers can be designed and optimised without the need of building the physical drone. Finally, [Section 11.7](#) describes the control architecture used to achieve altitude and lateral control both in horizontal flight and in vertical flight.

11.1. Reference Frames

In order to describe the forces acting on the drone, it is useful to express these forces on different frames. This section introduces the three reference frames that are useful to describe all the forces acting on the drone; the inertial frame I , the aerodynamic frame A and the body frame B .

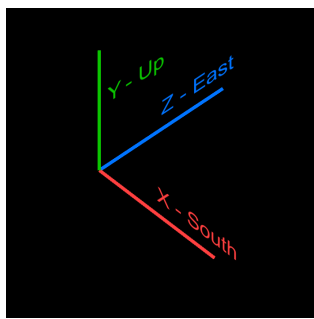


Figure 11.1: Inertial Frame (I)

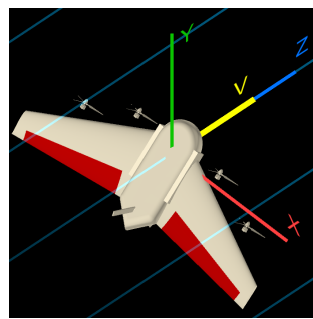


Figure 11.2: Aerodynamic Frame (A)

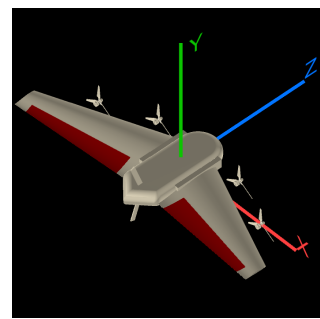


Figure 11.3: Body Frame (B)

Inertial Frame

An inertial frame of reference has the property that when the forces acting upon a body are represented in such frame, the body does not accelerate. In other words, such a body is static or moving at a constant velocity. In an inertial frame, Newton's second law $F = ma$ is always satisfied, making it suitable to express the kinematics of a body. The inertial frame for the simulation has been chosen to be the Earth frame. The Earth is not rigorously an inertial frame of reference. Objects at the surface of the Earth are actually subject to inertial effects due to the rotation of the Earth. However, such effects are negligible for bodies that move at low speeds. The chosen inertial frame of reference I also assumes flat Earth, and is depicted in [Figure 11.1](#), with X_I pointing South, Y_I pointing up (vertical to ground), and Z_I pointing East.

Aerodynamic Frame

The aerodynamic frame A (sometimes also referred as wind frame) is convenient to express aerodynamic forces acting on a body. As depicted in [Figure 11.2](#), the Z_A axis points towards the positive direction of the velocity vector of the drone relative to the air. The Y_A axis is perpendicular to the Z_A axis and in the plane of symmetry of the drone. Finally the X_A axis is perpendicular to both Y_A and Z and follows the direction of a left-hand axis system.

Body Frame

The body frame B is a frame of reference that has its origin and its axes remain fixed relative to the body, meaning that the relative orientation of the inertial frame and body frame indicates the attitude (orientation) of the body. As depicted in [Figure 11.3](#), the X_B axis points towards the right wing, the Z_B axis points towards the nose of the drone and the Y_B axis follows from a left-hand axis.

11.2. Control Inputs

As described in [Subsection 10.3.4](#), there are six control inputs that can be adjusted directly. These are the four propeller rotational speeds ($RPM_1, RPM_2, RPM_3, RPM_4$) and the two elevons deflections ($\delta_{e_1}, \delta_{e_2}$). Both the elevons and the propellers are numbered from left to right along the wingspan direction, making it consistent with the stability analysis in [Chapter 10](#). The outboard propellers rotate inboard up (IU) and the inboard propellers rotate outboard up (OU). The elevon deflections are defined to be positive when rotating down (see [Figure 11.4](#)).

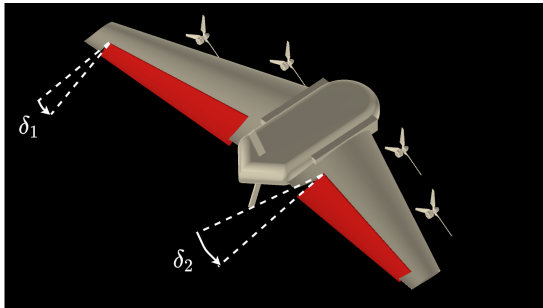


Figure 11.4: Direction of deflection of the elevons

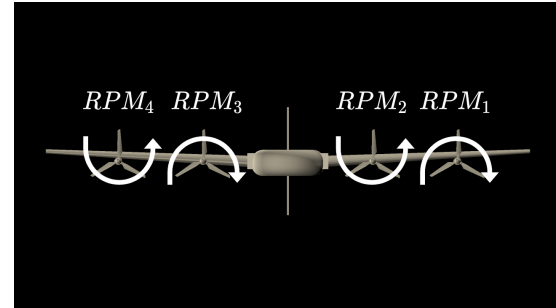


Figure 11.5: Direction of rotation of the propellers (front view)

11.3. Forces

In order to describe the dynamics of a body, it is necessary to describe all the forces acting on the body. In this section, the gravity force is described in [Subsection 11.3.1](#), the propulsion forces are described in [Subsection 11.3.2](#), and the aerodynamic forces are described in [Subsection 11.3.3](#).

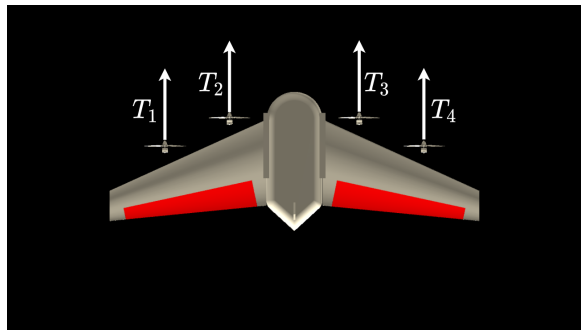


Figure 11.6: Thrust acting on the body frame

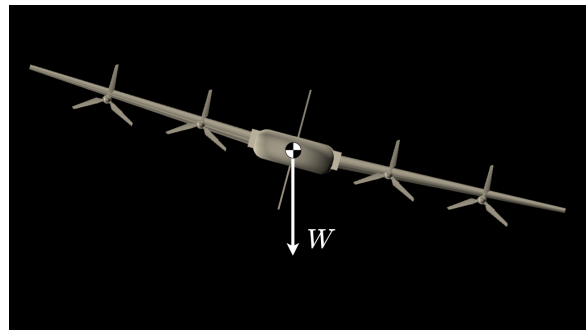


Figure 11.7: Weight acting on the inertial frame

11.3.1. Gravity

As the gravity remains fixed in the inertial frame, as it always points down (see [Figure 11.7](#)), it is convenient to express the gravity in the inertial frame I in the following form:

$$\mathbf{W} = [0, -mg, 0]^T \quad (11.1)$$

Where m is the mass of the drone and g is the gravitational acceleration.

11.3.2. Propulsion Forces

As all four propellers are attached to the body, it is convenient to express the propulsion forces in the body frame B . The propellers are placed pointing on the positive Z_B axis (see Figure 11.6), such that:

$$\mathbf{T}_1^B = [0, 0, T_1]^\top \quad (11.2)$$

Where the thrust is a function of the angular rotation of the propeller so that $T_1(\text{RPM}_1)$ as specified in Subsection 7.3.4. Homologous expressions follow for propellers 2,3 and 4.

11.3.3. Aerodynamic Forces

The difference of pressures generated by the flow of particles around the aerodynamic surfaces causes the drone to experience aerodynamic forces. The main aerodynamic surfaces present in the drone are the main wing, the elevons and the vertical fin. Since the aerodynamic forces depend on the relative velocity of the drone respect to the air, the aerodynamic frame A is ideal to express such forces.

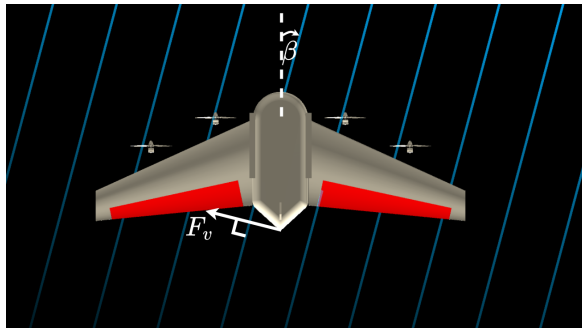


Figure 11.8: Lateral Force acting on the aerodynamic frame

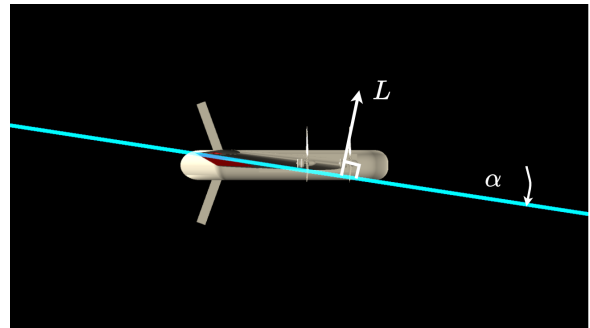


Figure 11.9: Lift Force acting on the aerodynamic frame

Main Wing force

The aerodynamic force generated by the main wing is:

$$\mathbf{F}_w = [0, L_w, -D_w]^\top \quad (11.3)$$

$$L_w = \frac{1}{2} \rho C_L(\alpha) V^2 S \quad (11.4)$$

$$D_w = \frac{1}{2} \rho C_D(\alpha) V^2 S \quad (11.5)$$

Where L_w is the wing lift and D_w is the wing drag. With $C_L = C_{L_0} + C_{L_\alpha} \alpha$ and $C_D = C_{D_0} + K \alpha^2$, the expressions for L_w and D_w are expressed in (11.4), where ρ is the free-stream air density, C_L is the aircraft lift coefficient, V is the airspeed, and S is the wing surface area.

Elevon Forces

The aerodynamic force generated by the left elevon e_1 is:

$$\mathbf{F}_{e_1} = [0, L_{e_1}, -D_{e_1}]^\top \quad (11.6)$$

$$L_{e_1} = \frac{1}{2} \rho C_{L_{e_1}}(\delta_{e_1}) V^2 S \quad (11.7)$$

$$D_{e_1} = \frac{1}{2} \rho C_{D_{e_1}}(\delta_{e_1}) V^2 S \quad (11.8)$$

Where L_{e_1} is the lift generated by the elevon and D_{e_1} drag generated by the elevon. The expression of how the lift and drag coefficients of the elevon vary as a function of the elevon deflection is explained in Subsection 10.3.4. With that, the lift of an elevon follows from (11.7) and (11.8), where δ_{e_1} is the left elevon deflection. Note that S is the surface of the main wing, as $C_{L_{e_1}}(\delta_{e_1})$ and $C_{D_{e_1}}(\delta_{e_1})$ are non-denormalised in XFLR5 [21] using the surface area of the main wing. A homologous force is present for the right elevon e_2 .

During vertical flight, when the airspeed of the drone is negligible, the main aerodynamic forces are induced by the velocity induced by the propellers. The propeller interaction with the aerodynamic surfaces has been analysed in Section 9.3. However, this effect has not yet been quantified in the dynamics of the drone and remains as a task to do in the future.

Vertical Fin Force

The aerodynamic force generated by the vertical fin is:

$$\mathbf{F}_v = [-L_v, 0, -D_v]^\top \quad (11.9)$$

$$L_v = \frac{1}{2} \rho C_{L_v}(\beta) V^2 S \quad (11.10)$$

$$D_v = \frac{1}{2} \rho C_{D_v}(\beta) V^2 S \quad (11.11)$$

Where L_v is the vertical fin lift (lateral force) D_v is the fin drag. With $C_{L_v} = C_{L\beta}\beta$ and $C_{D_v} = C_{Dv_0} + K\beta^2$, the expressions for L_v and D_v are stated in (11.10) and (11.11).

It is important to note that during vertical flight the aerodynamic force generated by the vertical fin will be negligible, since the airspeed is negligible and the vertical fin is placed outside the slipstream of the propellers.

11.4. Control Analysis

In this section, a control analysis is performed to explain how controllability can be ensured in each of the three body axis (roll, pitch and yaw) by guiding the control inputs. Note that the drone has to be controllable both during horizontal flight and vertical flight, where the aerodynamic forces are low due to the low airspeed. Several diagrams are presented to illustrate how roll, pitch and yaw control are ensured. Note that the diagrams shown are not complete free-body diagrams, as they only display the forces relevant to describe the control analysis. Roll control is described in [Subsection 11.4.1](#), pitch control is described in [Subsection 11.4.2](#) and yaw control is described in [Subsection 11.4.3](#).

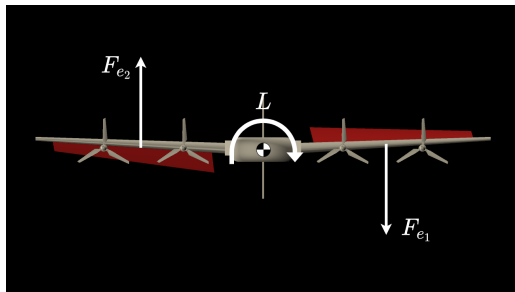


Figure 11.10: Roll control using elevon deflection

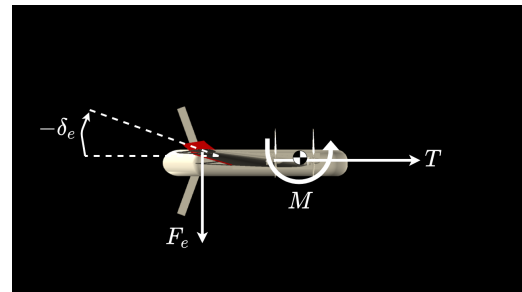


Figure 11.11: Pitch control using elevon deflection

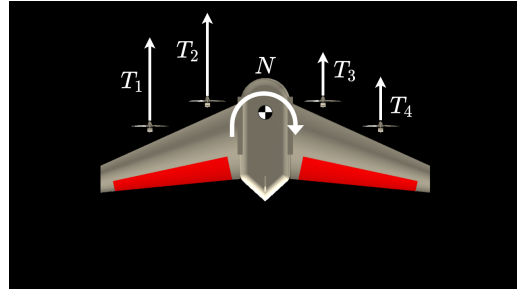


Figure 11.12: Yaw control using differential thrust

11.4.1. Roll Control

Roll was initially proposed to be controlled in two different ways; by elevon deflection and by using the differential torque from the propellers. The rotation configuration of the propellers was initially defined different from [Figure 11.5](#), with the difference that propeller 3 and propeller 4 were rotating in the opposite direction. This propeller direction setting was ideal to decouple roll (from differential torque) from yaw (by differential thrust), thereby allowing to control the roll of the drone during vertical and horizontal flight only with the use of differential torque of the propellers (no need for elevon deflection). However, such configuration was asymmetric in the plane of symmetry of the drone and this resulted in an asymmetric lift profile generated by the induced velocity from the rotation of the propellers, which would result in both structural and control problems. Due to these complications, the rotation configuration of the propellers was redefined to be as depicted in [Figure 11.5](#). With that setting, it is not suitable to roll using the differential torque from the propellers, since that would induce a yawing moment. Therefore, the only available option to roll during both vertical and horizontal flight is the use of the elevons. By deflecting the elevons in opposing directions, a rolling moment is generated, as depicted in [Figure 11.10](#). This is possible both during vertical flight, when the aerodynamic forces come from the induced velocity of the propeller and during horizontal flight, when the aerodynamic forces are generated from the airspeed of the drone. It is important to note that roll control is very important due to make up for the passive

instability of the spiral motion described in [Section 10.6](#).

11.4.2. Pitch Control

Pitch control is also achieved using elevon deflection. The reason why the elevons also perform the function of an elevator is to avoid including a tail structure to place the elevators separately, which would increase weight and drag. Furthermore, in order to achieve pitch and roll control during vertical flight, it is necessary to have such control surfaces in the wing, where they can be placed in the slipstream of the propellers.

The change in lift generated by the deflection of the propellers creates a pitching moment (see [Figure 11.11](#)). In addition to the pitching moment induced by the aerodynamic forces of the elevons, there is an extra contribution to the pitching moment. When elevons are deflected, the c.g of the drone is slightly shifted from the plane of action of the thrust forces, which also creates a pitching moment, as the propellers are no longer aligned with the c.g (see [Figure 11.11](#)). This phenomenon therefore adds to the moment created by the elevons themselves. This is beneficial especially for the transition manoeuvres, when a high pitch rate is desired to transition from vertical flight to horizontal flight and vice-versa.

11.4.3. Yaw Control

Yaw control is achieved using differential thrust, which acts as a replacement for a rudder. Differential thrust is preferred over rudder deflection for several reasons. First, the deflection of the rudder generates induced drag. Moreover, adding rudders would increase the structural weight and the complexity of the control system. But most importantly, the effect of an rudder would be insignificant during vertical flight, as the vertical fin is positioned in the plane of symmetry of the drone, out of the slipstream of any of the propellers. This implies that aerodynamic forces acting on the rudder during vertical flight would be negligible, making it unsuitable for yaw control.

The propeller configuration is such that yawing moments can be generated without producing rolling moments. To do so, the following constraints are defined; the total thrust generated by all four propellers should be kept constant, so that no additional acceleration is generated in the positive X_B direction, resulting in [\(11.12\)](#). Furthermore, in order to prevent rolling moments from being generated, as the two propellers on the right wing are counter-rotating, they should increase in thrust by the same magnitude such that no additional torque is generated, resulting in [\(11.13\)](#). Similarly, for the propellers in the right, [\(11.14\)](#) is defined.

$$\Delta T_1 + \Delta T_2 + \Delta T_3 + \Delta T_4 = 0 \quad (11.12)$$

$$\Delta T_1 = \Delta T_2 \quad (11.13)$$

$$\Delta T_3 = \Delta T_4 \quad (11.14)$$

With such constraints, the relation $\Delta T_1 = \Delta T_2 = -\Delta T_3 = -\Delta T_4$ derives, which implies that the increase of thrust of the propellers on one side of the wing would have to be equal to the decrease of thrust of the propellers on the other side of the wing. With such relation a yawing moment could be generated without the appearance of an undesired rolling moment, which can be generated both during vertical flight and horizontal flight, as the thrust forces are independent of the airspeed. However, it is important to mention that during vertical flight, the thrust generated by the propellers is closer to the maximum thrust they can generate. This implies that the extra amount of thrust the propellers can generate is lower than during horizontal flight, and therefore the yawing moment is also more limited.

11.5. Equations of Motion

Now, after having defined in [Section 11.3](#) all the forces acting on the drone, the differential equations that describe the dynamic behaviour of the drone can be written. As pointed out in [Section 11.1](#), it is convenient to express the second law of newton [\(11.16\)](#) in the inertial frame, as there are no forces that result from the acceleration of a reference frame itself (such as centrifugal or Coriolis forces), and therefore only forces described in [Section 11.3](#) have to be accounted for.

$$\dot{\mathbf{x}} = \mathbf{v} \quad (11.15)$$

$$\dot{\mathbf{v}} = \frac{\mathbf{RF}}{m} \quad (11.16)$$

$$\dot{\mathbf{R}} = \mathbf{R} \times \boldsymbol{\Omega} \quad (11.17)$$

$$\dot{\boldsymbol{\Omega}} = \mathbf{J}^{-1}(\mathbf{M} - \boldsymbol{\Omega} \times \mathbf{J}\boldsymbol{\Omega}) \quad (11.18)$$

Where $\mathbf{x} = [x, y, z]^\top$ represents the position of the drone in the inertial frame, $\mathbf{v} = [v_x, v_y, v_z]^\top$ describes the velocity of the drone in the inertial frame, $\mathbf{F} = [F_x, F_y, F_z]^\top$ represents the sum of all the forces described in [Section 11.3](#) expressed in the body frame. $\mathbf{M} = [M_x, M_y, M_z]^\top$ represents the sum of all the moments (generated from the forces acting on the drone) acting on the centre of gravity of the drone, \mathbf{R} represents the rotation from the body frame to the inertial frame, $\boldsymbol{\Omega}$ describes the angular velocity with respect to the body frame, and \mathbf{J} is the inertia tensor referenced to the body frame.

11.6. Control System Architecture

In order to achieve autonomous control, it is necessary to continuously update the control inputs that influence the dynamics of the drone. The high-level picture of such process is depicted in the block diagram shown in [Figure 11.13](#). The control inputs ($\delta_{e_1}, \delta_{e_2}, RPM_1, RPM_2, RPM_3$ and RPM_4) influence the forces and moments acting on the drone. With that, the drone undergoes a change in state, with $\mathbf{x}, \mathbf{v}, \mathbf{R}$ and $\boldsymbol{\Omega}$ being updated. The new state is then measured and estimated by the state estimation framework described in [Chapter 14](#). With that, the perceived state of the drone is known by the control system and can be compared with a reference state. The difference between the reference state and the perceived state is the error, which is used by the controller to update the control inputs so that the state of the drone gets closer to the reference state.

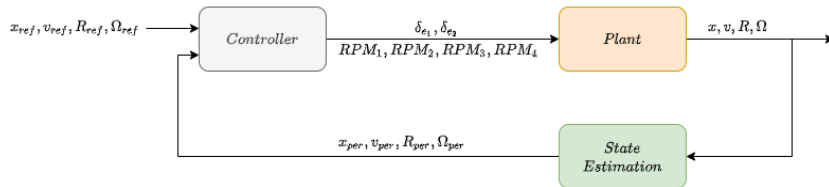


Figure 11.13: Block Diagram of Physical System

The aforementioned process, however, cannot be used to design the controller while designing the drone (which is the primary task of the control system). This is because a physical prototype of the drone is not yet available and therefore there is no existence of a plant that describes the dynamics of the drone. In order to solve this problem, a simulation has been built in Unity¹ that describes the motion of the drone using the modelled forces and moments acting on the drone described in [Section 11.3](#). With that, the equations of motion (11.16) and (11.18), describe how such forces and moments reflect on the linear acceleration $\dot{\mathbf{v}}$ and angular acceleration $\dot{\boldsymbol{\Omega}}$ of the drone. The linear acceleration is then used to update the linear velocity, which is used to update the position of the drone by means of an integration scheme. Similarly, the angular velocity is used to update the angular velocity, which updates the rotation of the drone by means of the forward Euler integration scheme. With that, the new state of the drone ($\mathbf{x}, \mathbf{v}, \mathbf{R}, \boldsymbol{\Omega}$) is known by the control system and can be compared with a reference state. The difference between the reference state and the new state is the error, which again is used by the controller to update the control inputs so that the state of the drone gets closer to the reference state (see [Figure 11.14](#)). It is important to note that in reality, the modelled equations of motion do not describe perfectly the dynamics of the plant, since the forces and moments acting on the drone are not always modelled perfectly (especially aerodynamic forces, which are sometimes stochastic and therefore difficult to model).

The simulation built on Unity has not only served as a tool to optimise the controllers, but it has also been useful to visualise the three dimensional motion of the drone and therefore use it as a visual framework for understanding its dynamics. The simulation has hence allowed us not only to design the controllers but also to optimise the design of the drone. During the design process it was easy to relate an undesired response to a design improvement just by visualising and understanding the simulation. Note that the simulation has not been validated, as a flight test would be needed to validate it. However, by evaluating the visual response of the drone, one can see that the simulation is adherent to a real dynamical system.

11.7. Controller Design

As described in [Section 11.6](#), the controller is in charge of autonomously guiding the control inputs by comparing a reference state with the current state of the drone. The reference state is ideally determined by path planning (described in [Chapter 12](#)). The path planning framework outputs a path that the drone has to follow, and therefore marks the reference position for the drone to be located in. However, given the complicated dynamics of the drone, it is not trivial to directly control the position of the drone, so different control architectures have been designed to control the position of the drone both for vertical flight and horizontal flight. First, [Subsection 11.7.1](#) describes the control architecture to achieve altitude control in horizontal flight. Thereafter, [Subsection 11.7.2](#)

¹<https://bit.ly/316AlwW> [Cited on 22-06-2020]

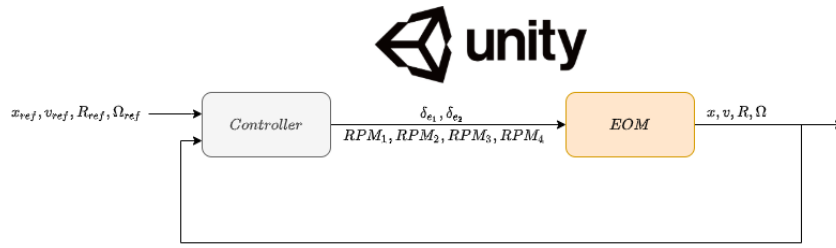


Figure 11.14: Block Diagram of Modelled System

describes the control architecture to achieve lateral control in horizontal flight. Then [Subsection 11.7.3](#) describes the control architecture to achieve altitude control in vertical flight. Finally, [Subsection 11.7.4](#) describes the architecture to achieve lateral control in vertical flight.

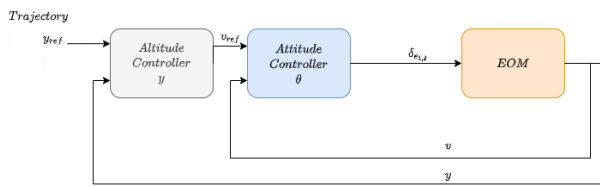


Figure 11.15: Block Diagram of altitude control in horizontal flight

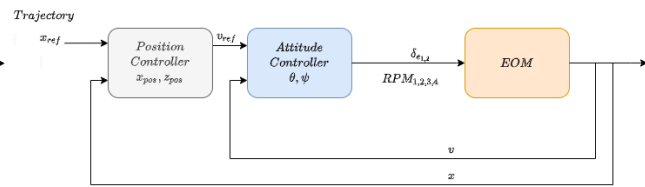


Figure 11.16: Block Diagram of lateral control in horizontal flight

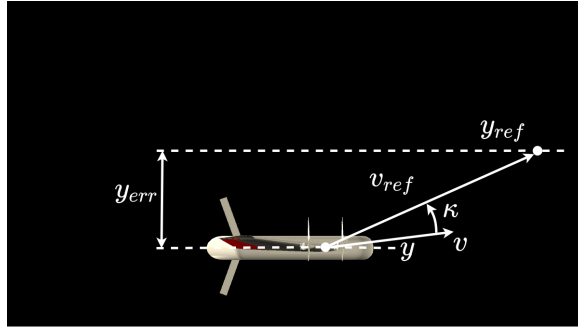


Figure 11.17: Altitude control in horizontal flight

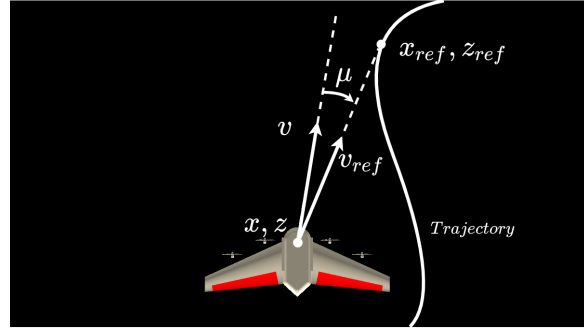


Figure 11.18: Lateral position control in horizontal flight

11.7.1. Altitude Control for Horizontal Flight

In order to control the Y_I coordinate imposed by the path planning, the drone has to vary the altitude by deflecting the elevons. On the first attempt, the deflection of the elevons was dictated directly by a unique PID controller that had as inputs y and y_{ref} (see [Figure 11.17](#)). With that, it was very difficult to tune the gains of the PID controller to achieve altitude control. This is because the elevons have only a direct influence on the pitching moment, which on the long term has an influence on the pitch of the drone, which on the long term has an influence on the altitude on the drone. As one can imagine relation between $\delta_{e1,e2}$ and the altitude is not a trivial one and a single control loop is not ideal. In order to ease the altitude control, a different approach is followed.

The idea behind this approach is that the altitude controller dictates the reference velocity direction v_{ref} of the drone by directly comparing y_{ref} and y . The attitude PID controller then determines the deflection of the elevons $\delta_{e1,2}$ by comparing the v_{ref} and the current velocity direction v (see [Figure 11.15](#)).

More in detail, the position controller simply compares y and y_{ref} and establishes a desired velocity direction v_{ref} (see [Figure 11.17](#)). v_{ref} is then compared in an inner loop (the attitude controller) with the current velocity direction v , and the angle κ between v_{ref} and v (see [Figure 11.17](#)) is taken as the input for the PID controller in the attitude controller. This approach has resulted in much better responses, since κ is much closer to what the elevon deflections have control over.

This controller architecture has been tested in the simulation on Unity and has resulted in a notable response of the drone for altitude control. The drone quickly converges towards the reference altitude and after that the drone remains trimmed. Furthermore, the elevon deflection is very close to zero, which results in a very low trim drag, as it was designed for in [Chapter 6](#).

11.7.2. Lateral Control for Horizontal Flight

In order to control the X_I and Z_I coordinates imposed by the path planning, the drone has to make lateral turns by using a combination of elevon deflection (to bank) and differential thrust (to yaw). Similarly to [Subsection 11.7.1](#), it is not trivial to determine the control inputs by directly comparing a reference position with a current position, so the architecture described in [Figure 11.18](#) is chosen for lateral control.

The approach followed is analogous to the one described in [Figure 11.17](#). The position controller simply compares x, z with x_{ref}, z_{ref} and establishes a desired velocity direction vector v_{ref} (see [Figure 11.18](#)). v_{ref} is then compared in an inner loop (the attitude controller) with the current velocity direction vector v , and the angle μ between v_{ref} and v (see [Figure 11.18](#)) is taken as the input for the PID controller in the attitude controller.

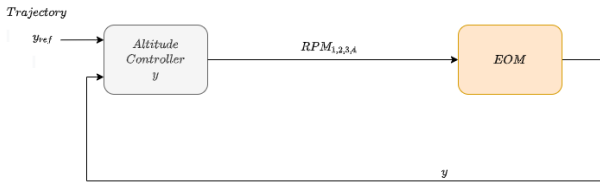


Figure 11.19: Block Diagram of altitude control in vertical flight

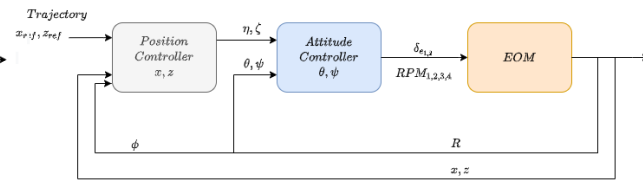


Figure 11.20: Block Diagram of lateral control in vertical flight

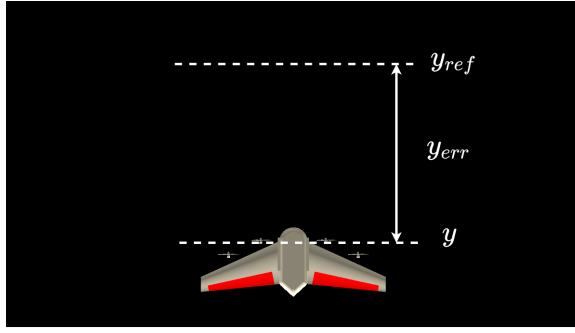


Figure 11.21: Altitude control in vertical flight

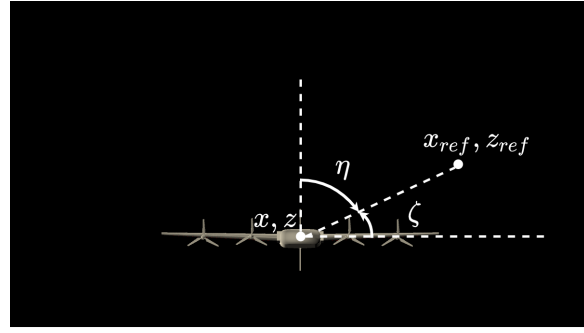


Figure 11.22: Lateral position control in vertical flight

11.7.3. Altitude Control for Vertical Flight

During vertical flight, it is crucial that the position of the drone can be controlled, as it has to avoid obstacles of known positions and it has to land on an exact position given by the perception framework (see [Chapter 13](#)). Similarly to horizontal flight, it is the case that altitude control can be decoupled from lateral control, altitude control being the control of Y_I coordinate and lateral control being control of X_I, Z_I coordinates.

In order to follow the Y_I coordinate imposed by the reference path, the drone adjusts $RPM_{1,2,3,4}$, which have an influence on the thrust generated by the propellers. This generates a vertical acceleration, which on the long term impacts the drone's altitude. With that, there exists a relatively straightforward relation between $RPM_{1,2,3,4}$ and the altitude. In order to dictate the necessary $RPM_{1,2,3,4}$ to achieve the reference altitude, y_{ref} is compared to y to obtain y_{err} (see [Figure 11.21](#)) in the altitude controller. This error is then the input for the PID controller that controls $RPM_{1,2,3,4}$ so that y gets closer to y_{ref} (see [Figure 11.19](#)).

11.7.4. Lateral Control for Vertical Flight

To control the drone laterally (X_I and Y_I), a combination of differential thrust and elevon deflections is needed. The differential thrust is used to yaw the drone to achieve motion in the spanwise direction, and the elevon deflections are used to pitch the drone to achieve motion in the spanwise direction of the vertical fins. Similarly to [Subsection 11.7.2](#), the relation between the control inputs and the reference position is not trivial and therefore there is a need for a position controller and a separate attitude controller (see [Figure 11.20](#)).

The approach followed is similar to the one described in [Figure 11.18](#). The position controller compares x, z with x_{ref}, z_{ref} and with the information on the drone roll angle, outputs ζ and η (see [Figure 11.18](#)). ζ and η give a sense on what ψ and θ should be so that it points towards x_{ref}, z_{ref} . ζ and η are then compared with the current θ and ψ to have a reference on how much the pitch or yaw should change. The result of $\zeta-\theta$ and $\eta-\psi$ is then scaled up by the distance to the reference position x_{ref}, z_{ref} so that the inputs are not very large when the drone is already nearby the reference position. With that, these results are passed as the error to the attitude PID controller, which determines what are the necessary control inputs to get closer to the reference position.

Path Planning

Path planning is the task of finding an optimal continuous path that connects the drone with a specified target. Optimal paths not only consist of short paths, but also paths that improve the mission characteristics, such as paths that avoid known obstacles, navigate in advantageous weather conditions, avoid no-fly areas and reduce the generation of noise nearby highly populated areas. In order to integrate all the above characteristics, the path planning framework has to contain an environment where static obstacles, weather forecast, no-fly zones and population density maps are modelled. Such model is described in [Section 12.1](#). Then [Section 12.2](#) describes the basics of the path planning algorithm and finally [Section 12.3](#) describes how does the framework constantly replan the path.

12.1. Cost Map

In order to determine a path that avoids the areas that are not optimal or even prohibited to fly over, the path planning framework has to include an environment with data from real-time weather forecast, population density maps, no-fly zones and static obstacles. When the characteristics of this data are retrieved, a cost map can be modelled. A cost map represents how expensive it is for the drone to be located at a certain position. Areas inside static obstacles or no-fly zones should be subject infinite costs (see [Figure 12.1](#) and [Figure 12.3](#)), since by no means the path should overlap with those. Moreover, highly populated areas or areas with unfavourable weather conditions should also have high costs (see [Figure 12.2](#) and [Figure 12.4](#)), as it would be preferable to obtain a path that goes over underpopulated areas and favourable weather conditions.

In order to integrate the influence of all the aforementioned models in the path planning framework, the cost maps are superimposed such that a combined cost map is determined. The combined cost map therefore provides a complete representation of the expensiveness for the drone to be located in an area. With that, the task of the path planning simplifies to search for the path that minimises the overlap between the path and the expensive areas of the cost map.

12.2. Optimal Path Determination

The resolution of the optimal path determination has been based on the A* algorithm ¹. A* is an algorithm that determines the optimal solution by maintaining a tree of paths originating at the start node and extend those paths one edge after each iteration until the target node is found. A* uses graph theory to find a path between two vertices (A and B) in a graph such that the sum of the weights of its constituent edges is minimised.

If the weights of the edges of the graph is set to the distance between the two vertices that the edge is connecting (V_1 and V_2), then the solution of such algorithms is the shortest path connecting its two vertices. However, the weight of the edges can be arbitrarily defined to minimise other parameters than the distance. If the weight of the edges is set to the average of the cost of its two vertices times the distance between its two vertices:

¹<https://bit.ly/3eIEvPf> [Cited on 22-06-2020]

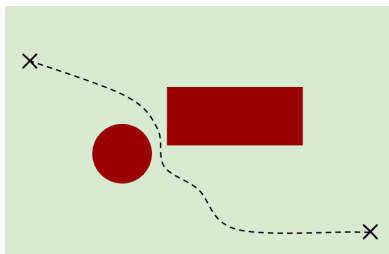


Figure 12.1: Static obstacles modeled in cost map

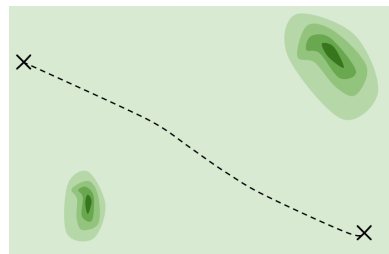


Figure 12.2: Weather forecast modeled in cost map

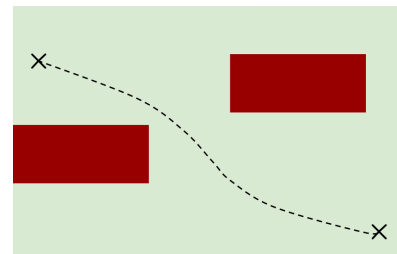


Figure 12.3: No-fly areas modeled in cost map

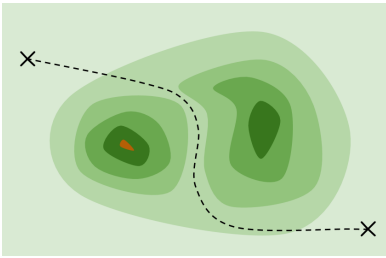


Figure 12.4: Population density modeled in cost map

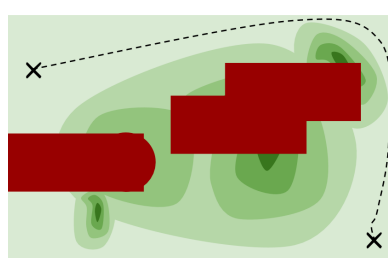


Figure 12.5: Cost map model

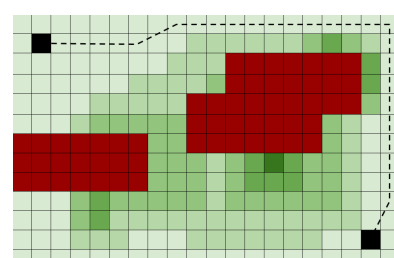


Figure 12.6: Discretized cost map

$$weight_{edge} = \frac{cost_{v_1} + cost_{v_2}}{2} length_{edge} \quad (12.1)$$

Then, the solution of the algorithm is a path that connects A such that the overlap between the path and the cost map is minimised (if the vertices cost are set according to the cost map).

It is therefore required to transform the cost map into a graph with vertices and edges. To do that, the combined cost map (Figure 12.5) is discretised into a matrix (see Figure 12.6). Then, each cell on the matrix consists of one vertex, and the edges of the graph are connecting cells with their neighbour cells. Therefore, the cost of a vertex its the cost of the cell on the discretized form of the cost map, and the cost of any edge is the average of the cost of its two vertices times the distance between its two vertices.

12.3. Real-Time Replanning and Optimisation

During flight, the drone might not always follow the reference path with a high accuracy. One reason for that is that the response of the drone might be subjected to delay. Another reason for that is that the state estimation framework might be measuring the incorrect state of the drone. Moreover, some points of the path planning might be unfeasible for the drone to reach given the controllability limitations. It is for these reasons that the drone is constantly navigating on a different position than the one imposed by the path planning. In most cases, instead of commanding the drone to go back to the reference way-point of the path, it is preferred to recalculate a path from the new position of the drone, so that the drone does not have to go back to the previous given path. In that scenario, path replanning would have to occur.

Other scenarios in which replanning would be needed would be when the weather forecast model is updated, or when the position of obstacles changes. It is for that reason, that path replanning has to occur constantly. Every time the path is replanned, the cost map is remodelled with the new costs from the dynamic characteristics of the environment (weather forecast, moving obstacles, etc) so that the cost of all nodes is recomputed. With that, the A* algorithm runs again and the path is recomputed.

In order to ensure that the drone always has a path that connects it to the target, the replanning has to occur as fast as possible. For that reason, the replanning framework includes the feature to use multiprocessing and multi-threading, so that different tasks of the A* algorithm can run in parallel and the solution can be reached faster. In order to speed up the process, another optimisation is done. The most time-consuming task of the algorithm on each iteration (expansion of node) is to look for the node with minimum cost, which happens in linear time $O(n)$ (more nodes implies more checks to find the node with minimum score). However, if a heap structure is maintained during the execution of the algorithm that store the score of the nodes, the node with minimum score can be retrieved in logarithmic time complexity $O(\log n)$, which drastically improves the run-time of the algorithm.

A simulation has been built on Unity that includes the model of the cost map and resolves the optimal path using the A* algorithm. The code of the simulation has been presented as open-source code in <https://github.com/SAVED-DSE-Project-TU-Delft-2020/PathPlanningSimulation>, where animations of the expansion of the A* algorithm and the real-time replanning results are also presented. Note that there is no need to write verification and validation code for the path planning framework. This is because the path planning simulation can be validated visually, as one can observe how the framework constantly finds the most cost-effective path.

Perception Pipeline Design and Analysis

The set of sensors and algorithms that substitute pilot's eyes and retrieve visual information from the environment are part of the perception pipeline. A good design of this infrastructure can be achieved by considering the cases during the mission where general sensing of the objects in proximity is required. Looking at [Figure 13.1](#) it is expected that during a nominal SAVED mission two cases will require intervention from the perception system.

Firstly, the drone is expected to monitor its front path to assert the absence of unpredictable obstacles that can result in a catastrophic crash. Ideally this should never be the case, as the path pre-computed at ground considers a wide number of variables in order to deliver an optimal and safe path. However, dynamic obstacles (such as a kid's balloon or a flock of birds) are sure to be missed, therefore preventive measures must be taken.

Secondly, once the drone reaches the landing area, is expected to quickly recognise the landing point and initiate the landing manoeuvre towards it. The two cases considered can then be reformulated as the two main perception subsystem requirements:

- **SAVED-CUST-COST-OPS-AFL-02:** The drone shall be able to detect unexpected obstacles on the flight path to avoid catastrophic crash
- **SAVED-CUST-COST-OPS-AFL-03:** The drone shall be able to detect the landing point while in flight

The following chapter will firstly perform an investigation on the obstacle detection issue, in [Section 13.1](#), to then proceed towards the topic of landing point detection, in [Section 13.2](#). Both assessments output a set of sensors and software packages able to perform the whole spectrum of perception tasks just exposed.

13.1. Design for Obstacle Detection

During flight, both in nominal or emergency state, the drone can encounter unexpected obstacles. Collision with one of these might lead to catastrophic crash. As a safety measure, the drone is expected to move to vertical position and stop (this allows to cope with the additional latency required for the path recomputing); this will allow for path re-planning calculation based on the detected obstacle. In order to stop before crash, the vehicle needs to process the detection well in advance. This is mainly dependent on three sensor features: lookahead distance (d), depth error (e_{depth}) and field of view (FOV). These should be such that in every instant during flight the detection sensor is capable to provide information with enough advance.

The section therefore finds the best sensor for this particular task by studying two limit scenarios that the vehicle is expected to encounter ([Subsection 13.1.1](#)) and conducting an assessment on several perception sensors on the market ([Subsection 13.1.2](#)).

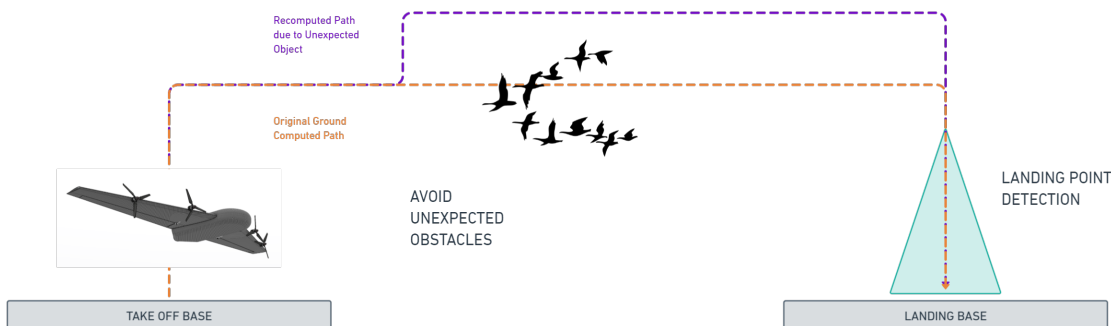


Figure 13.1: Events during SAVED mission that will require vision-based information retrieval

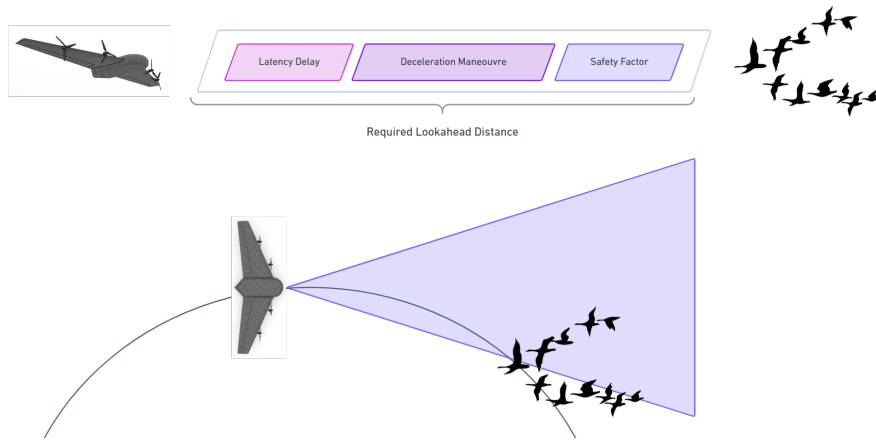


Figure 13.2: Limit scenarios for obstacle detection

13.1.1. Limit Cases Identification

The sensor design choice is then possible by considering two limit scenarios that the drone might encounter during operation. The first case sees the drone travelling at maximum velocity (V_{max}) on a straight line, while the second case sees the drone performing its steepest turn of radius (r_{min}) at the maximum allowable velocity ($V_{maxturn}$) for that manoeuvre (see Figure 13.2). The straight line case sets the boundaries for d , while steep turn case will impact the choice for FOV .

The interested parameters depend on the performance and controllability of the drone, as showed in (13.1) and (13.2) ($t_{latency}$ is the time required for the drone to process the detection, a_{avg} is the average deceleration of the drone, r_{min} is the minimum turning radius and SF is a safety margin).

$$d = \left(V_{max} t_{latency} + \frac{V_{max}^2}{2a_{avg}} \right) SF \quad (13.1)$$

$$FOV = \left(V_{max} t_{latency} + \frac{V_{max}^2}{2 * a_{avg}} \right) \frac{SF}{r_{min}} \quad (13.2)$$

13.1.2. Sensor Selection

At this stage, there is not enough flight performance information available to set a lower constraint for d and FOV . In order to tackle this lack of information, an assessment on the spectrum of perception sensors offered by the market is conducted. The assessment consists in a trade-off based on d , FOV , weight and cost. The most optimal outcome is expected to define an affordable upper limit for the performance of the drone.

In general, two main type of sensors are selected for perception tasks: LiDAR and cameras. If cameras are set up as stereo pair, both of them are capable of perceive depth. However, these present different advantages and drawbacks. Overall LiDAR excels at long distances, where stereo cameras perform poorly [56], as their depth error increases quadratically with distance¹ (see (13.3)) and the stereo matching algorithm introduces additional latency. Moreover LiDAR sensors allow on average for an higher FOV with respect to cameras, which makes them superior for this precise task. LiDAR systems are in general more expensive than stereo cameras and they weight more. However, due to the high demand and the huge investments made recently in the technology², new low weight and low cost solutions have been recently released, such as the Velabit™ (see Table 13.1) from Velodyne³.

This stream of innovation makes nowadays this sensor as the most suitable one for this kind of tasks, as showed in Figure 13.3. The sensor is mounted on the front on the drone, it will cover 100m with 60° of field of view, allowing for safe operation on the predicted path.

13.2. Design for Landing Point Detection

Designing for landing point recognition requires perception capabilities that differ greatly from the ones proposed in Subsection 13.1.2: while obstacle detection deals with avoiding unknown objects, landing point detection

¹<https://bit.ly/2B2eL1G> [Cited on 16-05-2020]

²<https://bit.ly/3cZcDVK> [Cited on 11-06-2020]

³<https://bit.ly/3cVZeNU> [Cited on 11-06-2020]

Table 13.1: LiDAR sensor Velabit™ specifications

Velabit™ Specifications				
	Cost	100	\$	
	FOV Horizontal	60	deg	
	FOV Vertical	10	deg	
	Lookahead	100	m	
	Weight	<0.4	kg	

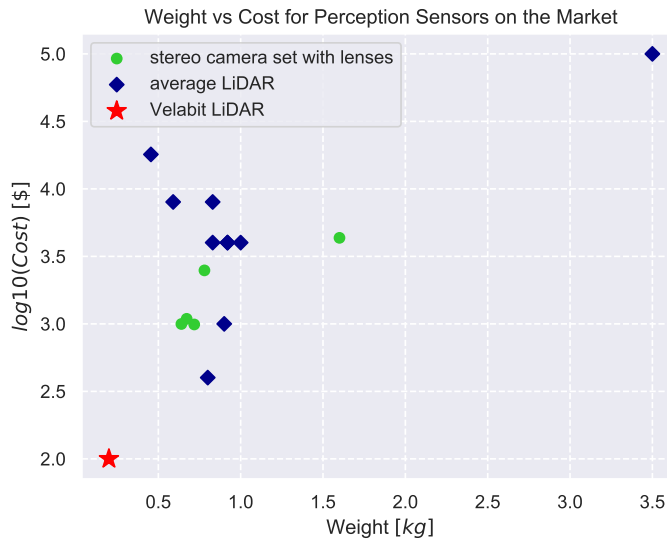


Figure 13.3: Comparison in cost and weight for Velabit™ with respect to stereo camera and other commercial LiDAR sensors

uses previous knowledge to detect the known object (i.e. the landing point) and move towards it. Without having information on how the final target looks like, the drone would not be able to locate it in space.

The pipeline required therefore needs to be "trained" to visually recognise the landing sign and locate it in space. This capability can only be achieved with the adoption of machine learning algorithms. Even though machine learning methods are being implemented on LiDAR sensors [45], detection of patterns on flat surfaces, such as an heliport, is still in larval state. On the other hand, plenty of robust detection algorithms for stereo camera sensors are available and sufficiently tested [60], which makes them currently the only possible choice. In addition to this cost and weight are expected to be less for stereo cameras (as pointed out in Subsection 13.1.2), adding few more points to the list of advantages.

The section presents a full hardware and software design capable of locating the target in a 3D space. Firstly, an assessment is conducted in Subsection 13.2.1 on the recognition task. Secondly, in Subsection 13.2.2, a setup for depth estimation is proposed and validated.

13.2.1. Object Detection Software: YOLOv3

Detection of the landing point, as already mentioned, requires previous knowledge about what needs to be detected. For this reason, methods used for such a task fall under the class of machine-learning and deep-learning algorithms. The current state-of-the-art object detection algorithm consists in a deep-leaning network named YOLO [59] [60] (You Only Look Once): as the name suggests, YOLO performs a detection with only one evaluation, making it exceptionally faster than other object detection software, such as R-CNN, Deep MultiBox and Overfeat.

Infrastructure Setup

For this report, YOLO has been implemented in a ROS⁴ framework, as it makes it easily deployable on the future drone's hardware. Together with the main algorithm, classification and training packages have been embedded. The infrastructure allows easy labelling and use of common .mp4 videos and .png images.

⁴<https://bit.ly/3cWGkqn> [Cited on 12-06-2020]

The object detection software has been trained to detect only one object, the landing point. To enforce the accuracy of detection, a customised landing point has been designed, as shown in [Figure 13.4](#). Due to the limited amount of time, 100 labelled landing point images were selected for training (nominal batches count up to 40000 images).

It should be mentioned that for the tests conducted during the realisation of this report run on an algorithm trained on images all in optimal conditions. It might happen in reality, however, that the landing sign might get corrupted by dirt or scratches. It might also be the case that heavy rainfall changes the appearance of this pad and therefore lead to unexpected outcomes. This can be solved by collecting a batch of landing sign images including also cases of heavy rainfall, dirt and light settings. The more variety of images is fed to the network, the more robust the detection will be.

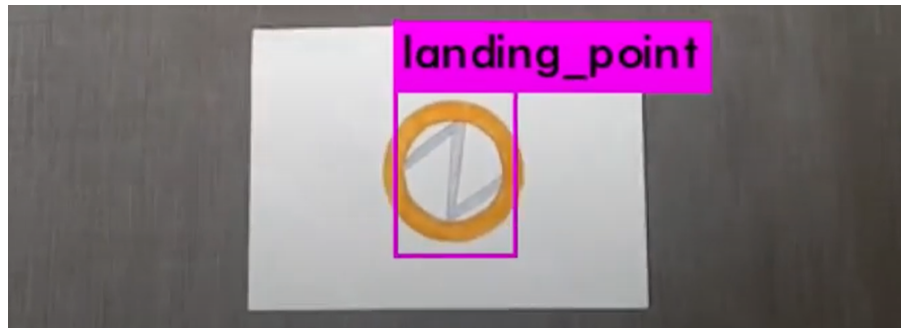


[Figure 13.4: Customised landing point correctly detected by YOLO](#)

Verification & Validation

The validation procedure tests the pipeline with three different video recordings. For the whole duration the landing point target of circular shape and 10cm diameter remains in the frame. The videos replicate three cases, more in detail:

- VIDEO I - “close”: Camera moves close and slowly around the landing point
- VIDEO II - “fast”: Camera moves close and fast around the landing point
- VIDEO III - “distance”: Camera moves away slowly from the landing point up to 5 meters distance

Each video (aspect ratio 16:9) is converted to different resolutions (from 128 to 768 pixel width) and frames per second (10 and 30). Each variant of each video is then run through the pipeline and general indicators of performance are derived. The example for VIDEO II is reported in [Figure 13.5](#) and [Figure 13.6](#).

The first thing that can be noticed by looking at the results is that a decrease in fps does not affect the count of missed detection for the same resolution. This is useful as less fps are beneficial to meet low latency requirements.

Secondly, it is clear from the two upper plots in [Figure 13.5](#) that the detection accuracy is not based on the number of pixels that the object occupies, but what percentage of the image it takes. For this trained algorithm, the limit fraction for detection is 2-3%. This outcome is also beneficial for latency, as high resolution does not seem to increase the accuracy of the tool.

To give a more general view on all the test samples and their performance, overall video accuracy for each version is plotted in [Figure 13.7](#). The plot confirms the low relevance of resolution and fps, but it also highlights the low accuracy when the object is occupies a small portion of the image. This weakness can however be significantly mitigated by training YOLO with a higher number of images at various distances.

Overall, based on the exposed results, the algorithm is expected to perform correctly at 10 fps, 384x216 of resolution and for objects occupying down to 2-3% of the full image. Such constraints define, together with the ones derived in the next section, the choice of hardware for SAVED.

13.2.2. Depth Estimation Software: EdgeStereo

An object detected in an image is not enough information to estimate the 3D location of this one. By looking at an image one can derive its 2D position, lacking the third dimension, which represents depth.

In computer vision, the process involved in depth estimation is referred as stereo-matching⁵: a pair of monocular

⁵<https://bit.ly/30DkMMO> [Cited on 12-06-2020]

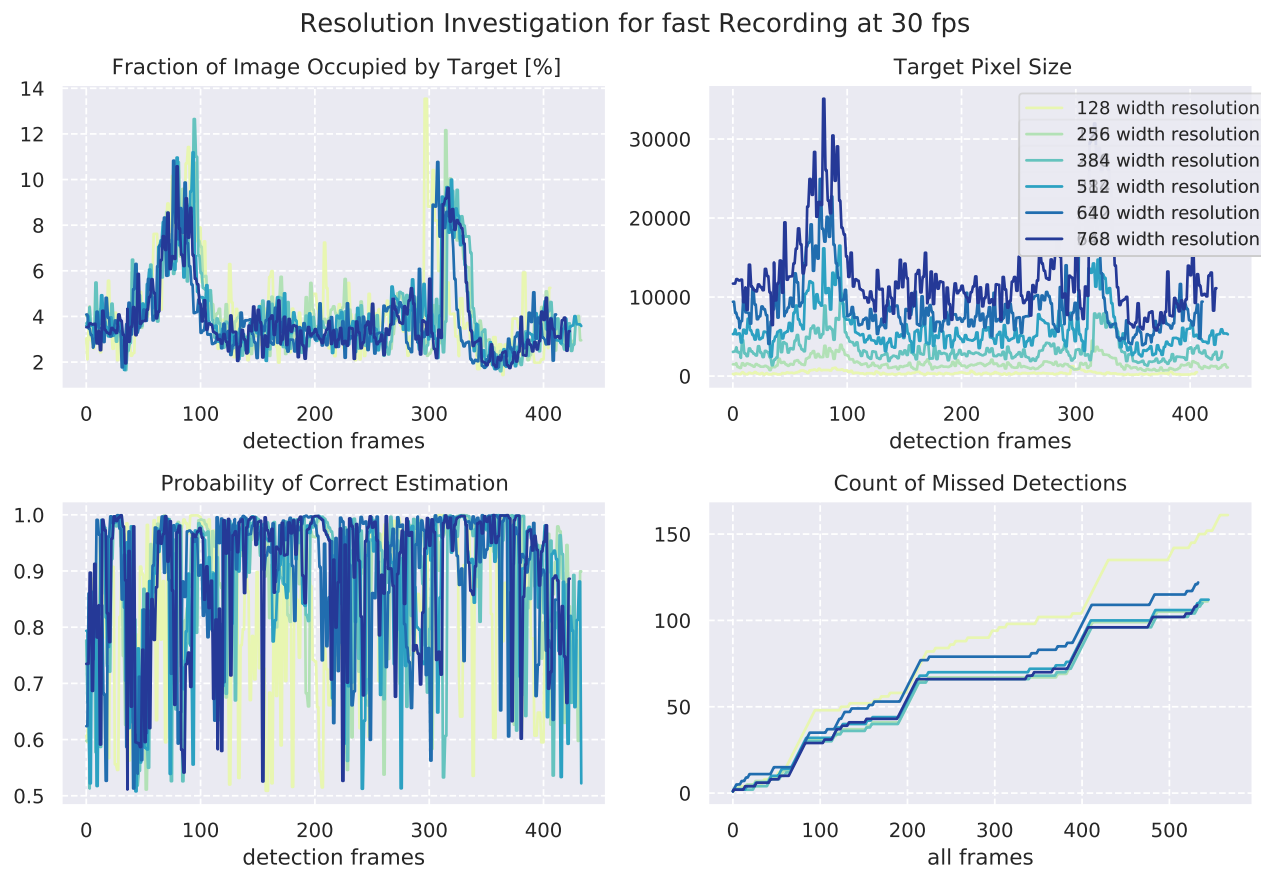


Figure 13.5: Performance of YOLO pipeline on a 30 fps video showing quick movements at a close distance

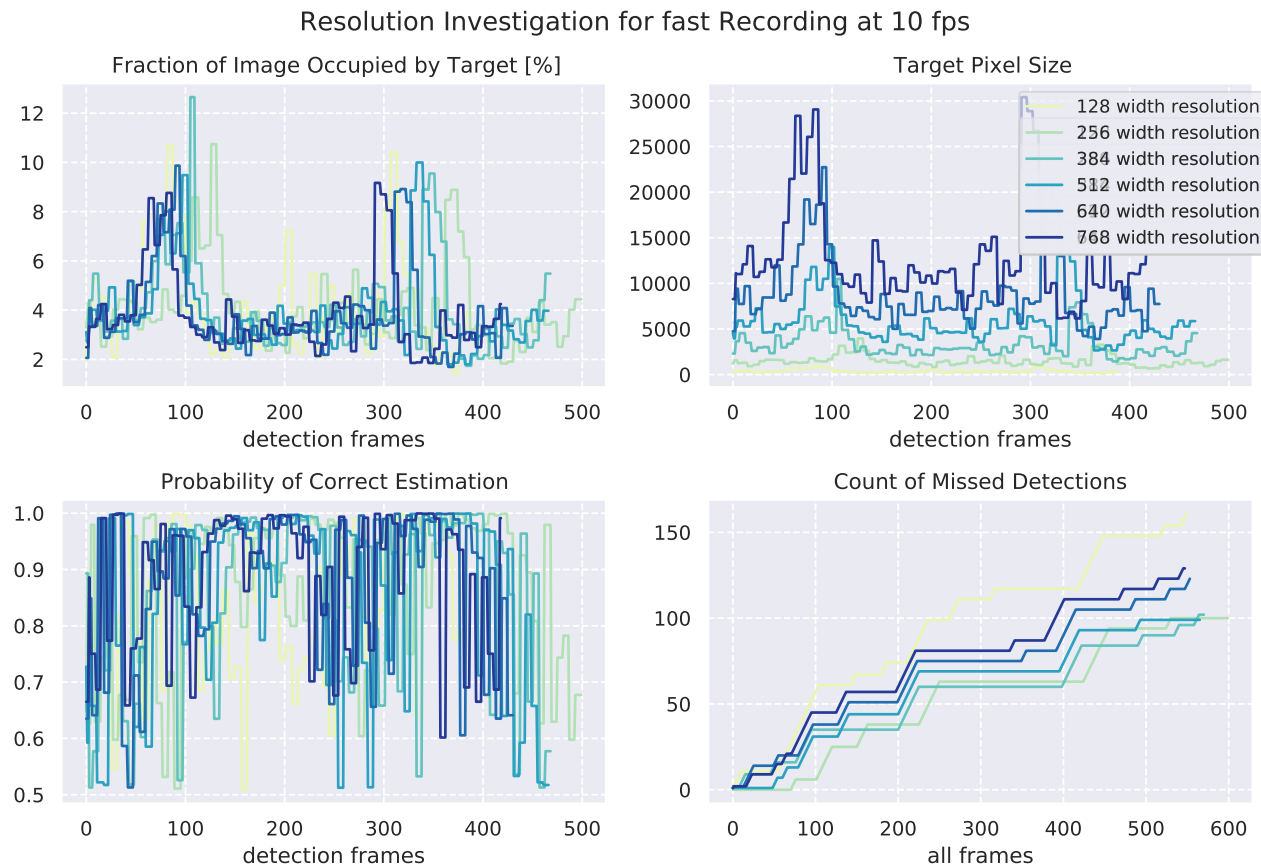


Figure 13.6: Performance of YOLO pipeline on a 10 fps video showing quick movements at a close distance

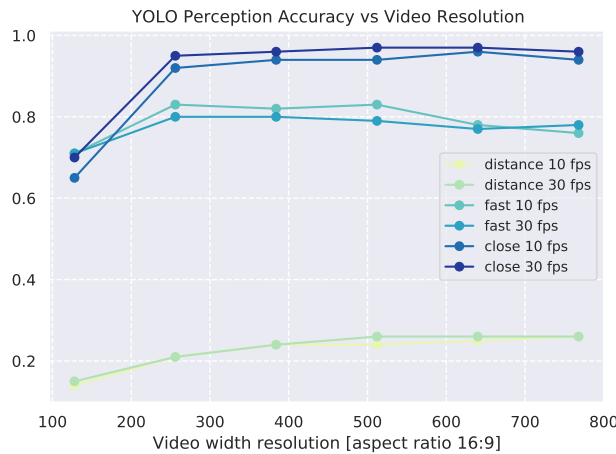


Figure 13.7: Average accuracy of YOLO pipeline on different videos, fps and resolution

cameras use the relative distance between each other and the overlap of their field of view to extrapolate the distance of each common pixel from the stereo pair. The performance of a stereo setup is measured therefore in its depth estimation accuracy and latency. Depth error can be estimated with [Equation 13.3](#), where z is the distance between stereo pair and object, b is the baseline of the stereo pair, f is the focal length of the lenses and ΔD is the RMS disparity error (all variables in m).

$$\Delta z = \frac{z^2}{bf} \Delta D \quad (13.3)$$

Currently, the offer of stereo matching algorithms is broad, as new methods are keep getting discovered to increase the accuracy and reduce the latency. Indeed, depth cannot be estimated perfectly, especially at long distances. In order to facilitate this selection, several ranking pages are currently available to deliver schematic comparisons about the performance of each one of them. The most famous one is the Middlebury⁶ stereo vision page [39]. Among the hundreds of algorithms proposed in the ranking, EdgeStereo [67] stands out for its excellent depth estimation performance (RMS disparity error of 9.84 pixels) and good latency (0.08s per MP).

By looking at [Equation 13.3](#), one can see that good software is however not enough to ensure the correct functioning of the apparatus: stereo camera setup and landing manoeuvre choice is equally influential, reason why it is extensively explored in the following section.

13.2.3. Hardware Setup

The choice of the right set of stereo cameras, lenses and arrangement is far from trivial. A pair of high resolution cameras need a high computing power to be processed, which can increase the weight and cost of the main computer to an unacceptable extent. On the other hand, poor performing cameras might be mechanically unreliable and deliver poor quality imagery, which decreases perception accuracy. In order to select the best setup, a first step can be to set constraints generated by the mission.

⁶<https://bit.ly/2UC8n86> [Cited on 12-06-2020]

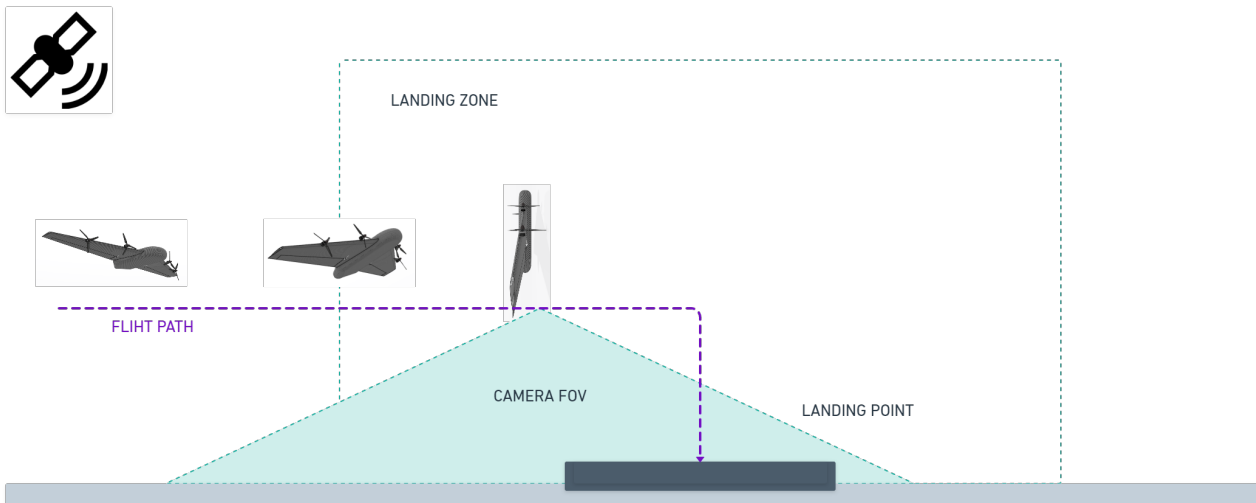


Figure 13.8: Representative sketch of the landing manoeuvre. Once the drone enters the landing zone, indicated by means of GPS, the vehicle rotates to vertical positions and activates cameras for landing point detection

As Figure 13.8 indicates, the drone is provided with a landing zone by means of GPS signal: within this zone, where the landing point is located, the drone is expected to actively look for the target and descend towards it. The area of this zone, given the current GPS accuracy⁷, is expected to have a radius of 5m. Assuming that the sensor is pointing perpendicular to the ground, and considering that it should be able to cover the whole zone at the beginning of the manoeuvre, independently from its orientation, the drone *FOV* shall be able to contain a square of land of 30m edge. Stereo camera baseline design will therefore focus in satisfying the following requirements:

- **SAVED-CUST-COST-OPS-AFL-04:** At the beginning of the landing manoeuvre, cameras field of view shall cover a land area of at least 30 m in width and height.
- **SAVED-CUST-COST-OPS-AFL-05:** At the beginning of the landing manoeuvre, the perception setup shall correctly detect the landing point.

Complying with the above implies a smart selection of cameras and lenses, as well as the stereo baseline (i.e. the distance between two cameras) and altitude of the start of the detection together with the size of the landing pattern. The elevated number of variables makes the seeking for an optimal design challenging, as they are all strongly correlated. In order to give a better understanding of the relationship between variables, a correlation map is presented in Figure 13.9.

Based on the relationships just exposed and Equation 13.3, multiple iterations over the variables have been conducted by considering five machine vision camera models. A combination of design choices that is compliant with all the previously imposed constraints sees the use of the FLIR FireFly DL⁸ Camera, in combination with Edmund Optics Green Series M12 Imaging Lenses⁹ with a baseline of 20cm. The system is also expected to function properly up to 25m (also considering the requirements in Subsection 13.2.1) given a landing point of at least 3m in diameter. The given setup is also such that the depth error typical of stereo cameras is acceptable. As showed in Figure 13.10, the error during decent decreases exponentially and error bars are never big enough to go below the ground. The drone is therefore expected to update the 3D position of the landing point with more accurate indications while descending.

Information retrieved throughout this chapter is summed up schematically in Table 13.2.

⁷<https://bit.ly/30xte09> [Cited on 12-06-2020]

⁸<https://bit.ly/2MOSIOs> [Cited on 12-06-2020]

⁹<https://bit.ly/2AwJ6oV> [Cited on 12-06-2020]

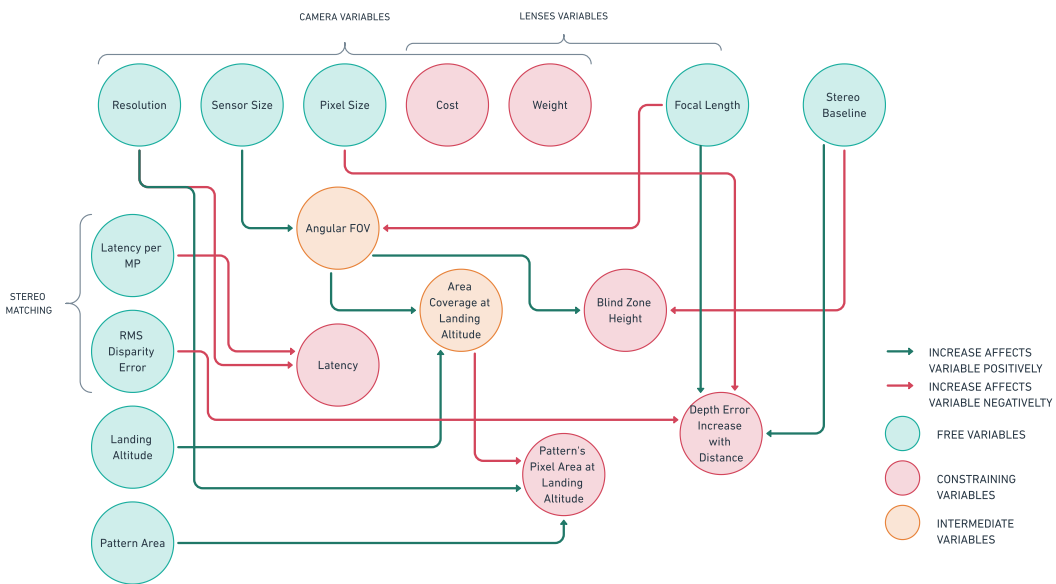


Figure 13.9: Correlation map representing relations between all the variables to be defined for a complete object detection and localisation pipeline

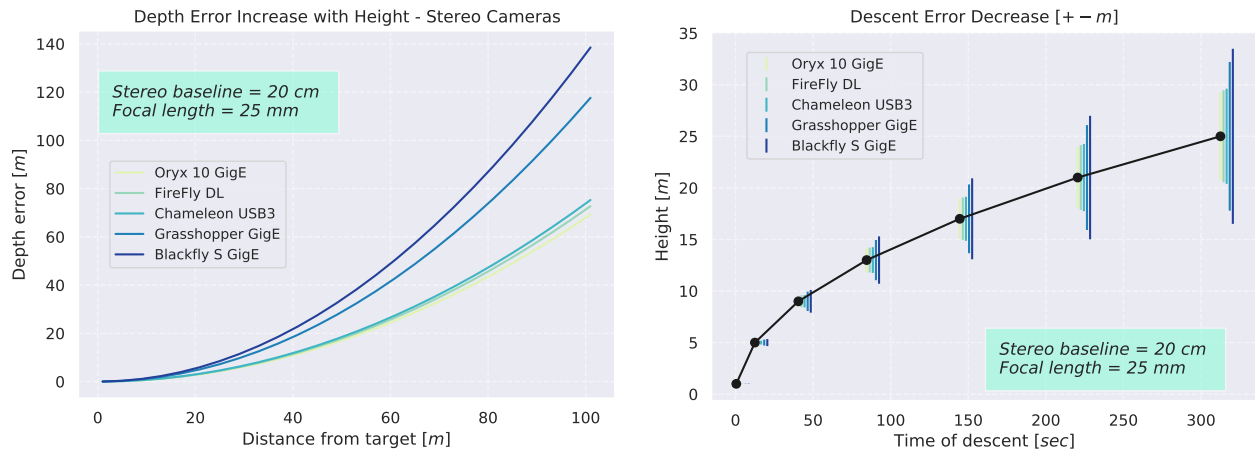


Figure 13.10: Stereo setup depth error performance and error decrease with descent

Table 13.2: Summary of hardware and software selection for object detection and localisation pipeline

Perception System Hardware Setup for Landing Point Detection		
Firefly DL Monocolor		
Max Resolution	1440 x 1080	pixels
Sensor Format	1/2.9"	in
Pixel Size	3.45	μm
Green Series M12		
Mount	S - Mount	-
Focal Length	25	mm
Setup		
Stereo Baseline	20	cm
Landing Height	25	m
Pattern Diameter	3	m
Stereo Matching Algorithm	Edge Stereo	-

State Estimation Design and Analysis

State estimation is the field of an autonomous system that retrieves the necessary information to continuously define the state of the drone which includes: 3D position and orientation in space, 3D linear and angular velocities and 3D linear and angular accelerations. Such information can be obtained with the use and interrelation of several sensors. The choice of which is based on determining trade criteria such as cost, weight and reliability.

This chapter firstly proposes a minimal design for the state estimation infrastructure in [Section 14.1](#) to then reinforce its reliability by means of a risk assessment in [Section 14.2](#) and a redundant sensor and software selection in [Section 14.3](#).

14.1. Baseline Sensor Selection

For the SAVEDs mission, the drone's position and path are expected to be known with respect to the take-off point coordinates. To estimate lateral and longitudinal distances as well as vertical with respect to the reference point, the most logical choice appears to be GPS. Its good accuracy and high reliability is optimal for such long distances. In addition GPS information can be differentiated in time to retrieve the drone's velocity.

For attitude and acceleration estimation, The most adopted solution is the implementation of an Inertial Measurement Unit (IMU), a self-contained system that uses a triad of gyroscopes and a triad of accelerometers.

Even if the two instruments above can provide all the necessary information to fully estimate the state of the system, the current setup is not enough for a safe, robust and accurate pipeline. This is due to several factors, such as: unreliability of the system and its average measurement error. To understand the influence of these factors for the proposed setup, a tailored risk assessment has to be conducted, as shown in the next section.

14.2. Risk Hazard Identification and Mitigation

As most aerial vehicles, the drone designed needs to be safe and reliable during flight, in other words, it needs to consistently follow the pre-determined path without excessive divergence. The capability of estimating its full state during flight can have significant impact on the safety of an autonomous drone: as no human being is monitoring it, the vehicle shall be ready to cope autonomously with the most frequent or dangerous hazards that might occur during operation.

Hazard identification is therefore a necessary step to account for in the design process, as its mitigation defines the amount of additional sensors, software and models to add for a final safe design. The following subsections investigate the weak points of the minimal design proposed in [Section 14.1](#) and explore solutions to bring the system to an acceptable level of reliability and robustness.

14.2.1. SE-01: Short GPS Signal Loss in Unpopulated Areas (< 30 seconds)

GPS systems are well known for their lack of immunity to jamming [40] [5]: the presence of forests or mountains, as well as cities, can lead to a temporary loss of signal. Without global guidance for navigation, the vehicle would rely fully on IMU measurements and its numerical integration. If no correction is made, the accumulation of error can drive the drone off path, increasing the risk of catastrophic crash or entering prohibited zones.

The use of IMU solely as backup is therefore not enough, as error is expected to diverge quickly. This error is expected to increase faster especially in cruise condition (the longest part of the flight), where strong accelerations are rare [44] and therefore velocity estimation is poor. Such divergence can be limited significantly with the addition of a small, low-cost sensors for velocity measurements, such as a pitot tube, and for altitude estimation, such as a barometer. This implementation is expected to give more time for the GPS signal to restore.

14.2.2. SE-02: Short GPS Signal Loss in Populated Areas (< 30 seconds)

GPS signal loss is expected to happen more often in areas with buildings and radio interference. The likelihood of the event and the risk associated with it (drone can crash and hurt civilians) makes this hazard the one with the highest risk and needs to be mitigated carefully.

The solution adopted here consists in drastically reducing the likelihood of the drone to fly over densely populated areas. This is achieved by the path planning algorithm (see [Chapter 12](#)) and does not necessarily require other sensors in addition to the ones mentioned in [Subsection 14.2.1](#).

14.2.3. SE-03: Long GPS Signal Loss (<2 min)

It might happen that GPS signal loss is more severe, due to strong interference or sensor malfunctioning. By considering this scenario, the solution proposed in [Subsection 14.2.1](#) might not be enough to avoid excessive divergence.

An excellent solution often adopted for this scenario sees the introduction of visual perception systems, such as mono or stereo cameras, to map the terrain and extrapolate useful information [44] [5] [40] [15]. Fusion between vision-based and IMU measurements, often referred as Visual Inertial Odometry (VIO) [63], would therefore greatly reinforce the navigation accuracy.

14.2.4. SE-04: Definitive GPS Signal Loss (>= 2 min)

As a limit case, the complete loss of GPS signal for the whole flight should be considered, as even if the likelihood of the event is low, the consequences can likely be catastrophic. In such a scenario, the drone can again benefit from the presence of the cameras pointing at the ground (see [Section 13.2](#): during flight, visual information can be stored in an on-board memory, allowing the drone to remember its previous moves and trajectories. This information could allow the drone to abort the mission and safely fly back to base by following its own tracks.

The approach used to add such a feature is called Simultaneous Localisation and Mapping (SLAM), which allows to construct or update a map of an unknown environment while simultaneously keeping track of an agent's location within it [23].

14.2.5. SE05: Definitive GPS Signal Loss and non Observable Terrain

GPS malfunctioning and signal loss might happen in a scenario where SLAM might not be able to run properly (e.g. in foggy conditions or while flying over water). In such a difficult scenario, no global navigation sensor is activated, bringing the severity back to the level in [Subsection 14.2.4](#).

The only backup that could be implemented in this case concerns the use of an emergency beacon, activated at the closest charging station to the vehicle. During this operation, the drone can follow the indications given by the beacon and approach it, using the obstacle detection pipeline as reinforcing backup.

14.2.6. Risk Mitigation Map

The above hazards and solutions were derived by means of risk assessment procedures which estimated the risk by likelihood and severity. The newly integrated hardware is expected to strongly mitigate risks in a subsystem for which the word "reliability" is imperative.

As observable in [Figure 14.1](#), the measures taken greatly reduce the high initial risk associated with the baseline design (see [Section 14.1](#)). The final result identifies a safe, robust and cost effective system.

14.3. Low Risk Design

To finalise the design of the pipeline, proper hardware and software needs to be selected. The selection needs to comply with the functionalities presented above but also consider the general constraints for the flying vehicle design, more importantly cost and weight.

14.3.1. Hardware Selection

As anticipated in the previous report [9], the market offers several flight controllers equipped (or compatible) with an overwhelming number of sensors. Considering the previously found constraints, the most logical choice

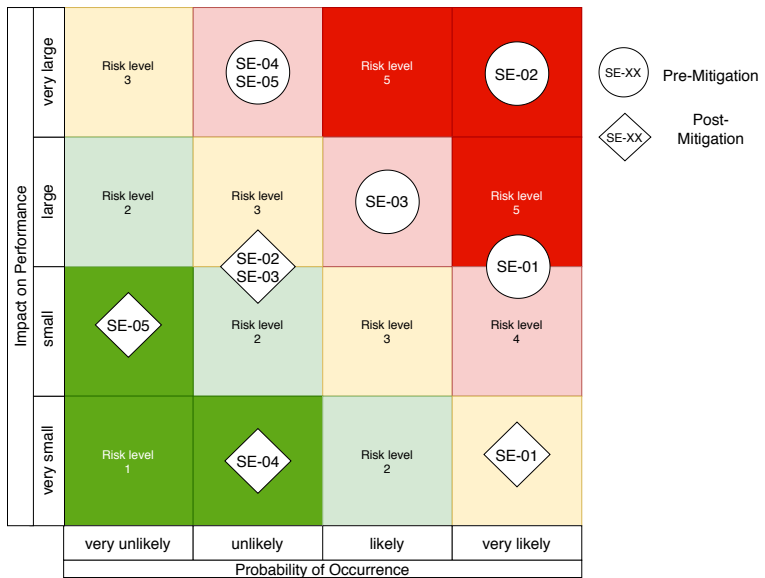


Figure 14.1: Risk mitigation map for state estimation pipeline on SAVED drone. The reduction in risk is possible by addition of redundant sensors and software packages.

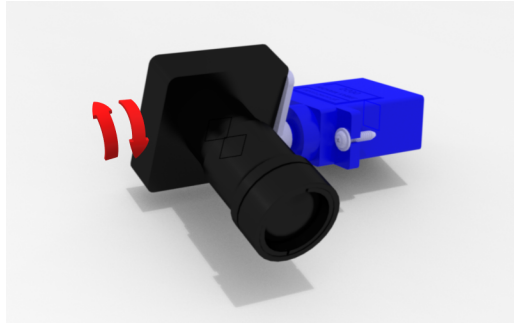


Figure 14.2: Servo and camera assembly. Such arrangement allows *FOV* rotation to allow compatibility between VIO and landing detection usage

appears to be the PixHawk4 from HolyBro¹. The autopilot embeds several mentioned sensors (i.e. barometer, IMU) and it offers compatibility with external ones (i.e. GPS trimble, pitot tube, telemetry antenna). For VIO [63] operation, the stereo camera pair selected in Section 13.2 can be used. However, a fixed mount of the cameras on the drone would not be able to perform landing point detection and VIO, because of the two different drone orientations in the manoeuvres. To cope with such issue, lightweight, low cost servos have been selected (Micro Servo SG90²) and mounted. The arrangement allows the desired rotation as showed in Figure 14.2

14.3.2. Software Selection

As the whole autonomous system infrastructure is based on ROS³, this is also the case for the state estimation software. PixHawk4 offers several drivers that make it compatible with this system and easy to use.

Unifying Information: the Extended Kalman Filter

As mentioned, state estimation relies on sensor redundancy for an accurate performance. However, in order to come up with a single, accurate result, sensor output needs to be processed all together through a tool that can extrapolate the truth from such. Most state estimation pipelines on UAV [48] resort to the Extended Kalman Filter⁴ (or EKF): the filter produces an estimate of the state of the system based on the previous state and the new measurements by means of a weighted average. The use of EKF is expected to be necessary especially for a correct VIO functioning.

¹<https://bit.ly/2BOagYG> [Cited on 19-06-2020]

²<https://bit.ly/3d2KcWC> [Cited on 14-06-2020]

³<https://bit.ly/37POKio> [Cited on 19-06-2020]

⁴<https://bit.ly/2Y0kwpp> [Cited on 16-05-2020]

Software and Hardware Integration

The extensive subsystem design process conducted in this report provided a detailed list of hardware and software packages that are to be implemented in the drone. In order to unify these elements, some additional gear and an integration maps are required, thus ensuring every part can communicate and work properly.

This chapter therefore proposes a set of physical processors to handle the stream of data in the drone ([Section 15.1](#)), which are then to be integrated in the whole structure ([Section 15.2](#)).

15.1. Processor Selection

As stated in [Chapter 13](#) and [Chapter 14](#), the autonomous software package requires the input data from cameras, LiDAR and other sensors to be further processed in different pipelines before providing useful data for navigation.

The PixHawk4 autopilot already partially contributes to this, as it is able to process navigation data from GPS, pitot tube, telemetry and Inertial Measurement Unit (IMU), together with the capability of sending commands to the control systems. Another significant part of data is processed within the cameras: the model selected (Firefly DL) is indeed capable of running deep learning neural networks within its internal processors, without the need of external processors for this kind of task. Object detection, an expensive task to run on a CPU aided computer, is therefore not to be taken into account.

The hardware choice so far pruned a substantial part of the data handling tasks required for vehicle operations. Several computations that require the help of an additional computer, however, are still left. These are running the LiDAR driver, the Visual Inertial Odometry (VIO) [63] pipeline, the ORB-SLAM [23] pipeline and the EKF [48], together with depth estimation during landing.

These tasks should be handled by an extremely low weight processor. As the above actions can also be performed without the aid of GPU, the choice of selecting the Raspberry Pi 3B+ (as stated in [9]) can be confirmed. It is however hard to estimate whether the stream of data and its handling can be processed with an acceptable latency. Because of this uncertainty, extensive testing needs to be conducted to assert whether an upgrade in processing power is necessary or not. An interesting backup option for future integration can be the NVIDIA Jetson Xavier Nano, a highly computing GPU driven computer with superior capabilities, but higher weight. For future development, assessments will be conducted on the selection of one of the two pieces of presented hardware.

15.2. Hardware and Software Diagram

The previous chapter closed the long list of hardware and software items chosen for SAVED. As already mentioned in [Subsection 13.2.1](#) and [Subsection 14.3.2](#), the vast majority of the apparatuses are built in ROS infrastructure¹, the most popular framework used for robots development. For this case ROS is preferred as it enables easy communication between different processes through the use of independent nodes broadcasting information.

In order to represent graphically this type of framework and its integration in the drone's hardware and software tools, an infrastructure map is created and presented in [Figure 15.1](#). This map shows the flow of information (grey arrows) between different nodes of the system (grey for hardware integrated nodes and dark yellow for standalone software nodes). Software nodes are incorporated in the Raspberry PI and PixHawk systems, as they are processed there. The light yellow boxes represent the external inputs and outputs needed for the operation. Finally, the green boxes located in the bottom right side of the diagram represent motors, lights, parachutes or any other control system that is directly affected by the output commands of the autonomous systems.

¹<https://bit.ly/37POKio> [Cited on 19-06-2020]

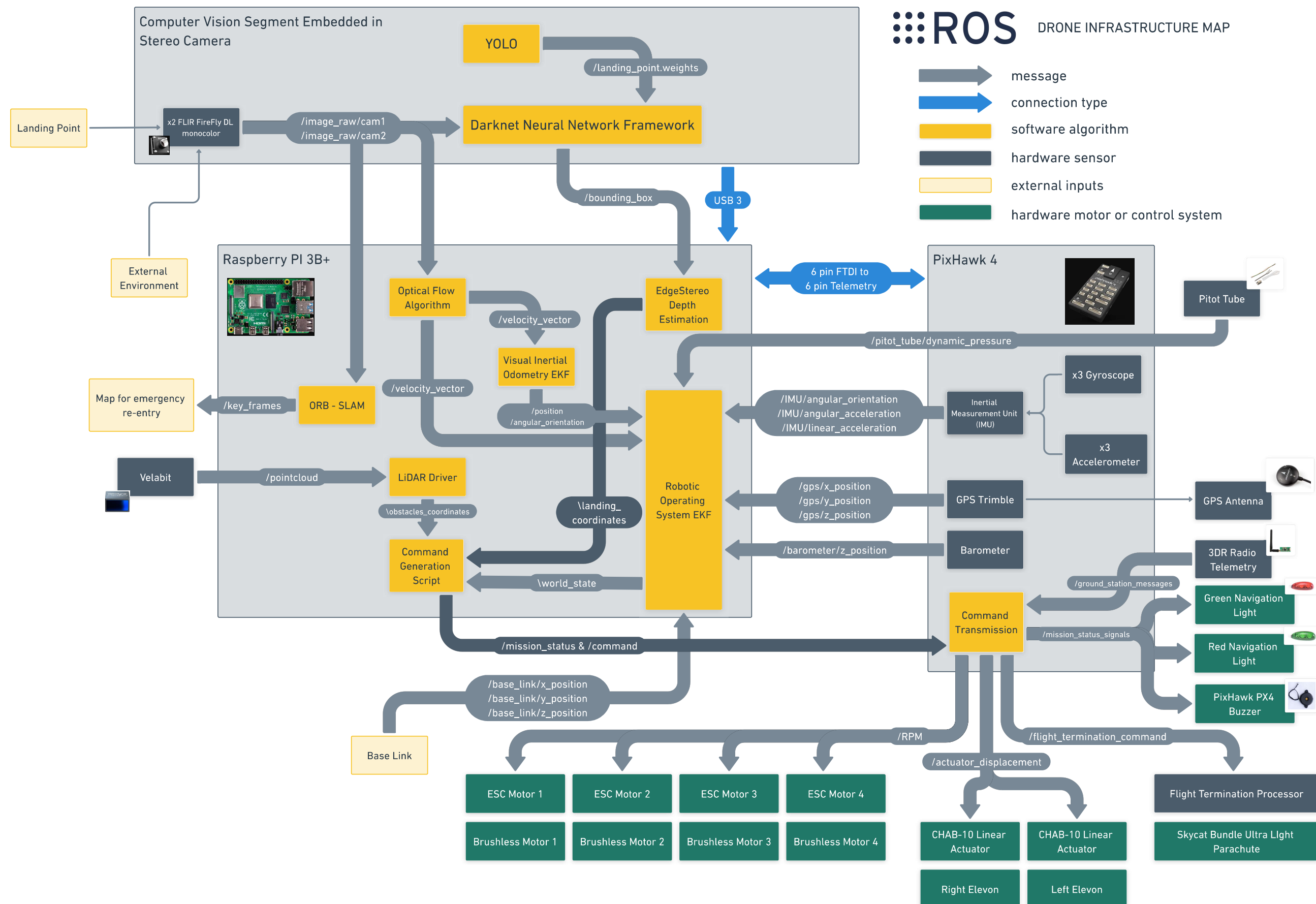
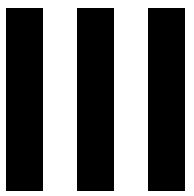


Figure 15.1: Full hardware and software integration on ROS based infrastructure



System Characteristics

16

Flight Performance Analysis

Now that all subsystems have been designed, sized, and integrated, in this chapter, the system's flight performance as a whole is analysed. This flight performance analysis is performed in order to assess whether the system complies with the performance requirements mentioned in [Chapter 17](#). SAVED's flight performance diagrams are presented in [Section 16.1](#). Next, a sensitivity analysis is performed in [Section 16.2](#). In this section, the robustness of the system with respect to the performance requirements is assessed.

16.1. Performance Diagrams

In this section, SAVED's performance diagrams are presented. The flight envelope and gust-load diagram are presented in [Subsection 16.1.1](#) in order to define SAVED's mission profile even more clearly. The payload range diagram is presented in [Subsection 16.1.2](#) in order to assess the change in SAVED's range with change in payload mass.

16.1.1. Flight Envelope

During any given flight, SAVED will perform a variety of manoeuvres. Whilst performing these manoeuvres, the lift produced may be larger or smaller than the weight of the drone. If the magnitude of this lift is too high relative to the drone's weight, the airframe may be overloaded and damaged. Therefore, it is important to understand how big the loads from these manoeuvres are on the drone's structure. The load factor parameter, n [-], defined as the lift over weight L/W [-], is used to describe this mathematically. The faster the drone flies, the more lift its wing produces. It is thus informative and appropriate to plot the expected maximum load factor against airspeed in a graph to understand what load factor the drone should withstand for a manoeuvre at a given airspeed. This is called a manoeuvring envelope and is shown by the coloured limits on [Figure 16.1](#).

The upper and lower limits of 3.8 and -1.52 for the load factor are both obtained from the Recommendations for Certification Specification for Light Unmanned Aeroplane Systems (JARUS CS-LUAS 337) [29]. The quadratic curves leading to those limits represent the stall limits, which indicate the load factor experienced when the drone is flying at maximum lift coefficient ($C_{L_{max}}$) [-] for different airspeeds. The design dive speed, V_D [m/s], is obtained by multiplying the cruise speed, V_{cruise} [m/s], by a factor of 1.4, as stated in CS-VLA 335 [1]. This graph also indicates a manoeuvring speed, V_A [m/s], of around 27.3m/s. This is the maximum speed at which the drone can make full or abrupt manoeuvre without causing structural damage to the aircraft. Note that this manoeuvring speed is greater than V_{cruise} , which is 22.3m/s. This means that when the drone is cruising, it does not have to change speed to make abrupt manoeuvres.

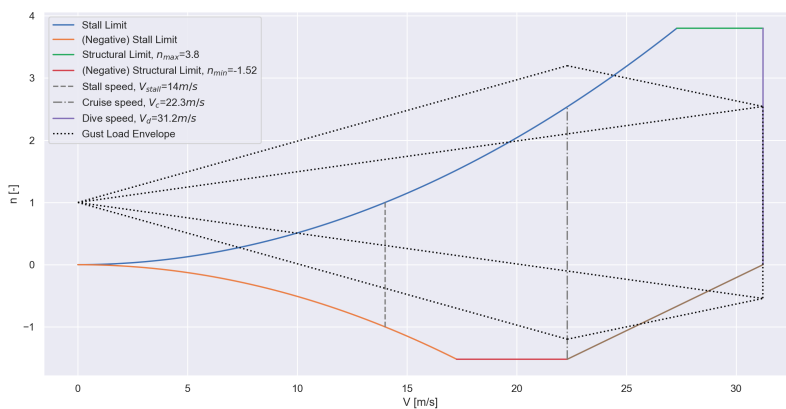


Figure 16.1: Flight Envelope

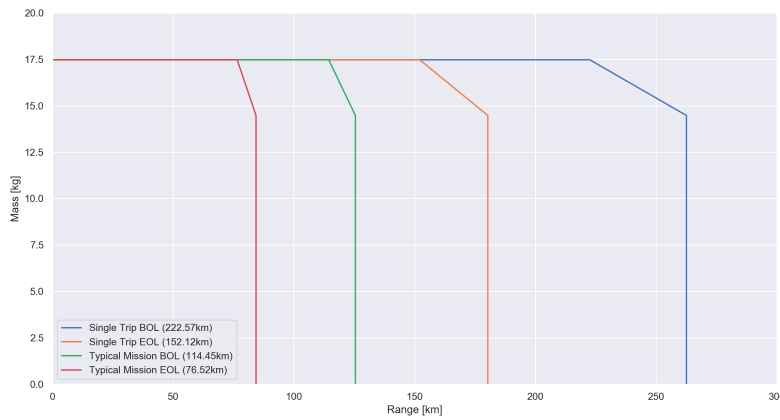


Figure 16.2: Payload Range Diagram for Single Trip and Typical Mission at both BOL and EOL

The other way that a drone might encounter large load factors is through the disturbance from gusts. Gust loads may cause a sudden change in lift, ΔL , which results in a change in load factor, Δn . CS-VLA 333 specifies gust velocities of 15.24m/s and 7.26m/s to consider when flying at V_{cruise} and V_D , respectively [1]. The equations specified in CS-VLA 341 [1] are shown in (16.1).

$$n = 1 + \frac{\rho_{SL} C_{L\alpha} V K_g U_{de}}{2W/S} \quad (16.1)$$

$$K_g = \frac{0.88\mu_g}{5.3 + \mu_g} \quad (16.2) \qquad \mu_g = \frac{2(M/S)}{\rho c C_{L\alpha}} \quad (16.3)$$

In (16.1), ρ_{SL} refers to sea-level density [kg/m^3], $C_{L\alpha}$ refers to the lift curve slope [$1/\text{°}$], V to the equivalent airspeed [m/s] and U_{de} [m/s] to the gust velocities specified in CS-VLA 333 [1]. K_g is the gust alleviation factor [-] and is defined as in (16.2), while μ_g [-] is a mass ratio as defined in (16.3). Moreover, one last consideration is made concerning these equations. [47] considers the CS-VLA conditions and then makes use of a simulation to compare results. The paper concludes that the CS-VLA conditions, which are made for aircraft of up to 750kg, are not entirely suitable for small UAV as these impose limits that are 92% greater than the results from said simulation. Therefore the gust load limits are divided by a factor of 1.92, which represents a more realistic scenario for SAVED. This issue relates back to the fact that there are still no official certification specifications in place for UAV and current existing regulations are often not well suited for drones. The results are plotted on a gust envelope, shown in Figure 16.1 by the dotted lines.

16.1.2. Payload Range Diagram

A payload range diagram is generally used to visually depict the trade-off between the amount of payload on board and the range that the aircraft is able to fly. This diagram is useful to demonstrate not only the range of the drone at maximum payload, but also the absolute range of the drone, which is the maximum range without any payload on board. However, unlike conventional payload range diagrams, payload weight cannot be exchanged for fuel weight to extend the range because the drone is electric and charged batteries weigh virtually the same as uncharged batteries. Meaning that a payload range diagram for an electric UAV like SAVED demonstrates two relevant scenarios: range at maximum payload, and range at zero payload. Figure 16.2 shows the range and payload combinations for a single trip as well as for a two-way journey for begin-of-life and end-of-life for a payload of 3kg. This particularity is relevant because a two-way journey will have two of each flight phase and is applicable to the mission profile described in Section 3.1. Therefore, a two-way journey covering a certain distance will have a greater energy consumption than a single trip that covers twice that distance.

From Figure 16.2, it can be seen that **SAVED-CUST-RANGE-02** is met for the most stringent mission profile, that is, the typical mission profile as described in Section 3.1 at end-of-life (EOL) conditions. It is therefore clear that any hospital or health centre within 75km of the base is supplied with medical products such as blood, vaccines and other, as implied by the customer requirements. The begin-of-life (BOL) values are overwhelmingly larger than **SAVED-CUST-RANGE-02** because they represent the BOL performance characteristics of the battery, meaning the detrementation of the battery which has been designed for has not occurred yet.

Table 16.1: Model outputs for complete mission when increasing the structural mass

$t_{mission}$ [s]	$E_{consumed}$ [MJ]	$E_{requiredbat}$ [MJ]	$m_{bat_{actual}}$ [kg]	$m_{bat_{required}}$ [kg]
7307	1.76	1.95	3.6	3.6

Table 16.2: Model outputs for complete mission when increasing C_{D_0}

$t_{mission}$ [s]	$E_{consumed}$ [MJ]	$E_{requiredbat}$ [MJ]	$m_{bat_{actual}}$ [kg]	$m_{bat_{required}}$ [kg]
7419.37	1.76	1.95	3.6	3.6

16.2. Performance Sensitivity Analysis

In this section a sensitivity analysis of the performance analysis is provided. A sensitivity analysis is included to assess the robustness of the results obtained in [Chapter 7](#), and the change in performance as a result. To evaluate this robustness it was decided to change several design parameters and subsequently verify by how much these parameters could be changed such that **SAVED-CUST-RANGE-02** is met. In this sensitivity analysis, parameters are considered that are both evaluated with some uncertainty and potentially have a significant impact on the performance of the drone. The zero-lift drag coefficient C_{D_0} [-] and structural mass were selected for this analysis. Evidently, the structural mass evaluation bears uncertainty at this design stage and an unexpected increase could complicate the mission. Furthermore, C_{D_0} was estimated using semi-empirical methods which limit the accuracy of the value ([Section 9.2](#)). This parameter is vital for justifying the tailless configuration and is therefore also included in this analysis. Since the fuselage bulge was modelled as an ellipsoid rather than a blended wing body, the actual value could also be lower. Therefore both an increase and decrease in C_{D_0} is investigated. The latter is important in assessing the need for expensive wind-tunnel testing.

The increase of the mass is evaluated in [Subsection 16.2.1](#). Next, the effect of increasing C_{D_0} is analysed in [Subsection 16.2.2](#). Lastly, the effect of lowering C_{D_0} is examined in [Subsection 16.2.3](#).

16.2.1. Consequence of Increasing the Structural Mass

In this subsection the structural mass is increased gradually. It is analysed by how much it can be increased, such that **SAVED-CUST-RANGE-02** is met. From this analysis it is obtained that this component of the mass can be increased by 3.7%, which equals adding a mass of 0.3kg to the total mass. This leaves sufficient room for unforeseen additions to the structural mass. The parameters of said mission can be found in [Table 16.1](#).

16.2.2. Consequence of Increasing C_{D_0}

In this subsection the C_{D_0} is increased gradually. Again, it has been analysed by how much it can be increased such that **SAVED-CUST-RANGE-02** is met. From the analysis it is obtained that the C_{D_0} can be increased by 4%. Therefore, in the unlikely event that the C_{D_0} in reality is higher than evaluated, there is still some contingency. The parameters of said mission can be found in [Table 16.2](#).

16.2.3. Consequence of Decreasing C_{D_0}

In this subsection C_{D_0} is decreased by 15% and consequently the results of this modification are analysed. The C_{D_0} is decreased by 15% because of it is believed that this C_{D_0} is a more realistic value for a flying wing concept. The parameters of this modification can be found in [Table 16.3](#).

Table 16.3: Model outputs for complete mission when reducing C_{D_0}

$t_{mission}$ [s]	$E_{consumed}$ [MJ]	$E_{requiredbat}$ [MJ]	$m_{bat_{actual}}$ [kg]	$m_{bat_{required}}$ [kg]
7158	1.61	1.79	3.6	3.33

System Requirements Compliance

In this chapter, system-level requirements which were found during the Baseline phase [8] are evaluated and the compliance of the designed system to these requirements is checked. Note that subsystem requirements stemming from these higher-level requirements have been reported in the relevant chapters of [Part II](#). It is also important to note, that some system requirements which were determined during the Baseline phase are not necessarily applicable (or verifiable) at this stage of the design (conceptual design). There are a number of them which are too in-depth to verify, some that are not required anymore and some that have been replaced fully by subsystem requirements. All of these were deemed unnecessary to report here but they will become useful in the future of the project. For this reason please refer to [8] for the full list. To not distract from the key and driving requirements, this chapter is hence only focused on those.

The original needs of the customer [30] have been reformulated over the course of the project into requirements which are summarised in [Table 17.1](#). These are now considered to be the *key* requirements. Most of these had been presented in the original Baseline Report [8], however, there have admittedly been some oversights in some regards at the time when the Baseline report was created. The fact that the vehicle shall perform VTOL manoeuvres was considered on a subsystem level, but there was not a clear trace to a high level requirement stating this need. For this reason, the requirement **SAVED-CUST-VTOL-01** has been added.

Table 17.1: Key requirements reformulated from customer needs stated in [30]

Code	Statement	Compliance	Verified in/by
SAVED-CUST-COST-OPS-AFL-01	Flight from take off to landing, included, shall be performed autonomously	Needs hardware testing	-
SAVED-CONS-SD-POP-01	SAVED shall use electric propulsion or hybrid concepts.	Yes	Design choice (Section 25.1)
SAVED-CONS-SD-POP-02	The charging/refuelling point of SAVED shall use a sustainable source of energy (e.g. solar, wind/hydrogen, synthetic fuels).	Yes	Design choice (Section 25.1)
SAVED-CONS-DIM-01	SAVED shall not have a width of more than 3 meters	Yes	Demonstration (Chapter 19)
SAVED-CONS-DIM-02	SAVED shall not have a length of more than 1.5 meters	Yes	Demonstration (Chapter 19)
SAVED-CONS-DIM-03	SAVED shall not have a height of more than 1.5 meters	Yes	Demonstration (Chapter 19)
SAVED-CUST-RANGE-02	Loaded with maximum payload of 3 kg, SAVED shall reach its delivery target at least 75 km away from base, being able to return back with no payload	Yes	Analysis (Section 7.2)
SAVED-CUST-VTOL-01	SAVED shall take-off and land vertically	Needs hardware testing	-
SAVED-CONS-CERT-01	SAVED shall satisfy all the requirements set by EASA for UAS in the 'certified' category	Partly	See Table 17

Furthermore, there are additional requirements which are not key but still inform the current design to some

extent. These are shown in [Table 17.2](#). Again, some of these were already present in the Baseline. However, some were added or reconsidered from being subsystem requirements to system level. In particular, requirements **SAVED-CONS-FLIGHT-02**, **SAVED-CONS-FLIGHT-03**, **SAVED-CONS-FLIGHT-04**, **SAVED-CONS-FLIGHT-05**, **SAVED-CONS-FLIGHT-06** and **SAVED-CONS-FLIGHT-07** were created in [Chapter 6](#) for designing the wing planform.

Table 17.2: Additional system requirements which are relevant at this stage of the design

Code	Statement	Compliance	Verified in/by
SAVED-CUST-FAST-TVL-SPD-01	SAVED drone shall have a cruise speed minimum of 20m/s	Yes	Analysis (Section 9.2)
SAVED-CUST-PLD-01	Payload hold shall allow for a payload with the following dimensions [mm]: 118x278x295	Yes	Demonstration (Chapter 19)
SAVED-CUST-PLD-032	The cargo bay hold shall be made modular such that other types of payload can be implemented (e.g. embedded camera)	Yes	Demonstration (Chapter 19)
SAVED-CONS-SD NOI-01	The sound pressure level shall be below 110dB at 1.5m during VTOL conditions	Yes	Analysis (Sub-section 25.1.3)
SAVED-CONS-SD NOI-02	The sound pressure level shall be below 35dB at a distance of 500m during cruise conditions	Yes	Analysis (Sub-section 25.1.3)
SAVED-CONS-FLIGHT-01	SAVED shall fly at a cruise altitude of 500m	Yes	Design choice (Section 3.1)
SAVED-CONS-FLIGHT-02	The aircraft shall be longitudinally stable	Yes	Analysis (Section 10.6)
SAVED-CONS-FLIGHT-03	The design shall fly at maximum <i>L/D</i> during cruise flight	Yes	Demonstration (Section 9.2, Subsection 11.7.1)
SAVED-CONS-FLIGHT-04	The aircraft shall be trimmable	Yes	Demonstration (Sub-section 11.7.1)
SAVED-CONS-FLIGHT-05	The aircraft shall have stable stall behaviour	Needs hardware testing	-
SAVED-CONS-FLIGHT-06	The aircraft shall be laterally stable	Partly	Analysis (Section 10.6)
SAVED-CONS-FLIGHT-07	The aircraft shall be directionally stable	Yes	Analysis (Section 10.6)
SAVED-CONS-SD-PP-0 2	SAVED shall detect and avoid the areas with a population density of more than 20,000 [1/km ²] outside a range of 10km from the target location	Yes	Demonstration (Section 25.4)
SAVED-CUST-COST-PROD-01	The cost of a single SAVED vehicle shall not exceed 25 000€	Yes	Analysis (Section 26.2)
SAVED-CONS-SD-EM-02	if a fully electrical system is used, SAVED shall have 50% less greenhouse gas emissions per payload distance than a conventional car, accounting for the manufacturing of the batteries	Yes	Analysis (Section 25.1)
SAVED-CONS-SD-MAT-01	30% of the mass of structural materials shall come from a recycled source	Yes	Analysis (Section 25.2)
SAVED-CONS-SD-MAT-02	80% of the mass of structural material shall be recycled after decommissioning of the drone	Yes	Analysis (Section 25.2)

Certification Requirements

As stated in [Table 17.1](#), according to **SAVED-CONS-CERT-01**, SAVED needs to adhere to EASA (European Union Aviation Safety Agency) requirements to fit in the 'certified' category. During the Baseline phase, a number of certification requirements were determined through literature research. So far, some of these can be shown to have been implemented in the design. Some others are too detailed to be considered at this stage but will be considered in future design. A table of certification requirements can be seen in [Table 17.3](#)

Table 17.3: Certification requirements.

Code	Statement	Complied	Verified in/by
SAVED-CONS-CERT-TECH-PFC-01	SAVED shall autonomously perform a pre-flight check before each flight	Future req.	Test
SAVED-CONS-CERT-TECH-PFC-02	The pre-flight check shall include battery charge and temperature, control surfaces deflections and others (engine, payload etc.)	Future req.	Demonstration
SAVED-CONS-CERT-TECH-PFC-03	SAVED shall communicate the results of the pre-flight test to the Autonomous Flight Traffic Control	Future req.	Test
SAVED-CONS-CERT-TECH-PFC-04	SAVED shall autonomously proceed or abort operations following the result of the pre-flight checks (PFC)	Future req.	Test
SAVED-CONS-CERT-TECH-PFC-05	Autonomous Flight Controllers shall not be able to override SAVED's decision following the PFC	Future req.	Test
SAVED-CONS-CERT-TECH-TERM-01	SAVED shall be equipped with a parachute if heavier-than-air UAV	Yes	Demonstration (Chapter 18)
SAVED-CONS-CERT-TECH-FLIGHT-01	SAVED shall be equipped with navigation lights in accordance with EASA guidelines	Yes	Demonstration (Chapter 15)
SAVED-CONS-CERT-TECH-TERM-02	SAVED shall be equipped with a remotely triggered flight termination system	Yes	Demonstration (Chapter 15)
SAVED-CONS-CERT-TECH-TERM-03	SAVED shall be equipped with an autonomously triggered flight termination system if a seriously critical situation is detected	Yes	Demonstration (Chapter 15)
SAVED-CONS-CERT-TECH-TERM-PARA-01	SAVED's emergency parachute shall deploy whenever the flight termination system is triggered with a reliability of 95% or higher	Future req.	Test
SAVED-CONS-CERT-TECH-FLIGHT-RAS-01	SAVED shall be equipped with an up-to-date map of the restricted airspace	Yes	Demonstration (Chapter 12)
SAVED-CONS-CERT-TECH-FLIGHT-NAV-01	SAVED shall be equipped with a satellite navigation system	Yes	Demonstration (Chapter 15)
SAVED-CONS-CERT-TECH-FLIGHT-TTC-01	SAVED shall communicate telemetry parameters to AFTC, including but not limited to: airspeed, groundspeed, vertical speed, coordinates, altitude, heading, yaw, pitch, roll, angle of attack, etc. (see full list in [8])	Future req.	Test
SAVED-CONS-CERT-TECH-FLIGHT-TTC-02	SAVED shall send telemetry data to AFTC with a frequency of 1Hz take off and landing	Future req.	Test
SAVED-CONS-CERT-TECH-FLIGHT-TTC-03	SAVED shall send telemetry data to AFTC with a frequency of 1/5Hz during cruise flight	Future req.	Test
SAVED-CONS-CERT-TECH-TERM-04	SAVED shall autonomously trigger the flight termination command if ground connection is lost for more than <tbd> seconds	Future req.	Test
SAVED-CONS-CERT-TECH-FLIGHT-NAV-02	SAVED shall be equipped with a system that allows AFC to instruct the UAV to change heading, airspeed and altitude at any time after take-off	Yes	Demonstration (Chapter 11)

Technical Risk Management

The goal of this chapter is to identify the technical risks of the system and analyse how these have been mitigated. It is of utmost importance that SAVED is designed with the risk management philosophy in mind to ensure a high reliability of the drone. Firstly, all the risks are identified per subsystem in [Section 18.1](#). In this section the mitigation procedures implemented in the design process are also stated. Lastly, in [Section 18.2](#) the risk maps can be found from before and after mitigation.

18.1. Risk Identification & Mitigation

In this section the risk events are identified and evaluated. Subsequently, the risks have been mitigated by implementing design choices that reduce the risks respectively. This is done for all technical departments, apart from AI which has performed its own risk assessment in [Subsection 14.2.6](#).

18.1.1. Structures, Materials and Manufacturing

SMM-01: Drone Tips over after Landing

The event in which the drone tips over after landing. This might happen due to serious wind gusts or an inclination of the landing location. This event is unlikely to likely to happen and has a small to large impact on the performance, depending on the structural damage of the drone.

In order to reduce the probability of this event the drone must be designed to prevent this from happening. The solution to this problem is that the drone will land on its vertical fin and its wing. Due to this design consideration the drone now has four landing points, which reduces the probability of this event to very unlikely.

18.1.2. Aerodynamics

AE-01: Complete Loss of Lift over the Main Wing due to Stall in Cruise

The event in which flow separation occurs near the leading edge of the wing, resulting into a loss of lift over a significant portion of the wing. The results of this are catastrophic, in case no action is carried out. The unstable stall will not automatically recover and SAVED crashes towards the earth causing destruction of the entire drone. Therefore, the impact is very large and if no measures are taken, it is also likely to occur.

To prevent the event of losing lift over the main wing of happening, stall performance was taken into account in the trade-off of the main wing airfoil in [Section 9.1](#). By selecting an airfoil with good stall performance, the probability was reduced to unlikely. Furthermore, a control system was developed to address the stall recovery of SAVED. With this, the impact of a stall is now small.

AE-02: Loss of Controllability due to Wing Tip Stall

The event in which a loss of lift occurs at the most effective area of the elevons. This leads to a significant decrease in controllability. This loss of controllability has a large impact on SAVED, because it can potentially cause uncontrollable scenarios and even crashes. Furthermore, wing tip stall is likely to occur when no measures are taken.

In order to prevent wing tip stall from happening, the rotation of the propellers was adjusted in such a way that the effective angle of attack at the wing tips is reduced. Thereby, the probability of this event has been decreased to unlikely. Next to this, the risk is also mitigated by increasing the spanwise dimension of the elevons. This significantly reduces the impact by increasing the controllability. Therefore, the impact of this event after implementing the changes to the elevons is now small.

18.1.3. Control and Stability

CS-01: Loss of Longitudinal Stability

The event in which too much mass is distributed towards the tail, which causes the centre of gravity to be aft of the neutral point. This will result in a destabilising pitch after a change in angle of attack. If this is not taken into account during the design it is likely to happen and when this happens it has a very large impact on the performance, because the drone isn't stable during flight.

To ensure longitudinal stability the drone must be designed for this. In SAVED's case this is done by putting the engines and the battery more to the front of the drone. This prevents this event from happening, and thus reduces the probability to very unlikely.

CS-02: Destabilised Rolling with Sideslip Disturbance

The event in which a sideslip is introduced and $C_{l\beta}$ is positive. This will lead to a destabilising roll. Which has a very small impact on the performance, but if it is not taken into consideration while designing the event is likely to occur.

To address this risk, a positive sweep is included into SAVED's design. This will prevent this event from happening, which decreases the probability of this event to very unlikely.

CS-03: Loss of Weathervane Stability

The event in which a sideslip is introduced and $C_{n\beta}$ is negative. This will lead to a destabilised yaw. If this is not accounted for in the design it will have a large impact and is likely to happen. Therefore, it must be considered in order to reduce the risk of this event to an acceptable level.

To solve this problem two design implementations have been considered. Firstly, the previously mentioned sweep, which reduces risk "CS-02: Destabilising rolling with sideslip disturbance", also has a positive effect on the weathervane stability. Secondly, the landing fins are increased in order to prevent this event from happening. Due to these design implementations the probability will reduce from likely to very unlikely.

CS-04: Destabilised Roll after a Rolling Disturbance

The event in which an extra roll occurs after a roll disturbance. This will lead to a destabilised rolling moment. This will have a large impact on the performance and if during the design nothing is altered the probability will be unlikely.

In order to reduce the risk "CS-03: Loss of weathervane stability" the area of the landing fins has been sized accordingly. This design consideration will however also reduce the probability of the destabilised roll to very unlikely. Consequently, by increasing the area of the landing fins two risks have been mitigated.

CS-05: Loss of Engine

The event in which an engine is lost while performing the mission. The loss of an engine is in general an unlikely event. In the earlier stages of the design process SAVED was a drone configuration with two engines. If in this case an engine were to fail the drone would be completely uncontrollable, resulting in a crash. This would therefore have a catastrophic impact on the design.

The solution implemented here is to include two additional engines, making SAVED a drone configuration with four engines in total. This will reduce the impact of the loss of an engine significantly, namely from very large to small. This is due to the fact that SAVED will remain controllable and will able to descend on its own.

CS-06: Jammed Actuator

The event in which an actuator is jammed. This event is likely to happen if no actions were to be taken to account for this during the design process. In case an actuator is jammed the drone must perform an emergency landing which can have a very big impact on the design. To prevent this from happening well-considered measures must be taken.

The solution implemented to solve this problem is that the elevons are connected at its extremities by means of ball-joints, which is further discussed in [Subsection 21.3.2](#). This reduces the probability of this event considerably, namely from likely to very unlikely.

18.1.4. Power and Propulsion

PP-01: Battery not Properly Charged

The event in which the battery is not properly charged and the drone takes off to its target location with insufficient energy. The result could potentially be catastrophic. This will cause SAVED to suddenly lose all power and crash towards the earth, leading to destruction of the drone and damage to the surroundings. Although the impact is thus very large, it is an event that is unlikely to occur.

To address this problem, a battery percentage sensor has been included in the design. By doing this, the chances of the drone taking off without a fully charged battery are so small that this event can be considered very unlikely. This means the risk is prevented by including this sensor.

PP-02: Power Circuit Failure

The event that the battery or another component of the power circuit fails during flight is unlikely to happen. However, in case it does happen and the engines stop working for example, the impact will be catastrophic and the drone will most likely be destroyed by the crash. To avoid this from happening mitigation must be performed.

The solution implemented here is to include a parachute in the design of the drone, which will be deployed if the drone is unable to fly autonomously back to the surface. The parachute model was chosen to be the SKYCAT BUNDLE ULTRA LIGHT from the company Fruity Chutes. This parachute is made for drones up to 20kg and it weighs 0.47 kg. However, in the analysis for SAVED this mass is rounded up to 0.5kg to account for additional attachments¹. The inclusion of the parachute significantly reduces the impact of this event, namely from very large to small and ensures a safe recovery of the drone. Furthermore, the implementation of a parachute also further decreases the risks: "PP-01", "CS-01" and "CS-06". Since these risks are also related to the drone crashing, they can not only be considered prevented, but also mitigated to a small impact.

PP-03: Failure to Deploy Parachute

The event that the parachute cannot be deployed due to a malfunction in the power circuit is unlikely to happen, but will again have a catastrophic impact on the system. This must by all means be prevented from happening.

The answer to solve this problem is to include a small back-up battery which is only connected to the mechanism that deploys the parachute. This reduces the probability of this event from unlikely to very unlikely and ensures that the parachute can deploy in case the main power circuit fails.

18.2. Risk Prioritising & Mapping

Now that all possible technical risks related to the mission are identified and evaluated, a risk map has been created taking into account the event's probability of occurrence and its impact on the performance. Based on these two categories 5 levels of risk are distinguished. Each event is placed in one of these levels to indicate the relative importance of the events. Two risk maps have been included, one before mitigation is performed and one after mitigation is performed. These risk maps can be found in [Figure 18.1](#) and [Figure 18.2](#) respectively.

Risk level 1 and 2 refer to events with a very low and low risk and both are deemed acceptable. Which means that no additional measures that involve significant resources should be spent on reducing the risk of these events. Risk level 3 indicates moderate risk. This is tolerable for some events, for example in cases where it is very costly to reduce the risk level. Risk level 4 and 5 indicate high and very high risk respectively. These risk levels are deemed unacceptable. Therefore, action must be taken to reduce the risk of these events, if possible. Suitable actions are mitigation and prevention. As can be seen in [Figure 18.1](#) the majority of the risks before mitigation were in risk levels 3 to 5. However, due to the mitigation and prevention techniques, which are discussed in [Section 18.1](#) and which are also included into the design, the risk levels of the final design are between 1 to 3. This is deemed an acceptable result for SAVED's final design, meaning no further risk mitigation actions have to be performed in the future.

Table 18.1: Average Risk Levels before and after Mitigation

	Average Risk Level	Standard Deviation
Before Mitigation	3.8	±0.96
After Mitigation	1.7	±0.62

¹<https://bit.ly/3dgS3jE>, [Cited on:19-06-2020]

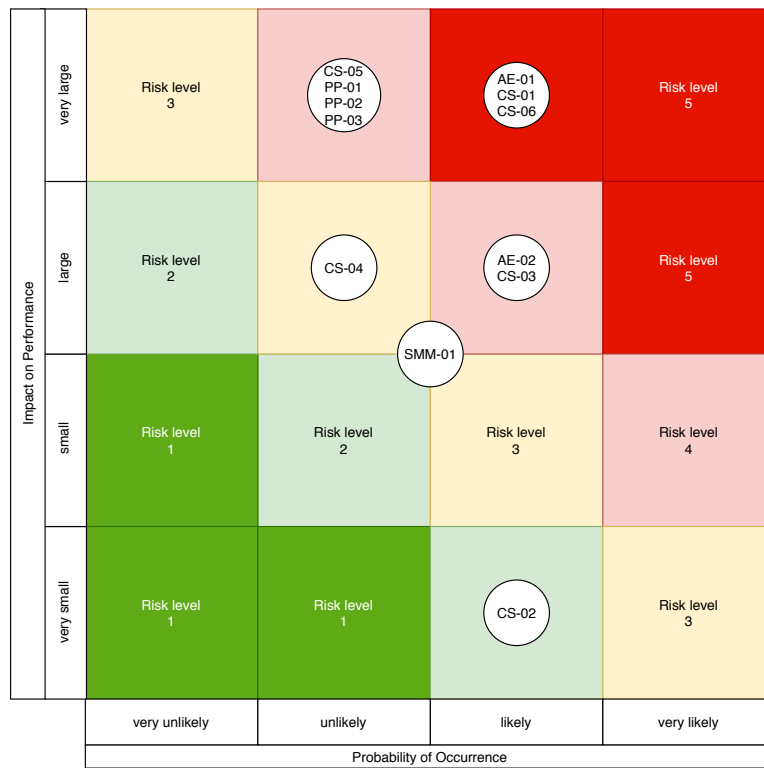


Figure 18.1: Risk Map before Mitigation

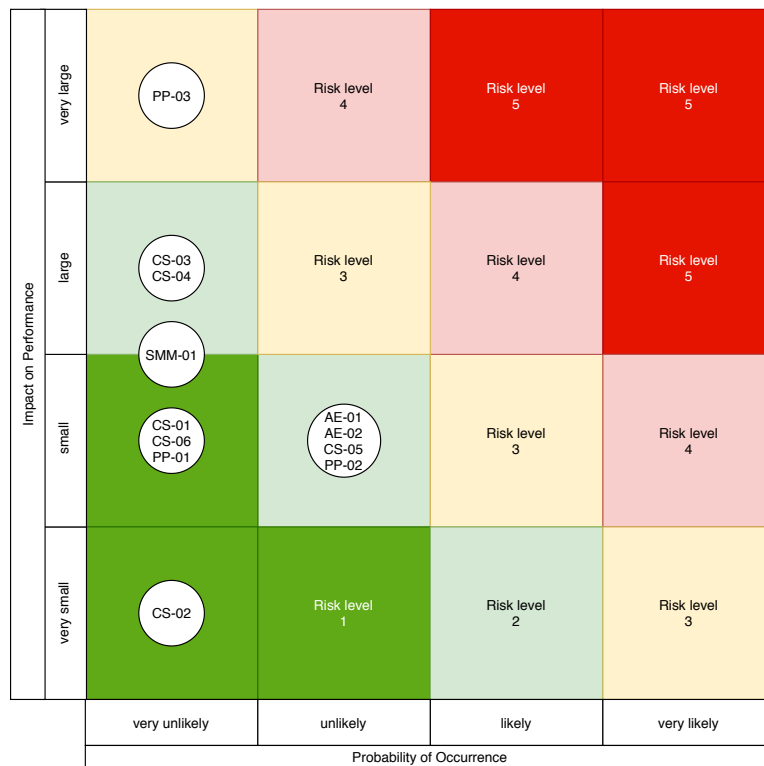


Figure 18.2: Risk Map after Mitigation

Final Design Overview

Now that all the geometric and performance parameters, which comply with the requirements set, have been computed and iterated, important specifications of the final design of SAVED are listed in [Figure 19.1](#). Also, a technical drawing of SAVED with all its relevant dimensions on different point of views is shown in [Figure 19.2](#).

Technical Specifications

Dimensions	Battery Specific Energy	Payload
300 x 67.3 x 79.3 cm	246 Wh/kg	Up to 3kg
Payload Dimensions	Maximum Thrust	Maximum Take-Off Mass
29.5 x 26.8 x 11.8 cm	206 N	17.4 kg
Material	Endurance	Operational Empty Mass
Carbon Fibre Reinforced Polymers + Aluminium	3.6 h	10.8 kg (excl. batteries)
Speed	Noise Level	Flight Mode
Stall: 50 km/h - Cruise: 81 km/h VTOL: 0 - 22 km/h	Cruise: 9 dB @ 500 m Take-off: 106 dB @ 1.5 m	Fully autonomous
Range (incl. payload)	Cruise Altitude	Take-off & Landing Manoeuvre
Single trip: 220 km Return trip: 115 km	500 m	VTOL
Battery Type	Drive	Mission Path Planning
LiPo (3 packs x 6 cells)	Fully electric	Fully autonomous



Figure 19.1: SAVED's technical specifications.

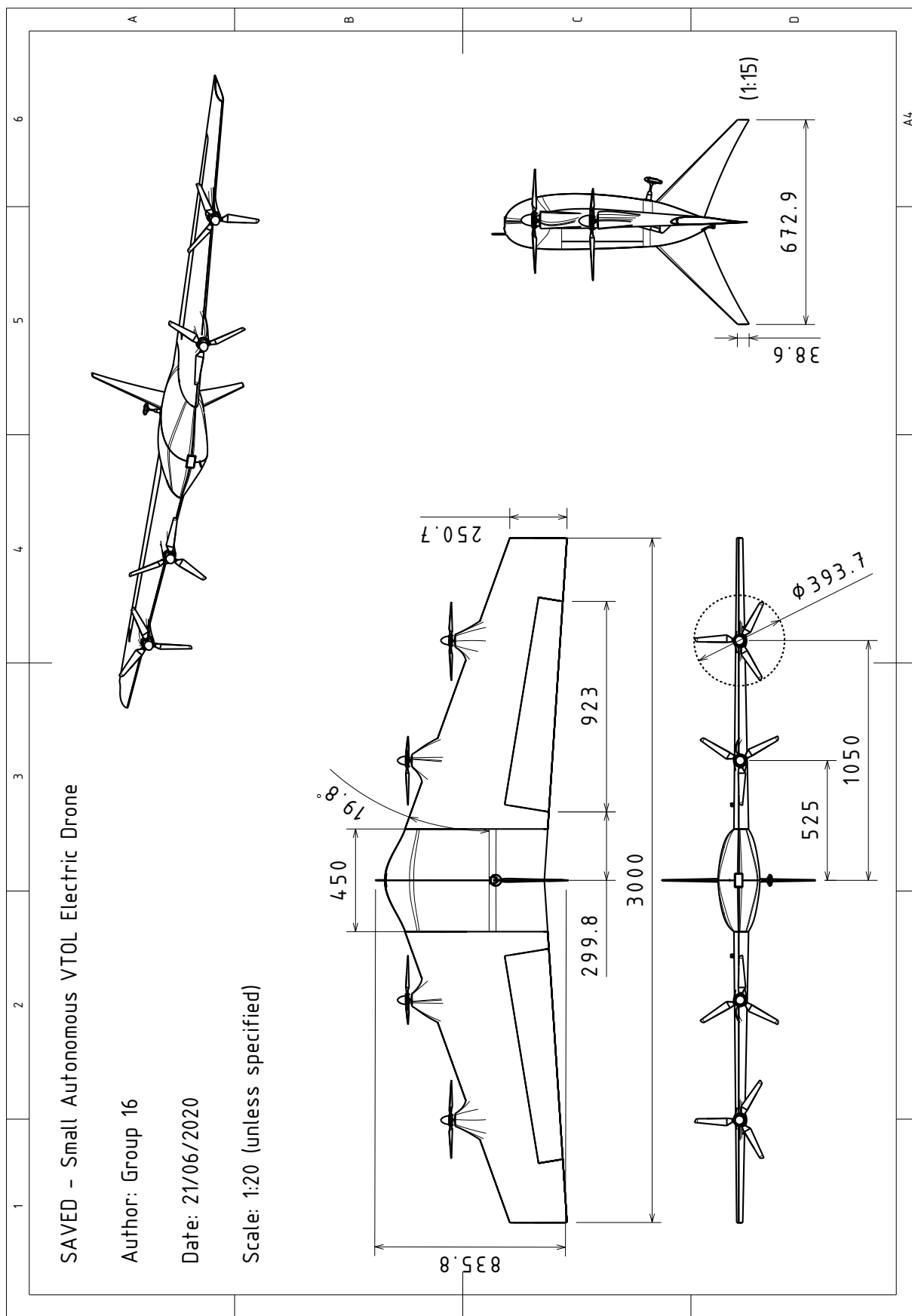


Figure 19.2: Technical drawing of SAVED. Note that the real scale is not as specified in the figure, but slightly larger, due to document formatting.

IV

Project Design and Development

20

Project Design and Development Overview

In order to ensure effective continuation of the project after the design synthesis exercise (DSE), the future design and development has to be well defined. These activities are crucial for a successful launch of SAVED on the market. This chapter serves as an overview of all future project design and development activities post DSE. A work flow diagram (WFD) describing the flow of the post DSE activities is shown in [Figure 20.2](#).

The explanation of [Figure 20.2](#) is as follows: right after the end of the DSE, activities have to be carried in order to ensure that the project is financially covered. This is done by consulting external parties such as venture capitalists (VC's) and/or investment banks (IB's) or by means of private equity (PE). Meanwhile, a prototype of SAVED needs to be developed and tested. The prototype will be used for improvement of the design, as well as marketing. Once ensured that the prototype complies with all requirements, the case study discussed in [Section 2.3](#) is further analysed in order to select potential customers and base locations. Once the project is financed, a customer is selected, and the prototype is tested and validated, SAVED's infrastructure can be built. The infrastructure constitutes the manufacturing and assembly facilities, as well as the storage facilities and the operation bases. This is further elaborated upon in [Section 22.1](#) and [Section 22.2](#). Once the infrastructure is in place, the drones can be manufactured according to the production plan discussed in [Chapter 21](#) and [Section 23.2](#) and distributed to the location of operation as further elaborated upon in [Section 23.3](#). When everything is in place in the country of operation, the deployment of the entire operation can be set in motion. Once SAVED is deployed, its needs to be operated and maintained, which is a continuous process until end of operation and further discussed in [Chapter 24](#). Meanwhile, when all of the aforementioned processes are taking place, SAVED is continuously being marketed in order to find the next client.

Finally, [Figure 20.2](#) is shown in the form of a high level Gantt chart. The Gantt chart is displayed in [Figure 20.1](#) and serves as a visual backup for [Figure 20.2](#) such that the order of tasks performed is easier to understand.

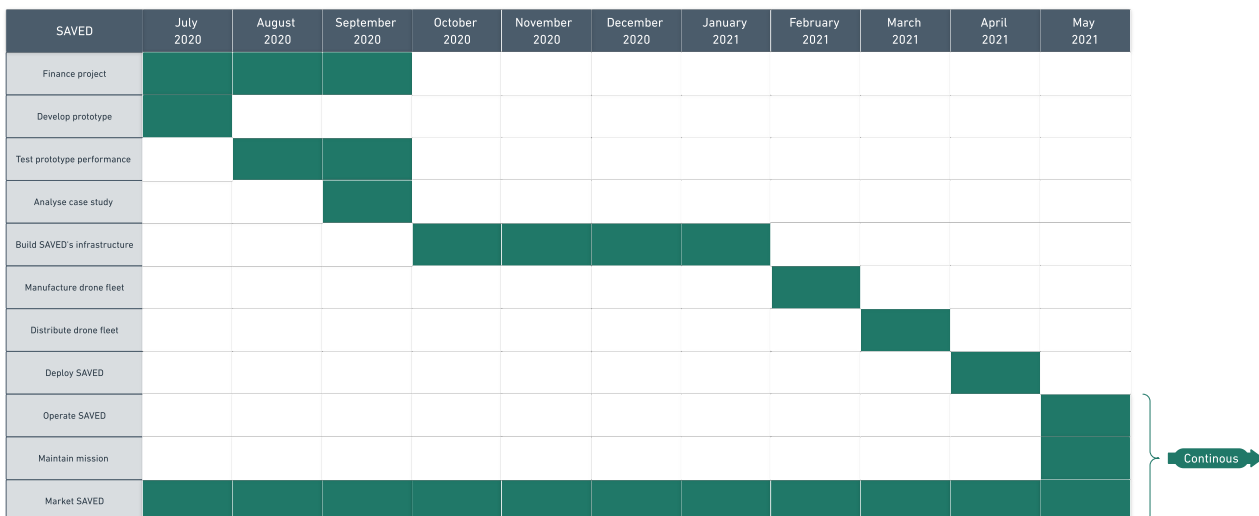


Figure 20.1: SAVED Post DSE project Gantt chart.

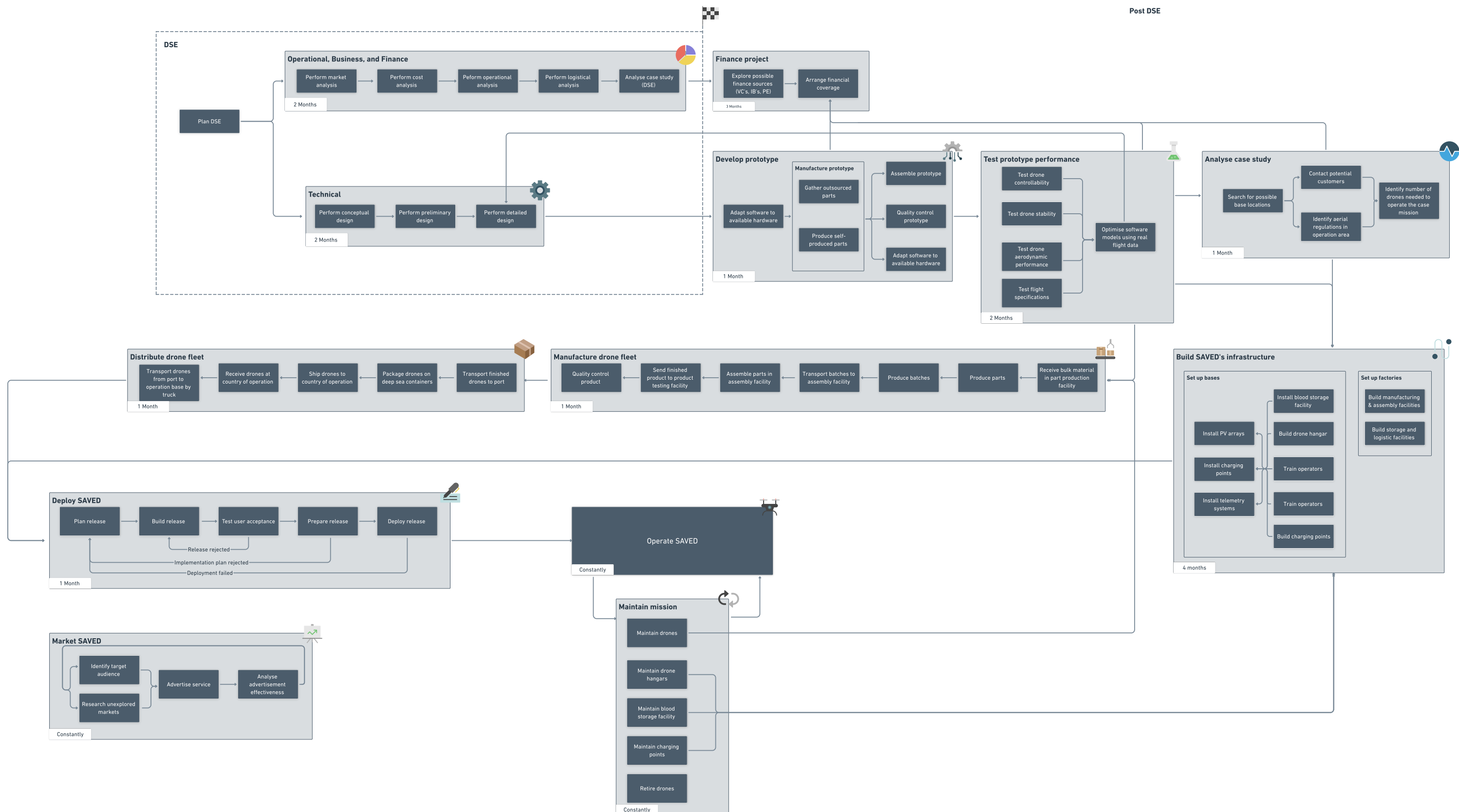


Figure 20.2: SAVED Post DSE WFD.

Production Plan

In this chapter an extensive overview is presented on the production plan of SAVED together with a corresponding estimation of the manufacturing costs. Firstly, [Section 21.1](#), the logistics of the manufacturing process will be briefly discussed and an estimation of the total manufacturing costs of the drone is presented. Following this, the production of the structural parts as designed in [Chapter 8](#) is discussed in [Section 21.2](#). Furthermore, in [Section 21.3](#), the assembly process of the parts and their corresponding joining method is explained. Finally, in [Section 21.4](#), the quality control of the produced parts and final assembly is discussed to ensure that the produced drone meets the design requirements.

21.1. Logistics of Manufacturing and Cost Estimation Method

The manufacturing of the drone is split into two separate processes. The first part consists of the procurement of parts, which is discussed in [Section 21.2](#). The manufacturing of most parts will be outsourced to subcontracted companies. Using this method, excessive tooling costs are avoided at the cost of a small profit margin to the subcontractors. The relatively small production scale of SAVED economically justifies this manufacturing philosophy. Some parts such as the skin panels, are too specific to outsource. Other less crucial parts of more versatile design and low tooling costs, are self-produced to allow easy change in part design. In the end all manufactured parts are transported to a central assembly facility in which the drone is assembled. To omit additional transport cost, the self-produced parts will be manufactured in the same assembly facility.

21.1.1. Remarks on Assembly Facility

Due to the complex tasks involved with both production of the self produced parts as with the assembly of the drone, the assembly facility has to be in a region with highly trained personnel rather than low wage countries. The process of manufacturing of the skin panels, operating and programming the tooling and calibrating of the drone requires a highly skilled staff. Therefore, the assembly and manufacturing facility has to be located in an industrialised country. This will most likely be somewhere in the north-west of Europe with good access to port infrastructure. Although it is more expensive to operate in this region, it has the necessary skilled workforce and infrastructure required.

21.1.2. Labour Cost Estimation

As is found in [Subsection 21.1.1](#), the production and assembly facility has to be in a industrialised region. This has a direct effect on the labour costs for the part production and drone assembly. In order to incorporate indirect costs that are difficult to assess independently, several cost aspects are incorporated in the labour cost per man hour. Such indirect costs include facility costs, supervision & administrative cost and small tooling and consumables. This estimation is based on [69] and is presented in [Table 21.1](#). Especially the direct cost component, the hourly wage and on-costs, is expensive in industrialised countries.

21.2. Parts Manufacturing

The first part of the production plan involves the procurement of the parts. There are three distinct categories in which the parts are obtained. [Subsection 21.2.1](#) elaborates on the structural components that are bought off-the-shelf and need minimum processing. In [Subsection 21.2.2](#), the more complex parts that are outsourced to subcontractors are discussed. Finally, in [Subsection 21.2.3](#), the production of the self-produced parts such as the wing skin and engine fairings is presented.

21.2.1. Off-The-Shelf (Structural) Parts

In this subsection the production and procurement of the outsourced parts is discussed. The subcontracting of other companies allows reduced tooling costs for several parts. An overview and cost estimation for these

Table 21.1: Breakdown of the labour cost per man hour, based on data obtained from [69]

Component	Cost [€/h]
Direct	
hourly wage & on-cost	80
Indirect	
Supervision	25
Training	5
facility costs & maintenance	20
workshop equipment & small tools	10
administration	10
total cost [€/h]	150

Table 21.2: Part production cost estimation outsourced parts

Part	Quantity	Source	Production cost per part [US\$]	Post processing
Front spar	2	Off-the-shelf	40 ¹	drilling
aft spar	2	Off-the-shelf	40	drilling
stiffeners	14	Off-the-shelf	25 ²	minimal
total part costs				510

parts is listed in [Table 21.2](#).

Manufacturing Of the Spars

As discussed in [Section 8.3](#) the main and aft spars will be non-tapered aluminium hollow shaft profiles. This very simple part geometry allows for the off-the-shelf outsourcing of these parts to avoid expensive tooling cost. Minimal post-processing will be needed and can be done on the assembly site. Although the thickness is different for the front and aft spar, the part procurement cost is the same as most of the cost will be determined by the tooling of the subcontractor.

Manufacturing of The Stiffeners

The stiffeners, as described in [Section 8.3](#), will be made of solid pultruded carbon tubes with a constant cross section. These components will be outsourced with minimal post-processing needed. The basic geometry allows them to be bought off-the-shelf cheaply from large producers cut in the right length.

21.2.2. Outsourced Parts

Manufacturing of the machined ribs, Centre section spars and engine mounts

The aluminium ribs located at the engine mount, centre section and wing tips need to be more complex. Each of these will have to be able to transfer principal loads between skin spars and other elements such as the engine mounts. Therefore, these ribs will need several unique joints and attachment points. To obtain such geometry in single parts with high accuracy, machining was concluded to be necessary. The same holds for the engine mount connections. The machining of these parts will be outsourced, to avoid excessive tooling costs. 3D CAD drawings of these parts will be supplied to these external manufacturers which will be used to produce the parts. The CNC milling tools are not part specific and can therefore be excluded by outsourcing. The same holds up for the central spar connections. The cost of these parts is based on material block cost of aluminium 6061 and hourly machine cost of industrial 5-axial CNC machines. An estimation of the needed machine hours per part is based on the volume and part complexity. It is assumed all machined parts need 5-axial CNC operations ³. Labour cost for this process are assumed to be minimal, since the CAD drawings are made beforehand and the multi-axial machining requires minimal handling. An overview of the production cost estimation is presented in [Table 21.3](#). transportation costs of the outsourced and off-the-shelf parts is already incorporated in the procurement price.

³<https://bit.ly/2Bsdh0z>[Cited on 11-6-2020]

Table 21.3: Part production cost estimation outsourced parts

Part	Quantity	block size [l"/w"/t"]	block cost [€] ⁴	machining time [hr]
Forward Centre spar	1	15/5/1	20	0.25
Aft Centre spar	1	15/5/1	20	0.25
Eng. mounts in	2	7/4/4	50	0.50
Eng. mounts out	2	7/4/4	50	0.50
Machined Ribs (avg)	8	20/5/1	25	0.50
machining cost [€/h]	80 ⁵			
total part costs [€]	960			

21.2.3. Self-Produced Parts

This subsection gives a brief overview of the self-produced parts and their corresponding production methods. Apart from the material and labour costs, tooling will make up a significant fraction of the part cost for these self-produced parts. An overview of the estimated costs is presented in [Table 21.4](#).

Manufacturing of Simple Ribs

The simple ribs will be produced using laser cutting techniques. This technique allows for short production times and high accuracy. All the ribs can be nested and cut from single aluminium plates. The aluminium sheet material used is very cheap and the required labour hours are extremely low. From one large sheet multiple nested parts can be cut, without handling of the machine. The tooling required for such methods is relatively inexpensive as is indicated in [Table 21.4](#). As an additional benefit, this tooling can also be used to make other parts which allows for a more versatile production system.

Manufacturing of The Skin & Elevons

The manufacturing of the skin is one of the key processes driving the design and cost of the drone production. Each skin panel has a unique complex geometry which requires specific moulds to be produced. This prevents the outsourcing of these parts and highly influence the production costs of the drone. From sustainability requirements following the circular economy philosophy the skin was designed to be thermoplastic composite rather than thermoset. This greatly affects the cost of the production process, since thermoplastic tooling is significantly more expensive than their low cycle thermoset counterparts. The 6 panels will be made using compression moulding with aluminium tooling. This will lead to excessive tooling cost considering the low production number considered in [Chapter 2](#). Yet, this number is a reference for the case-specific operational concept. With increasing production numbers, the relative importance of this tooling cost will decrease. Initially, before final production, during prototyping and testing of the drone it is advised that cheaper, thermoset composite skins are used which allow for more versatile and cheap single use moulds. For the scope of this production plan, the elevon production is assumed to be part of the skin production, since the most expensive part is the skin which is incorporated in the surface area of the wing. The elevon rib geometry is not considered separately, but the mass and cost is integrated in the wing rib analysis. To account for the effect on the cost, an increased labour and material cost is incorporated in [Table 21.4](#)

After production of the skin panels the stiffeners will be attached by means of thermoplastic induction welding to the skin. Additionally, the clips will be glued on to the inner surface. The precise alignment needs to be very accurate. Therefore, a styrofoam mould is used with cutouts for the specific clips. The clips will be fitted into this mould and then an adhesive layer is applied to the the mould and clip surface and is placed on top of the skin. After curing, the styrofoam is removed from the skin. Additional costs are incorporated for this process. The estimated cost is indicated in [Table 21.4](#)

Manufacturing of The Engine Fairing, Payload Module and System Casings

The engine fairing, payload module and system casings are designed to be non-load carrying. Apart from some relatively small loads originating from drag or system attachments, these parts do not carry any of the primary loads of the structure. The main design requirements for these parts derive from specific geometry needs for attachment interface and the aerodynamic profile of the engine fairing. For this reason, 3D printing was selected as production method for these components. The cost of the tooling fur such production methods is relatively low, and mainly based on the volume constraints and the complexity of the parts. Thermoplastic PLA filaments are relatively cheap and the automated process, based on a CAD model input prevents high labour costs.

Table 21.4: Part production cost estimation for self-produced parts. The total part cost excludes the indicated tooling cost

Part	Quantity	Production Method	Material & Labour cost [€]	Tooling cost [€]
Simple ribs	8	Lasercutting (2D)	10	10,000 ⁶
Wing skin panels	6	Compression moulding	600	150,000
System casings	1	3D printing	100	15,000 ⁷
engine fairings	4	3D printing	20	[–]
Landing fin	1	3D printing	100	[–]
total part costs [€]	3,960			
tooling cost[€]	175,000			

In addition to these parts 3D printing is also considered for the production of the relatively small landing fin. Although this part will be load carrying during ground operations and the landing manoeuvre and will experience some aerodynamic load during cruise, 3D printed part is considered to be sufficient in terms of strength and stiffness. This being said, more analysis and testing is necessary to verify this performance. This will be done after conceptual design stages.

21.3. Assembly Process and Mounting Divisions

In this section, the assembly process of the manufacturing process of the drone is outlined, together with an estimation of the assembly costs. First, in [Subsection 21.3.1](#) and [Subsection 21.3.2](#) the sub-assembly division and their corresponding assembly procedures are explained. Then, in [Subsection 21.3.3](#), the final assembly procedure is discussed.

Several sub-assemblies are distinguished in the assembly process using mounting and production divisions. This is for production efficiency, logistical, maintenance and inspection purposes. In this section these sub-assemblies and their corresponding assembly processes are shortly described. Note that due to the nature of this conceptual design stage, the detail of the assembly process is limited. This overview aims to provide a general overview of the assembly process.

21.3.1. Centre Section Assembly

The middle section of the wing distinguished by the first machined rib on both wing sections forms one of the three main sub assemblies. This division is made due to production difficulties induced by the bulge at the centre section. This sub assembly consists of the following structural parts as described in [Table 21.5](#)

Table 21.5: Assembly parts of the centre section

Centre section parts
Front centre spar
Front aft spar
2 Machined central ribs
Upper centre skin panel
Lower centre skin panel
Payload module
Systems & attachment casings
Landing fin

Table 21.6: Assembly parts of the wing section

Wing section parts
Main spar
Aft spar
2 Machined engine ribs
2 Machine tip chord ribs
4 Laser-cut ribs
2 Engine mounts
Top wing skin panel
Bottom wing skin panel
Elevon
Actuator

Assembly Process Centre Section

The assembly process is as follows: First, the 3D printed payload module and system attachment frames are bolted to the centre spars. Hereafter the non-removable systems such as the avionics and the parachute are positioned, and the wiring is put in according the electrical diagram described in [Section 7.1](#). After this, the 2 ribs are bolted to this centre section, together with the landing fin. In the end, the upper and lower skin part are bolted on the machined rib parts to form the complete sub-assembly. The estimated assembly processes and costs are listed in [Table 21.7](#)

Table 21.7: Assembly Tasks and Estimated Costs For the Centre Section

Assembly process Description	Estimated labour hours [h]
Bolting 3D printed attachment frames to front and aft spar	1
Placing of non-removable systems and wiring	2
Bolting landing fin and centre Ribs	0.5
Bolting upper and lower skin section	1
Testing electronic interfaces	0.5
Labour cost [€/h]	150
Sub-assembly cost [€]	750

Table 21.8: Assembly tasks and estimated costs for the wing section

Assembly process Description	Estimated labour hours [h]
Joining and positioning of Ribs and main spar framework	3
Assembling aft spar and elevon	2
Installing actuator	0.5
Installing wiring and interfaces	1
Testing electronic interfaces	0.5
Testing elevon mechanism	0.5
Placement and joining of bottom skin panel	1.5
Labour cost [€/h]	150
Sub-assembly cost [€]	1350

21.3.2. Wing Section Assembly

The wing section stretches from the first machined rib to the wingtip. The left and right wing are symmetric with respect to the drone's longitudinal axis. Therefore only one wing section assembly is discussed, since the assembly process for both sections will be similar. The wing section consists of the parts as described in [Table 21.6](#)

Assembly Process Wing Sections

The assembly process for the wing sections is shortly described. First, the main spar will be bolted to the machined tip spar. Thereafter the outboard ribs will be slid on to these spars and positioned on their designed position using rings. Concurrently, the engine mounts and will be slid on these spar rib connection and positioned by similar rings and pins. While positioning the engine mounts, wiring is threaded through the the inside of the main spar to the engine mount interface, actuator attachment and the tip rib. When all ribs are positioned the aft spar and elevon will be slid through the sub assembly. The actuator is fastened on the first engine rib and connected to the elevon pin. In the end, the bottom wing skin panel is attached by first pushing the clips on the laser cut ribs and secondly bolting the skin to the trailing edge of the machined rib parts. This concludes the wing assembly. The upper skin panel remains disassembled at this stage. The estimated assembly processes and costs are listed in [Table 21.8](#)

21.3.3. Final Assembly

Now, after the sub-assembly of the centre section and wing sections the final drone can be assembled. This process consist mainly of bolting the individual sections together, attaching the upper skin panels, and placing the engines and corresponding fairings. The processes and estimated costs are listed in [Table 21.9](#).

21.4. Quality Control and Testing

An important aspect of manufacturing process of the drone is quality control. In the manufacturing aspect, quality control relates to whether the manufactured drone meets the requirements envisioned in the design. Any discrepancies from the design stemming from manufacturing inaccuracies, damages during assembly or deviations from the production plan must be identified and resolved to ensure that the final product meets the standards. Apart from this, the control mechanisms, electrical circuit and engine needs to be tested on system level. The quality control will mostly consist of visual inspection of both parts and assembly. Most parts are outsourced which guarantee high certainty that the parts meet the specific standards. The self-produced parts

Table 21.9: Final assembly tasks and estimated costs.

Assembly process Description	Estimated Labour hours [h]
Bolting the wing sections to the centre section	2
Connecting the wiring interfaces	0.5
Attaching the upper wing skin panels	1
Attaching the engines into the engine mounts	1
Fastening the fairings to the engine mounts	0.5
Labour cost [€/h]	150
Sub-assembly cost [€]	750

Table 21.10: Processes involving quality control and system testing and their corresponding estimated cost.

Assembly process Description	Estimated labour hours [h]
Compliance inspection outsourced parts	2
Visual inspection self-produced parts	4
System scale circuit tests	2
Elevon mechanism calibration	2
Engine testing and calibration	2
Avionics software calibration	2
Labour cost [€/h]	150
Sub-assembly cost [€]	2100

however and the assembly process are more vulnerable to manufacturing discrepancies. Therefore, additional visual inspections are implemented in the manufacturing process to ensure the quality of the product. The processes involving quality control and system testing are listed in [Table 21.10](#). More drastic methods of Non-destructive testing are not considered, since the high accessibility of the removable joint design allows for easy inspection and maintenance.

21.5. Total Manufacturing Cost

To summarise this chapter, a total cost estimation is presented in [Table 21.11](#). Note that this overview consists merely of the manufacturing cost - not the production cost. A more complete estimation of the total production costs and business plan is discussed in [Section 26.2](#). As is indicated in [Table 21.11](#), the manufacturing cost consist of the individual part cost, assembly cost and tooling costs. The fraction of the tooling cost that contributes to the total cost is found by dividing the initial investment cost by the expected production numbers found in [Section 23.2](#), for the first production batch of about 100 products. The relatively low number will increase the tooling cost fraction. This, and also part cost fractions are expected to drop when the production number is increased.

Table 21.11: Overview of total manufacturing cost of the drone.

Component	cost [€]
Part cost	5430
Assembly Cost	2850
Quality control & testing	2100
Tooling costs	1750
Total manufacturing cost:	12130

Operational Concept

The mission needs to be supported by an operational concept. Despite the top level description remaining the same as described in the midterm phase [9], new insights in the technical performance and market research provide additional information on its implementation. The aim of this concept is to merge the product and market of interest into the most feasible, cost effective and commercially attractive solution.

As follows from the updated market analysis, the operations supporting SAVED consist of a tailored service to a country or region rather than a product to sell, reason for which its generalisation is difficult. Since the aim of this chapter is to provide the most detailed explanation of the concept possible, the approach taken is the following: while a general description of the service is first shown in [Section 22.1](#), a more detailed case study is done for Sri Lanka, a prime candidate for SAVED, in [Section 22.2](#).

22.1. General Concept for Operations

The operational concept is to converge towards the most optimal solution of the problem identified in the market analysis. This problem is, at its core, the need for time efficient logistics during the delivery of critical goods. This need originates in countries where these (for instance blood bags) are centralised in one location and cannot be transported to other regions within a reasonable span of time, which can be due to several reasons. First, an inefficient network of roads, leading to time consuming logistics among regions of the country. Secondly, an absence of all-season roads, resulting in inaccessible locations or even obstruction of roads to main hospitals. With these combined, the procurement of critical goods such as blood bags, gathered only at far reaching locations, is considered to be ultimately insufficient.

Solving this issue in logistics and road networks with a reliable road transportation system would take too many years in which countless lives could be saved. The solution for this general problem can be found in a small, autonomous VTOL electric drone carrying these critical supplies, also resilient to wind gusts and light rain. The operational concept thus consists of a network of bases housing this fleet of drones to compensate for the conventional alternative, proved deficient. Therefore, instead of trying to transport blood bags to all hospitals in the country once they need it, they are transported only to a few locations systematically, decentralising the goods and allowing for their delivery in a flexible manner, covering for all unpredictable circumstances. This allows for a much better flexibility and responsiveness in situations of emergency, also making them useful outside hospitals. Since the number of bases, drones and other intricacies of the operation depend heavily on the geography and number of hospitals of each case, the operations supporting SAVED are considered as a service. Each of these bases, however, can be generalised to consist of the following elements.

- **Storage and recharge module:** provides storage for the medical supplies (by means of a cooler in the case of blood bags) and the battery recharging system.
- **VTOL platform module:** the VTOL platform simply serves as the area, of dimensions not much larger than SAVED's wingspan (3m), for it to land and take-off vertically. Due to the fact that a runway is not needed, the size and location of the base can be optimised.
- **Hangar module:** the hangar serves as a storage for the drones themselves while they are not used for maintainability purposes.
- **PV array:** all of the above requires electrical energy. After studying all possibilities extensively [9], it becomes clear that the most feasible option for energy generation is a PV system, complying with the requirements for a fully sustainable recharging point. This, however, it is to still be connected to the grid in case of no sunlight conditions, returning power to it when an excess of electricity is generated.
- **Operators:** the size of each specific base determines the number of trained technicians needed to manage it. Their tasks are to manage the payloads, recharge the batteries and handle the drones from the hangar to the VTOL platform. Moreover, technicians are to receive the delivery orders and there must be always one person overseeing the air traffic for safety purposes.

The more bases implemented in the region, the larger the coverage of the operation. If bases are within range of one another, this means that drones can, as an alternative to the typical delivery missions, also change base and transport medical supplies between bases. This opens a wide new range of possibilities and is very helpful in an emergency situation if a certain location is in urgent need of being supplied. Additionally, a future consideration would be to use SAVED drones to get the medical supplies and bring them to the bases for storage. This could greatly improve the supply chain efficiency, yet significantly increases the costs, which the initial operation plan does not account for. The discussion continues for the "basic" operation only: covering as much region as possible whilst minimising costs, for which the medical goods need to be transported to the base by road.

The inputs and outputs of the base are the following. First, each of these bases is to be delivered with the necessary medical goods by road, as well as the drones themselves before the start of their operational life. As mentioned, this base is to be equipped with a solar panel array for its self-sufficiency, yet it is to also be connected to the grid. This ensures electricity in no sunlight conditions and the base returns its energy excess during peak hours. The output of the base, on the other hand, consists only of the drone going to the hospitals at reach, as well as any other location in which an emergency situation arises within the range of SAVED.

22.2. Case Study

The general description above can be put into more detail if a specific case is studied. From the market analysis it is clear that the countries in need of this service are those with a deficient logistical network to transport critical goods, yet able to invest in this cheaper alternative. As mentioned, Sri Lanka is a prime example of such a country. Not only does this country lack of the aforementioned efficiency in road logistics, but the rainy season appears at different times in different regions of the country, making it extremely unpredictable to know what roads will be inaccessible when. Moreover, large regions are rural and of difficult access, for which a VTOL capability is desired. Lastly, this issue has already been identified by the Sri Lankan government, and they are openly eager to invest in medical drone delivery to suffice for it¹. The number of bases are identified in Subsection 22.2.1 and their characteristics are given in Subsection 22.2.2.

22.2.1. Identification of Base Locations

The specifics of each base depend on the number of bases that are deployed in the region. To identify how many are needed, several approaches can be taken, which comes determined by the objective of the operation. The first and foremost objective is to spread the bases such that all of the main hospitals are within the range of the drones of at least one base. The second objective is to cover for the need for emergency situations outside of the hospitals, for which it is desired to plan the bases in a way that cover as much area as possible. When ensuring these two objectives, the bases are laid out such that all of the main hospitals are within the reachable range and the total area covered is maximised in the country. This is the approach taken for the initial deployment of the project and is visualised in Figure 22.1. This shows a possible solution for the country; it is established that the blood bags are only gathered in the capital, Colombo², marked with a blue circle. All General District Hospitals of the country are marked in red and they all need to be reached by SAVED. For their complete coverage, it is seen that four bases are needed, located at the centre of each grey circle of 75 km radius. By doing so, if the base is systematically replenished of blood bags by road, the mission would allow for complete freedom in choosing where to bring them to: hospitals or any other reachable location in need (smaller hospitals, individuals, etc.) provided the landing point is available or the GPS signal is sufficient to find the coordinates. Essentially, this means that the current pull system in the logistics, impossible to suffice in demand due to its slow responsiveness, is changed to a push-pull system, as seen in Figure 22.2.

Although not accounted for the start of the project deployment, another approach that can be taken once the operations are more developed is the fact that the logistics could rely on the network of bases to avoid doing a roundtrip. Without it, not only there is double the range for cruise, but also

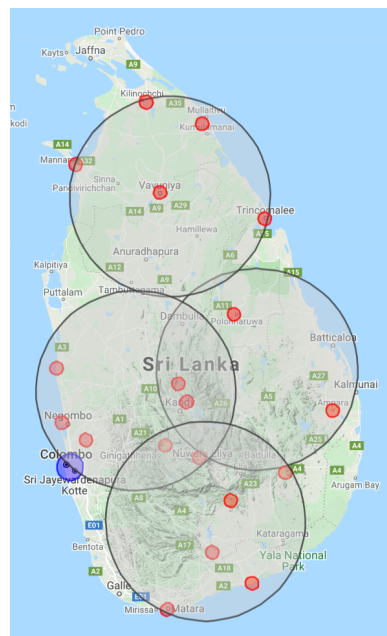


Figure 22.1: Coverage of the operational concept in Sri Lanka

¹<http://bitly.ws/8MgD> [Cited on 16-06-2020]

²<http://bitly.ws/8MgD> [Cited on 16-06-2020]

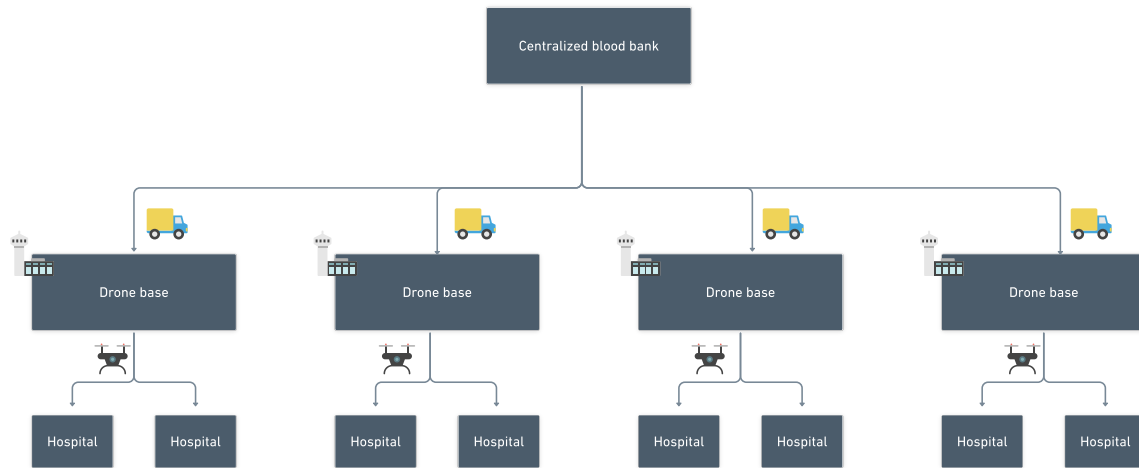


Figure 22.2: Push-pull logistical system

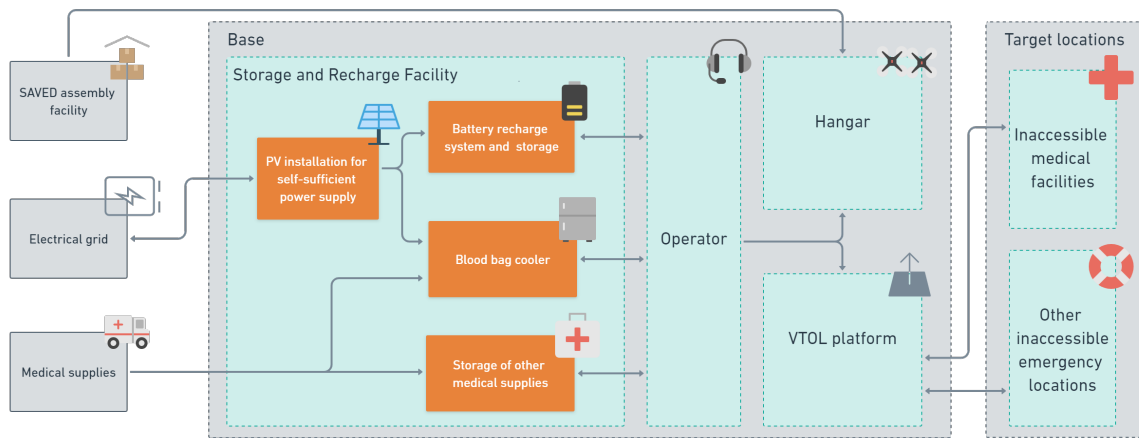


Figure 22.3: Inputs and outputs of the base system [9]

half of the energy reserved from the VTOL phase is saved. This would allow to increase time efficiency simply by interchanging the drones from one base to another. If one of them also covers Colombo this means that a drone can go from there to another base, its payload be interchanged and then proceed subsequently, making redundant the replenishment of goods by road. This can be further studied once the basic operational concept proves successful.

In other words, implementing more bases does not only increase the efficiency of the network by allowing an easy interchange of drones from one base to another, but also can eliminate the need for the "push" segment of this logistical network. If Colombo is covered, the drones can go from the nearest base to the centralised blood bank, return and transport the payload by a series of drones from base to another, covering all of the island. This would be necessary in case the monsoons were to be strong enough for the "push" segment not to be possible, for which all of the transport then needs to be done by air. Moreover, this would also account for another common-use case in which SAVED could help the current logistical system: if all of the country can be covered by air, test samples from remote locations can be taken immediately to Colombo for testing without the need of road transportation.

22.2.2. Specifics of the Base

Once the location of all bases needed has been determined, the specific needs of each can be given. These specifics flow down from the number of hospitals the base is at reach: North, West, East and South bases are to give coverage to five, seven, four and seven General District Hospitals, respectively, as well as the many more smaller ones in the region. Each of the bases is visualised as a system as in [Figure 22.3](#).

Number of Drones Required

The first decision to make is how many drones to have at each base. When comparing it to the operations of Zipline in Ghana, the country with the highest coverage, it can be understood they have a drone for each 248,000 inhabitants³. By applying the same proportion, this leads roughly to 88 drones for the entire operation in Sri Lanka, thus 22 per base. Although the countries and mission profiles are different, this ratio is deemed applicable for two reasons. First, a number of the order of around 100 units is desired from the business and finance perspective, due to the aforementioned high costs in production for the thermoplastic skin. Second, SAVED has a mission profile that is advantageous with respect to Zipline: the inclusion of VTOL capabilities make for a more versatile vehicle, potentially fulfilling more needs. For these reasons, Zipline's ratio of drone per inhabitants seems applicable as a first estimation.

This accounts not only with coverage of the General District Hospitals, but also for emergencies in any other location, including smaller hospitals, individuals and such. Only a few regions are left without coverage, which again can be further improved by implementing more bases if the first proved successful and there was to be a need for more. Moreover, it is important to consider that this basic coverage focuses on rural areas, whilst coastal are usually better connected to the capital through the railway system or can move within the range of one of the bases. Despite this decision seemingly being too large of an initial investment, it is also important to consider that the higher the number of drones produced the more depreciated the initial costs are going to be.

Energy Generation

As already established, in order to optimise the operating time of the drones the batteries are made modular, retrievable and rechargeable separately from the drone. This decision, although adding weight to the structure, is made for the purpose of economic sustainability, as the availability of the drones is greatly improved. In order to eliminate the time a drone is inactive, the only consideration left is just to ensure a battery will always be recharged once a mission starts. This means there should be more batteries than drones, and it needs to be accounted that an average mission takes around two hours to complete (with a cruise speed of 22.5 m/s and a range of 150 km).

The number of the batteries estimated for each base, combined with the rest of energy needed for keeping the base operative every day, a total power required can be derived. With this information, the solar arrays required can be sized for each specific case. Sri Lanka has already 10,389 installations of rooftop systems of solar PV arrays⁴, for which its acquisition can be assumed to be made locally. Moreover, the Ministry of Power and Renewable Energy just extended the loan scheme for rooftop panel systems⁵, further proving the aim of the country to exploit its solar potential.

Traffic Management Plan

Planning the management of drone traffic within the country of operation is based on two factors: administrative compliance and overseeing the system's autonomy. Together, these are to ensure a safe, continuous, efficient and certified traffic management.

The first, administrative compliance, consists of subscribing to the laws and cooperating with the air traffic management framework of the country, thus agreeing and warning when a mission is taking place with civil aviation authority for safe operations. In a more general view, however, the operations are to follow the several guidelines⁶ in air traffic management provided by the International Civil Aviation Organization (ICAO), a branch of the United Nations. These international and local guidelines are to be directly implemented in the path planning algorithm as a means of compliance with regulations and allowing the certification of the mission.

The second, overseeing the system's autonomy, consists of ensuring that the autonomous segment of the operation is safe. With several drones operating autonomously at the same time, this segment must be as complete as possible, as well as overseen. For the autonomous behaviour, an extensive path planning algorithm is developed and simulated [9]. This accounts for the interaction of the drone with surrounding elements including obstacles, no fly zones, populated areas and other real time data such as the dynamic behaviour of the weather. Moreover, the obstacle avoidance algorithm from the perception module avoids crashing into other drones or movable obstacles. With the path planning and obstacle detection algorithms, traffic management can safely rely on the autonomous capabilities of SAVED. Nonetheless, since several drones are to be operative at the same time, this traffic must be overseen at all times by one of the operators. This is done for safety purposes to mitigate the impact of unpredictable circumstances.

³<http://bitly.ws/8Mry> [Cited on 16/06/2020]

⁴<http://bitly.ws/8Ms7> [Cited on 16/06/2020]

⁵<http://bitly.ws/8Ms8> [Cited on 16/06/2020]

⁶<http://bitly.ws/8NiD> [Cited on 18-06-2020]

23

Logistical Concept

The aim of this chapter is to explain the logistical concept supporting the operation of the mission. [Section 23.1](#) explains the testing procedures following from the detailed design of the drone before the large scale manufacturing takes place. [Section 23.2](#) explains the top level procedure for manufacturing, following from the production plan in [Chapter 21](#). Lastly, [Section 23.3](#) gives an overview of the logistics in the transportation.

23.1. Testing Procedures

The first step in the logistics following from the finalisation of the design consists of the testing procedures. These depend on the subsystem and the components involved. Firstly, the SMM department does not count with testing procedures outside of the quality control done on each of the systems produced and explained in [Section 21.4](#), thus not diverting costs to destructive testing. Secondly, the testing procedures for Power and Propulsion start once the components of the subsystem are gathered. First, the engine is tested to ensure that it has the efficiency as specified by the manufacturer, as well as checking that it can indeed manage the power needed. Analogously, for the batteries, normal flight cycles will be simulated in order to check the battery behaves as expected. Thirdly, the testing planned to be carried out by the aerodynamics department is twofold, both consisting of wind tunnel experiments. First, a scale model of the entire drone is created to ensure that the lift drag polar computed is being complied with. Secondly, a full scale model of the half wing is used to gather experimental results on the interaction between propeller and wing. Lastly, once the first prototype is produced, the stability and control capabilities of the drone are tested. The aim is therefore to ensure that, as expected from the eigenvalues and responses, the only unstable motion is the spiral and it can indeed be corrected by deflecting the elevon. For control, the requirements on controllability are assessed by seeing how the drone reacts to certain control inputs. In other words, the prototype is used to ensure that the model reflected the real behaviour of the drone to an acceptable extent, including the linearisation of the control inputs.

23.2. Manufacturing and Assembly

As explained in [Section 21.1](#), the manufacturing of most parts is outsourced to subcontractor companies to avoid excessive tooling costs. Other parts are self-produced for being either too specific for SAVED or because it is desired to stack on versatile parts for replacements, simple enough to be self-produced. To minimise transportation costs, the self-produced parts are already produced in the general assembly facility, while the outsourced parts are to be transported there. This assembly facility requires of highly skilled personnel for which it is located in Europe. Despite the higher wages, basing the project in an industrialised country ensures a good quality in production and the availability of materials and other resources. This decision is done in accordance with the Business and Finance and SMM departments, as the complexity in production and high investments required are such that production and assembly cannot be entirely outsourced to the country of operations. Assembly of the system is done with several sub-assemblies, using mounting and production divisions, for the reasons of production efficiency, economic purposes, accessibility and maintenance.

23.3. Transport

Since the manufacturing and assembly are to be done in Europe, the systems are transported to the country of operation. This transport might induce additional loads due to vibrations, already accounted for in the safety factor of the structural design. Moreover, the transport is done in rigid containers, protected by foam. Lastly, the batteries are to be shipped separate from the systems not to damage them in case of fault. Both are to be shipped by boat in cargo containers from the country of production and assembly to the country of operation. Nonetheless, it is desired for the bases of operation to be constructed using local resources entirely, including the acquisition of the solar panels, as explained in the operational concept in [Chapter 22](#). Given that the initial implementation of the operation concept proves successful, it is desired to also outsource the production and assembly of the drones to the country of operations to reduce costs and invest in local economy and talent.

24

RAMS Analysis

In this chapter the Reliability, Availability, Maintainability and Safety (RAMS) evaluation is presented. It is of utmost importance that these criteria are taken into account while designing, as it will significantly reduce potential costs of the drone in the future. In [Section 24.1](#) the reliability of SAVED is discussed and an explanation is given on how SAVED has been designed for high reliability. Next, in [Section 24.2](#) a description is given on how SAVED is able to reach an excellent maintainability score. Following this, in [Section 24.3](#) is described how the logistics ensure that SAVED will be available when its abilities are requested. Lastly, in [Section 24.4](#) a detailed explanation is given on how SAVED has planned to reduce the probability of harming third parties during the mission to a minimum.

24.1. Reliability

Reliability is defined as the probability that a system will perform without failure over a specific period of time. Ideally, the reliability is defined as a percentage of dividing the number of failures by the total number of missions. However, in this stage of the design process this will not be based on true events, and will therefore have a large uncertainty. Consequently, it was decided to express the reliability score in a qualitative way. In [Chapter 18](#) a detailed risk analysis has been conducted taking into account the risks' probability of occurrence and their impact on SAVED's performance. Based on these categories 5 risk levels have been distinguished. To ensure a high reliability it is of paramount importance that the average risk level of SAVED is between risk level 1 and risk level 2 with no risks scoring higher than risk level 3. A more detailed explanation on how the risks are prevented and mitigated to guarantee a high reliability is presented in [Section 18.1](#). From this chapter it can also be concluded that the average risk score is 1.7, with only one risk in risk level 3 and the remaining ones are all scored in risk level 1 and risk level 2. It can therefore be said that SAVED has been designed to reach a high reliability during the actual missions. More accurate reliability scoring can be given in the next phases of the design, when actual flights have been performed.

24.2. Maintainability

Maintainability is defined as the ease with which an item can be maintained. In this RAMS analysis the maintenance is divided into two groups: preventive maintenance and corrective maintenance. Firstly, preventive maintenance, which corresponds to scheduled maintenance is described. This maintenance is related to the general inspection of the drone and the time it takes before the drone is ready for take-off. Corrective maintenance, which corresponds to unscheduled maintenance is strongly related to the reliability factors, since these determine the frequency corrective maintenance has to be performed. The equation that determines the Mean Time Between Maintenance (MTBM), and how preventive and corrective maintenance influence this can be found in [\(24.1\)](#).

$$MTBM = \frac{1}{\frac{1}{MTBM_{unscheduled}} + \frac{1}{MTBM_{scheduled}}} \quad (24.1)$$

SAVED has been designed such that it can be maintained in the least amount of time possible. This is done by only considering non-permanent joints such as clips and bolts in part assembly. Permanent joints such as rivets and adhesive bonding were intentionally avoided in the structural design to ensure relative easy disassembly, without weakening the structure. A more detailed explanation is given in [Section 8.3](#). In addition to this replaceable batteries are used in SAVED's design. This results into minimal maintenance time when the battery must be removed. This feature will also improve SAVED's availability. This will be further analysed in [Section 24.3](#).

In this stage of the design process it is however too early to set values to this, because it will not be based on true events. This will need to be further analysed in the next phase of the design process. In this phase the actual maintenance time of the drone will repeatedly be timed to get a better expectation of this value. However,

for now it must be said that SAVED has been designed for MTBM to be at the lowest possible level, especially because of the non-permanent joints.

24.3. Availability

Availability is defined as the degree that a system will be available for use when its service is required. SAVED's availability heavily depends on its maintainability, which is described in [Section 24.2](#) and the number of operating drones per base.

As mentioned in [Section 24.2](#), SAVED has been designed in a way that minimises the required maintainability time by using replaceable batteries and aluminium clips. On top of this the case study described in [Section 2.3](#) states that there will be 22 drones operative per base, which is explained in more detail in [Subsection 22.2.2](#). Taking the minimal maintenance and the number of operating drones into consideration, it is expected that in general at least one of SAVED's drones always will be available to perform the mission when a request comes in.

Similarly to the maintainability it is too early in the design process to set a final value as availability score. This will be further analysed and verified in the next phase of the design process. Similar to the maintenance time, in the first couple of months of testing the availability score can assessed and it will be evaluated if the amount of operating drones is sufficient.

24.4. Safety

Safety is defined as the ability of not harming the environment and the system itself while performing a mission. This is achieved by safety engineering, which means reducing the risk of harming any third parties and itself in case system failure occurs during the flight.

To prevent this from happening SAVED has been designed according to the safety engineering standards [32]. First of all, in [Section 18.1](#) an extensive explanation is given about how risk mitigation is included in the design process. Furthermore, to reduce the probability even more of causing any damage whatsoever to any third parties, SAVED will also avoid highly populated areas as much as possible as explained in [Chapter 12](#). These design considerations make SAVED's operations as safe as possible and reduces the probability of causing any damage to third parties and itself to a minimum.

Sustainable Development Strategy

Adopting a critical view of the environmental, economic and social implications of a project is considered to be the cornerstone to ensure its sustainable development. For this reason, the sustainable development aspect of the project has been thoroughly accounted for throughout every stage of the conceptual design. The EcoDesign Strategy Wheel, as considered in the Project Plan [10], gives an idea of the systematic approach carried out during the process, used to optimise the life cycle of the product from conceptual design to its End of Life (EOL). Adhering to this, guidelines could be developed for subsystem design in a more detailed sustainable development strategy in the Baseline Report [8]. From these, the ones impacting the concept trade-off were expanded in [9], giving a greater insight in the recyclability of the concepts. The Sustainable Development Strategy of this project has proven to be a living aspect, converging together with the technical design. This chapter thus draws final conclusions about how the design accounts for sustainability and its contribution to it. The chapter is structured as follows. Firstly, the results of the considerations in the subsystems of Power and Propulsion and SMM are given in [Section 25.1](#), [Section 25.2](#) and [Section 25.4](#), respectively. Secondly, insights on Aerodynamics and Autonomous Flight are given in [Section 25.3](#) and [Section 25.4](#). Lastly, Business, Finance and Operations concepts, as well as the main social sustainability implications, are assessed in [Section 25.5](#) and [Section 25.6](#), respectively.

25.1. Power and Propulsion

For the design of this subsystem, several considerations on environmental sustainability are made. [Subsection 25.1.1](#) gives an assessment of the design decisions affecting the energy consumption, while [Subsection 25.1.2](#) makes a comparison in terms of emissions with a conventional road transportation system. Lastly, [Subsection 25.1.3](#) verifies the requirements on noise generation for the chosen propeller.

25.1.1. Energy Consumption

The top level user requirements on energy consumption solely consist of using a sustainable recharging point for a fully electric or a hybrid system. Adhering to these, the analysis done in [9] investigated all of the possible options to assess the best combination of energy recharging and propulsion system. In order to fully comply with the requirements, the most feasible option was concluded to be that of a fully electric propulsion system. This decision is supported by the power and propulsion department, as the technical feasibility of the mission using only electric energy is proven [9]. Moreover, the operations concept supporting the mission set as preference using a photovoltaic (PV) system for energy generation. For these reasons, the detailed design has focused on a fully electric propulsion system and battery recharging using solar panels. In conclusion, a fully electric system is used and recharged by solar energy, a non-depletable source. These design decisions directly verify the two requirements set on energy consumption, which are **SAVED-CONS-SD-POP-01** (SAVED shall use electric propulsion or hybrid concepts) and **SAVED-CONS-SD-POP-02** (the charging/refuelling point of SAVED shall use a sustainable source of energy).

25.1.2. Emission of Greenhouse Gases

Given that the entire mission is done using electric energy and its recharging is sustainable, no greenhouse gases are emitted at any point during the operation of SAVED, thus verifying requirements **SAVED-CONS-SD-EM-01** and **SAVED-CONS-SD-EM-03**. To gain a greater insight into the environmental footprint of the battery production, requirement **SAVED-CONS-SD-EM-02** is to be verified. This states that SAVED shall have 50% less green-house gas emissions per payload per distance than a conventional car, accounting for the manufacturing of the batteries. This analysis is not to compare the mission performance or objectives, but to make a top level comparison in terms of carbon emissions, detached from the problem at hand. The emissions are normalised over the distance travelled and payload carried so that it also accounts for the excess in payload the car would transport. To perform this analysis it is assumed the car would transport 100 times SAVED's payload. For the

conventional car, it is gathered that its consumption is around 130 gCO₂/km¹. If the payload capacity is 300 kg, this yields the emissions per distance per payload of 0.43 gCO₂/km/kg.

For the case of SAVED, the emissions from the battery production need to be normalised over its entire lifetime. First, the greenhouse gases emitted are computed from the battery specifications. Three packs of energy packs are set in parallel, with each one consisting of six cells in series, each with a capacity of 11.6 Ah². This results in a total capacity of three times the pack capacity (34.8 Ah or, equivalently, 0.8039 kWh). Battery manufacturing of a Li-Po battery is estimated to be around 100kg CO₂ per kWh³. With this estimation, it is gathered that the battery manufacturing footprint is 80.39 kg of CO₂ per drone produced, arguably the greatest contribution to its environmental footprint. It is also estimated to endure around 3,000 cycles (until its capacity reaches 0.725, accounting for a Depth of Discharge of 90%). Since each of the cycles is a single mission (150 km) the total distance travelled in its lifetime is straightforwardly computed. Also, the payload weight taken is 3 kg. This yields an emission of greenhouse gases of 0.0595 gCO₂/km/kg, easily complying with the requirement. In conclusion, it has been well established that, even when accounting for the battery production, SAVED is below the standards of greenhouse gas emissions when compared with road transportation.

25.1.3. Sound Level

As planned during the midterm phase, an analytical tool is built to assess that the noise generation is within acceptable levels. This is done as part of the selection of the propeller in Subsection 7.3.4. For the construction of this analytical model, sound pressure levels are determined with respect to the position from the drone. The final requirements are defined to be **SAVED-CONS-SD NOI-01** (the sound pressure level shall be below 110 dB at 1.5 m during VTOL conditions) and **SAVED-CONS-SD NOI-02** (the sound pressure level shall be below 35 dB at a distance of 500m during cruise conditions). These requirements are thus verified as an approximation by assessing the noise level from outside a radius of 1.5m from the centre of gravity. Furthermore, it is assumed that the noise is transferred spherically and atmospheric attenuation is neglected. These assumptions do not account for the interference between propellers, which makes the result in Subsection 7.3.4 to be overestimated. Still, this results in verifying both requirements successfully, as the noise generated in sound pressure level is of 106.2 dB at 1.5 metre during VTOL and 9.02 dB at 500 metre in cruise conditions.

25.2. Structures, Materials and Manufacturing

This section aims to perform the final assessment in the development of the SMM department. Material Selection, Manufacturing and Assembly are presented in Subsection 25.2.1, Subsection 25.2.2 and Subsection 25.2.3. Final considerations on the decommission of the system are drawn in Subsection 25.2.4.

25.2.1. Material Selection

Following the established guidelines of recyclability [9]: **SAVED-SD-SMM-MAT-01** (30% of the mass of structural materials shall come from a recycled source) and **SAVED-SD-SMM-MAT-02** (80% of the mass of structural material shall be recycled after decommissioning of the drone). The recyclability of the materials was also considered during the concept trade-off as a decision criteria using the Material Circularity Indicator (MCI)⁴ [9].

To comply with the requirements, the decision was made early on in the design to heavily rely on aluminium and thermoplastics for the skin. This however comes with the disadvantage of increasing the costs of tooling. Still, considering the scale of production, it is considered feasible. This way, recyclability was not only part of the trade-off but a major driver for the design itself. This resulted in having a total structural weight percentage of 42.3% from recycled materials and a 91% of recyclable ones, thus verifying both requirements for recyclability and ensuring a sustainable availability and use of the materials. The computation of the percentages is found in Table 8.5, where semi recyclability is assumed as 50% recyclability.

25.2.2. Manufacturing

An emphasis is put on the manufacturing process to reduce waste of material, especially that which is non-recyclable. This comprises of two factors. Firstly, to reduce the amount of non recyclable bulk material it is important to consider the amount of material that is recyclable. This, however, is already considered during the material selection from the requirements on recyclability. Secondly, to reduce the waste of resources in

¹<http://bitly.ws/8PCC> [Cited on 12-06-2020]

²<http://bitly.ws/8KQQ> [Cited on 12-06-2020]

³<http://bitly.ws/8KQS> [Cited on 12-06-2020]

⁴<http://bitly.ws/8NbT> [Cited on 18-06-2020]

general, manufacturing is to adhere to a lean philosophy. Lean manufacturing consists of reducing waste in every possible instance of the process⁵. For example, transport is minimised by producing the self-produced parts in the assembly facility, waiting times are to be minimised so as to reduce inventories and ease the sorting, and control quality procedures are to be followed systematically yet stringently to keep the procedure efficient.

25.2.3. Assembly

During assembly, the focus is put into using mounting divisions for economic and environmental purposes. Sub-assemblies allow for adding more expensive parts later, making production more efficient and improving the accessibility and maintainability of the drone during operations. Firstly, this allows for an easier disassembly and therefore a successful recyclability of the materials. These ideals were integrated into the design by driving decisions on the joints used as explained in the production plan [Chapter 21](#). Using removable joining methods, such as bolts or clips, allows for a good maintainability and disassembly for recyclability purposes.

25.2.4. Decommission

A sustainable use and operation of the drone is incomplete without a responsible decommission of the vehicle at its end of life. This sustainable EOL is anticipated and designed for already. When verifying the requirements on the material selection, it is seen that an 86% of the structural materials is recyclable. Moreover, retrieving these materials is doable due to the emphasis put into the use of removable joints such as clips and bolts.

Upon decommission of the vehicle, the drone is dismantled into the different components and then sorted into three categories. First, working (and usually expensive) components like sensors can be reused and taken to the assembly facility. Secondly, non-critical structural parts made of non-recyclable materials can also be taken to assembly facility. Lastly, the critical load-bearing parts are disposed, whether they are recyclable or non recyclable, and sorted based on their material. The recyclable materials are taken to the recycling facility and the non-recyclable materials to disposal facilities. As further recommendation, the procedure to discard the electric batteries in an economical and safe manner must be studied.

25.3. Aerodynamics

Despite its small influence on the project's sustainable development, the selection of the airfoil is considered for this department. It was decided for SAVED to make use of an already existing airfoil, selected in [Section 9.1](#), resulting in saving resources for its testing. Alternatively, if the airfoil was designed, a larger amount of resources would have had to be spent on testing and validating the performance during the following phases of the project.

25.4. Autonomous Flight

The autonomy in flight relies on a robust path planning algorithm as shown in [Chapter 12](#), setting the optimal path to the target point by importing information on weather information, no fly zones, static and dynamic obstacles. This allows to compute the most efficient solution whilst still ensuring a safe operation of the system. This does not only relate to economic sustainability, but is also actively used to minimise the impact of the operation in populated areas in terms of noise pollution. By doing so, a constraint is set on the population density of the areas that SAVED can fly over. A population density map is implemented in the path planning algorithm and the more populated areas can be avoided in a non-binary, continuous manner. Nevertheless, it is also set as a requirement not to fly over areas with more than 20,000 inhabitants per kilometre squared, unless it is within a range of 10km from the target location. This figure, comparable with the most populated cities in Europe, is set to avoid cruising over very populated cities and thus avoid increasing their noise pollution. Nevertheless, the 10 km serve as the exception so that the target location can be reached without any restrictions, for example the hospital at the centre of a major city. This is verified directly by designing the path planning algorithm [9] such that the areas from the population density map of over $20,000 \text{ pop}/\text{km}^2$ outside a range of 10km from the target location are modelled by implementing them as no-flight zones.

25.5. Business, Finance and Operations

This section covers the sustainability implications coming from the perspective of the business, finance and operations supporting the project. [Subsection 25.5.1](#) describes the philosophy of adding value to the product without using more resources. [Subsection 25.5.2](#) assesses the plan for the transport and distribution of the

⁵<http://bitly.ws/8Q6D> [Cited on 18-06-2020]

drones in the country of operation. Lastly, [Subsection 25.5.3](#) assesses the Reliability, Availability, Maintainability and Safety (RAMS) aspects of the drone and operations.

25.5.1. Function Integration

If the product manufactured can serve for more purposes rather than the one that is being designed for, it is more versatile and able to enter other markets, following from the EcoDesign Strategy Wheel goals in [10]. This contributes to the economic sustainability of the project, as the drone can be sold for other purposes rather than the service explained in [Chapter 22](#). In other words, the drone can be used for other applications without additional constraints or investments in resources, but rather exploiting the pre-existing ones to result in a more flexible product. As concluded from the market analysis in [Chapter 2](#), the need found is the service for a VTOL drone of long range, used to connect centralised goods to other locations in need when the logistical roads are inefficient, and the product developed is optimised for this need. Nonetheless, the modular payload compartment allows for flexibility in the service provided, and combined with the unique VTOL capability and long range, the possibility arises for selling the drone detached from the base design and operational concept. This makes selling the drone as a standalone product a secondary stream of revenue, aiding in the economic sustainability of the project.

25.5.2. Transport and Distribution

Considering again the target service, the transport and distribution is to be done in an economic and socially sustainable manner. For ease in attaining the resources needed, manufacturing and assembly are to be done where the company is based (i.e. Europe). This is because on the complexity of production, which to be done in the country targeted would require extremely high initial investments. Therefore, the systems are assembled in Europe and then transported to the target location, where they are distributed to the bases of operation. The first transportation occurs between manufacturing and assembly. To minimise transportation costs, the self-produced parts are already being produced in the general assembly facility, while the outsourced parts are the only ones to be transported there, minimising the transportation resources and logistics before assembly.

For economic and social sustainability, however, it is desired for these bases to be built using solely regional resources, thus generating positions for locals and investing in the country's economy, which is to also help in the cooperation and funding from authorities. In summary, the entire construction of the base, including the acquisition of the solar panels, is to be done in the country of operation, whilst only the drones themselves are sent there. For the future, if development costs of the drone can be lowered and enough capital is available, it is desired to have the manufacturing and assembly of the drones in the country of operation too.

25.5.3. RAMS Analysis

The RAMS aspects of the operation, as extensively explained in [Chapter 24](#), aid in the purpose of an economically sustainable project operation. Together, these aspects aim to have at the base the minimum number of vehicles that suffices the expected needs, thus sparing economic resources and maximising revenue. Firstly, reliability is provided after the extensive risk assessment and mitigation procedures throughout the project, with the final risk score to be set at 1.7, significantly favourable given the five risk levels and the previous score. Secondly, availability also reduces the need for redundancy of systems. For this purpose, as well as to depreciate more easily the initial investments in production and assembly, SAVED is to be deployed for each 248,000 inhabitants, which gives an indication that a system will always be available for a mission. Thirdly, for the purpose of a good maintainability of the system, replaceable batteries and mounting divisions (bolts and clips) have been used. This allows for ease of accessibility when repairing it, which further strengthens the availability of the drones. Lastly, safety has been considered in the design with driving decisions such as the inclusion of a parachute and the avoidance of highly populated areas. This mitigates the risk of the system to hurting others and the system itself in the case of a major fault occurred.

25.6. Social Sustainability

Concerns regarding the use of Unmanned Systems grow by the day, making it important to inquire on the impact they can have on society. For SAVED, these factors have been considered from the start of the project and will continue to be at the forefront of the project's values. This project as a whole presents a short term solution to an otherwise permanent problem: the lack of reliable logistics in developing countries. Delivering medical goods in critical situations where the road access is inefficient makes for a socially focused product. Moreover, to support the creation of healthy, equitable and viable communities, this project as a whole is aiming to hire and train local talent as much as possible, thus investing in the economy and people of the target country.

26

Business Plan and Financials

This chapter explores SAVED's financial feasibility and profitability. [Section 26.1](#) outlines a possible business model for SAVED's operations. [Section 26.2](#) analyses the non-recurring as well as the recurring costs involved in setting up such a business and presents a cost breakdown structure of the drone's production costs. Finally, [Section 26.3](#) estimates the revenue that could stem from this business model, a return on investment (ROI) and possible funding options.

26.1. Business Model

The most important aspects of a potential business model for SAVED are briefly explored in this section.

- **Potential Customer.** This would be a government of a developing country that manifests a need for more efficient healthcare logistics and is severely impacted by the last mile problem - people living in remote, rural areas that do not have good access to vital health products. An example of this would be Sri Lanka.
- **Specific Value Proposition.** The on-demand just-in-time drone delivery of health products (i.e. blood, vaccines and medicines) to remote areas from a centralised inventory will offer benefits such as reduced delivery times, reduced expiries and reduced stock-outs. SAVED will also reduce the last mile problem by making previously inaccessible regions within range of the base and potentially save numerous lives.
- **Partnerships & Stakeholders.** SAVED will have the local government as the main stakeholder for this project as they will be not only the customers but also the suppliers and regulators. The individual hospitals and health centres will be the end-users of the service and are the ones making order requests. Pharmaceutical companies would be useful partners to provide medical expertise for storage and handling of the health products. In more general terms, the local labour force is a stakeholder as SAVED will provide jobs for operators at the base and private investors and non-governmental-organisations (NGO)'s could be potential partners for funding purposes.
- **Revenue Streams.** The principal revenue stream would be the monthly payment made by the government to SAVED. Exact figures would be negotiated and agreed on beforehand with the government and the best price mechanism would be to have a minimum and maximum price per month and then the payment made would depend on the number of deliveries made by SAVED to the health centres. This is the main revenue stream for this business model that should be able to cover the initial costs.

This covers the main components of a potential business model and the following sections will explore in more detail the monetary implications of such business model in order to deduce the project's financial feasibility.

26.2. Cost Analysis

In this section, a cost analysis is conducted on the drone production as well as a high-level consideration of costs of setting up and operating the business outlined in [Section 26.1](#). In [Subsection 26.2.1](#), the development costs are analysed and discussed. Following from that, [Subsection 26.2.2](#) elaborates on the unit production costs. Then, other non-recurring costs that are needed for SAVED to launch are brought into more detail in [Subsection 26.2.3](#). In addition to this, the recurring costs are investigated in [Subsection 26.2.4](#). Finally, in [Subsection 26.2.5](#), the final cost is estimated. Note that the cost analysis is performed based on the Sri Lanka case study.

26.2.1. Development Costs

Development costs account for the research and development involved in the design of a certain product that is being realised¹. In [Subsection 21.1.2](#), the labour costs for an engineer is estimated to be around €150 per

¹<https://bit.ly/2UPGk1D> [Cited on 16/06/2020]

Component	Unit Cost [€]	Amount [-]	Total Cost [€]
x2 Firefly DL Monocolor	285	2	560
x2 Tech Spec Green Series M12	75	2	150
Velabit	100	1	100
PixHawk 4	200	1	200
Raspberry Pi 3B+	40	1	40
PixHawk GPS Antenna	45	1	45
Final Cost			1095

Table 26.1: Simulation & AI cost estimation.

hour. This means that the company will also pay around €150 per hour per employee. This project lasts for ten weeks, whereby one engineer works 8 hours per day. For SAVED, 11 aerospace engineers are working on the design, meaning that the total cost is estimated to be around €660,000. After the DSE, development of this design would continue and an estimate for the extra time used for further development would be another 10 weeks. This yields a total development cost of around €1,320,000. This number is rounded up to €1,400,000 to account for unforeseen activities.

26.2.2. Unit Production Costs

The manufacturing cost has the largest contribution to the unit cost of the drone. The breakdown of this cost is shown on [Table 21.11](#) in [Section 21.5](#). The part cost is estimated to be €5,430. Moreover, the assembly of these parts is found to be €2,350 while €1,900 are added to account for quality control and testing expenses. Finally, the tooling costs were considered to equal around €1,750 per unit. Adding up all these contributions results in a manufacturing cost of €12,130.

For the cost of the Power & Propulsion subsystem, off-the-shelf components are considered. First, the battery must be able to generate sufficient power during a single operation and for its entire lifetime. The chosen battery was the Lithium Polymer battery 'Kokam SLPB065070180'. Three packs of six cells are needed, resulting in a total battery cost of €815.4². For the motors of the drone, the 'KDE4215XF-465' is selected and the 'KDE-CF155-TP' was the selected propeller choice for all four locations. The costs of the motor³ and propellers⁴ are €132.4 and €106.6, respectively. The final cost for the Power & Propulsion subsystem is €1,771.4 without any contingencies included, since all the costs are known and taken from valid sources.

The cost of the autonomous system from the Midterm Report[9] was left unchanged. In [Table 26.1](#) the autonomous system components are listed with each corresponding unit cost. The final cost is €1,095. Again, no contingency factor is added here since all of these components are off-the-shelf and their prices are known.

Some other additional costs for SAVED are considered, namely the parachute and the actuator cost. The chosen parachute is the 'Skycat Bundle Ultra Light' and is found to be €870⁵. In [Section 8.4](#), off-the-shelf actuators were determined for the elevons and the cost was found to be around €300 each.

Adding up all the costs that were obtained in the aforementioned sections yields a final unit cost of approximately €16,500. In [Figure 26.1](#), the entire cost breakdown is shown on a pie chart.

26.2.3. Other Non-recurring Costs

After the drone is designed, a prototype is manufactured and permission has been granted to launch the project in Sri Lanka, it is necessary to determine the cost of setting up this project. This includes setting up the buildings of the bases and the infrastructure of each base. Also, the number of drones per base needs to be taken into account. In [Subsection 22.2.2](#), the number of drones that are required was determined to be 88 drones. The total cost for the drone production is therefore around €1,500,000.

For the infrastructure of a base, the main components were considered in order to arrive at an estimate of the setup costs of a base. The main components include, for example, the solar arrays, the battery charging stations, the hangars and the blood refrigerators. Also, the area on which the base will be built must be taken into account, as this also concerns the cost. Research has been conducted on similar missions such as Zipline and a top-level estimation on the base cost has been performed. A rough estimation method yielded a cost of €100,000 per base. This results in a final estimate of €400,000 for the costs of setting up the four bases.

²Kokam, personal communication. [Cited on 10-06-2020]

³<https://bit.ly/3hxSn0G> [Cited on 16-06-2020]

⁴<https://bit.ly/30U9Pxe> [Cited on 16-06-2020]

⁵<https://bit.ly/2UTFm8b>. [Cited on 18-6-2020]

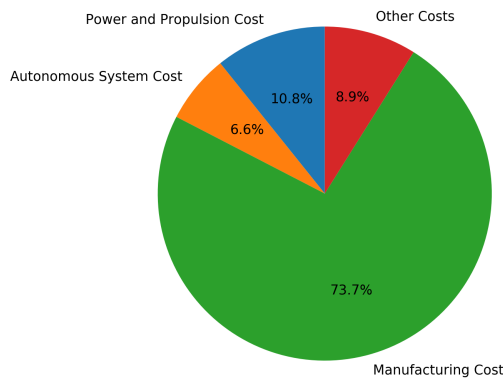


Figure 26.1: Breakdown of SAVED's unit cost.

26.2.4. Recurring Costs

The recurring cost is the cost that is not paid once, but monthly or maybe yearly. This holds for example for the salaries of the employees, who are performing maintenance on the base itself and the drones, preparing the drones for flight, observing the drones during mission, refilling of blood samples, charging the batteries and communicating with clients. After performing research on the salary of a local technician in Sri Lanka, it was determined that one technician will earn around €350 per month. If indirect costs are included, this becomes €800 per month. In one base, there will be around 5 technicians, which is 20 for four bases. This means that monthly €16,500 will be paid on labour costs.

26.2.5. Final Cost

For the final costs of the SAVED's project, the non-recurring costs will be added together. This yields in a final cost of €3,300,000. In addition to this, another €200,000 will be added to consider the uncertainty involved at this stage of the design. This means that €3,500,000 is needed to launch SAVED. When SAVED is launched, the recurring costs will be included, which are around €16,000.

26.3. Revenue Estimation, ROI and Funding

An approximate revenue estimation is useful in informing the financial feasibility. The most similar example of an existing company with such a business model in a comparable country is Zipline's operations in Ghana. The monthly payment made by the Ministry of Health in Ghana to Zipline was therefore used as a reference number. The Ministry pays around US\$88,000 per base per month⁶. Given that Sri Lanka's GDP per capita is almost three times larger than Ghana's and its health expenditure per capita is more than double, a factor was applied to this monthly payment to consider Sri Lanka's increased willingness and ability to pay for a similar service. A factor of 2 was applied, which also takes into consideration the increased benefit of SAVED's service when compared to Zipline's, especially regarding the VTOL capability that allows for a wider variety of missions. Converting this to euros yields a monthly payment by the Sri Lankan government of around €150,000 per base. This implies an approximate total revenue of €600,000 per month.

Given the current estimates, it is possible to estimate the time taken to cover the costs and start making profits, also known as the break-even point. Current values estimate that SAVED would break-even after 6 months of operating this business. Moreover, after one year, a profit of around €3.5M would be obtained. This represents an 100% return on investment after just one year of operations. This means that the entire €3.5M in initial costs would be covered and an additional 100% would have been generated. If the return on investment is calculated for the first three years, this value could potentially skyrocket to 500% ROI.

Given the prospects of financial feasibility, there are two types of institutions that could be considered for funding the initial costs. The first group of institutions are private investors, seeking to invest in high-risk, high-reward ventures. A second type concern private and public foundations as well as NGOs and other nonprofits, focused on the enhancement of healthcare and reduction of poverty around the world. A good example would be the Bill and Melinda Gates Foundation, which has granted over US\$4M to Zipline's efforts in Africa⁷.

⁶<https://bit.ly/2YQOSd6> [Cited 15-06-2020]

⁷<https://gates.ly/2zYwgje> [Cited 15-06-2020]

Concluding Remarks

There is a growing need for the delivery of small crucial cargo such as medicine to remote and inaccessible areas. The concept of SAVED offers a promising solution to this two-folded problem. SAVED combines the long-range capabilities of a fixed-wing drone with the Vertical Take-off and landing accessibility of multi-rotor drones. In this feasibility study, it was found using theoretical analysis and empirical estimation methods that the envisioned design proved capable of autonomously delivering a payload of up to 3kg at a range of 150km. Its wing design, autonomous control system and engine configuration provide the aerodynamic efficiency of conventional tailless designs without the typical drawbacks in stability and control. The sustainable design approach resulted in a fully electric operational concept, in which both the drone and its supporting operational infrastructure are powered solely on sustainable energy sources. Additionally, the innovative structural design of SAVED offers a modular and easy to disassemble design, yielding both excellent maintainability and recyclability properties. Throughout the conceptual design process, technical risk assessment played a crucial role, which yielded a safe and reliable product. SAVED is estimated to achieve all these feats at comparable or lower cost compared to existing systems.

This conceptual study proves the potential of the design solution SAVED offers. In the next phases, this potential has to be further evaluated. Key in this process are scale model wind-tunnel tests and extensive simulations to validate the aerodynamic efficiency and controllability characteristics. When this proves successful, full-scale prototyping can start and SAVED can start test operations.

All in all, SAVED promises an innovative solution to an increasingly relevant humanitarian problem. The conceptual study found promising results which indicates the potential of further research on this concept.

References

- [1] Certification specifications for very light aeroplanes cs-vla. Technical report, European Aviation Safety Agency, 2009.
- [2] A. Granta. CES Selector, 2020.
- [3] J. D. Anderson. *Fundamentals of aerodynamics*. McGraw-hill Publishing Co., 2007.
- [4] J.D. Anderson. *Introduction to Flight*. 2015.
- [5] C.V. Angelino, V.R. Baraniello, and L. Cicala. High altitude uav navigation using imu, gps and camera. pages 647–654, 01 2013. ISBN 978-605-86311-1-3.
- [6] B. Aulet. *Disciplined Entrepreneurship: 24 Steps to a Successful Startup*. John Wiley & Sons, Inc., 2013.
- [7] A. Bacchini, E. Cestino, and G. Romeo. PhD thesis.
- [8] I. Benyahia, C. Bononi Bello, P. Campolucci, M. Desiderio, R. van Ewijk, C. Kanaar, M. Martinez Ruts, A. Nederkoorn, E. Perestrelo, E. Rodriguez, and M Travnik. Design synthesis exercise baseline report group16. Technical report, TU Delft, 2020.
- [9] I. Benyahia, C. Bononi Bello, P. Campolucci, M. Desiderio, R. van Ewijk, C. Kanaar, M. Martinez Ruts, A. Nederkoorn, E. Perestrelo, E. Rodriguez, and M Travnik. Design synthesis exercise midterm report group16. Technical report, TU Delft, 2020.
- [10] I. Benyahia, C. Bononi Bello, P. Campolucci, M. Desiderio, R. van Ewijk, C. Kanaar, M. Martinez Ruts, A. Nederkoorn, E. Perestrelo, E. Rodriguez, and M Travnik. Design synthesis exercise project plan group16. Technical report, TU Delft, 2020.
- [11] E. Smeur K. van Hecke F. van Tienen E. van der Horst B. Remes C. De Wagter, R. Ruijsink. Design, control, and visual navigation of the delftacopter vtol tail-sitter uav. Technical report, TU Delft, 2018.
- [12] J. Carvill. *Mechanical Engineer's Handbook*. Elsevier, 2009.
- [13] V.P. Castelli and M. Gatti F. Giulietti. Design and prototyping high endurance multi-rotor. Technical report, Universit'a di Bologna, 2015.
- [14] P. Chung, D. Ma, and J. Shiao. Design, manufacturing, and flight testing of an experimental flying wing uav. *Applied Sciences*, 9(15):3043, 2019.
- [15] M. Coppola, K.N. McGuire, C. De Wagter, and G.C.H.E. de Croon. A survey on swarming with micro air vehicles: Fundamental challenges and constraints. *Frontiers in Robotics and AI*, 7:18, 2020. ISSN 2296-9144. doi:10.3389/frobt.2020.00018.
- [16] Teal Group Corporation. 2019 world civil unmanned aerial systems market profile & forecast. Technical report, Teal Group Corporation, 2019.
- [17] M.J. Crocker. *Handbook of Acoustics*. John Wiley & Sons Inc., 1998.
- [18] F. de Melo Constanzo. Theoretical and experimental analysis of the fuselage influence on the wing aero-dynamic center position at low speed conditions. *22nd International Congress of Mechanical Engineering*, 11 2013.
- [19] A. Deperrois. Modal analysis and experimental validation, 2011.
- [20] Allen F. Donovan. *Aerodynamic components of aircraft at high speeds*. Princeton University Pres, 2016.
- [21] Mark Drela. Xflr5, 2003.
- [22] D.G. Dunn and N.A. Pealx. Aircraft noise source and contour estimation. Technical report, NASA, 1973.
- [23] H. Durrant-Whyte and T. Bailey. Simultaneous localization and mapping: part i. *IEEE Robotics Automation Magazine*, 13(2):99–110, 2006.

- [24] M.O. Dündar and T.Ü. Bilici. Design and performance analyses of a fixed wing battery vtol uav. *Elsevier*, 02 2019.
- [25] H.K. Epema. *Wing Optimisation for Tractor Propeller Configurations*. 2017.
- [26] R. Eppler. Praktische berechnung laminarer und turbulenter absauge-grenzschichten. *Ingenieur-Archiv*, 32(4):221–245, 1963. doi:10.1007/bf00533036.
- [27] R. Eppler. Turbulent airfoils for general aviation. *Journal of Aircraft*, 15(2):93–99, 1978. doi:10.2514/3.58320.
- [28] S. Esteban. Static and dynamic analysis of and unconventional plane: Flying wings. *University of Missouri-Rolla*, 01 2010.
- [29] M. Farner. Jarus cs-luas recommendations for certification specification for light unmanned aeroplane systems. Technical report, JARUS, 2016.
- [30] M. Gerritsma and A. Sciacchitano. *Project Guide Design Synthesis Exercise*. Delft University of Technology, 2020.
- [31] World Bank Group. *SRI LANKA: Country Snapshot - October 2015*. World Bank Group, 2015.
- [32] R.J. Hamann. System engineering & technical management techniques. Technical report, 2006.
- [33] W. Heike. Framework for the evaluation of cost-effectiveness of drone use for the last-mile delivery of vaccines. Technical report, 2017.
- [34] M. Hepperle. Javafoil, 1996.
- [35] M. Hepperle. Javafoil's user guide. Technical report, 2017.
- [36] M. Hepperle. Basic Design of Flying Wing Models, 2018.
- [37] S.F. Hoerner. *Fluid Dynamic Lift*. L. Hoerner, 1985.
- [38] H.H. Hubbard. Propeller-noise charts for transport airplanes. Technical report, NASA, 1993.
- [39] A.L. Kaczmarek, M. Szwoch, and D. Bartoszewski. Using open source libraries for obtaining 3d scans of building interiors. In L. Borzemski, J. Świątek, and Z. Wilimowska, editors, *Information Systems Architecture and Technology: Proceedings of 39th International Conference on Information Systems Architecture and Technology – ISAT 2018*, pages 201–210, Cham, 2019. Springer International Publishing. ISBN 978-3-319-99981-4.
- [40] P. Kaniewski and W. Grzywacz. Visual-based navigation system for unmanned aerial vehicles. In *2017 Signal Processing Symposium (SPSympo)*, pages 1–6, 2017.
- [41] C. Kassapoglou. *Design and Analysis of Composite Structures: With Applications to Aerospace Structures*. Wiley, 2010.
- [42] Kokam. Kokam technical data sheet rev.1.6. Technical report, 2020.
- [43] J.G. Leishman. *Principles of Helicopter Aerodynamics*. Cambridge University Press, 2006.
- [44] T. Liu and S. Shen. High altitude monocular visual-inertial state estimation: Initialization and sensor fusion. In *2017 IEEE International Conference on Robotics and Automation (ICRA)*, pages 4544–4551, 2017.
- [45] O. Lorenzo, J. Martínez Sánchez, D. Vilariño, T. Pena, J. Cabaleiro, and F. Rivera. Landing sites detection using lidar data on manycore systems. *The Journal of Supercomputing*, 73, 11 2016. doi:10.1007/s11227-016-1912-7.
- [46] J.E. Made and D.W. Kurtz. A review of aerodynamic noise from propellers, rofors, and liff fans. Technical report, NASA, 1970.
- [47] A. Majka. Flight loads of mini uav. Technical report, Rzeszów University of Technology, 2013.
- [48] G. Mao, S. Drake, and B. Anderson. Design of an extended kalman filter for uav localization. pages 224 – 229, 03 2007. ISBN 1-4244-0902-0. doi:10.1109/IDC.2007.374554.
- [49] T.H.G. Megson. *Aircraft Structures for Engineering Students*. Elsevier Aerospace Engineering Series, 2017.

- [50] J.A. Mulder, W.H.J.J. van Staveren, J.C. van der Vaart, E. de Weerdt, C.C. de Visser, A.C. in 't Veld, and E. Mooij. *Flight Dynamics Lecture Notes*. TU Delft, 2013.
- [51] R. Nederlof. *Improved modeling of propeller-wing interactions with a lifting-line approach*. 2020.
- [52] K. Ngo and T.L. Huynh. *Airfoil Selection for Fixed Wing of Small Unmanned Aerial Vehicles*, pages 881–890. 03 2016. ISBN 978-3-319-27245-0. doi:10.1007/978-3-319-27247-4_73.
- [53] F. Oliviero. Systems Engineering and Aerospace Design Lecture Slides. Brightspace, mar 2020.
- [54] F. Oliviero. Aerospace design & systems engineering elements ii: Aircraft part, May 2020.
- [55] N.W.L. Pann, L.K. Nang, and M.T. Hla. Longitudinal and lateral dynamic system modeling of a fixed-wing uav. *University of Missouri-Rolla*, 04 2017.
- [56] P. Pinggera, D. Pfeiffer, U. Franke, and R. Mester. *Know Your Limits: Accuracy of Long Range Stereoscopic Object Measurements in Practice*. Springer, Cham, 2014.
- [57] C. Rans. Structural Analysis and Design Lecture 6: Structural Idealisations, 2019.
- [58] D.P. Raymer. Aircraft design: A conceptual approach. 2004.
- [59] J. Redmon, S. Divvala, R. Girshick, and A. Farhadi. You only look once: Unified, real-time object detection. In *2016 IEEE Conference on Computer Vision and Pattern Recognition (CVPR)*, pages 779–788, 2016.
- [60] Joseph Redmon and Ali Farhadi. Yolov3: An incremental improvement, 2018.
- [61] J.W. Rosen. Zipline expands drone delivery of medical supplies. *MIT Technology Review*, 08 2017.
- [62] G.J.J. Ruijgrok. *Elements of airplane performance*. Delft Academic Press, Delft, 2013.
- [63] D. Scaramuzza and Z. Zhang. Visual-inertial odometry of aerial robots, 2019.
- [64] M. Scherrer, N. Quendez, and C. Döll. An analytical aproach to trimming and performance coupling of flying wings. *24th International Congress of The Aeronautical Sciences*, 9 2004.
- [65] L.V. Schmidt. *Introduction to aircraft flight dynamics*. American Institute of Aeronautics and Astronautics, 1998.
- [66] T. Sinnige, N. Van Arnhem, T.C.A. Stokkermans, G. Eitelberg, and L.L.M. Veldhuis. Wingtip-mounted propellers: Aerodynamic analysis of interaction effects and comparison with conventional layout. *Journal of Aircraft*, 56(1):295–312, 2019. doi:10.2514/1.c034978.
- [67] X. Song, X. Zhao, L. Fang, and H. Hu. Edgestereo: An effective multi-task learning network for stereo matching and edge detection, 2019.
- [68] P. Tortora, , B. Wang, Z. Hou, Z. Liu, Q. Chen, and X. Zhu. Preliminary design of a small unmanned battery powered tailsitter. *International Journal of Aerospace Engineering*, 05 2016.
- [69] J. Trevelyan. *The making of an expert engineer*. CRC press, 2014.
- [70] E. Triantaphyllou and A. Sánchez. A sensitivity analysis approach for some deterministic multi-criteria decision-making methods*. *Decision Sciences*, 28:151 – 194, 01 1997. doi:10.1111/j.1540-5915.1997.tb01306.x.
- [71] L.L.M. Veldhuis. *Propeller Wing Aerodynamic Interference*. PhD thesis, 2005.
- [72] R. Vos and J. Melkert. 1aerospace design andsystems engineering elements i: Wing and propulsion system design, 2018.
- [73] J.E Williams and S.R. Vukelich. The USAF stability and control digital DATCOM. Volume II. Implementation of DATCOM methods. Technical report, MCDONNELL DOUGLAS ASTRONAUTICS CO ST LOUIS MO, 1979.
- [74] G.A. Williamson, B.D McGranahan, B.A. Broughton, R.W. Deters, J.B. Brandt, and M.S. Selig. *Summary of Low-Speed Airfoil Data*, volume 5. 2012.
- [75] Wingtra. Wingtraone drone technical specifications. Technical report, Wingtra AG, 2020.